Electronic Theses and Dissertations

1988

Electric field distribution and flashover voltage measurements of shaped spacers in compressed gases.

Mohamed Sayed Mohamed. Rizk
University of Windsor

Follow this and additional works at: http://scholar.uwindsor.ca/etd

Recommended Citation

NOTICE

AVIS

The quality of this microform is heavily dependent upon the quality of the original thesis submitted for microfilming. Every effort has been made to ensure the highest quality of reproduction possible.

If pages are missing, contact the university which granted the degree.

Some pages may have indistinct print especially if the original pages were typed with a poor typewriter ribbon or if the university sent us an inferior photocopy.

Previously copyrighted materials (journal articles, published tests, etc.) are not filmed.

Reproduction in full or in part of this microform is governed by the Canadian Copyright Act, R.S.C. 1970, c. C-30.

La qualité de cette microforme dépend grandement de la qualité de la thèse soumise au microfilmage. Nous avons tout fait pour assurer une qualité supérieure de reproduction.

S'il manque des pages, veuillez communiquer avec l'université qui a conféré le grade.

La qualité d'impression de certaines pages peut laisser à désirer, surtout si les pages originales ont été dactylographiées à l'aide d'un ruban usé ou si l'université nous a fait parvenir une photocopie de qualité inférieure.

Les documents qui font déjà l'objet d'un droit d'auteur (articles de revue, tests publiés, etc.) ne sont pas microfilmés.

La reproduction, même partielle, de cette microforme est soumise à la Loi canadienne sur le droit d'auteur, SRC 1970, c. C-30.

Canadä

ELECTRIC FIELD DISTRIBUTION AND FLASHOVER VOLTAGE

MEASUREMENTS OF SHAPED SPACERS

IN COMPRESSED GASES

by

MOHAMED SAYED MOHAMED RIZK

A Dissertation
Submitted to the
Faculty of Graduate Studies and Research
through the Department of
Electrical Engineering in Partial Fulfillment
of the requirements for the Degree
of Doctor of Philosophy at
the University of Windsor

Windsor, Ontario, Canada
1988

DEDICATION

TO MY PARENTS

ABSTRACT

Spacer profiles are proposed and examined both experimentally and theoretically to yield improved withstand voltage at high gas pressures of SF_6 and nitrogen. Typically the dc flashover voltage of a 10 mm long spacer increased by up to 23% using a concave shape over a rectangular cylindrical spacer. The flashover voltage using dc, ac (50 Hz) and 1.2/50 us lightning impulse of the shaped spacers has been measured using the gases SF_6, N_2, air, CO_2 and H_2 at different pressures in the range (1 to 7) x 10^5 Pa (1 to 7 bar). The spacer efficiency which is defined as the ratio of the surface flashover voltage of a spacer to the gas breakdown voltage with the absence of the spacer can be increased to 96% by using this profile.

A computation of the potential and the electric field distributions of a concave spacer, aimed to optimize the design of the spacer, has been made using the charge simulation technique. The optimum contact angle of the spacer with the conductor is determined to be 45°. A significant reduction in both the tangential and the total field at the triple junction has been achieved by using the proposed profiles. The dependence of the electric field on the radius, contact angle, length, radius of curvature and

permittivity of the spacer has been studied. Also the electric field at locations inside and outside the solid dielectric spacer has been calculated.

An analytical study of the critical avalanche length and the space charge field at the onset of the breakdown has been carried out in SF_6 and N_2. A good agreement between the space charge field and the breakdown field (calculated from the flashover measurements and the calculated electric field) has been found in SF_6 and N_2.

The effect of a recess in the conductor and a metal insert into the spacer on the electric field distribution has been examined. The normalized electric field at the cathode junction of an electrode geometry with a groove in one electrode to hold the spacer decreases when a metal insert is used. The depth of the metal insert causes a larger reduction in the electric field than its diameter. The dependence on the recess angle, depth of the recess, length of the spacer, permittivity, radius of the groove and dimensions of the metal insert on the electric field distribution has been studied.

The flashover voltage of a cylindrical spacer placed between recessed electrodes and with a metal insert into the spacer has been measured in SF_6 and N_2 for different values of pressure. The efficiency of the spacer under ac can be increased in SF_6 to 92% with recessed electrodes (recess angle =60°) and to 30% with metal inserts into the spacer.

The dc surface flashover decreases by almost 12% in SF_6 and N_2 when 5 spacers placed in parallel are used instead of one. However the reduction in the flashover voltage is only 7% when the contact area of a single spacer with the electrodes increases by 5 times.

ACKNOWLEDGEMENTS

TABLE OF CONTENTS

FIGURE CAPTIONS

TABLE CAPTIONS

NOMENCLATURE

V	Applied voltage to the top electrode
E_g	Electric field in the gas
E_d	Electric field in the dielectric
ε_r	Relative permittivity of dielectric
ϕ	Computed potential
S	Space charge density
P_{ij}	Associated potential coefficient at a contour point i due to charge at a location j
F_{ij}	Associated electric field coefficient at a contour point i due to charge at a location j
d_q	Distance between contour point and its corresponding charge
d_c	Distance between two successive contour points
β	Assignment factor = d_q/d_c
ε_0	Permittivity of free space
E_{n_1}	Computed normal electric field in the gas side
E_{n_2}	Computed normal electric field in the dielectric side
ε_1	permittivity of gas
ε_2	permittivity of dielectric

L	Gap distance between the electrodes
E_{av}	Average electric field in the gap = V/L
ϕ^*	Normalized potential = ϕ/V
Z	Axial distance determined from bottom electrode
Z^*	Normalized distance = Z/L from bottom electrode
θ	Angle between the tangent to the surface of the insulator and the normal to the electrode at the contact point of the triple junction
R_o	Minimum radius of the solid insulator
E^*t_1	Normalized tangential field in the gas side
E^*t_2	Normalized tangential field in dielectric side
E^*n_1	Normalized normal field in the gas side
E^*n_2	Normalized normal field in the dielectric side
E^*T_1	Normalized total electric field calculated in the gas side
E^*T_2	Normalized total electric field calculated in dielectric side
E^*n_1c	Normalized normal field calculated at the triple junction
E^*t_1c	Normalized tangential field calculated at the triple junction
E^*T_1c	Normalized total field calculated at the triple junction
E^*T_1a	Normalized total electric field at the anode junction
E^*t_1m	Normalized maximum tangential field
E^*n_1m	Normalized maximum normal field
E^*T_1m	Normalized maximum total field

E^*z_1	Normalized axial field in the gas side of the interface
E^*z_2	Normalized axial field in the dielectric side
r	Radius of groove edge
r_0	radius of the corner of metal insert
w	Diameter of the metal insert
t	Thickness of the metal insert
d	Depth of the recessed electrode
γ	Angle between the solid insulator and the inclined edge of the recessed electrode
R_a	Radius of the concave section profile 'a'
R_b	Radius of the concave section profile 'b'
R_c	Radius of the concave section profile 'c'
R_d	Radius of the concave section profile 'd'
R_x	Radius of the convex section profile 'b'
R_y	Radius of the convex section profile 'd'
α	Townsend's first ionization coefficient
η	Electron attachment coefficient
ν	Secondary ionization coefficient
$\bar{\alpha}$	Net ionization coefficient $\bar{\alpha} = \alpha - \eta$
n_0	Initial number of electrons emitted from the cathode
N	Gas density
N_c	Critical number of electrons
E_r	Space charge field
Z_c	Critical avalanche length

Chapter I

INTRODUCTION

With the increased economic activity throughout the industrialized countries and particularly in North America, Europe and Japan, the demand for electric power is beginning to rise. This necessitates development of additional distribution and transmission systems. Compressed Gas insulated transmission (CGIT) cables, substations and switchgear have been found suitable to meet the increased demand for power particularly in large cities during the seventies and they are also likely to be so in the future [1-3].

Compressed sulphur hexafluoride (SF$_6$) gas is being widely used as an insulating medium for many applications in gas insulated systems including cables, transmission systems, circuit breakers, current transformers, high voltage test transformers, and other high voltage apparatus and equipment [2-5]. The construction of high voltage systems usually incorporates solid dielectric spacers for supporting the high voltage conductor. The withstand voltage of the spacer is generally lower than that of the insulating gas [2,7]. Therefore it is desirable to increase the voltage hold-off capability of the spacer by suitable designs so that it is as close as possible to that offered by the gas alone.

1.1 Advantages of GIS

Gas insulated systems (GIS) have several advantages over conventional systems as summarized below [1,2,6,7,8]:

1. Excellent voltage insulating properties which can apply to all voltage ratings. For SF_6 the dielectric strength is from 2.5 to 3.0 times higher than that of air.

2. Smaller capacitance compared to conventional oil impregnated paper cable, therefore longer lengths of cable can be installed without a need for reactive power compensation.

3. Lower dielectric losses because of the lower permittivity of the gas i.e. lower loss tangent compared to oil impregnated paper cables.

4. Compressed gases have better efficiency of heat convection between conductor and sheath and hence offer a possibility of using larger current carrying capacity.

5. Offer considerable saving in size compared to air. Typically for switchyard the ratio of space requirements for air/SF_6 is 10 to 1.

1.2 Support Insulators

The use of gas insulated systems requires a solid insulator(spacer) for the physical support of high voltage conductors. It has been reported by many authors that the

critical part in the overall design of GIS is the insulating spacer [3,9-12]. It has been considered to be one of the factors which affects the reliability and the efficiency of gas insulated systems.

The insulation level of GIS is governed by the flashover voltage of the spacers used. This is because the presence of the spacers leads to a reduction of the withstand voltage capability of the whole system as the surface flashover voltage of the solid dielectric is lower than the breakdown of the gas by itself [2,7,13-20]. An increase in the withstand voltage capability of the spacers would lead to improvement in the reliability and/or a reduction in the size, weight and cost of gas insulated apparatus and equipment [13].

There are many factors influencing the surface flashover of the insulating spacer which need to be studied before they can be controlled.

1.3   Review of Previous Work

The flashover voltage of insulating spacers is a function of many factors including, spacer-conductor-gas (triple junction), spacer shape and dimensions, spacer material, type of voltage application, particle and surface contamination, type of gaseous insulation and pressure, and shape and dimensions of the conductors.

1.3.1 Spacer-conductor-gas (triple junction)

The spacer-conductor-gas (triple junction) at the cathode is the source for the initiatory electrons which ultimately lead to the surface flashover of the spacer [4,15,21,22]. Due to possible imperfections in the contact of the spacer with the conductor, the electric field in the contact region could be enhanced by a factor close to the relative permittivity of the solid dielectric. The higher localized field could lead to the development of a discharge in the gas pocket between the spacer and the conductor, which ultimately extends to a full surface flashover [23-25].

In addition to maintaining clean environment and providing particle traps various methods of increasing the withstand voltage capability of insulating spacers have been reported. These include casting the spacer directly onto the conductor, shielding the triple junction, and metallizing the spacer surfaces in contact with the electrodes. An important method is shaping the insulator profile at the electrodes in order to reduce the electric stress at the triple junction [4,12,14,26,27].

1.3.2 Spacer material

There has been continuous interest to develop new insulating materials to satisfy the requirements of volume and surface stresses in addition to thermal and mechanical stresses. The properties considered in the selection of the spacer material for GIS are: 1) Permittivity of the spacer;

2) Dielectric strength; 3) Surface and volume resistances; 4) Arc tracking resistance; 5) sensitivity of the material to contamination and decomposition of SF_6 during discharges; 6) mechanical properties; 7) ease of manufacture; 8) operating temperature and 9) Impact resistance.

The flashover voltage is dependent on the relative permittivity εr. Generally, there is a reduction in the flashover voltage with increasing εr. This is because the material with a high permittivity results in an increased local field at the surface of the irregularity of the spacer [2,4,18].

If we assume that the thickness of a spacer having a permittivity εr is d and a very small gas gap of thickness g is present between the spacer and the electrode, then under a uniform field condition,

$$V = Eg \cdot g + Ed \cdot d \qquad (1.1)$$

where V is the applied voltage, Eg and Ed are the electric fields in the gas and in the solid dielectric, respectively. The relation between Eg and Ed is

$$Eg = \varepsilon r \cdot Ed \qquad (1.2)$$

From equations (1.1) and (1.2) .

$$V = Eg \cdot g + (Eg/\varepsilon r) \cdot d \qquad (1.3)$$

$$Eq \stackrel{*}{=} \frac{\varepsilon_r \cdot V}{\varepsilon_{r-q} + d} \qquad (1.4)$$

If $d \gg \varepsilon_r \cdot q$

$$Eq = \varepsilon_r \cdot V/d \qquad (1.5)$$

It is preferable to use a material with a lower permittivity to reduce the intensification of the local field in the gap if present between the spacer and the electrodes.

Only cast epoxy spacers are used in service in GIS and CGIT. Porcelain has been used extensively in outdoor insulators [2,13,15,28] and has the disadvantage of high permittivity and lower dielectric strength. Thermoplastics [13,18,25,28,29,30] have been widely used in other than GIS applications as insulating materials but they are easily deformed at high temperature arcs, especially Polypropylene and Polycarbonate. Teflon has a low permittivity, but poor arc tracking resistance. Machinable Macor glass- ceramic also suffers from the same problem at high gas pressures.

Cycloaliphatic epoxy resin in conjunction with alumina, silica or aluminum trihydrate as fillers has been used in GIS [12,24,31,32,33]. It has the advantage of high arc track resistance and excellent electrical properties, but it suffers from the disadvantage of higher permittivity, and irregularities on its surface produced during casting.

1.3.3   Spacer_profiles

1.3.3.1   Cylindrical spacer

For better understanding of the physical phenomena involving surface flashover as well as the factors influencing the flashover characteristics in gas insulated systems, cylindrical spacers in uniform field have been widely used [9,15,18,20,21,22,25,34,35]. For the right angle cylindrical spacer, the flashover is mainly affected by the quality of the contact between the spacer and the electrode and the surface condition of the spacer [2,18,35].

1.3.3.2   Post spacer

The post type spacer has been used in GIS as a physical support because it has the advantages of simplicity, less surface area to collect contaminant particles and relatively low cost, especially at UHV [7,32,36,37]. Metal inserts have been used with this profile to fulfill the requirements of mechanical connection at one or both ends in addition to reducing the electric field along the surface of the spacer and at the spacer conductor interface. The geometry of the post spacer has been optimized depending on the electrode configuration, the geometry of the metal insert and the permittivity of the insulator material [37]. This design has the advantage of a lower electric field along the surface of the spacer and a higher surface flashover voltage. However,

the major disadvantage is that the electric field between the metal inserts, within the insulator, increases because of the reduced gap length between the metal inserts. The higher field could lead under extreme conditions to the onset of partial discharges and a volume breakdown of the spacer [7].

In order to reduce the possibility of volume breakdown with metal inserts at both ends another design has been used in which the post spacer is cast directly onto the inner conductor of the coaxial system with a metal insert at the other end of the spacer. It was reported that this design had a lower internal field than the first type [24,38,39,40]. The corrugated insulator has been successfully utilized in outdoor systems because under a contaminated environment the performance is improved with increasing the creepage length. For this reason, some designers tried to test a corrugated spacer in compressed gas insulated systems, but the results were conflicting. In some cases, the flashover decreased [4,7,13], increased or had no effect [8,13,41,48] on the flashover voltage. However, corrugated spacers appear to have a better performance for contaminated conditions in gas insulated systems [3].

1.3.3.3   Disc spacer

The disc spacer has been used in the earliest GIS systems as a physical support [6,8,29,42,43,44,45] and as a gas barrier [12,14] because it is easier to manufacture and costs less than other profiles. Optimal profiles for a disc spacer have been determined [14]. The electric field along the surface of a disc spacer has been calculated for different contact angles with the conductor by using the charge simulation technique. It has been found that the optimal contact angle is within 60° - 70° depending on the permittivity and the spacer dimension and this leads to 20 to 30% decrease in the maximum field strength [14]. A corrugated disc spacer has been tested under ac and transient voltages. It reduces the performance by 20% under ac voltage, but it has more consistent performance than a smooth disc, particularly for a transient voltage [8].

Disc spacers with a special design have been developed for a flexible gas cable [45,46]. The spacer is of the split design having a thin I-beam cross-section with two halves clamping around the conductor and clipping together.

1.3.3.4   Conical spacer

The conical insulator has been used as a mechanical support for H.V. conductors and as a termination (stop joint) for gas insulated systems [8,33,47,48]. It was cast directly onto the conductor or captured between the flanges. An effort has been made to optimize the angle and the shape

of the conical spacer [14,49]. The cone spacer is less sensitive to contaminant particles than the disc spacer.

There are several new spacers which have been designed and tested for the application of GIS, but still none of them have been used in service [50]. The concept of the new designs is built on shaping the insulator to overcome the problem of highly stressed regions, in addition to lowering the cost of installation.

Multibladed spacers have a feature which makes them especially suitable for using in flexible cables with a high power rating [45]. The star shaped or trefoil and tripost spacers result in a higher flashover voltage compared to the conventional spacers and are suitable for flexible cables [50,51].

1.3.4   Type of voltage application

The surface flashover voltage of a spacer depends on the type of the applied voltage: ac, dc, and transient (lightning and switching impulses).

The voltage distribution within and along the surface of the spacer under ac and impulse conditions is determined by the capacitance grading, and therefore the voltage distribution is dependent on the relative permittivity (ε_r). Under-dc conditions, the situation is different because the voltage distribution will be determined by the resistivity of the dielectric material [4,13].

dc gas insulated systems have been developed and tested for use in HVDC transmission. The potential distribution near the spacer surface in the case of dc voltage application is modified due to the large accumulation of surface charges. The surface charges distort the local electric field, · leading to a reduction · in the flashover voltage [52-56]. The surface charge has been measured on cylindrical, post and conical spacers [52,57]. It has been found that the charge accumulated on the surface of the spacer was strongly influenced by the surface condition, the material and the applied ·electric stress. For HVDC applications, improved designs must be further developed to reduce the effect of insulator charging.

1.3.5 Contamination effect

The contaminants in gas insulated systems are mainly free particles and surface contaminants.

Particle contaminants might be introduced to the system during welding, with the gas filling or originate from friction between components. They have a deleterious effect on the dielectric performance of GIS. Particle contaminants can lower the gas breakdown voltage and the surface flashover voltage by more than 50% and the reduction becomes even larger at very high applied electric stress [4,8,9,32].

The flashover voltage of a spacer strongly depends on the position, the shape and the size of the particle and whether it is conductive or dielectric. It was reported that the

reduction in the flashover voltage became more pronounced when the particle was close to the high voltage conductor and placed radially on the spacer surface [58]. A conical insulator showed a better performance than that of the disc spacer under impulse conditions. Corrugated spacers gave relatively better flashover performance in contaminated conditions compared to without corrugations [8].

The surface of the spacer can be contaminated with other materials such as oil, grease, moisture, decomposed by-products from arcing and charged particles from the gas under the influence of the electric field. It has been reported that clean oil has little effect on the flashover voltage of the spacer under ac or impulse voltages, but the flashover voltage might decrease by 25% under dc voltage [4].

The dielectric performance of the spacer decreases considerably, by more than 50%, due to condensation of moisture on the surface. The level of water content in GIS must be less than 200 ppm for best dielectric performance [9]. Therefore, it is necessary to maintain a cleanliness in GIS at a very high level.

Since the charged particles in the gas move under the influence of the electric field traps have been designed and used in GIS to keep the particles in a region of low electric field. Details of some particle traps can be found in [1,59].

1.3.6 Flashover voltage measurement in compressed gases

The flashover voltage of spacers has been determined in different compressed gases and gas mixtures in order to obtain the best performance of both the solid dielectric and the gaseous media under high electric stress.

Spacers have been tested in many gases such as CO_2 [13], air [13,15], N_2 [5,11,13,18,22] and CCL_2F_2 [6,15,17]. It has been found that there is not much difference between the flashover voltage in air and N_2, especially at lower gas pressures for the same conditions. In CO_2, the flashover voltage appears to be lower than in N_2 and in air. CCL_2F_2 (Freon) has a high dielectric strength but when exposed to an arc discharge it dissociates into large amount of excited carbon which may deposit on the spacer surface [6]. This reduces the flashover voltage of the spacer. Investigation of the flashover characteristics in compressed helium has been carried out for filling the gap between the tubes in super conducting cables [34]. Also, the flashover voltage in $CCL_2F_2-N_2$ and CCL_2F_2-air has been measured [15,17].
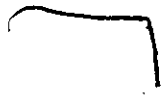
However, most of the work in the literature refers to SF_6 as it is commonly used in GIS. This is because it has an excellent insulating strength, is chemically stable and has superior electric and thermal performances [6,7,8,9,12,24,29,33,50,54]. Gas mixtures, like SF_6-N_2, $SF_6 - CO_2$ and SF_6-air have been studied [13,20,58,60] because of their potential cost reduction, lower incidence of particle

induced flashover and lower liquification temperatures. However, there are still some questions concerning the reliability and the cost effectiveness of the proposed mixtures which need to be addressed before adoption in the industry as summarized in [61].

1.4   Scope of This Research

Since gas insulated systems have been brought to service in 1969, support insulators remain the most critical part in the design [1,62]. It has been reported that the spacer is as much a quality problem as it is a design problem [63] and it should be properly designed to minimize the degradation in the dielectric performance of GIS [8,9,12,19]. In order to enhance the reliability of GIS and/or reduce the size of the equipment, the flashover field of the spacer should be increased. One way of achieving this is by optimizing the design of the spacer to yield a higher withstand voltage under the same operating conditions. In general more research to obtain better designs and improved performances of spacers would be valuable.

The objectives of this research study are:

1.   To optimize the spacer design by a suitable shaping of its profile.

2.   To reduce the local field at the triple junction, which is the source of electrons for initiating discharges.

3. To study the effect of different parameters, such as length, diameter and permittivity of the spacer, contact angle and shielding the triple junction on the potential and electric field distributions.

4. To determine the flashover voltage characteristics for different contact angles, different gases and different pressures.

5. To study the effect of the contact area and the number of parallel spacers on the total withstand voltage.

6. To study the effect on the surface flashover of shaping the conductors, by using either a recess in one or in both conductors.

7. To investigate the effect of metal inserts into the spacer on the field distribution and the flashover voltage of the spacer.

Chapter II

APPLICATION_OF_CHARGE_SIMULATION_TECHNIQUE_TO

H.V._INSULATOR_DESIGN

2.1   Introduction

A knowledge of the potential and the electrical field distributions is necessary in order to maximize the withstand voltage when designing H.V. systems.

The computation of the potential and the electric field distributions requires the solution of Laplace's or Poisson's equations. The field equation in any homogenous medium is given by Poisson's equation,

$$\nabla^2 \phi = - S/\varepsilon \qquad (2.1)$$

where ϕ = potential,

S = space charge density

ε = permittivity of the medium.

If the space charge is zero, the above equation becomes Laplace's equation,

$$\nabla^2 \phi = 0 \qquad (2.2).$$

The solution to equations (2.1) or (2.2) can be obtained either analytically or by numerical methods. Since the physical systems are often complicated the analytical solution becomes very difficult, and in some cases may be impossible. Therefore numerical methods are commonly used for engineering applications [64-66]. In high voltage applications, there are many numerical techniques used for calculating the potential and the electric field. These include, Finite Difference Method (FDM), Finite Element Method (FEM), Integral Equation Method (IEM), Monte Carlo (MC) and Charge Simulation Method (SCM).

The Finite Difference Method (FDM) [67-69] is based on dividing the region under study into a large number of subdivisions. The squares and triangles meshes are commonly used. Then Laplace's equation can be replaced by the difference equation at each node point. A set of simultaneous equations for the unknown node potential ϕn can be obtained. By knowing the potential at the conductor V, these equations can be solved by using an iterative technique to obtain the potential ϕn at each node. FDM has the disadvantages of requiring long computing time and contains errors which might be introduced by neglecting the higher order terms of Taylor's expansion used in the difference equations. It is not a practical method, especially with a complicated geometry. The electric field can not be determined to a high accuracy, as it depends on

the mesh size and the choice of the latter is critical because of the inherent instability of the approximate differentiation [70,71].

The principle of the Finite Element Method (FEM) [72-74] is based on dividing the region of interest into elements and by expressing the unknown potential inside each element in terms of an assumed appropriate function. The approximating functions are defined in terms of the potential at the specified node points of each element which become the new unknowns. The concept of FEM depends on minimizing the energy in the region of interest. Hence for a system with a Laplacian field, the system of equations can be written in the form [75],

$$\frac{\partial J}{\partial \phi} = 0 = [H] \cdot [\phi] \qquad (2.3)$$

where   J   is the energy functional of the system.

[φ]   is the potential vector for all nodes

[H]   is the stiffness matrix.

Solving the above equation for the unknown node potential [φ], the potential function representing the potential distribution within each element can be determined. The field distribution can be calculated by the differentiation of the potential functions within each element. FEM can be applied for complicated geometries because the shape and size of the element can be chosen to fit the boundary. Also

it is applicable to non-homogenous and anisotropic systems. It has the disadvantage that large numbers of elements are needed to obtain an adequate accuracy. This requires long execution time, in addition to the time for subdividing the system. Furthermore, FDM and FEM are useful only in bounded regions. However, many practical problems are unbounded.

In the Monte Carlo (MC) method, the Laplacian potential $\phi(r_0)$ at a given point r_0 within a certain region, can be determined. A series of random walks n is constructed, each starting at r_0 and taking equal small steps on a rectangular grid until it reaches a point r on the boundary, where the potential ϕ is known.

The average of potential $\phi(r) = (1/n) \sum_{j=1}^{n} \phi(r_j)$

It is a statistical estimate of the unknown potential $\phi(r_0)$ which converges to the correct value as the number of random walks increases [65,76]. The accuracy of the estimated potential depends on the number of random walks n. It increases as n increases and for this reasons, it is a very slow process.

The concept of Integral Equation Method (IEM) is the use of integrals of Laplace's or Poisson's equations [77,78]. The electrode surface is divided into subsections of charges and by approximating the integral as the sum of these subsections along the electrode surface, a set of equations

can be obtained which can be solved for the unknown segment of charges.

In the Charge Simulation Method (CSM), the field can be approximated in the region under study with the field formed by a discrete set of fictitious charges placed inside the electrodes [79,80]. It has been successfully employed in many geometries used in high voltage applications.

The details of the method and the simulation is discussed in the following sections.

2.2   Charge Simulation Technique

The Charge Simulation Method is based on simulating the conductor by a set of discrete fictitious charges arranged within the conductor. The charges should be placed outside the space where the electric field is to be calculated. A number of contour points n corresponding to one or more simulated charges are chosen on the conductor boundary [81]. The relation between the location of the charge and the corresponding contour point is determined by the assignment factor β which is defined as the ratio of the distance between a contour point and its corresponding charge dq to the distance between two successive contour points dc.

$$\beta = dq/dc \qquad (2.4)$$

By using the concept of superposition, the contributions from all fictitious charges give the potential at any i-th contour point.

$$\phi = \sum_{j=1}^{n} P_{ij} Q_j \qquad (2.5)$$

where P_{ij} is the associated potential coefficient

Q_j is the unknown simulated charges.

ϕ is the potential at i-th contour point.

n   is the number of simulating charges.

The potential coefficient P_{ij} is a function of the contour and the charge locations and depends on the type of the charge used to simulate the system. ϕ is the potential at contour points which is equal to the applied potential V at the top electrode and zero at the bottom electrode. The application of equation (2.5) to all contour points in the system yields a number of linear simultaneous equations in terms of the unknown charges.

The system can be represented in a matrix form,

$$[P] \cdot [Q] = [V] \qquad (2.6)$$

Then solving for the unknown charges

$$[Q] = [P]^{-1} \cdot [V] \qquad (2.7)$$

The potential at any point in the region of interest can be determined.

$$[\phi] = [P] \cdot [Q] \qquad (2.8)$$

To satisfy the boundary condition, one of the equipotential surfaces resulting from the fictitious charges must coincide with the conductor surface potential.

The electric field at any point can be calculated,

$$[E] = [F] \cdot [Q] \qquad (2.9)$$

where [E] is the field matrix, and [F] is the field coefficient matrix.

The potential can be calculated at chosen test points on the surface of the conductor and the difference between the computed value and the conductor potential is the "potential difference". The charges used to simulate different systems are the point charge, the line charge (finite or infinite) and the ring charge. A combination of them can be used according to the system configuration and the desired accuracy. Also the simulation is difficult in very thin electrodes or boundaries. However, it has the advantages that the electric field can be calculated without resorting to a numerical differentiation, the amount of effort and time required is greatly reduced, and it needs no numerical integration to construct the matrix [80].

The Charge Simulation Method has been shown to be successful in the case of three dimensional field problems [79,82], multidielectrics [66,79,83] and field distribution with non axial symmetry [34]. CSM has been applied to calculate the voltage and field distributions in single and three core cables [85,86]. The field calculation of twin cylindrical conductors has been done by using this method [87,88]. It has been used in the design of support insulators in gas insulated systems [12,26,80,89,90].

2.3 Charge Simulation Applied to Two Dielectric System

If a dielectric material is subjected to a high electric field, polarization processes take place and dipoles are aligned by the field. They compensate each other in the interior region, but they appear as charges on the surface of the dielectric. When more than one dielectric material is sandwiched between two electrodes, the electric field distribution along the boundary is seriously distorted by the surface charges existing on the boundary. The distortion depends on the permittivity of the material, whereas in a homogeneous dielectric, the absolute value of its permittivity does not contribute to the field strength [75]. Therefore, a supplementary procedure must be introduced in the charge simulation method to be adapted to two dielectric arrangements. The electrodes can be replaced by a discrete number of fictitious charges placed inside the electrodes [79].

The effect of the surface charge distribution is equivalent to the identical effect of other charges located beyond the surface of dielectric. Therefore, a dielectric boundary can be simulated by a discrete number of fictitious charges located at both sides of the boundary. A cross section of a concave spacer, shown in Fig.2.1, is chosen to demonstrate the simulation.

The electrodes are replaced by a number of fictitious charges Ne corresponding to equal number of the contour points on the electrodes surface. If the number of the contour points on the gas side of each electrode is nq, then the number of the contour points on each electrode but in the side of the spacer is equal to ((Ne/2)- nq).

The solid dielectric boundary is replaced by Nd contour points, and the surface charges are simulated by a discrete number of charges 2Nd divided equally on both sides of the boundary. Therefore for each contour point there are two corresponding charges on both sides of the dielectric boundary. The distribution of the charges on the boundary is: (1 to Nd) in the gas side and (Nd+1 to 2Nd) on the dielectric side.

The contributions from the fictitious charges on the electrodes and the gas side of the dielectric interface give the potential and the electric field in the dielectric side. The fictitious charges on the electrodes and the dielectric side are used in the calculation of the potential and the electric field in the gas side.

The system of equations used to determine the unknown fictitious charges are formulated and the boundary conditions which must be satisfied are given below.
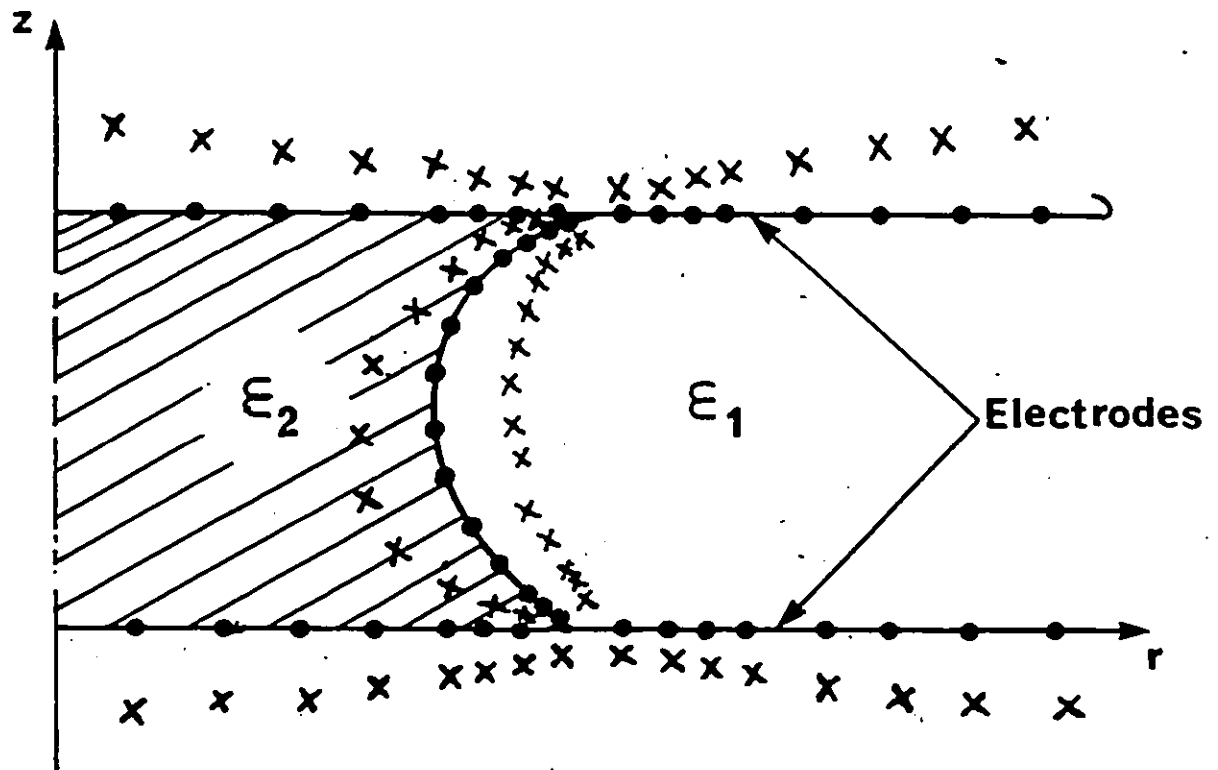
Figure 2.1: Contour points and charge locations of a concave spacer. ● Contour points, ✗ Charge location

1) High voltage electrode

The potential at the i-th contour point on the gas side is

$$\sum_{j=1}^{N_e} P_{ij} \cdot Q_j + \sum_{j=N_e+1}^{N_e+N_d} P_j \cdot Q_j = V$$

$$i = 1, n_g \tag{2.10}$$

The potential at the i-th contour point on the side of dielectric is

$$\sum_{j=1}^{N_e} P_{ij} \cdot Q_j + \sum_{j=N_e+N_d+1}^{N_e+2N_d} P_{ij} \cdot Q_j = V$$

$$i = n_g+1, \ N_e/2 \tag{2.11}$$

2) Low voltage electrode

The potential at the i-th contour point on the gas side is

$$\sum_{j=1}^{N_e} P_{ij} \cdot Q_j + \sum_{j=N_e+1}^{N_e+N_d} P_{ij} \cdot Q_j = 0$$

$$i = (N_e/2) + 1, \ Ne/2 + N_g \tag{2.12}$$

The potential at the i-th contour point on the side of dielectric is

$$\sum_{j=1}^{N_e} P_{ij} \cdot Q_j + \sum_{j=N_e+N_d+1}^{N_e+2N_d} P_{ij} \cdot Q_j = 0$$

$$i = (N_2/2) + n_g + 1, \ N_e \qquad (2.13)$$

3)Continuity of potential along the interface of the dielectric

The potential at boundary contour points is unknown and must be continuous; therefore the potential at each contour point is the same whether it is calculated from the side of the dielectric or from the gas side.

$$\sum_{j=1}^{N_e} P_{ij} \cdot Q_j + \sum_{j=N_e+1}^{N_e+N_d} P_{ij} \cdot Q_j = \sum_{j=1}^{N_e} P_{ij} \cdot Q_j + \sum_{j=N_e+N_d+1}^{N_e+2N_d} P_{ij} \cdot Q_j$$

By simplifying

$$\sum_{j=N_e+1}^{N_e+N_d} P_{ij} \cdot Q_j - \sum_{N_e+N_d+1}^{N_e+2N_d} P_{ij} Q_j = 0$$

$$i = N_e+1, \ N_d \qquad (2.14)$$

4)Continuity of the normal flux density

The normal flux density at the i-th contour point on the boundary calculated from the gas side Dn_1 must be equal ε_r times that calculated from the side of dielectric Dn_2 when there is no residing electric charge on the surface.

$$Dn_1 = Dn_2$$

Hence

$$\varepsilon_0 \; En_1 = \varepsilon_0 \varepsilon_r \; En_2$$

(where En_1 and En_2 are the normal components of the electric field in the gas and the dielectric side, respectively. ε_0 is the permittivity of the free space ($\varepsilon_0 = 8.85 \times 10^{-14} \; Fcm^{-1}$).

Then,

$$\varepsilon_r \left(\sum_{j=1}^{N_e} F_{ij} \cdot Q_j + \sum_{j=N_e+1}^{N_e+N_d} F_{ij} \cdot Q_j \right) = \sum_{j=1}^{N_e} F_{ij} \cdot Q_j + \sum_{j=N_e+N_d+1}^{N_e+2N_d} F_{ij} \cdot Q_j$$

By simplifying,

$$(\varepsilon_r-1) \sum_{j=1}^{N_e} F_{ij} \cdot Q_j + \varepsilon_r \sum_{j=N_e+1}^{N_e+N_d} F_{ij} \cdot Q_j - \sum_{j=N_e+N_d+1}^{N_e+2N_d} F_{ij} \cdot Q_j = 0$$

$$i = N_e+1, \; N_d \qquad\qquad (2.15)$$

Since the geometries studied in this work have a rotational symmetry, the simulation is carried out by employing ring charges to model the electrodes and the solid dielectric boundary. The equations for the potential and the electric field of the ring charge are given in Appendix A. The locations of the contour points (.) and the ring charges (x) are shown in Fiq.2.1.

The number of the equations representing the system (Ne + 2Nd) is equal to the number of the unknown charges used for the simulation. These equations can be written in a matrix form.

$$[A] \cdot [Q] = [V] \qquad (2.16)$$

where [A] is the potential and the field coefficients matrix.

Solving for the unknown charges,

$$[Q] = [A]^{-1}[V] \qquad (2.17)$$

The potential and the electric field can be calculated at any location from the known charges and using equations (2.8) and (2.9).

2.4 Evaluation of the method

The accuracy of the calculated potential and the electric field, the time and therefore the cost required for computation are largely affected by 1) the position of the charges; 2) types of charges used in the simulation and 3) the number of charges required to simulate the system. These three factors depend on the system geometry and the electrodes configuration. The quality and accuracy of the solution increase as the number of charges increase, but beyond a certain number, any further increase has little effect on the accuracy of the solution [66]. In general, a higher density of charges is usually located in the regions where more precise results are required. A practical criterion known as the assignment factor is chosen as an adjusting parameter in the arrangement of the charges. Investigation by the author shows that the assignment factor should be kept between 0.8-2.1, depending on the nature of the problem, to obtain higher accuracy.

To check the accuracy of the simulation, the potential and the electric field should be calculated at chosen test points other than at the contour points used to formulate the system of equations

The following criteria are used to evaluate the accuracy of the solution:

1) Potential error: defined as the difference between the potential of the electrode V and the computed potential ϕ at

various test points on the electrode surface. The potential error should be less than 1% if an accuracy of 1% is desired in the electric field strength. It is found that the maximum potential error in the system shown in Fig.2.1 is about 0.12% for Macor glass-ceramic ($\varepsilon_2=5.8$) which occurs in the vicinity of the triple junction and smaller elsewhere.

2) Potential discrepancy: is defined as the difference between the computed potentials ϕ_1 and ϕ_2 at test points across the dielectric interface. ϕ_1 and ϕ_2 are the potentials at a fixed location but calculated from the gas and the dielectric sides, respectively. The potential discrepancy should be also less than 1%. It is found that the maximum potential discrepancy is 0.016% ($\varepsilon_2=5.9$) near the triple junction (Fig.2.1).

3) Tangential field discrepancy: defined as the difference in the tangential fields Et_1 and Et_2 calculated at test points across the dielectric interface on both sides. Et_1 and Et_2 refer to the gas and the dielectric sides, respectively. The equality of the tangential field across the interface is not an imposed boundary condition in the potential coefficients matrix. The maximum tangential field discrepancy in the system of Fig.2.1 is 0.88% ($\varepsilon_2=5.8$) which occurs close to the triple junction and smaller elsewhere.

4) Discrepancy in the normal flux density: The normal flux density at the boundary must be continuous $Dn_1 = Dn_2$ or

the relation between the normal component of the electric field En_1 in the gas side and the normal component En_2 in the dielectric should be $En_1/En_2 = \varepsilon r$. The discrepancy can be defined as the deviation from the permittivity εr of the dielectric material, if it is ploted against En_1/ En_2. The maximum discrepancy which occurs close to the triple junction ($\varepsilon_2 = 5.8$) is 0.23% for the system of (Fig.2.,1)

If the error and discrepancies mentioned above do not exceed the desired level, the simulation is considered sufficient for the system. On the other hand, if they are high, the simulation should be modified by rearranging the number and the locations of the contour points and the charges.

2.5 Calculation of The Normal and The Tangential Field

The fictitious charges are used to calculate the field components, Er in the radial direction of the r-axis and Ez in the axial direction of the z-axis. To calculate the normal En and the tangential Et fields, a transformation ratio is used.

To transfer from (r-z) coordinates shown in Fig.2.2 to (n-t) coordinates, the following matrix has been used,

$$\begin{bmatrix} an \\ \\ at \end{bmatrix} = \begin{bmatrix} \cos\psi & \sin\psi \\ \\ -\sin\psi & \cos\psi \end{bmatrix} \begin{bmatrix} ar \\ \\ az \end{bmatrix}$$
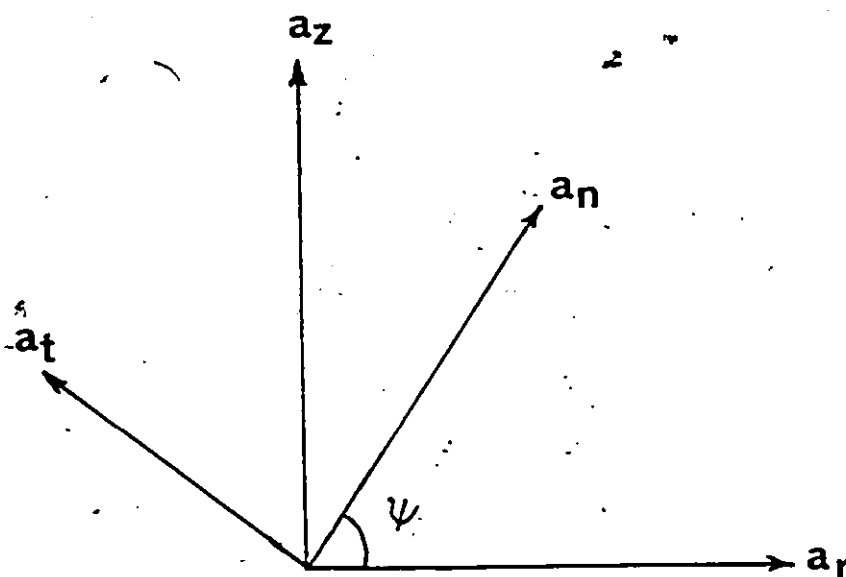
Figure 2.2: Coordinate transformation

where ψ is the angle between an and ar.

$$En = \cos\psi \cdot Er + \sin\psi \cdot Ez$$

$$(2.19)$$

$$Et = -\sin\psi \cdot Er + \cos\psi \cdot Ez$$

where ar and az are the unit vectors in the r and the z directions, respectively. an and at are the unit vectors in the normal and the tangential directions to the surface, respectively.

All the calculated values have been normalized and presented using the per unit (pu) system.

$$E^* = E / Eav$$
$$Eav = V / L$$
$$\phi^* = \phi / V \qquad\qquad (2.19)$$
$$Z^* = Z / L$$

where V=1 is the applied voltage to the top electrode and V=0 to the bottom electrode. L is the gap distance between the electrodes. Eav is the average electric field in the gap. E^* and ϕ^* are the normalized field and the potential, respectively. E and ϕ are the computed values of the electric field and potential, respectively. The notations t and n refer to the tangential and the normal field components, Et and En, respectively. ET is the total field. r and z refer to the radial r-axis and the z-axis, respectively. Z^* is the normalized distance. The subscripts 1 and 2 refer to gas and the solid dielectric media, respectively.

2.6   Computer Program

A computer program has been developed by the author for computing the potential and the electric field distributions for the different configurations used in this research. The program is written in WATFIV language for IBM 3031 computer available at the computer centre of the University of Windsor. For high accuracy, double precision has been used in the calculation.   The Gauss elimination method with complete pivoting   is used   to solve the system   of simultaneous equations for the unknown charges.   The maxima in the numbers of the contour points and the charges used in this study are 122 and 194, respectively. The CSM technique has been found suitable and yields accurate solutions.   A flow chart indicating the main steps used in the calculation is shown in Fig.2.3.

```
                        ┌─────────┐
                        │  START  │
                        └─────────┘
                             │
                  ╱──────────────────────╱
                 ╱   Input data and      ╱
                ╱  geometric parameters ╱
               ╱──────────────────────╱
                             │
                  ┌──────────────────────┐
                  │     Generation of    │
                  │    contour points    │
                  └──────────────────────┘
                             │
                  ┌──────────────────────┐
                  │  Generation of charges│
                  │  simulating the system│
                  └──────────────────────┘
                             │
                  ┌──────────────────────┐
                  │ Computation of potential and│
                  │  field coefficient matrix   │
                  └──────────────────────┘
                             │
                  ┌──────────────────────┐
                  │   Solution of the system of │
                  │      equations for the      │
                  │       unknown charges       │
                  └──────────────────────┘
                             │
                  ┌──────────────────────┐
                  │ Computation of the potential│
                  │    and the electric field   │
                  │       at contour points     │
                  └──────────────────────┘
                             │
              ╱─────────────────────────╲          ┌──────────────────┐
             ╱     Are the boundary       ╲   No   │ Rearrangement of │
             ╲   conditions satisfied?     ╱ ────> │   contour and    │
              ╲─────────────────────────╱          │ charge locations │
                             │ Yes                 └──────────────────┘
                  ┌──────────────────────┐
                  │ Generation of test points│
                  └──────────────────────┘
                             │
                  ┌──────────────────────┐
                  │ Computations of the potential│
                  │   error, potential and field │
                  │        discrepancies         │
                  └──────────────────────┘
                             │
           ╱────────────────────────────────╲
          ╱  Are the errors and discrepancies ╲   No
          ╲   within the desired accuracy?     ╱ ────>
           ╲────────────────────────────────╱
                             │ Yes
                  ╱──────────────────────╱
                 ╱    Print and plot      ╱
                ╱   potential and field   ╱
               ╱     distributions        ╱
              ╱──────────────────────╱
                             │
                        ┌─────────┐
                        │  STOP   │
                        └─────────┘
```

Figure 2.3:   Computer program flow chart

Chapter III

POTENTIAL AND ELECTRICAL FIELD DISTRIBUTIONS FOR SHAPED SPACERS

3.1 Introduction

A knowledge of the potential and the electric field distributions is useful in the design of high voltage spacers. The flashover voltage of the spacer is controlled by many factors, the most important of which is the electric field at the cathode triple junction and at locations adjacent to the spacer-gas interface.

The tangential field $E't_1$ at the surface of the spacer affects the movement of charges on the surface and may also be used to determine the potential distribution on the surface.

The normal field $E'n_1$ to the surface is important as it affects the deposition of charged contaminants on the surface of the insulator and the migration of charges from within the insulator to the surface as well as the deposition of surface charges from the gas region.

The total field $E'T_1$ determines the production of charged species in the gas adjacent to the surface of the insulator by impact ionization processes which are functions of the localized total electric field. $E'T_1m$ is calculated because

it is important since it leads to a growth in the number of electrons at a distance of the order of the critical avalanche length. E^*t_im and E^*n_im are also identified to give the highest values at the surface of the spacer.

The field components are required for both fundamental studies of the processes leading to flashover and for an optimum design of the spacer.

In the present study the potential and the electric field distributions have been calculated for different spacer geometries and for different insulating materials. Different spacer parameters such as the contact area with the electrode, the length, the contact angle and the radius of curvature of the spacer are varied in order to select a profile which gives a maximum withstand voltage for a fixed insulating gap. The optimum profile for a concave spacer has been chosen such that the total electric field has the lowest value at the triple junctions. This leads to a higher withstand voltage capability which is also validated experimentally in this work.

3.2 Spacer Configuration

The choice of the configuration of the spacer in gas insulated system must satisfy the condition of high withstand voltage in addition to possesing other requirements such as good mechanical and thermal properties.

Fig.3.1a shows a cross-section of a spacer with concave edges sandwiched between two parallel planar electrodes (termed profile 'a'). Fig.3.1b shows a cross-section of a concave edge shaped spacer (termed profile 'b') with a small vertical portion of length h near the conductor. The spacer of profile 'b' has a stronger mechanical strength than profile 'a' in the vicinity of the conductors. Both profiles contain a vertical cylindrical section with a length d. θ is the angle between the tangent to the surface of the insulator and the normal to the electrode at the triple junction. Ra and Rb are the radii of the concave sections of profiles 'a' and 'b', respectively. $2R_0$ is the minimum diameter of the solid insulator and L is the length of the gap between the electrodes. A smooth transition between the vertical and the concave regions is achieved by using a small convex region having a radius of curvature Rx which can be determined from the known Rb and s (Appendix B).

$$q - h = w$$

$$Rx = \frac{s^2 + 2\,sw}{2(Rb - \sqrt{Rb^2 + s^2 + 2\,sw} \cdot \cos(\tan^{-1}\frac{w + s}{\sqrt{Rb^2 - w^2}}))}$$

Ra is determined for different values of θ and then kept equal to Rb of profile 'b' for the sake of comparison (Ra = q/sin θ).

Fig.3.1c shows a cross-section of a concave shaped spacer
(termed profile "c") with a rotational symmetry and
sandwiched between two parallel planar electrodes. The
concave shape is assumed to be part of a circle having a
radius Rc with its centre in the mid-gap distance between
the electrodes. Fig.3.1d shows a cross-section of a concave
shaped spacer (termed profile "d") sandwiched between two
parallel planar electrodes. It has a vertical section having
a length q near each electrode. The vertical section is
required in some applications to yield larger mechanical
strength of the insulator in the vicinity of the electrodes.
Rd is the radius of the concave section of the insulator.
A gradual transition between the vertical and the concave
region is necessary and this is achieved by incorporating a
small convex section having a radius. Ry which can be
determined from the known Rd and s (Appendix C).

$$(L/2) - q = p$$

$$Ry = \frac{s^2 + 2\,sp}{2\left(Rd - \sqrt{Rd^2 + s^2 + 2\,sp}\ \cdot\ \cos\left(\tan^{-1}\dfrac{p + s}{\sqrt{Rd^2 - p^2}}\right)\right)}$$

The convex section must be arranged to be a tangent to
both the vertical and the concave sections as shown in
Fig.3.1 to obtain a smooth transition on both sides. The
contact angle θ in profile "c" is defined as the angle
between the tangent to the surface of the insulator and the
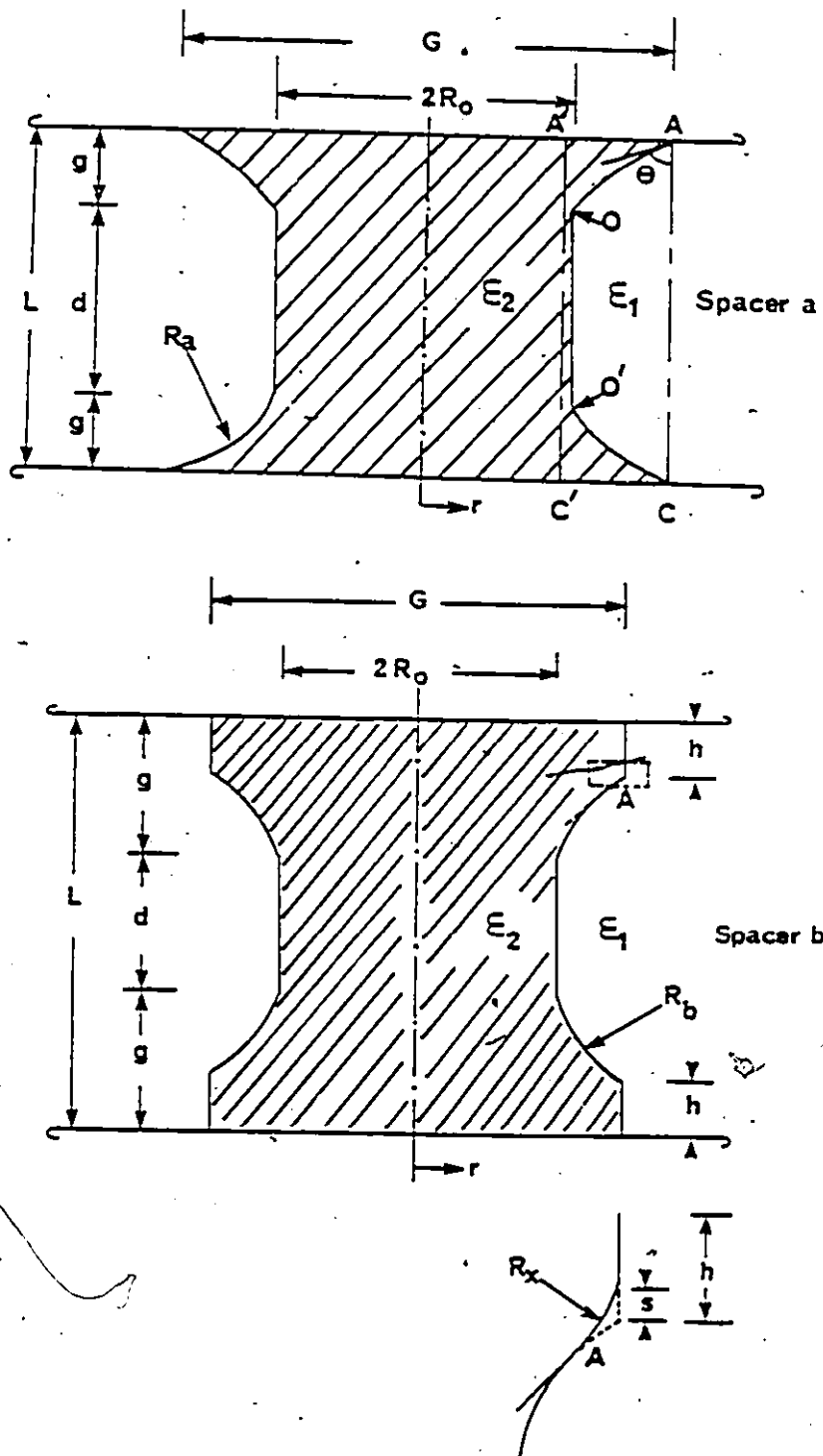
Figure 3-1: Solid insulator sandwiched between two planer electrodes. L gap distance, R_o minimum radius of insulator, ε_1, permittivity of gas, ε_2, permittivity of insulator
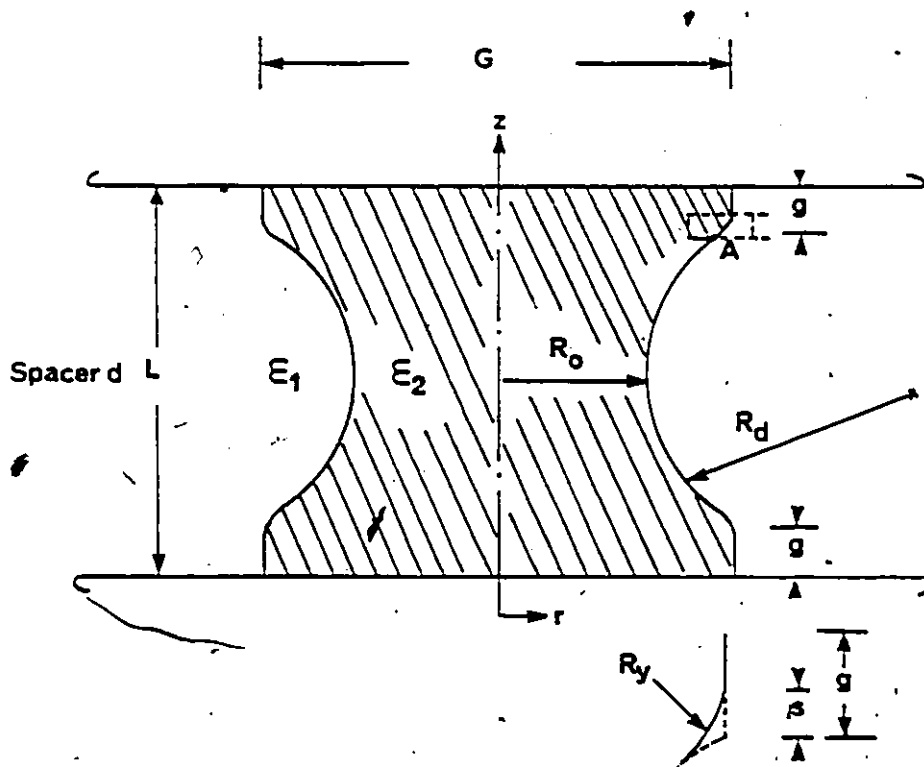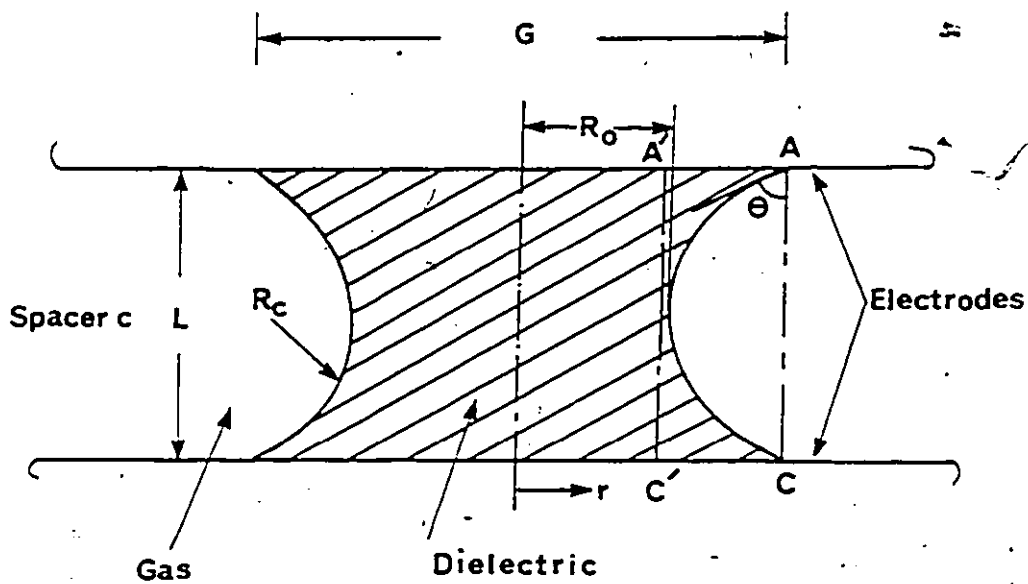
normal to the electrode at the contact point of the triple junction (electrode-insulator-gas). The relationship between the radius of curvature of the concave spacer R_c and the angle θ is $R_c = L/(2\sin \theta)$. R_c is determined for different values of θ and then kept the same value as R_d in both profiles, for the sake of comparison. Although s is arbitrarily chosen, it must have realistic values and these are given in the captions of the figures.

3.3 Potential and Electric Field Distributions for Profiles 'a' and 'b'

3.3.1 Potential distribution along the dielectric-gas interface of profile 'a'

The normalized potential distribution ϕ' along the dielectric-gas interface is shown in Fig.3.2 for $\theta = 0$(right angle cylindrical spacer), 15, 45 and 70° of an epoxy spacer ($\varepsilon_2 = 4.7$). It will be observed from Fig.3.2 that the contact angle affects ϕ'. As θ increases, the departure from linearity in ϕ' becomes more pronounced. For example, at $Z^* = 0.2$, which is close to the low voltage electrode, $\phi^* = 0.2$, 0.185, 0.17 and 0.16, respectively for $\theta = 0$, 15, 45, and 70°.

3.3.2 Dependence of the electric field at the triple junction on θ and R_b

The dependence of the electric field components E^*t_1c, E^*n_1c and E^*T_1c calculated at a distance very close to the triple junction ($Z^* = 0.01$) are shown in Table 3.1 for different values of θ. Also shown in Table 3.1 are the maxima in the tangential field E^*t_1m and in the total field E^*T_1m which occur at the surface of the spacer near points O and O' (Fig.3.1a). The corresponding values on the dielectric side of the interface boundary can be found from $E^*t_2 = E^*t_1$ and $E^*n_2 = E^*n_1/\varepsilon_2$. It can be seen from Table 3.1 that E^*T_1c is lower than the average applied field in
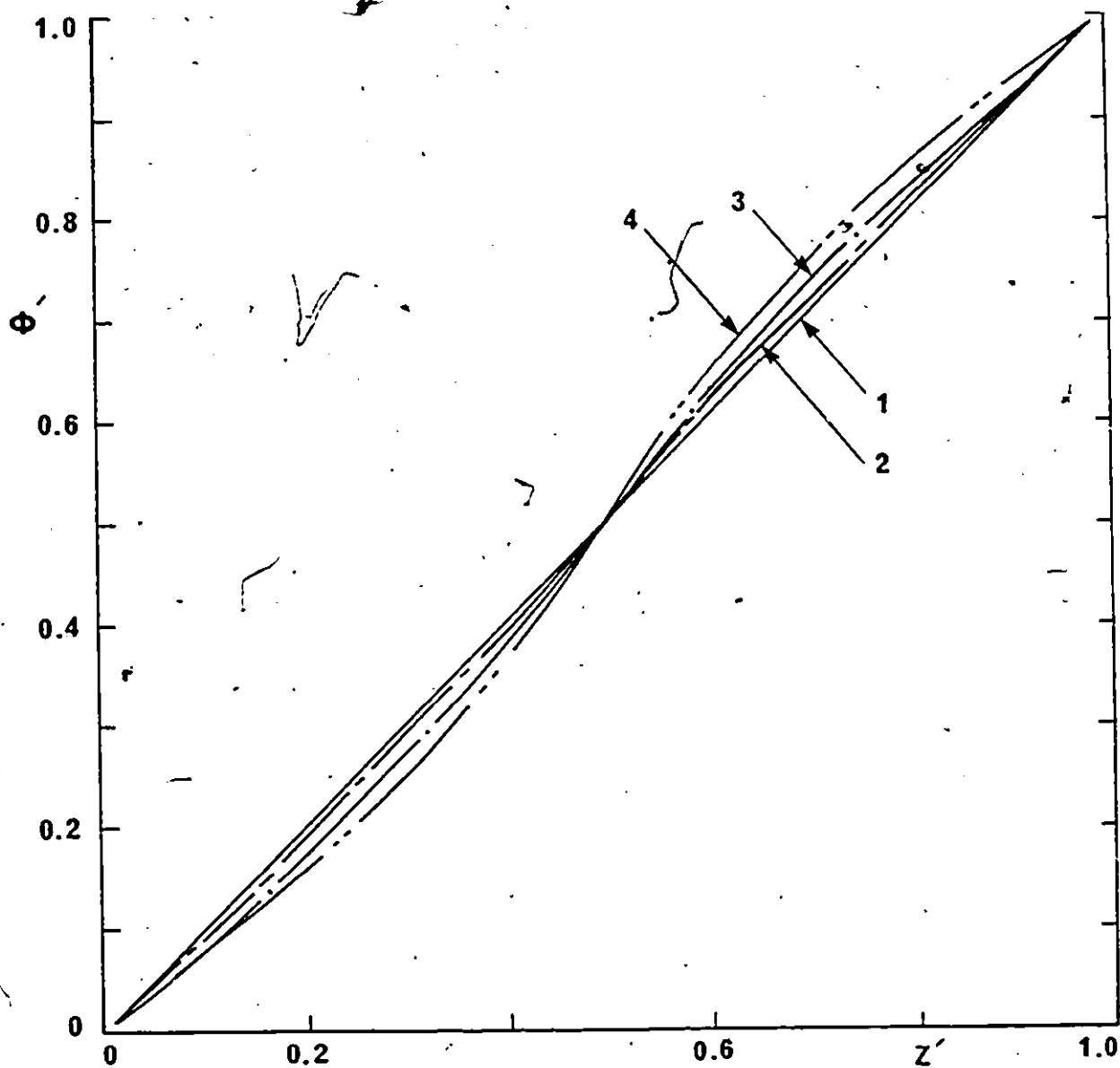
<u>Figure 3.2</u>: Normalized potential distribution ϕ^* of a
spacer having profile 'a' for different angles
θ. ϵ_2=4.7, L=50 mm, $2B_0$=40 mm, q=15 mm. curve
1, corresponds to θ=0, curve 2, θ=15°, curve 3,
θ=45° and curve 4, θ=70°.

the gas gap for $\theta > 0$. E'_{t_1c} decreases with increasing θ. Typically from 1.0 to 0.34 and 0.14 when θ increases from 0 to 45° and 70°, respectively.

Table 3.1: Dependence of the field components on the contact angle θ of profile 'a' (Fig.3.1a). $\varepsilon_2=$ 4.7, $2R_0 = 40$ mm, $g = 15$ mm, $d = 20$ mm and $L = 50$ mm.

$\theta°$	R_a mm	$|E'_{n1c}|$	$|E'_{n1m}|$	E'_{t1c}	E'_{t1m}	E'_{T1c}	E'_{T1m}
0	$R_0 = 20$	0	0	1.00	1.00	1.00	1.00
15	57.96	0.35	0.36	0.76	1.0	0.84	1.05
30	30.0	0.58	0.63	0.56	1.09	0.80	1.10
45	21.20	0.70	0.82	0.34	1.13	0.78	1.15
60	17.32	0.80	0.95	0.18	1.16	0.82	1.19
70	15.96	0.84	0.99	0.14	1.17	0.85	1.20

E'_{n_1c} increases with increasing θ from 0 for cylindrical spacer ($\theta=0°$) to 0.84 for $\theta=70°$.

Since the magnitude of the field at the spacer-conductor-gas junction is detrimental to the initiation of the electric discharge it is important to minimize the field at this junction. This is achieved at $\theta = 45°$ when E'_{T_1c} is at a minimum value (Table 3.1).

The calculated field components for spacer 'b' are shown in Table 3.2. It will be observed that, as Rb increases, $E't_1c$ and $E'T_1c$ increase. The normal field at the cathode decreases very slightly with increasing Rb but remains very small. It will be noted that Tables 3.1 and 3.2 are given for the same values of Ra and Rb so that a meaningful comparison can be made between the two profiles. The smaller $E'T_1c$ is achieved at $\theta=45^\circ$ (Ra=21.2 mm) for spacer 'a' (Table 3.1). For spacer 'b' the smaller $E'T_1c$ occurs at Rb= 15.96 mm (Table 3.2) but $E'T_1m$ is higher there.

Table 3.2: Dependence of the field components on the radius Rb for a spacer of profile 'b' (Fig.3.1b). $2R_0=$ 40 mm, L= 50 mm, q= 15 mm, d = 20 mm, h= q/3, s/h= 1/2 and ε_2= 4.7.

R_b mm	R_x mm	$\lvert E'_{n1c} \rvert$	$\lvert E'_{n1m} \rvert$	E'_{t1c}	E'_{t1m}	E'_{T1c}	E'_{T1m}
15.96	7.98	0.008	0.89	0.80	1.16	0.80	1.20
17.32	8.85	0.006	0.81	0.82	1.15	0.82	1.18
21.20	11.22	0.006	0.67	0.85	1.12	0.85	1.16
30.00	16.39	0.003	0.47	0.90	-1.09	0.90	1.12
57.95	32.35	0.002	0.25	0.95	1.05	0.95	1.08

3.3.3   Dependence on the permittivity ε_2 of the spacer

The dependence of the electrical field components on the permittivity in the range $\varepsilon_2 = 2.1$ to 100 for profile 'a' is shown in Table 3.3. It will be observed that varying the permittivity of the spacer has a great influence on the field components in the range covered. Table 3.3 shows that the field components at a location very close to the triple junction ($Z'=0.01$) decrease as the permittivity increases. The maxima of the field increase as the permittivity increases. Typically $E'_{n,m}$ increases from 0.74 at $\varepsilon_2 = 2.1$ (Teflon) to 0.91 at $\varepsilon_2 = 100$ (Rutile). The dependence of the electrical field on the permittivity ε_2 for profile 'b' almost follows the same trend of profile 'd' (Table 3.10) and therefore it is not shown for brevity. The reduction in the total electric field $E'_{T,c}$ is in agreement with the work reported by Pillai and Hackam [25].

Table 3.3 and 3.10 show that $E'_{T,c}$ decreases and $E'_{T,m}$ increases with increasing permittivity. The higher field in the vicinity of the cathode causes increased ionization and has strong effect on the formation of the avalanche. In the region near the critical avalanche length a small increase in the field causes a large increase in the number of electrons and in the space charge field as will be shown in chapter 6 and appendices D, E and F. This might explain the measurement reported by Jordan and others [25] which showed a decrease in the flashover voltage with increasing permittivity.

Table_3.3: Dependence of the field components on the permittivity of the spacer for profile 'a' (Fig.3.1a). $2R_0 = 40$ mm, $g = 15$ mm, $d = 20$ mm, $L = 50$ mm, $Ra = 21.2$ mm and $\theta = 45°$.

Material	ϵ_2	$|E'_{nlc}|$	$|E'_{nlm}|$	E'_{tlc}	E'_{tlm}	E'_{Tlc}	E'_{Tlm}
Teflon	2.1	0.72	0.74	0.51	1.07	0.88	1.08
Plexiglas	3.2	0.71	0.79	0.41	1.10	0.82	1.12
Epoxy	4.7	0.70	0.82	0.34	1.13	0.78	1.15
Macor glass-ceramic	5.8	0.70	0.83	0.32	1.14	0.77	1.17
Porcelain	9.0	0.69	0.86	0.28	1.16	0.74	1.19
Titanium dioxide	40	0.66	0.90	0.21	1.20	0.70	1.23
Rutile	100	0.66	0.91	0.20	1.20	0.69	1.23

Table_3.4: Dependence of the field components on g at a fixed L for a spacer having profile 'a' (Fig.3.1a). $2R_0 = 40$ mm, $L = 50$ mm, $\theta = 45°$ and $\epsilon_2 = 4.7$.

g mm	R_a mm	$|E'_{nlc}|$	$|E'_{nlm}|$	E'_{tlc}	E'_{tlm}	E'_{Tlc}	E'_{Tlm}
2.5	3.54	0.80	0.78	0.59	1.09	0.99	1.11
5.0	7.07	0.78	0.79	0.54	1.09	0.95	1.12
10.0	14.14	0.75	0.80	0.42	1.11	0.86	1.13
15	21.20	0.70	0.82	0.34	1.13	0.78	1.15
20	28.28	0.68	0.84	0.31	1.17	0.75	1.18

3.3.4   Effect of the length q

The effect of varying the length q of the concave portion
of profile 'a' (Fig.3.1a)   on the electric field components
at the triple junctions is shown in Table 3.4. L and θ are
kept constants. Therefore, in order to vary q, the radius Ra
must be varied according to the values given in Table 3.4.
It can be seen that as q increases the field components very
close to the triple junction decrease, although the maxima
in the field components increase slightly. Typically, E^*T_1c
decreases from 0.99 at q = 2.5 mm to 0.75 at q = 20 mm.
These results suggest that q should be chosen to be as large
as possible within the physical constraints of the system.

3.3.5   Dependence on the length of the vertical part d

The effect of varying the length d (Fig.3.1a)   on the
field components is shown in Table 3.5. q, Ra and θ are kept
constant.   As d is varied, L must also be varied in tandem
in order to keep the other parameters constant.   It can be
seen that varying the length d and L under these conditions
has little effect on the field components.

Table 3.5: Dependence of the field components on d (and L) at a fixed q, Ra and θ for a spacer having profile 'a' (Fig.3.1a). $2R_0 = 40$ mm, θ= 45°, Ra= 21.2 mm, q= 15 mm' and $\varepsilon_2 = 4.7$.

d mm	L mm	$\|E'_{nlc}\|$	$\|E'_{nlm}\|$	E'_{tlc}	E'_{tlm}	E'_{Tlc}	E'_{Tlm}
0.5	3.5	0.66	0.83	0.32	1.16	0.73	1.18
1.0	4.00	0.65	0.82	0.32	1.15	0.72	1.17
2.0	5.0	0.65	0.82	0.32	1.13	0.72	1.15
3.0	6.0	0.65	0.82	0.32	1.13	0.72	1.15
5.0	8.0	0.66	0.83	0.32	1.13	0.73	1.15
7.0	10.0	0.67	0.85	0.32	1.15	0.74	1.18

3.3.6 Dependence of the electric field on r

The total electric field $E'T_1$ is calculated at different radii r from the axis of the spacer both inside and outside the solid dielectric for a plexiglas spacer of profile 'a' with O=45° and is shown in Fig.3.3. The line AC is the most likely path of the flashover of the concave spacer at high gas pressures. It can be observed that the electric field distributions between the two electrodes is symmetrical inside the solid insulator despite the asymmetrical applied voltages to the electrodes V and O.
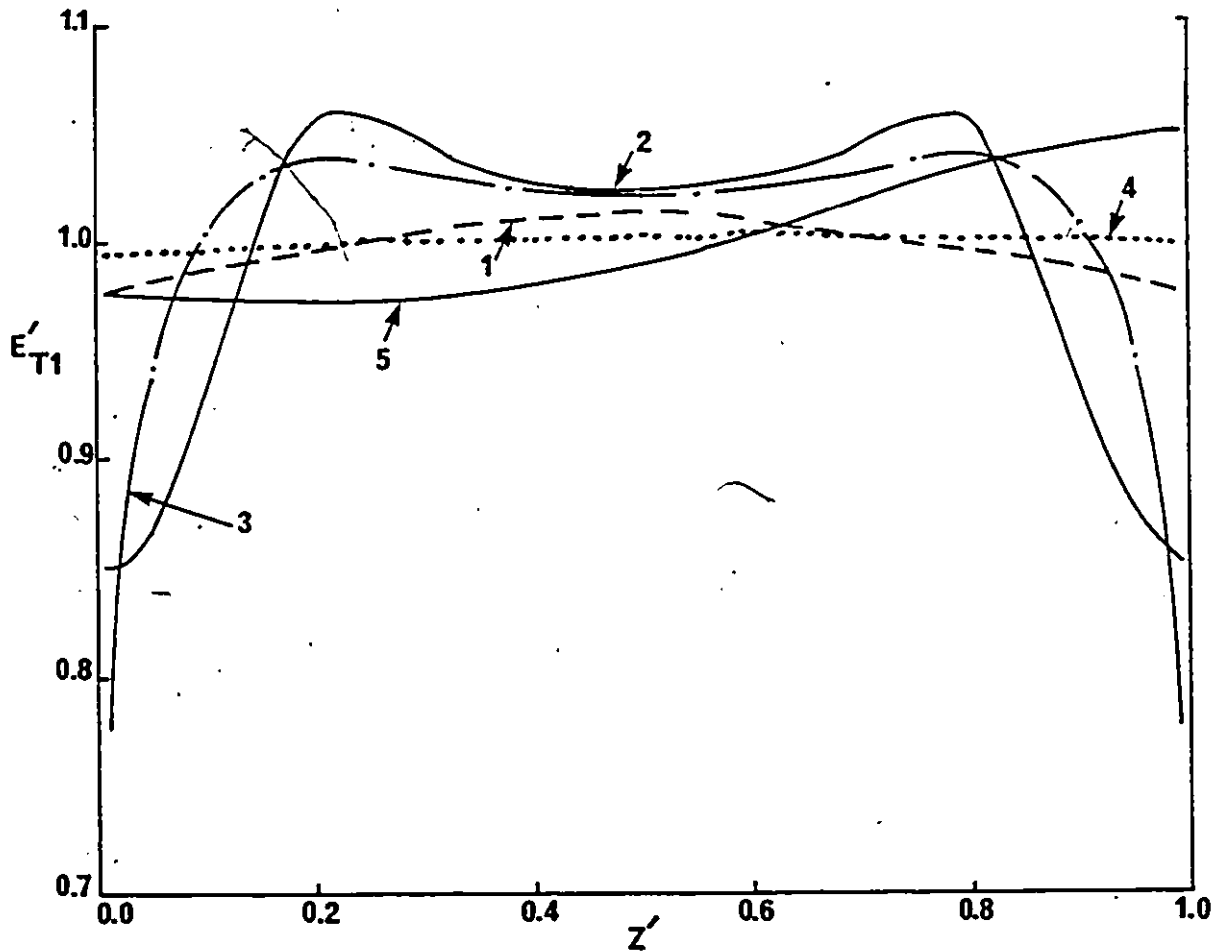
Figure 3.3: Normalized total field $E'T_1$ as a function of Z' for profile "a" at different radii r. $\epsilon_2 = 3.2$, L= 40 mm, $2R_0$= 40 mm, Ra= 14.14 mm, q=10 mm, curve 1 corresponds to $r/R_0=0.05$, curve 2, $r/R_0=0.95$, curve 3, $r/R_0=1.207$ (line AC), curve 4, $r/R_0=2$ and curve 5, $r/R_0=4$.

The electric field has a minimum value at the triple junction for line AC (curve 3) and also shows a symmetrical behaviour. At a location $r/R_0 = 2$ the electric field has nearly a uniform distribution though slightly asymmetric ($E'T_1a = 1.01 E'T_1C$). However, at $r/R_0 = 4$ which is near the outer periphery of the electrodes, the asymmetry in the electric field distributions increases. The field is higher by 7% near the high voltage electrode than at the other electrode (Fig.3.3, curve 5). This behaviour has been attributed to the effect of the asymmetrically applied voltages [91,92] and is more pronounced at the edges of the electrodes. It is in agreement with the recent work reported in [93].

3.4   Tangential, Normal and Total Field Distributions for Spacers 'a' and 'b'

$E't_1$, $E'n_1$, and $E'T_1$ are determined on the gas side of the interface for different contact angles θ, Ra and Rb.

Fig.3.4 shows $E't_1$ for epoxy ($\varepsilon_2 = 4.7$) spacers types 'a' and 'b' (Fig.3.1) and for varying θ and Rb (=Ra). It will be observed from Fig.3.4 that $E't_1c$ (= $E't_1a$) is lower than the average applied field in the gap. $E't_1m$ occurs at locations near points O and O' (Fig.3.1).

The dependence of $E'n_1$ on θ and Rb (=Ra) at the gas side of the interface of the spacer is shown in Fig.3.5. For spacer 'b' (Fig.3.1) $\left|E'n_1\right|$ is negligibly small at the triple

junction while for spacer 'a', $\left|E'n_1\right|$ increases with decreasing Ra.

Fig.3.6 shows $E'T_1$ for an epoxy spacer having different θ and Bb. The total field at the triple junction is seen to be lowest for $\theta = 45°$ (curve 2).

The total electric field $E'T_1$ for profile 'b' at different locations inside and outside the solid dielectric including the line Ac is shown in Fig.3.7. The behaviour of the electric field distribution is symmetrical inside the solid dielectric and along the line AC. The maximum in the electric field occurs near points O and O' of Fig.3.1. However, at a location away from the solid insulator at $r/R_0=2$, the electric field distribution becomes almost uniform except near the electrodes where a small distortion is found giving $E'T_1a = 1.02 E'T_1c$. At a location $r/R_0=4$ (curve 5) near the outer periphery of the electrode, there is a marked distortion in the electric field, especially near the high voltage electrode. Typically, $E'T_1$ is higher by about 19% than that at the low voltage electrode.
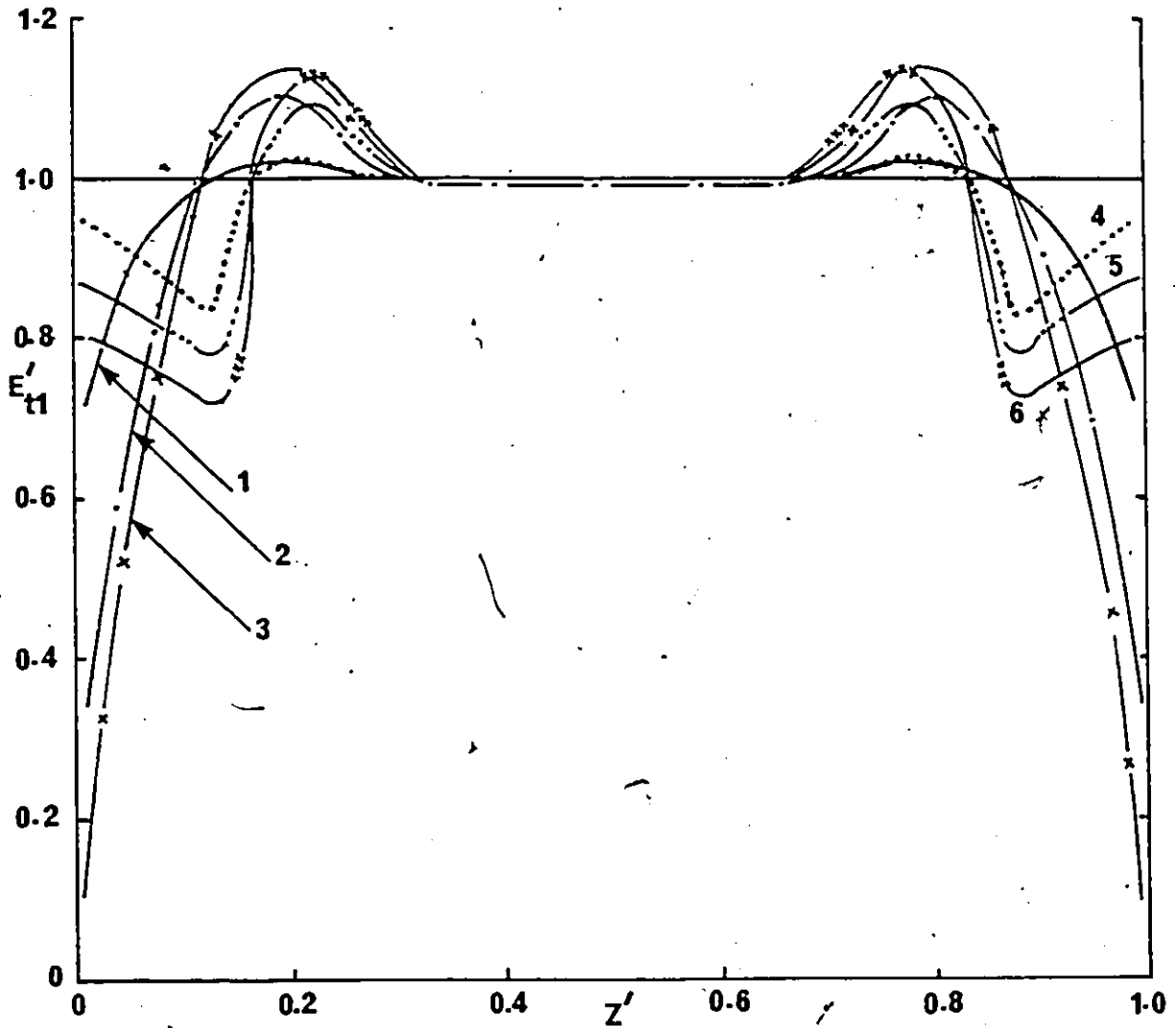
Figure 3.4: Dependence of normalized tangential field E'_{t1} on Ra in profiles 'a' and 'b'. $\varepsilon_2 = 4.7$, L= 50 mm, $2B_0 = 40$ mm, q= 15 mm, s/h= 0.5, h/q= 1/3, Ra=Rb. curves 1 and 4 correspond to Ra= 57.9 mm, curves 2 and 5, Ra= 21.2 mm, curves 3 and 6, Ra= 15.9 mm, curve 1, θ= 15°, curve 2, θ= 45°, curve 3, θ= 70°, Profile 'a': curves 1, 2 and 3; Profile 'b' curves 4, 5 and 6.
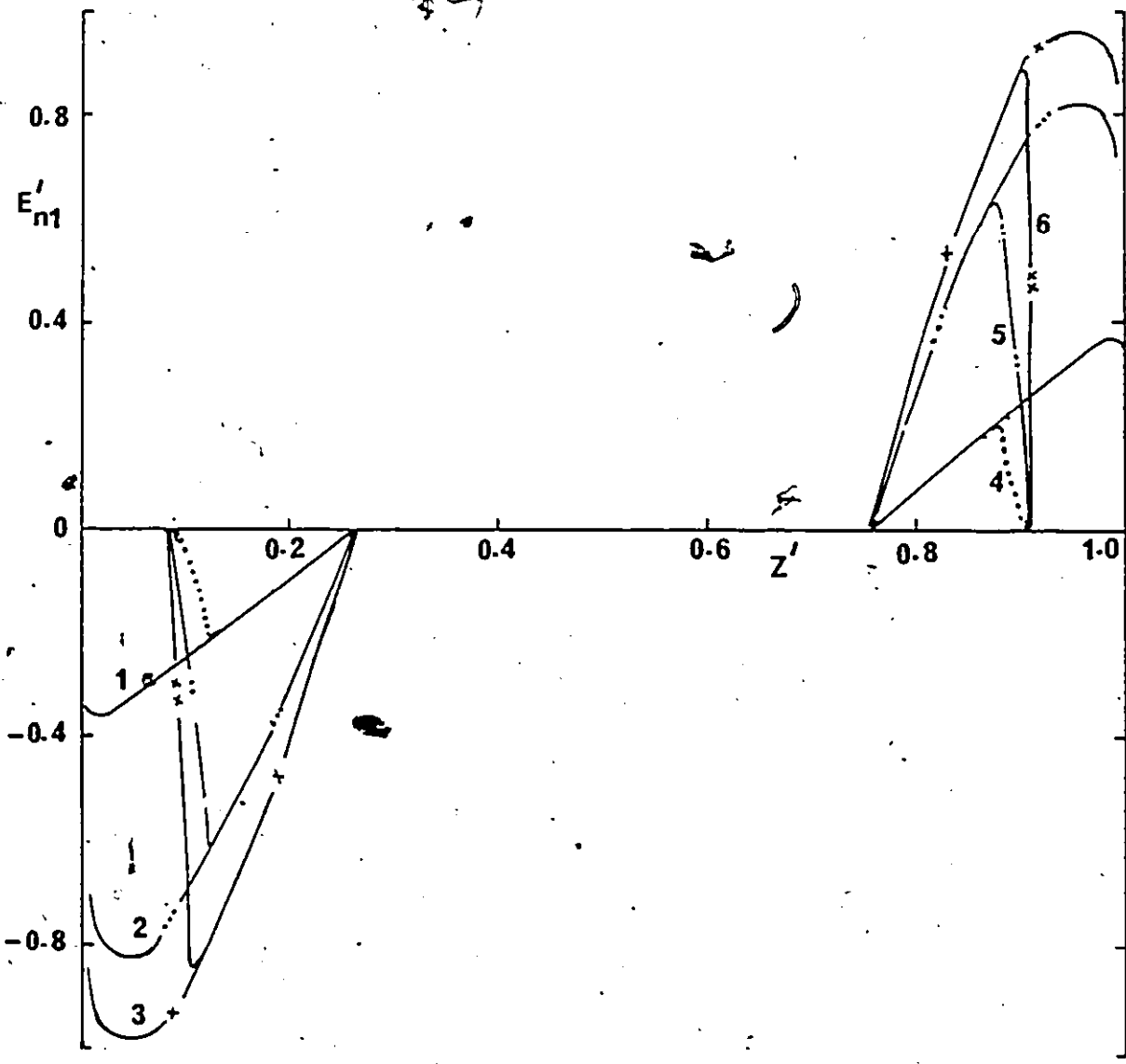
Figure 3.5: Normalized normal field E'_{n_1} distribution along the spacers interfaces. Conditions are as of Fig.3.4.

57
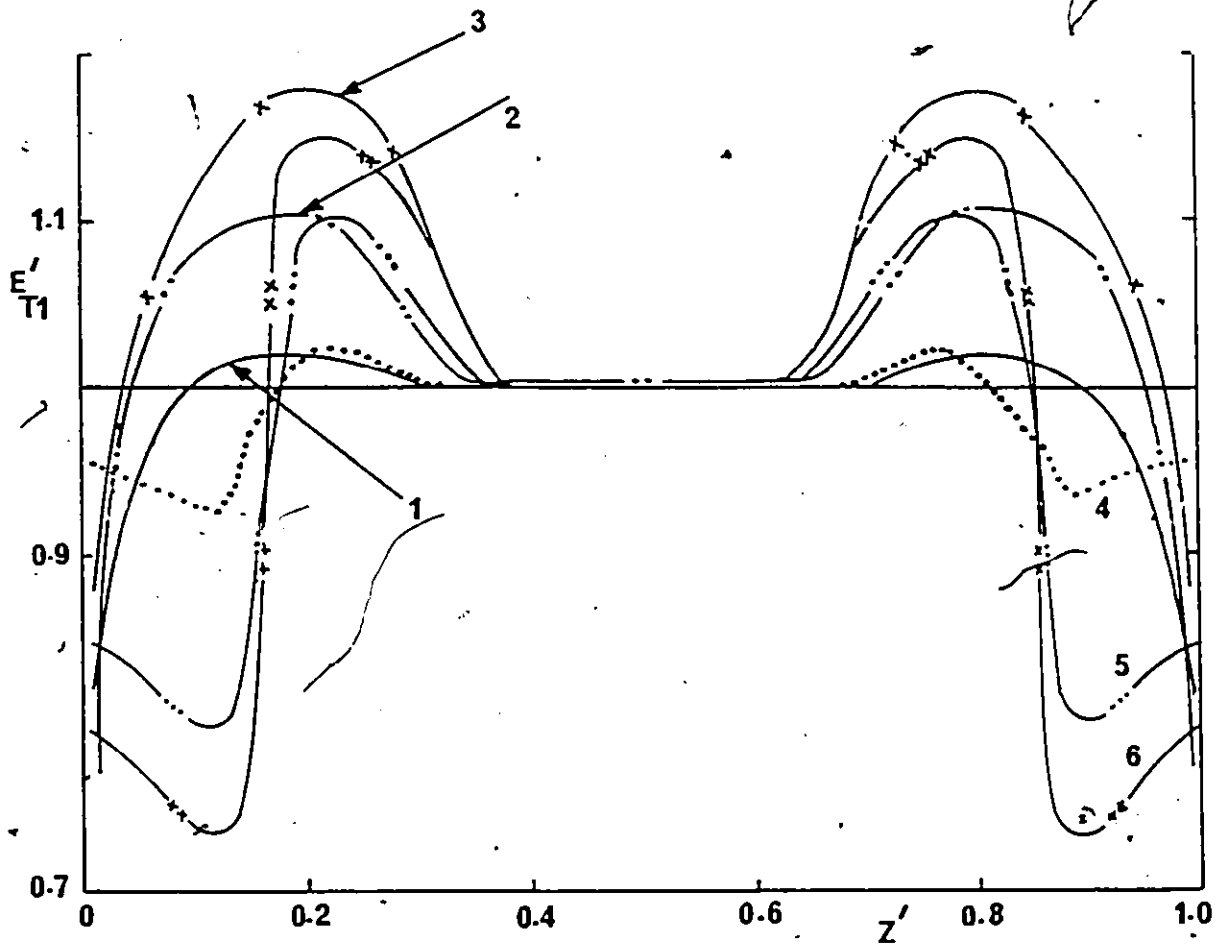
Figure 3.6: Normalized total field $E^\circ T_1$ distribution along the spacers interfaces on the gas side. Conditions are as of Fig.3.4.
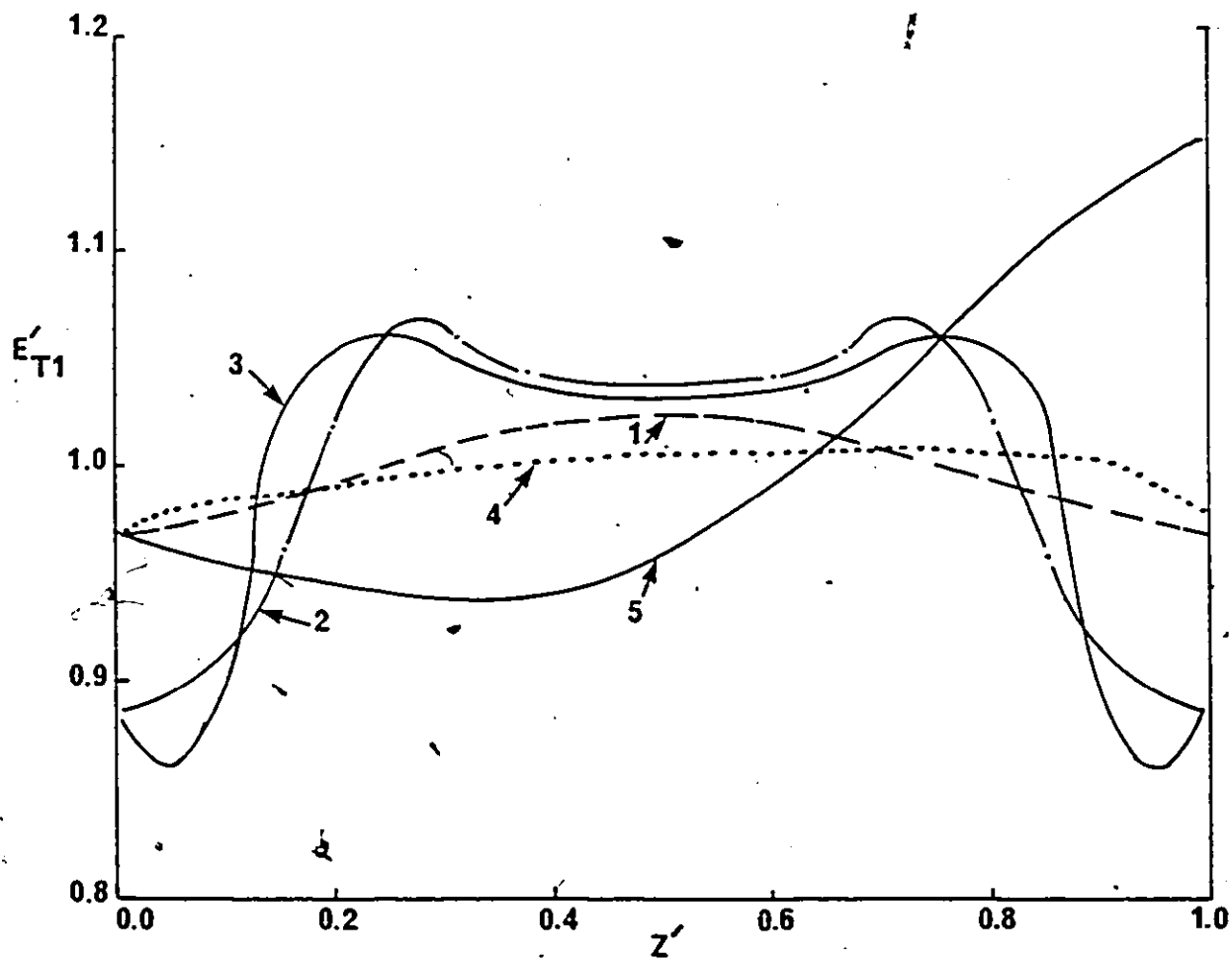
Figure 3.7: Normalized total field E^*T_1 as a function of Z^* for profile "b" at different radii r. $\varepsilon_2= 3.2$, L= 50 mm, $2R_0= 40$ mm, Rb= 21.21 mm, q=15 mm, s/h=0.4, curve 1 corresponds to $r/R_0=0.05$, curve 2, $r/R_0=0.95$, curve 3, $r/R_0=1.125$ (line AC), curve 4, $r/R_0=2$ and curve 5, $r/R_0=4$.

3.5 Potential and Field Distributions for Profiles 'c' and 'd' (Fig.3.1)

3.5.1 Effects of contact angle θ and Rd

Fig.3.3 shows ϕ' along the gas-spacer interface of profile 'd' (Fig.3.1d) using different radii of curvature Rd. The radius Rd of the Macor glass-ceramic (ε_2 = 5.3) spacer is varied in the range 21.3-77.3 mm. It will be observed that ϕ' is dependent on the radius Rd and the departure from linearity becomes more pronounced for smaller Rd. Typically at $Z' = 0.2$, $\phi' = 0.134$, 0.15, 0.18 and 0.2 for Rd = 21.3, 28.3, 77.3 mm and for a cylindrical spacer of R_0 = 20 mm, respectively.

Table 3.6 shows a summary of the influence of the contact angle θ in profile 'c' on the electric field components in the gas side calculated at the triple junction ($Z' = 0.01$). $E'n_im$ occurs close to the triple junctions at $Z' = 0.03$ and $Z' = 0.92$. As can be seen from Table 3.6 that $E't_ic$ decreases with increasing θ. $E'T_ic$ has a minimum value at $\theta = 45°$. Therefore this should give a higher flashover voltage. $E't_im$, $E'n_ic$, $|E'n_im|$ and $E'T_im$ increase with increasing θ from 0 to 70°.

Since a high field at the conductor-spacer-gas junction leads to initiation of electric discharges it is useful to minimize this field. In order to obtain the maximum improvement in the withstand voltage of the system of (Fig.3.1c) $\theta = 45°$ must be chosen (Table 3.5) where this
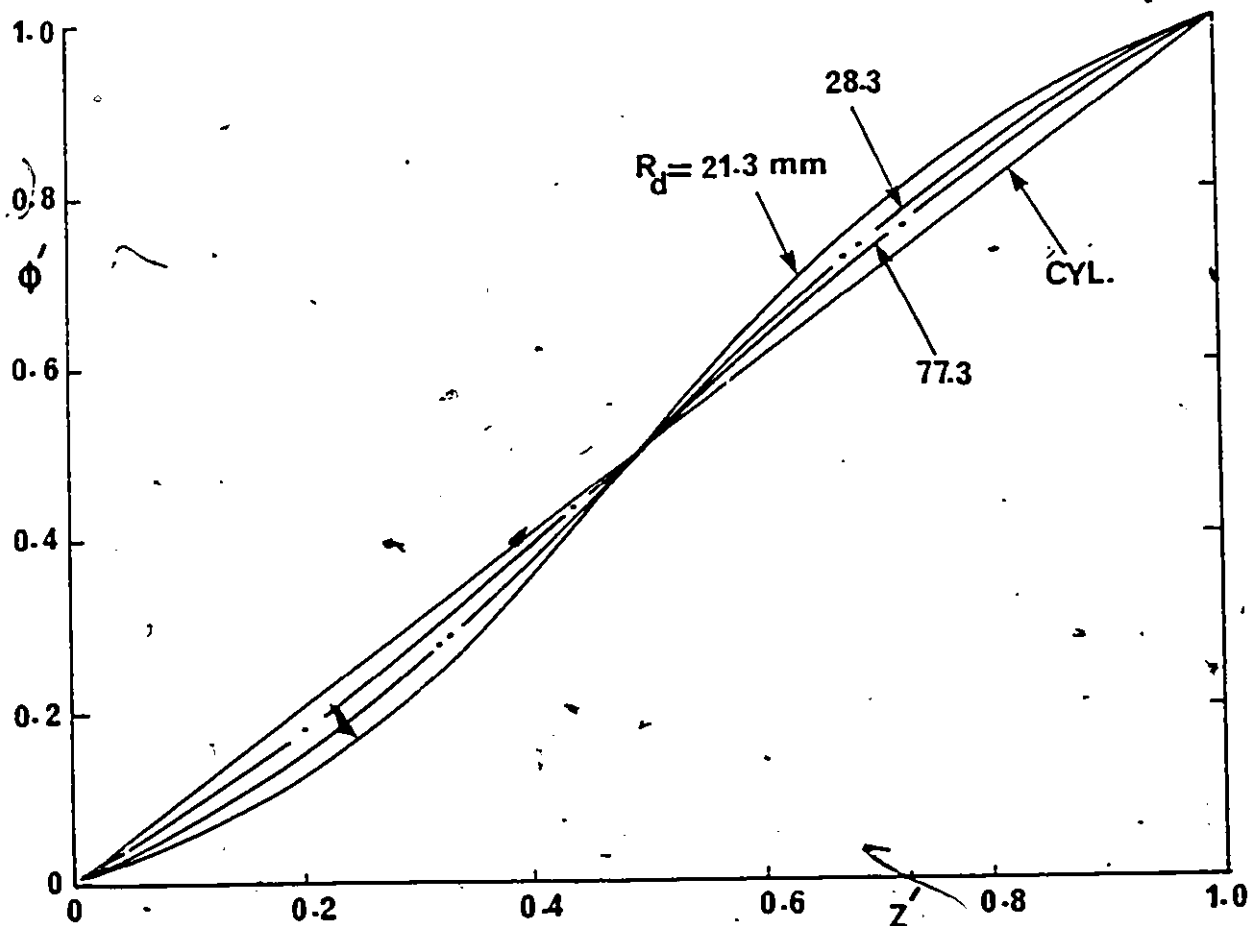
Figure 3.8: Normalized potential distribution ϕ' along the interface for different radii of curvature Rd of profile 'd'. $\varepsilon_2 = 5.8$, $2R_0 = 40$ mm, L=40 mm, q=5 mm and s/q= 0.1.

Table 3.6: Dependence of the field components on the contact angle θ in profile 'c' (Fig.3.1c) ε_2= 3.2, $2R_0$= 40 mm and L= 40 mm.

$\theta°$	R_C mm	$|E'_{nlc}|$	$|E'_{nlm}|$	E'_{tlc}	E'_{tlm}	E'_{Tlc}	E'_{Tlm}
0	R_o=20	0	0	1.0	1.0	1.0	1.0
15	77.3	0.32	0.34	0.79	1.07	0.85	1.07
30	40.0	0.53	0.60	0.57	1.13	0.78	1.13
45	28.3	0.66	0.81	0.38	1.18	0.76	1.18
60	23.0	0.77	0.95	0.25	1.22	0.81	1.22
70	21.3	0.83	0.99	0.14	1.24	0.84	1.24

Table 3.7: Normalized normal E'_{n1c}, tangential E'_{t1c} and total E'_{T1c} fields (at Z'= 0.01) as a function of Rd (profile 'd') ε_2= 3.2, $2R_0$= 40 mm, L= 40 mm, q= 5 mm and s/q=0.1

R_d mm	R_y mm	$|E'_{nlc}|$	$|E'_{nlm}|$	E'_{tlc}	E'_{tlm}	E'_{Tlc}	E'_{Tlm}
21.3	1.20	0.002	1.06	0.80	1.22	0.80	1.22
23.0	1.38	0.003	0.98	0.81	1.20	0.81	1.20
28.3	1.78	0.003	0.80	0.85	1.17	0.85	1.17
40.0	2.60	0.003	0.57	0.90	1.12	0.90	1.12
77.3	5.19	0.003	0.30	0.95	1.06	0.95	1.06

field is at a minimum value.   This finding is validated experimentally in the present study in compressed gases.

The calculated fields at a location very close to the triple junction ($Z^* = 0.01$) for profile 'd' using $\varepsilon_2 = 3.2$ are shown in Table 3.7. It will be observed from table 3.7 that, as Rd increases, both E^*t_1c and E^*T_1c increase, but $|E^*n_1m|$ decreases with increasing Rd. $|E^*n_1m|$ occurs at $Z^* = 0.125$ in the transition region between the vertical and the curved sections. Also given in Table 3.7 are E^*t_1m and E^*T_1m at the interface which occur at the mid gap ($Z^* = 0.5$) location.

Fig.3.9 shows the total field E^*T_1 along the line AC of profile c (Fig.3.1). The line AC is chosen because it is the most likely path of the flashover of the concave spacer at high gas pressures.   Fig.3.9 shows E^*T_1 along the line AC decreases as θ increases and reaches a minimum at $\theta=45^\circ$. With a further increase in θ, E^*T_1c starts to increase. Also E^*T_1c is lower than the average applied field in the gap.
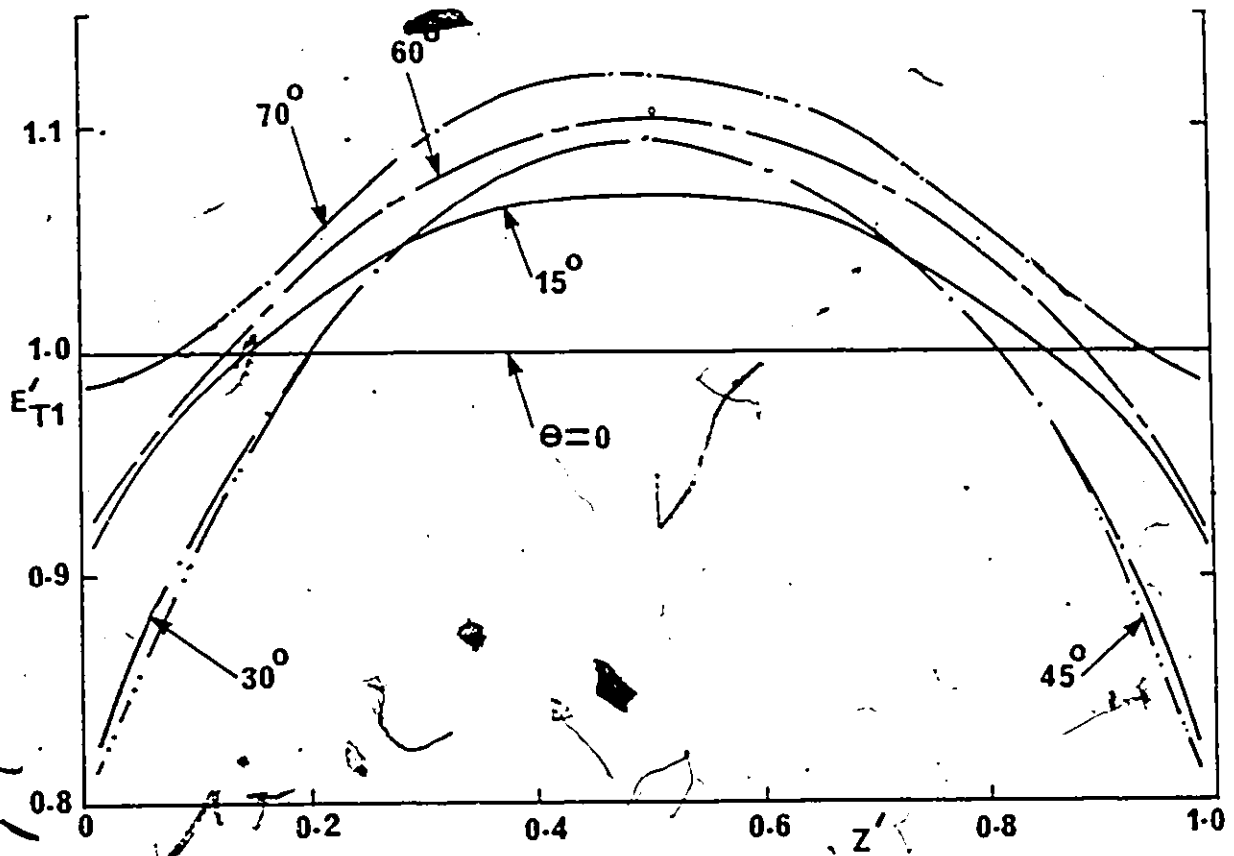
Figure 3.9: Normalized total field $E'T_1$ of profile 'c' for different contact angles along the line AC. Conditions: $\varepsilon_z = 5.8$, $R_0 = 20$ mm, $L = 10$ mm and $Rc = L/2 \sin \theta$.

3.5.2   Effect of radius Ro on $E't_1$ and $E'T_1$

The effect of varying the radius Ro of the spacer with profile 'c' from 10 mm to 50 mm on $E't_1$ and $E'T_1$ is shown in Fig.3.10 for $\theta = 45°$ and $\varepsilon_2 = 5.8$. It is useful to note that varying the radius has almost 10% and 5% influence on the values of $E't_1$ and $E'T_1$, respectively within the range covered.

3.5.3 · Effect of varying L on $E't_1$ and $E'T_1$

Fig.3.11 shows the effect of varying the gap length L on $E't_1$ and $E'T_1$ for $\varepsilon_2 = 5.8$ and $\theta = 45°$. It will be observed that $E't_1$ and $E'T_1$ depend on L, particularly in the region near the electrodes. Typically, for L = 10 mm, $E't_1c = 0.32$ and at L = 50 mm, $E't_1c = 0.24$. $|E'n_1c|$ is also found to depend on L. it increases with increasing L in the range 10 to 50 mm by about 10% (not shown for brevity). $E'T_1c$ decreases by 6 % with increasing L from 10 to 50 mm.

Fig.3.12 shows $E'T_1$ at different distances r from the axis of profile 'c'. It can be observed that the electric field behaviour has a symmetrical distribution inside the solid dielectric and along the line AC. But at $r/R_0=4$ the electric field is no longer symmetrical. The electric field at the high voltage electrode is 1.03 of that at the low voltage electrode. The maximum field $E'T_1m$ is 1.16 and occurs at mid gap. however, the minimum of $E'T_1c$ is observed for line AC (curve 3) which at $r/R_0=1.414$.
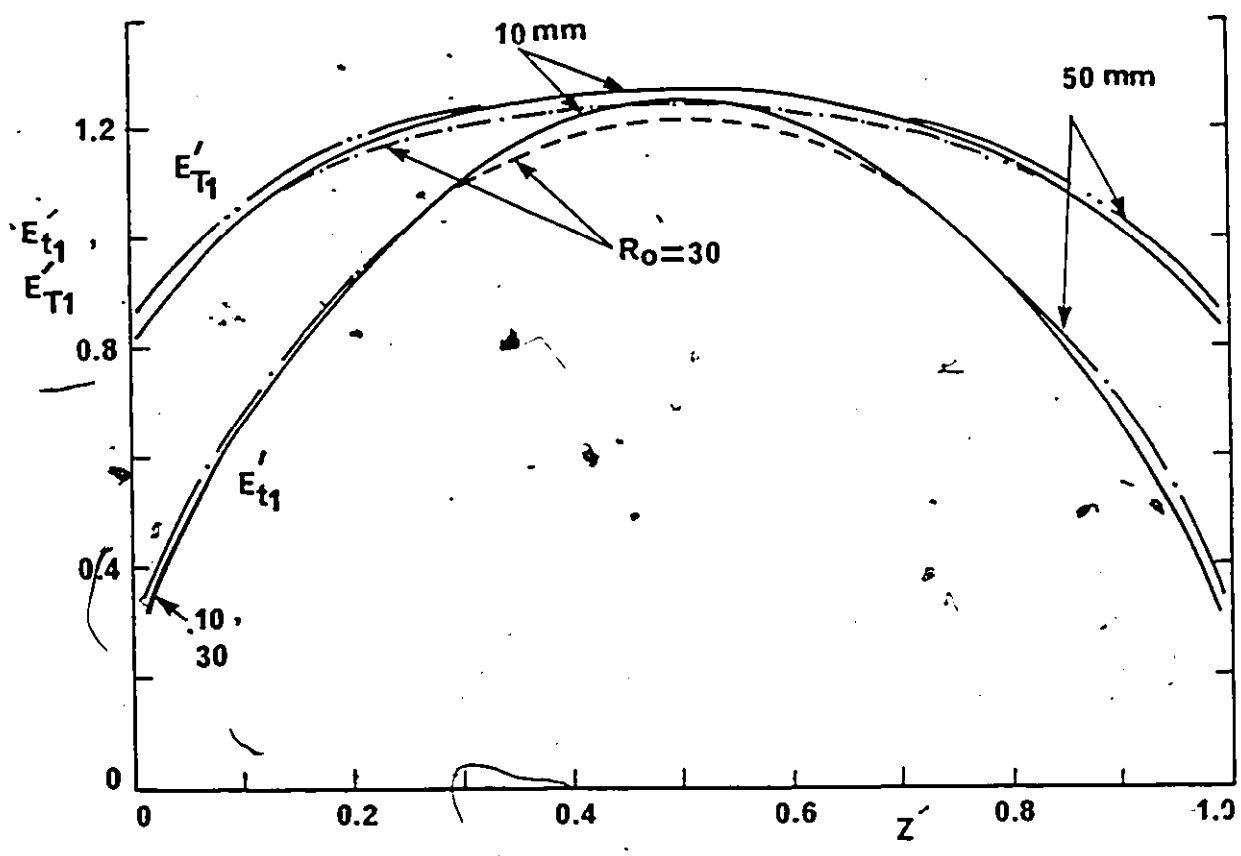
Figure 3.10: Normalized tangential $\varepsilon^\bullet t_1$ and total $\varepsilon^\bullet T_1$ fields on the gas side of the spacer-gas interface for different radii R_0 of profile "c". $\theta = 45°$, $\varepsilon_2 = 5.6$ and $L = 10$ mm.
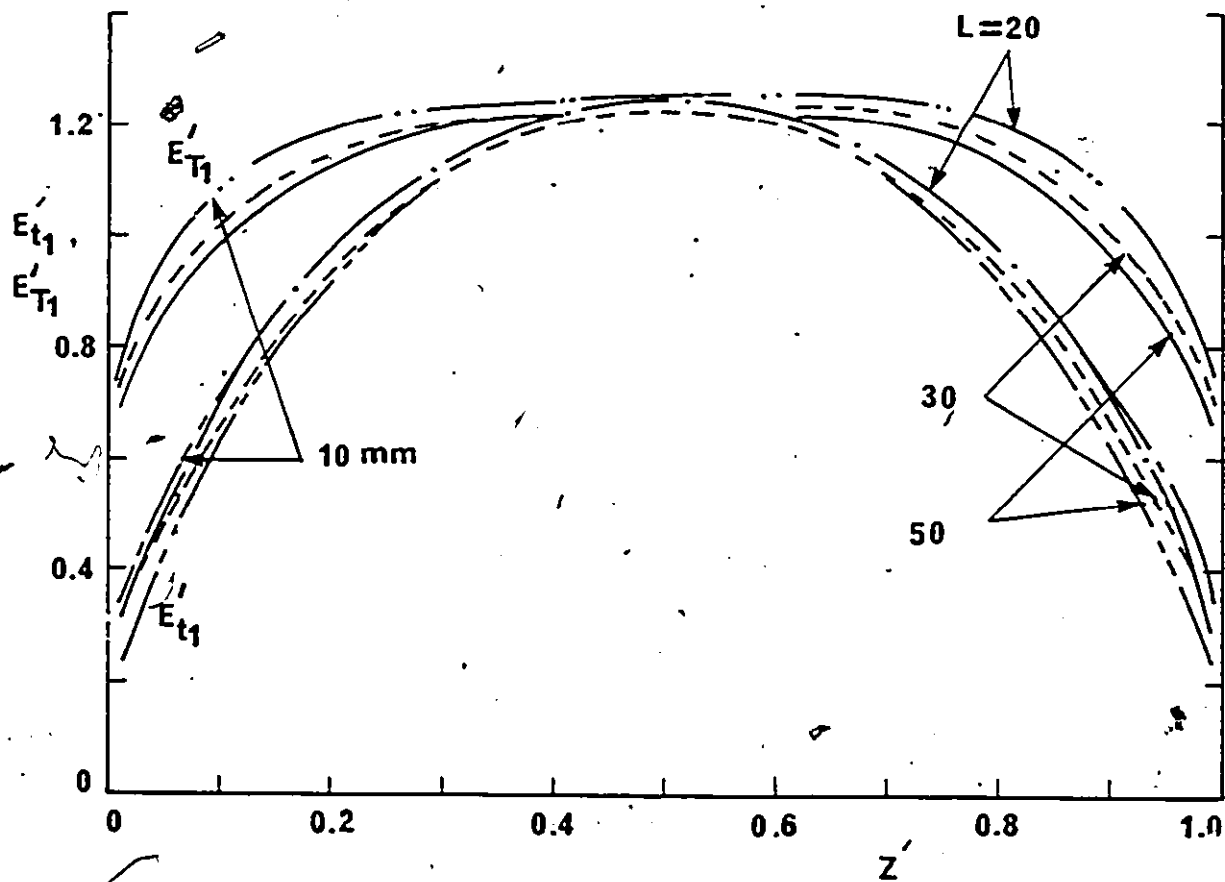
Figure 3.11: Normalized $E't_1$ and $E'T_1$ for different gap lengths of profile 'c'. $\theta = 45°$, $R_0 = 20$ mm and $\varepsilon_2 = 5.8$.
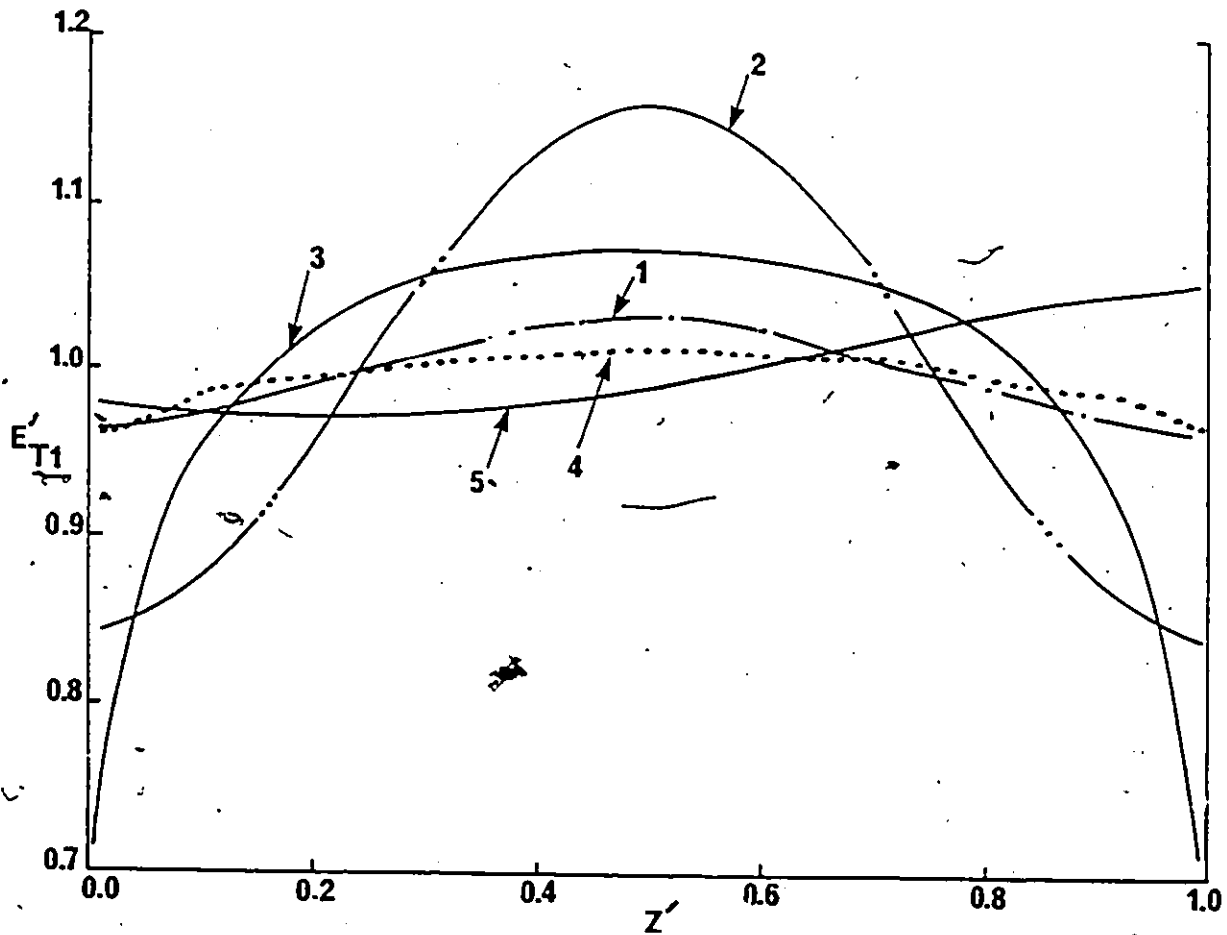
Figure 3.12: Normalized total field $E'T_1$ as a function of Z' for profile "c" at different radii r. $\epsilon_z = 3.2$, L= 40 mm, $2R_0$= 40 mm, $Ra = 28.3$ mm, curve 1 corresponds to $r/R_0=0.05$, curve 2, $r/R_0=0.95$, curve 3, $r/R_0=1.414$ (line AC), curve 4, $r/R_0=2$ and curve 5, $r/R_0=4$.

3.5.4 . Dependence on g

The effect of varying the length g of the vertical portion of the spacer near the electrodes on the electric field components at the triple junctions is shown in Table 3.8. In this case L and Rd are kept constants. Therefore, in order to vary g the radius Ry must also be varied according to the values given in Table 3.8 to obtain a smooth transition between the concave and the vertical sections such that the convex region remains asymptotic to both sections. The dependence of the field components on g (for fixed L and Rd) can not be separated from its dependence on Ry. It can be seen from Table 3.8 that E^*t_ic, E^*T_ic, $|E^*n_im|$ and $|E^*n_ic|$ show strong dependence on g and on Ry. E^*t_ic and E^*T_ic increase as g and Ry increase. But $|E^*n_im|$ which occurs in the transition region, and $|E^*n_ic|$ decrease as both g and Ry increase. It should be noted that as g/L increases, E^*t_im and E^*T_im, which occur at the interface in the mid gap, decrease slightly. Table 3.8 shows that g should be kept as small as possible to yield a low value of E^*T_ic but must be sufficient to provide adequate mechanical strength of the spacer near the electrodes.

Table 3.8: Dependence of the field components on g at a fixed L for a spacer having profile 'd'. $2R_0 = 40mm$. $L = 40$ mm. $Rd = 28.3$ mm. $s/q = 0.1$ and $\varepsilon_2 = 3.2$.

g/L	Ry mm	$|E'_{nlc}|$	$|E'_{nlm}|$	E'_{tlc}	E'_{tlm}	E'_{Tlc}	E'_{Tlm}
0.05	0.56	0.010	0.89	0.68	1.18	0.68	1.18
0.10	1.3	0.003	0.84	0.80	1.17	0.80	1.17
0.125	1.78	0.003	0.80	0.85	1.17	0.85	1.17
0.175	2.95	0.002	0.70	0.92	1.15	0.92	1.15
0.25	5.75	0.001	0.52	0.96	1.12	0.96	1.12

3.5.5 Dependence on the length of the spacer L.

Table 3.9 shows the dependence of the calculated fields at the cathode triple junction on the spacer length L in the range 10 - 100 mm. It should be noted that as L is varied both Rd and Ry also have to be varied in order to keep the same ratio g/L which is fixed at an arbitrary value but

realistically chosen to be $q/L = 0.125$. It will be observed from Table 3.9 that there is only a small influence on E'_{t1c} and E'_{T1c} with varying L, R_d and R_y when the parameters ε_2, q/L and s/q are kept constant, but there is a slight increase in $|E'_{n1m}|$ with increasing L.

Table 3.9: Dependence of the field components on the lengths L and q of profile 'd' spacer (Fig.3.1d). $2R_0= 40$ mm, $q/L= 0.125$, $s/q= 0.1$ and $\varepsilon_2= 3.2$.

L mm	R_d mm	R_y mm	$|E'_{n1c}|$	$|E'_{n1m}|$	E'_{t1c}	E'_{t1m}	E'_{T1c}	E'_{T1m}
10	7.07	0.443	0.006	0.78	0.87	1.15	0.87	1.15
20	14.14	0.886	0.005	0.79	0.87	1.15	0.87	1.15
40	28.30	1.780	0.003	0.80	0.85	1.17	0.85	1.17
60	42.43	2.658	0.003	0.83	0.85	1.18	0.85	1.18
100	70.70	4.430	0.001	0.89	0.82	1.21	0.82	1.23

3.5.6 Dependence on the permittivity ε_2 of the spacer.

The dependence of the field components of spacer 'd' on the permittivity in the range $\varepsilon_2 = 2.1$ to 12.000 are shown in Table 3.10. It can be observed that the field components exhibit a marked dependence on the permittivity in the range $\varepsilon_2 < 40$. Typically E'_{T_1c} decreases from 0.91 at $\varepsilon_2 = 2.1$ to 0.70 at $\varepsilon_2 = 40$. The dependence of the field components of spacer 'c' on the permittivity ε_2 at the triple junction follows the same behaviour as that of spacer 'a' (Table 3.3) and therefore it is omitted for brevity.

Table 3.10: Dependence of the field components on the permittivity of the spacer for profile 'd' (Fig.3.1d). $2R_0 = 40$ mm, $L = 40$ mm, $q/L = 0.125$, $s/q = 0.1$, $R_y = 1.73$ mm and $R_d = 29.3$ mm.

Material	ε_2	$\lvert E'_{n1c} \rvert$	$\lvert E'_{n1m} \rvert$	E'_{t1c}	E'_{t1m}	E'_{T1c}	E'_{T1m}
Teflon	2.1	0.001	0.70	0.91	1.11	0.91	1.11
Plexiglass	3.2	0.003	0.80	0.85	1.17	0.85	1.17
Epoxy	4.7	0.003	0.88	0.81	1.20	0.81	1.20
Macor-glass-ceramic	5.8	0.005	0.90	0.80	1.23	0.80	1.23
Porcelain	9.0	0.007	0.97	0.76	1.26	0.76	1.27
Titanium dioxide	40	0.008	1.06	0.70	1.32	0.70	1.32
Rutile	100	0.008	1.08	0.69	1.34	0.69	1.34
Titanates	1000 to 12000	0.008	1.10	0.68	1.34	0.68	1.34

3.5.7   Dependence on Ry.

The effect of varying the radius of curvature of the transition region Ry on the electric field components at the triple junctions are shown in Table 3.11. In order to be able to vary Ry for fixed values of Rd and q, s/q must be varied according to the values given in Table 3.11. It will be observed from Table 3.11 that Ry has no effect on the field components except on $|E'_{nrm}|$.

Table 3.11   Dependence of the field components on Ry for spacer having profile 'd' (Fig.3.1d). $2R_0 = 40$ mm, $L = 40$ mm, $\varepsilon_2 = 3.2$, Rd= 23.3 and q= 5 mm.

R_y mm	s/q	$|E'_{nlc}|$	$|E'_{nlm}|$	E'_{tlc}	E'_{tlm}	E'_{Tlc}	E'_{Tlm}
1.78	0.1	0.003	0.80	0.85	1.17	0.85	1.17
3.43	0.2	0.003	0.78	0.85	1.17	0.85	1.17
5.46	0.3	0.003	0.769	0.85	1.17	0.85	1.17
7.52	0.4	0.003	0.75	0.85	1.17	0.85	1.17
9.59	0.5	0.003	0.73	0.85	1.17	0.85	1.17
11.70	0.6	0.002	0.72	0.84	1.17	0.84	1.17

3.6 Comparison of Potential and Field Distributions of Different Spacers:

The potential distributions at the surface of different profiles: rectangular cylinder, profile 'a', profile 'b', profile 'c' and profile 'd' spacers are shown in Fig.3.13 for Macor glass-ceramic (ε_2 = 5.8). Ra=Rb= 21.2 mm for both profiles 'a' and 'b' and θ=45° for profile 'a'. Rc = 28.3 mm is the same as Rd for both profiles 'c' and 'd' and θ = 45° for profile 'c'. It can be inferred from the potential distributions that the electric field near the triple junction is smaller than the average applied field. This leads to a high withstand voltage of the gap.

Fig.3.14 shows E^*t_1 in profiles 'c' and 'd' (Fig.3.1) for three different radii of curvature Rc=Rd = 21.3, 28.3 and 77.3 mm. It will be observed from Fig.3.12 that E^*t_1c is lower than the average applied field in both profiles and decreases with decreasing Rd or Rc. E^*n_1 for Macor glass-ceramic is shown in Fig.3.15. It will be observed that $|E^*n_1c|$ increases with decreasing Rc of the spacer of profile 'c'. Similarly, E^*n_1 increases with decreasing Rd in profile 'd' and $|E^*n_1m|$ occurs near the transition region. The normal field is directed towards the solid insulator surface in the cathode region and is shown as having a negative value and away from the surface near the anode (positive value).
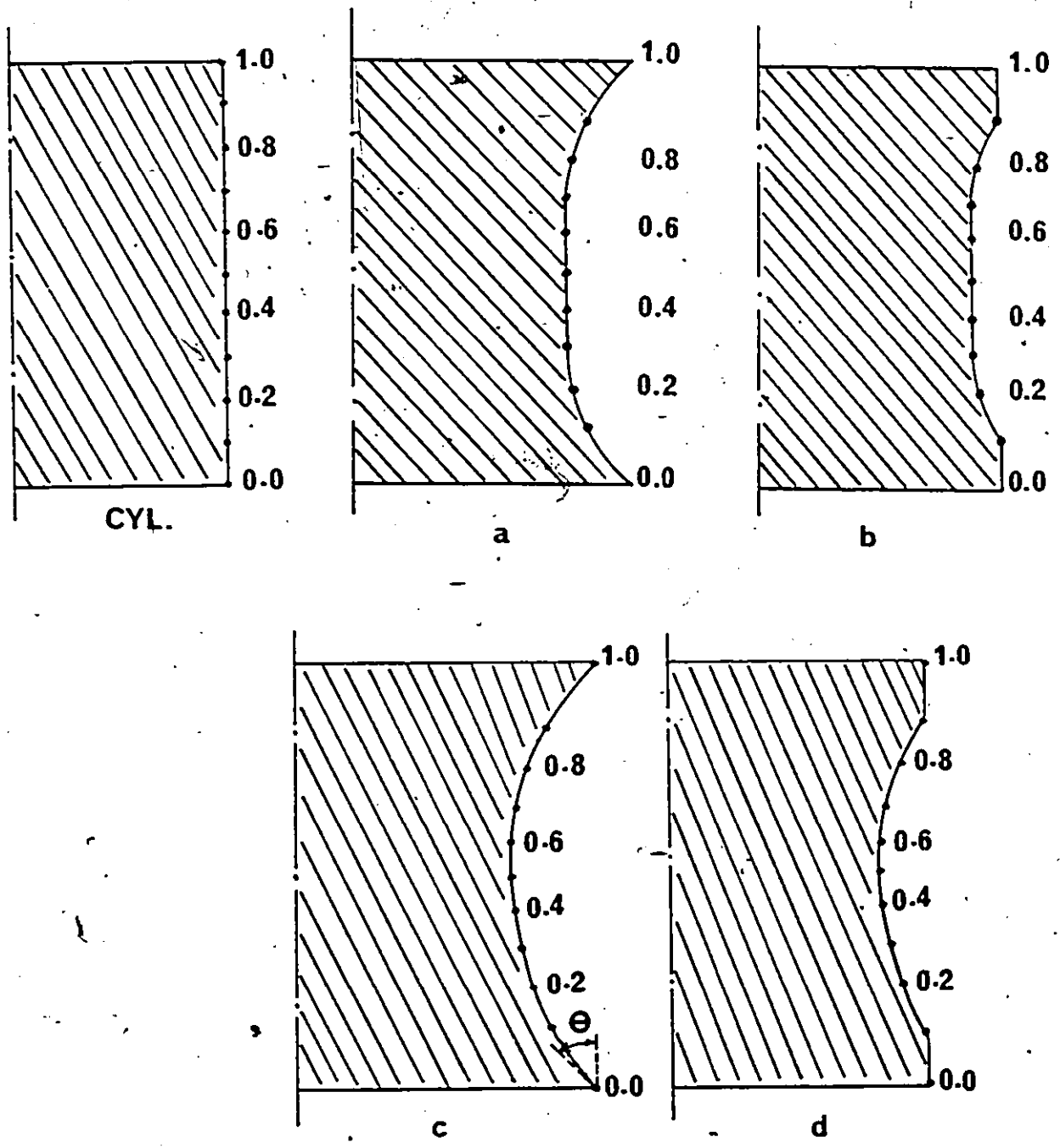
Figure 3.13: Potential distribution ϕ'along the interface of different types of spacers. $2R_0 = 40$ mm, L= 40 mm, $\varepsilon_2 = 5.8$, Cylindrical spacer, $R_0 = 20$ mm, Spacer of profile 'a', $R_a = 21.2$ mm, $\theta = 45°$, q= 15 mm, Spacer profile 'b', $R_b = 21.2$ mm, q= 15 mm, h= 5 mm, s/h=0.4 Spacer profile 'c', $\theta = 45°$, $R_c = 28.3$ mm, Spacer profile 'd', $R_d = 28.3$ mm, q= 5 mm, s/q= 0.1.
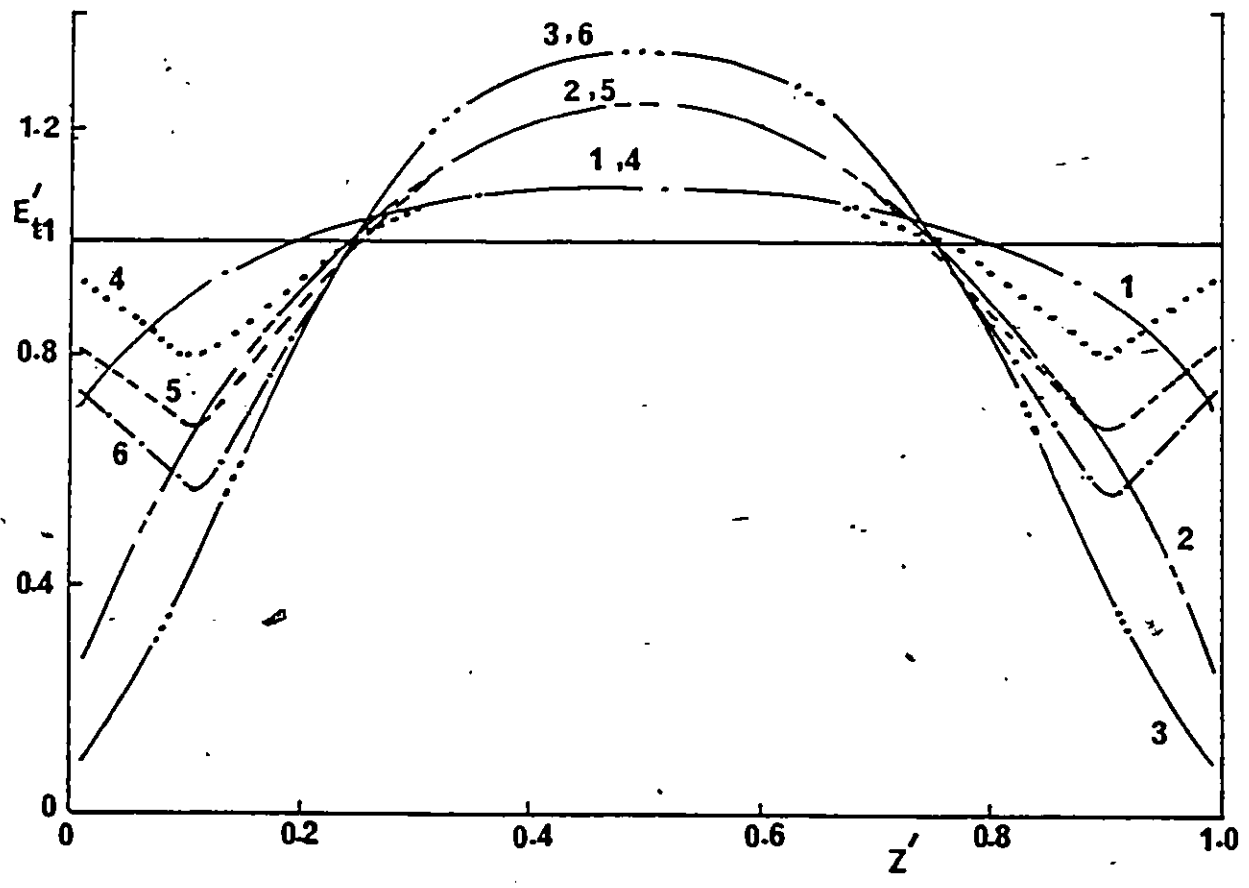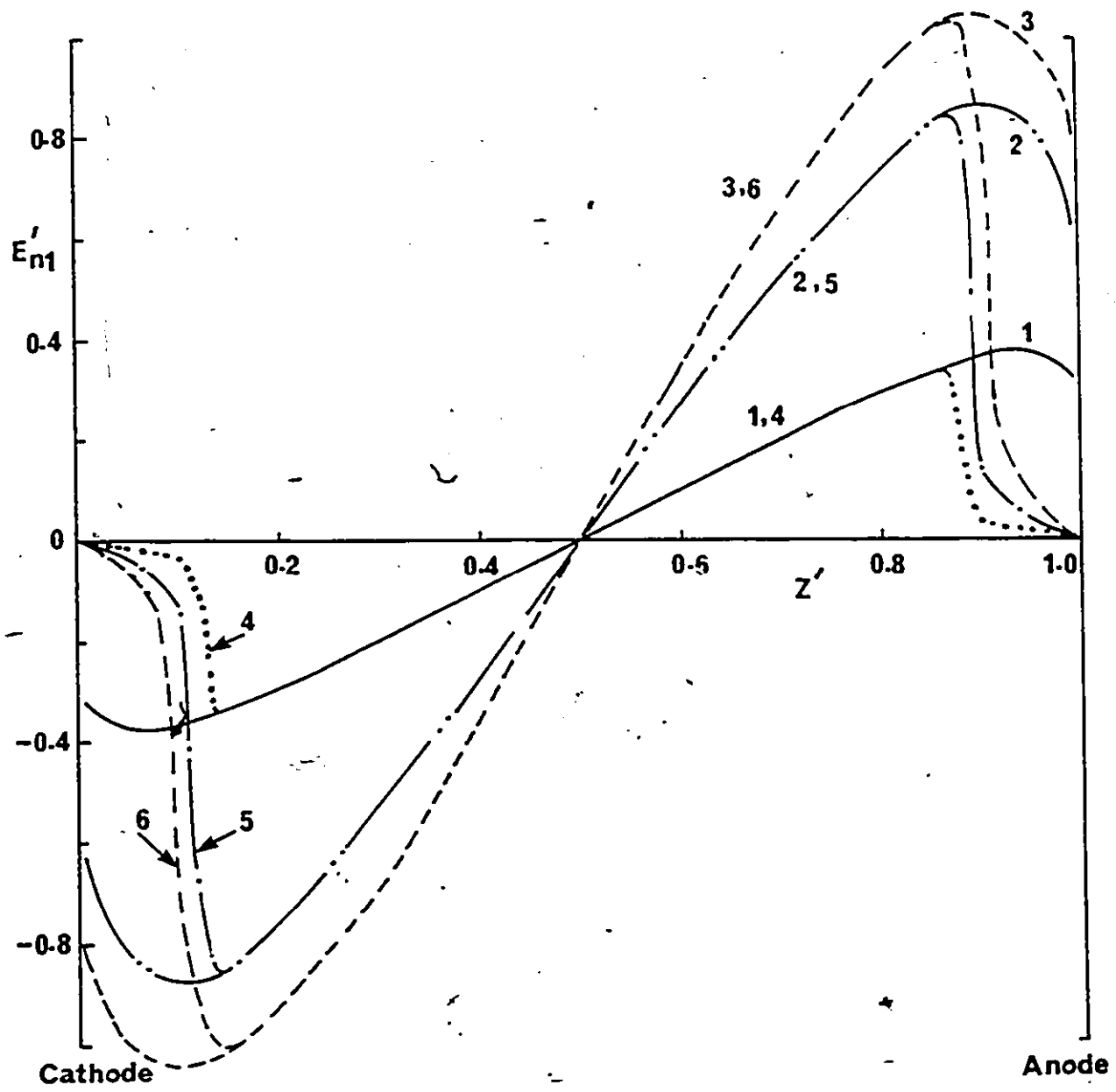
Figure 3.15: Normalized normal field $E^\bullet n_1$ distribution along the spacers interfaces. Conditions are as of Fig. 3.14.

The total field distribution E^*T_1 at the spacer-gas interface for $\varepsilon_2 = 5.8$ is shown in Fig.3.16, for profiles 'c' and 'd'. The value of E^*T_1 is less than unity in the vicinity of the electrodes and has the lowest value for profile 'c' when $\theta = 45°$ (corresponding to $Rc = 28.3$ mm for $R_0 = 20$ mm and $L = 40$ mm). E^*T_1 is also calculated at different radii r inside and outside the solid dielectric and is shown in Fig.3.17. Line AC is of special interest because it is the most likely path of the development of the avalanche leading to flashover in compressed gases. The highest field occurs in the mid gap region just inside the solid dielectric (Fig.3.16, curve 2) with a value of $E^*T_1m = 1.2$. Despite the latter increase in the field, which is not sufficient to initiate internal partial discharges at the nominal operating voltage of practical spacers, the enhancement of the surface flashover by lowering the field in the gas region is expected to be worthwhile since $E^*T_1c = 0.8$ (Fig.3.17, curve 3). At a location away from the solid dielectric $r/R_0 = 2$, E^*T_1 is almost at unity in the middle of the gap and a small asymmetry exists near the electrodes $E^*T_1a = 1.01 E^*T_1c$. However, at $r/R_0 = 4$, and near the electrodes edges the symmetry in the electric field distribution no longer exists. Typically, E^*T_1 is 1.1 and 0.95 at the high and the low voltage electrodes, respectively; giving an electric field which is 16% (curve 5) higher at the anode than at the cathode.
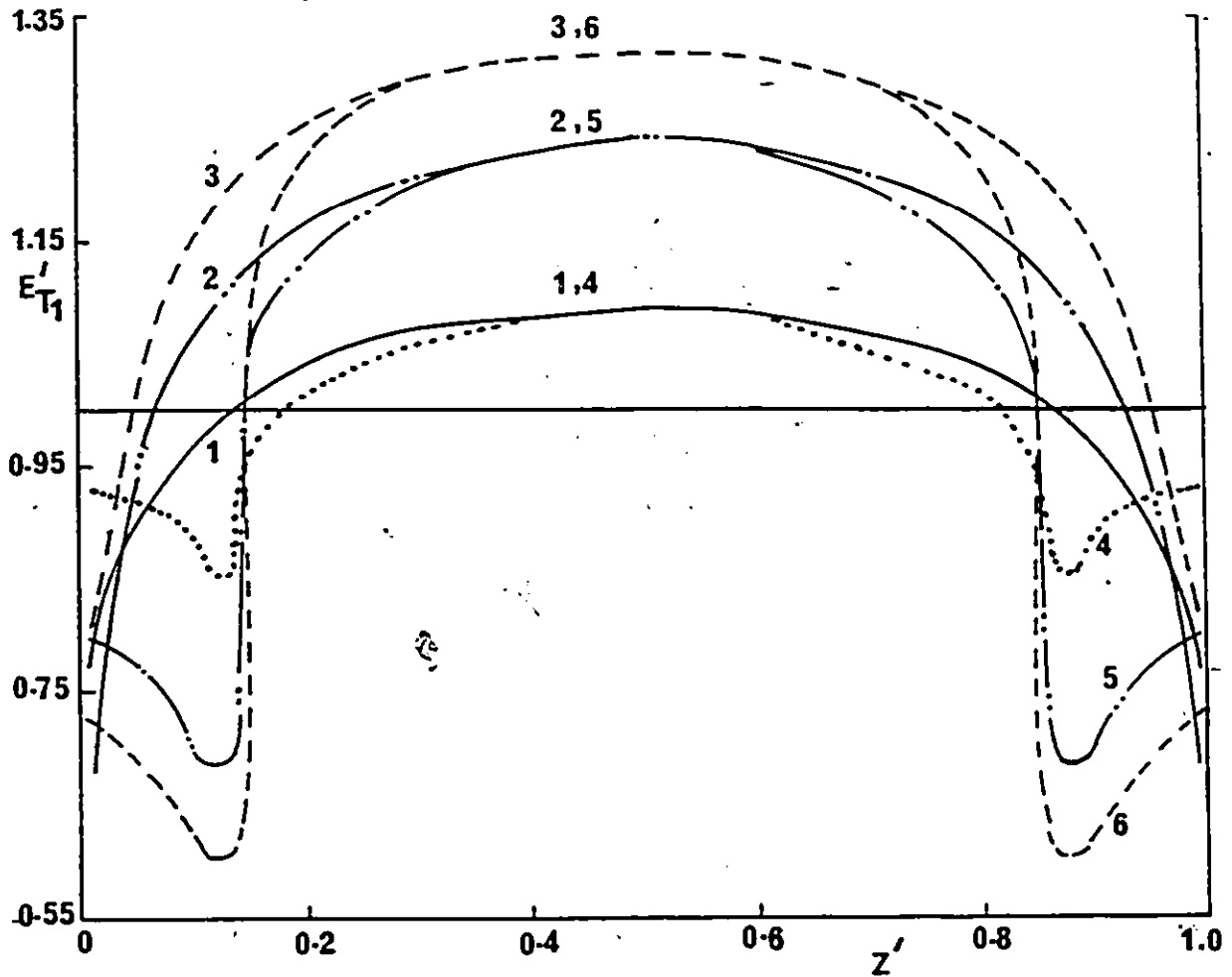
Figure 3.16: Normalized total field E'T₁ distribution along the spacers interfaces on the gas side. Conditions are as of Fig.3.14.
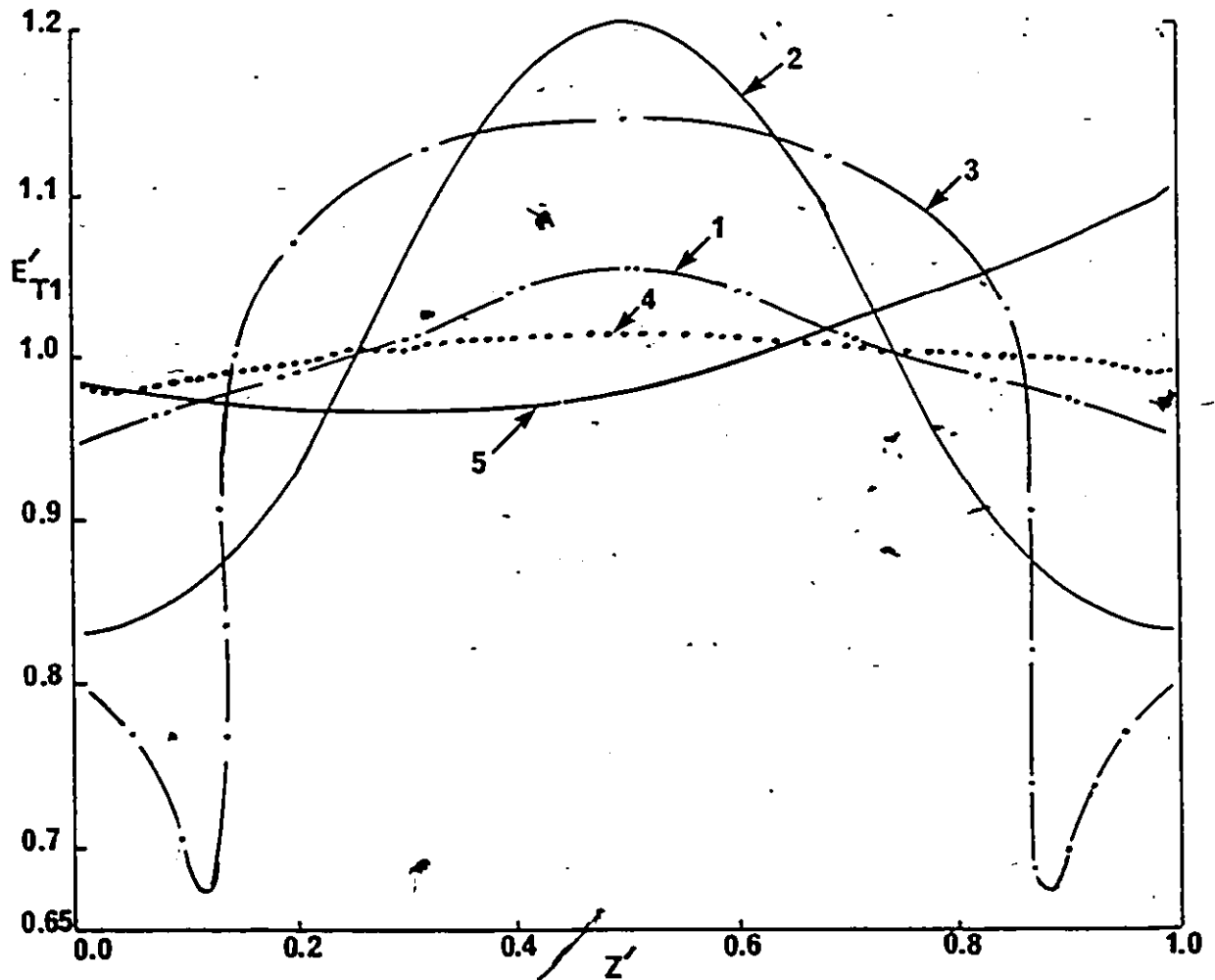
Figure 3.17: Normalized total field E'_{T1} as a function of Z' for profile "d" at different radii r. $\mathcal{E}_2 =$ 5.8, L= 40 mm, $2B_0 =$ 40 mm, Rd= 28.3 mm, q= 5 mm, s/q= 0.1, curve 1 corresponds to $r/R_0 = 0.05$, curve 2, $r/R_0 = 0.95$, curve 3, $r/R_0 = 1.215$ (line AC), curve 4, $r/R_0 = 2$ and curve 5, $r/R_0 = 4$.

3.7   Critical Conditions for Spacer Design

For the design of improved spacers it is necessary to reduce $E'T_{1C}$ at and the vicinity of the cathode junction as typically shown in Fig.3.16. A lower electric field at the cathode region results in a reduction of the Fowler-Nordheim field-emitted electrons from this electrode. This is particularly important at highly stressed gaps in high gaseous pressures of SF_6 and in vacuum devices.

It has been widely postulated that the onset of the surface flashover of the spacer occurs at a critical electron number ($\sim 10^8$) and hence at a critical electric current. Therefore with a lower local field at the electrodes in the concave geometry compared to the right angle cylindrical spacer, a higher applied voltage would be necessary to reach the critical current. This has been demonstrated for example with $\theta = 45°$ as shown in Figs.5.7 and 5.23.

The normal field at the spacer surface should also be reduced in order to minimize the deposition of pollution debris, other contaminants and surface charges. However, the contribution of the normal field to the flashover is indirect and of a much lesser degree than that of the axial field in the region of the gaseous gap. This is because the axial field is responsible for the movement of charges in the direction of the electrodes. The total electric field in the gaseous gap, adjacent to the spacer surface is

responsible for the production of charged species by
ionization processes which are strongly field dependent. At
high pressure of SF_6, and since the field no longer remains
uniform for a concave insulator, the avalanche length
becomes shorter than the gap length. Hence, if in the region
near the cathode the total field is reduced, as is the case
for $\theta = 45°$, (Fig.3.14), the production of electrons in the
gas region is also reduced. This also leads to a higher
withstand voltage as observed here (Figs.5.12 and 5.27).

Chapter IV

EXPERIMENTAL TECHNIQUES AND TEST PROCEDURE

In this chapter the experimental set up, the breakdown chamber, the high voltage power supplies including dc, ac, and impulse generators, the measuring circuit and the test procedure are described.

4.1 Breakdown Chamber

The breakdown chamber which has a volume of 30 l and is capable of a maximum gas pressure of 8 bar is shown in Fig.4.1. The chamber consists of two sections, the upper (1) is made of 0.94 cm thick carbon steel and the lower section (2) of 0.63 cm thick stainless steel. The upper section serves as an extension to accommodate the high voltages bushing which is capable of withstanding working voltage of up to 500 kV when it is pressurized in SF_6 at 2×10^5 Pa. It consists of a cone (3) and a corrugated bushing made of porcelain (4), two steel end plates, and a steel rod (5) mounted on a flange (6) to hold the top electrode (7). The top electrode is connected to the rod using a spring contact system (8). The space within the two porcelain sections and the end plates is pressurized with SF_6 at 2×10^5 Pa (absolute). The chamber contains two viewing ports (9).

Three pressure gauges are connected to the gas inlet. One gauge is used for measuring the gas pressure in the 300 psi range (resolution of 1 psi), while the other two, 0-50 mbar and 0-25 mbar (both, resolution of 1 mbar) are used during the evacuation of the chamber before starting the experiments. Pumping of the vessel is done via port (10) which is located at the base of the pressure vessel. The top electrode is fixed in position and the lower electrode is movable with the aid of a screw mechanism system (11) connected to a dial (12) (resolution of 0.01 mm) which shows the gap distance between the electrodes. The lower electrode is grounded using a copper strip (13) or connected to a small resistance for monitoring the breakdown current. A set of three screws (14) are used for levelling the lower electrode.
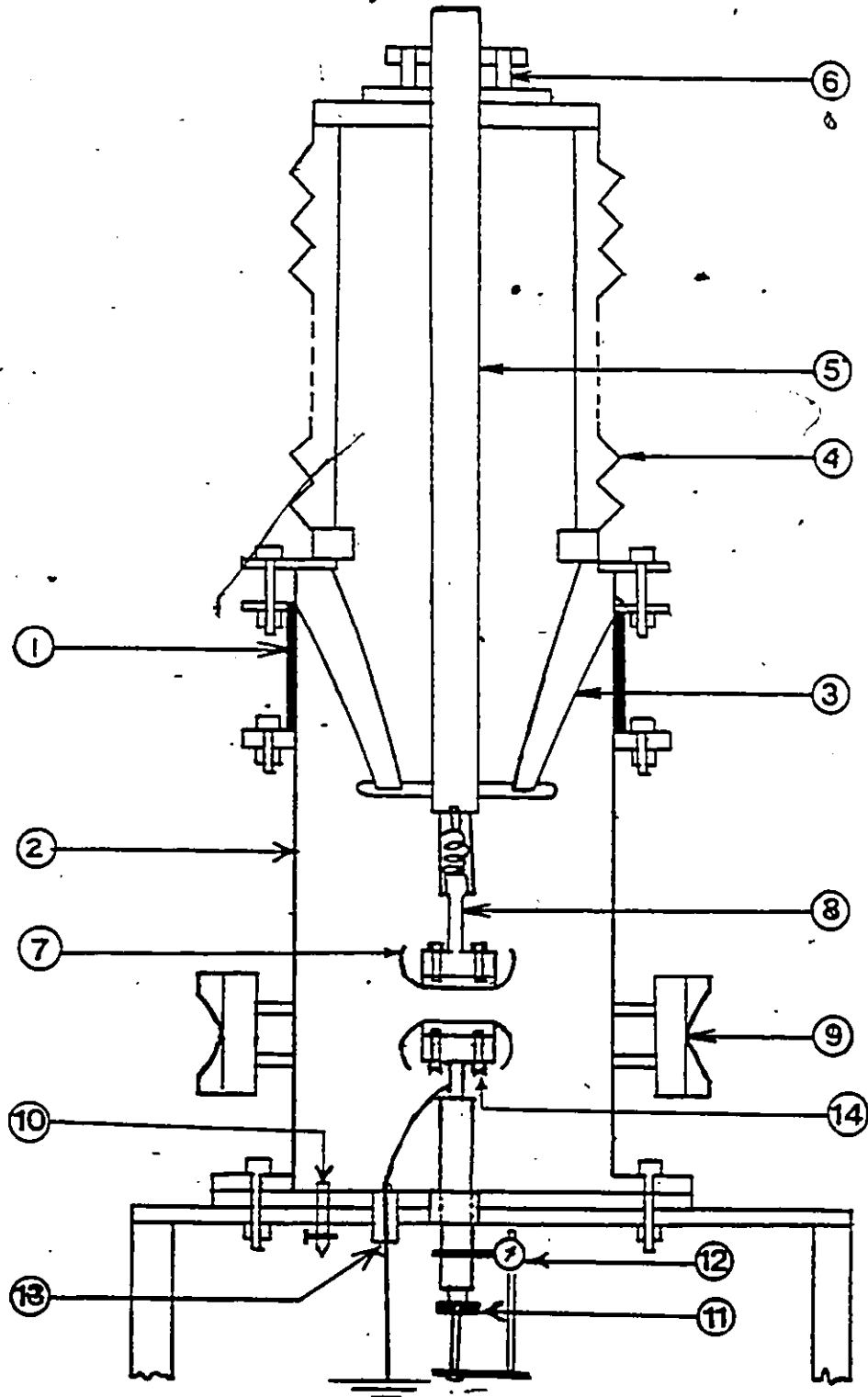
Figure 4-1: Breakdown chamber assembly

4.2   High Voltage Power Supplies

Surface flashover voltage of solid insulators are measured using dc, ac(60 Hz), and lightning impulse voltages. The description of the power supplies used are given below.

4.2.1   dc Power supply

The dc supply is a Deltatron model M-1000 power supply. The primary supply is a 208-240 V, 60 Hz, single phase, 8 kVA and the output voltage is 1.2 MV negative with respect to the ground at 2 mA. The generator has a load regulation of 0.1% and peak to peak ripple of 0.1% .

The Deltatron dc power supply is a cascade transformer with the secondary coils capacitively coupled to the primary coils of adjacent transformers. The primary power has a frequency of about 100 KHz. A Cockcroft Walton voltage multiplier is connected across the symmetry point of the circuit, and this produces the high voltage dc output at each stage. The secondary and the primary coils, capacitor network, diodes, and the series resistor form a deck unit which is encapsulated in epoxy 7.6 cm thick and 48.3 cm diameter and is capable of a maximum voltage of 60 kV. To build up the required dc voltage, 20 identical decks are stacked inside an insulating tube having 81 cm diameter and 298.5 cm long filled with SF_6 to provide cooling and insulation. The circuit diagram is shown in Fig.4.2.
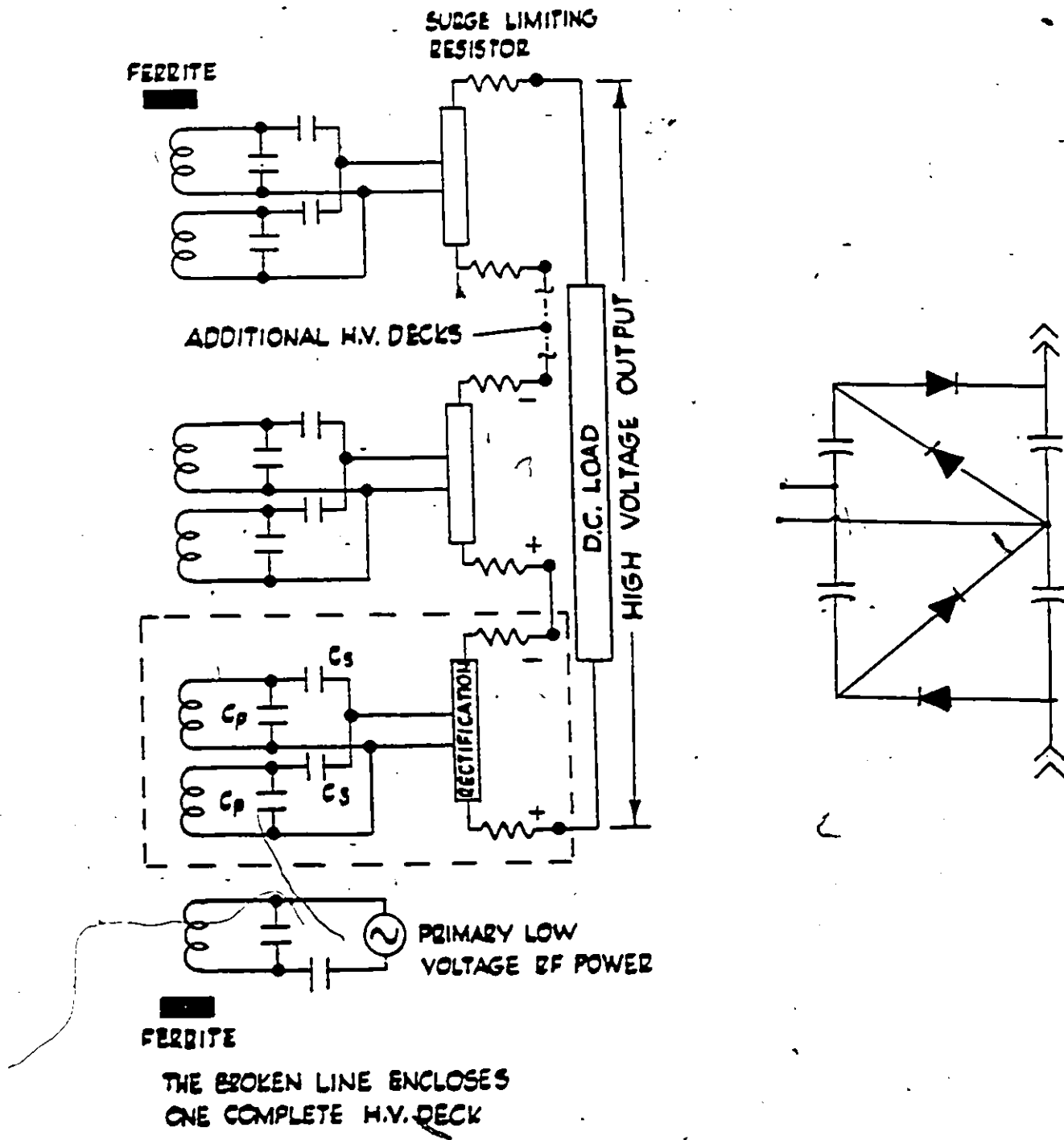
Figure 4.2: DC high voltage power supply

Stabilization, controls and monitoring are provided in a standard rack cabinet mounted on casters. Monitoring on the control panel is done with a voltmeter in the range (0-1.2 MV) and the current flowing in gap with an ammeter in the range (0-2 mA). The output voltage is calibrated with a 25 cm diameter sphere gap (accuracy of + 3%) up to 250 kV. The applied voltage is measured using a DVM (accuracy of $\pm$ 0.05%) connected across a resistive divider with a ratio of $10^6 : 1$.

4.2.2 Impulse generator

A schematic diagram of the impulse generator is shown in Fig.4.3. The impulse generator consists of 8 stages, each has two 0.2 uF capacitors connected in series. The capacitors in each stage are charged to a maximum voltage of 100 kV. The charging voltage is measured with a digital voltmeter (Sabtronics Model 2010A) with an accuracy of $\pm$ 0.05% using a resistive divider consisting of 600 MΩ, and 60 kΩ in the low end. The wave front resistance Rf and the wave tail resistance Rt are adjusted to obtain the required wave shape. The value of Rf and Rt are 169 Ω and 16 kΩ, respectively. In this experiment the standard 1.2/50 us impulse is used.

The impulse flashover voltage is measured by using a 549 Tektronix storage oscilloscope with a 1A1 plug in unit and a capacitive voltage divider (Haefley CB type 1000 kV wo. 550-225). The high voltage arm of the divider has a

capacitance of 1370 pF, the low voltage arm of the divider consists of a capacitor of 1.23 uF. The divider ratio is thus 1.23/0.00137= 898. The output of the generator is calibrated using a 25 cm diameter sphere gap (accuracy of $\pm$ 3%) up to 300 kV. It is necessary to terminate the cable with its characteristic impedance of 50Ω in order to eliminate the distortion of the wave form arising from multiple reflections at the cable termination which would otherwise introduce errors in the measurements.
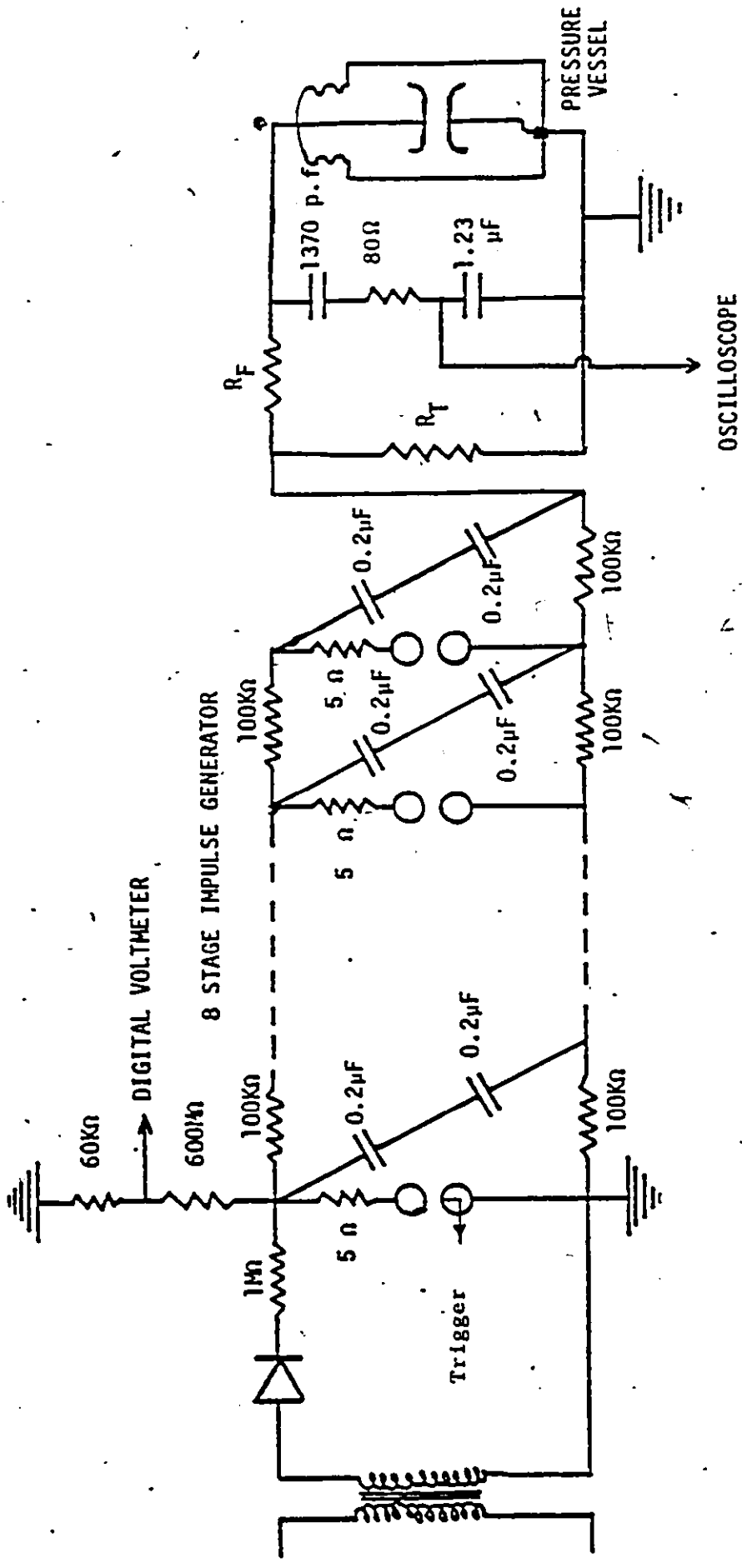
Figure 4.3: Impulse voltage generator

4.2.3   AC Power supply

The ac dielectric test unit MODEL 7150-150 CP manufactured by Hipotronics Universal Corp. is used. The high voltage transformer and the circuit diagram are shown in Fig.4.4. The input to the variac is fed from the mains at 4160 V, 50 A, 60 Hz. The output of the transformer is 150 kV rms, 150 kVA and 1 A. The duty cycle is 150 kVA for 1 h or 100 kVA continuous. The transformer is insulated with SF_6 at 10 Psi. Monitoring on the control panel is done with two voltmeters one of which is a storage voltmeter and the other has three ranges 0-37.5 kV (resolution of 0.5 kV), 0-75 kV (resolution of 1 kV) and 0-150 kV (resolution of 2 kV), and an ammeter for measuring the breakdown current in the range 0-1 A (resolution of 20 mA). The output voltage of the transformer is calibrated against a 25 cm diameter sphere gap (accuracy of $\pm$ 3%) up to 200 kV peak.
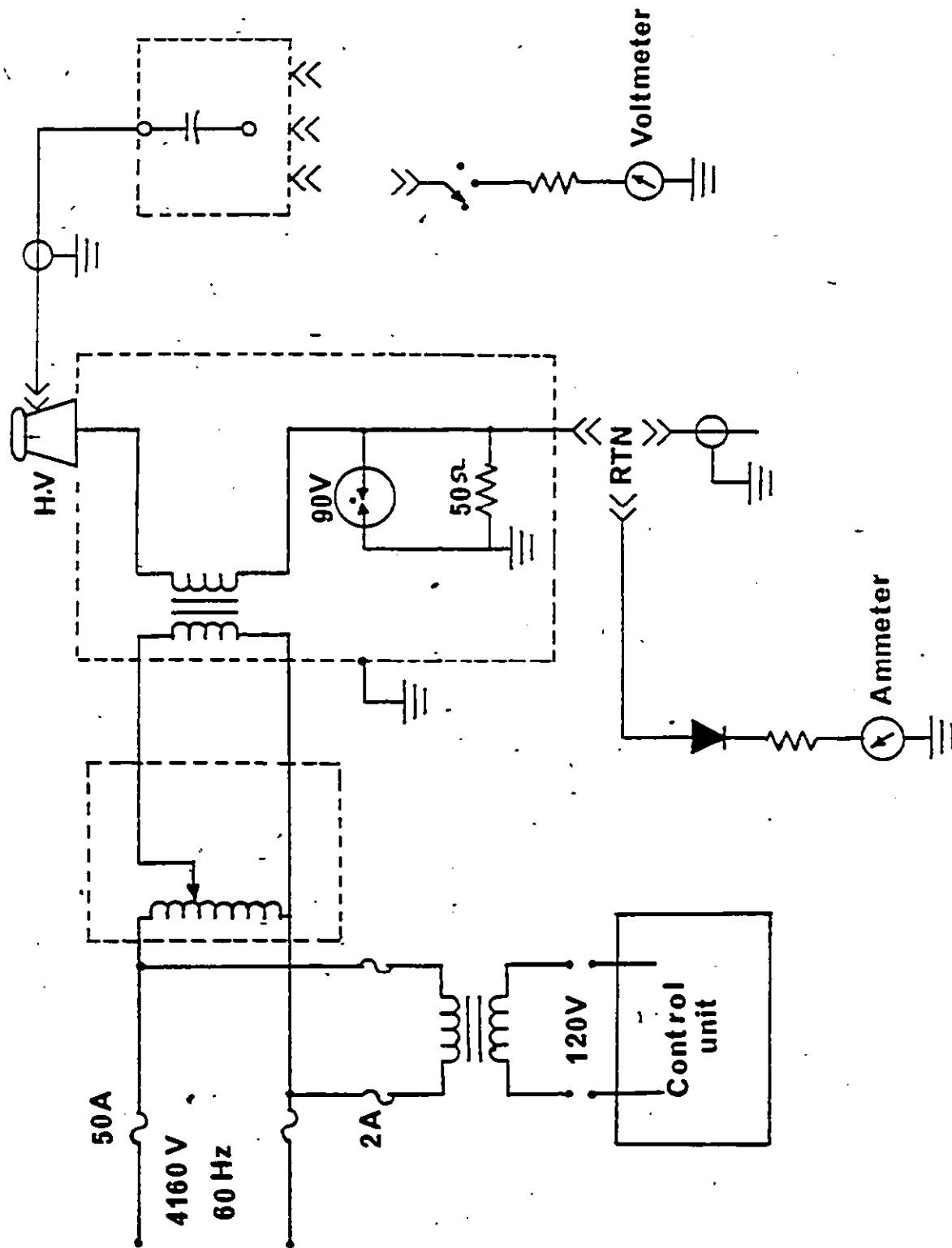
Figure 4.4: High voltage ac power supply

4.3 Gases used in This Investigation

Nitrogen, air and carbon dioxide at various pressures can be used as gaseous dielectrics and cooling media. Compressed air has been used in circuit breakers, bushings, current transformers and busbars [94,95]. Compressed nitrogen has less dielectric strength than air but does not promote oxidation and it has been used in current transformers and busbars. Carbon dioxide has no advantage as a dielectric over air or nitrogen. Hydrogen has been used for many years as a coolant medium for high speed turbo generators. Its use has an advantage in reducing the winding losses. It is more efficient in cooling than air [94].

Freon is considered an electronegative gas with high dielectric strength but it dissociates and yields a large amount of carbon when exposed to an arc discharge.

SF_6 is an electronegative gas with almost three times the dielectric strength of air and has a wide range of applications in the field of high voltage engineering. It is used in circuit breakers for arc quenching, high voltage transformers, capacitors, electrostatic generators, X-ray equipment and gas insulated equipment.

In the present work, N_2, air, CO_2, H_2, CCl_2F_2 and SF_6 are used to investigate the flashover characteristics of spacers. All gases are supplied by Liquid Carbonic Canada Ltd except SF_6 which is supplied in commercial grade (99.8%) purity by Allied Chemical Inc.

4.4   Electrode Profile

Since the   flashover strength is   sensitive to   the local
field,   care should   be   taken in   the   manufacture of   the
electrodes for studying the   flashover characteristics under
uniform field conditions.   Attention to the design   of the
electrodes, especially at the edges, is required so that the
electric field due to the curved edges should not exceed the
value of the average applied field in the gap.   Rogowski has
suggested an electrode profile for uniform field for axially
symmetrical systems. The details for determining the profile
can be   found in [75].   Another electrode profile   has been
proposed for uniform fields known as the Bruce profile [36].
It has a flat portion not   less than the maximum gap spacing
at   which   the electrodes   are   used   and a   curved   portion
continuing by a circular part to minimize the edge effect.

The Rogowski profile requires   a large electrode diameter
for   the electric field   to be   uniform   everywhere in   the
region,   but in   Bruce profile   the electric   field at   the
curved part   is about 10% higher   than that of the   field at
the centre of the electrode.   Therefore,   a profile known as
Harrison   profile   was   suggested   which   was   a   compromise
between the Bruce and the Rogowski profiles [97].

In the present study,   stainless steel planar electrodes
with a Harrison profile [97] and having a diameter of 115 mm
are used. For the purpose of studying the effect of recessed
electrodes,   a   Bruce profile   [96] has   been machined   from

stainless steel and having a diameter of 75 mm with a
recessed depth of 2 mm. The angle of recess is varied in the
range 10°-80°. Different pairs of these electrodes have
been manufactured to allow a wide range of applications.

4.5 Experimental Environment

Great care is taken to maintain a high degree of
cleanliness, comparable to an industrial production
environment of GIS power equipment, in the pressure vessel,
the electrodes, the samples and the gases used.

1. The pressure vessel is thoroughly cleaned. In order
   to remove any corrosive gas compounds which might
   result from the electrical discharge of SF_6 inside the
   pressure vessel, copper sulphate has been used inside
   the breakdown chamber. In order to replace the gases
   adhered to the surfaces of the spacers, the electrodes
   and chamber walls, the breakdown chamber is first
   evacuated to a background pressure < 10 Pa and then
   flushed twice with a fresh sample of the gas being
   used.

2. Before each series of tests with different spacers,
   the surfaces of the electrodes are carefully machined
   and polished with 600 sandpaper and then given a
   mirror finish with NEVR DULL (The George Basch Co.
   Inc. N.Y.) which is used for polishing metals. The
   electrodes are degreased with acetone, rinsed with

distilled water and dried before installation in the chamber.

3. The spacers are machined to a very smooth finish and finally polished using 600 grid sandpaper. The samples are degreased thoroughly using a mild detergent and rinsed in distilled water with the aid of an ultrasonic vibrator - and dried before installation in the breakdown chamber.

4. The samples and the electrodes are handled very carefully by using a polymer film gloves to maintain a high degree of cleanliness.

5. The gap between the electrodes is levelled using the three screws platform provided at the base of the lower electrode.

6. A water limiting resistance of 4 MΩ has been connected in series at the high voltage side, in order to limit the current at breakdown. Since a high breakdown current could result in a damage to the electrodes surface and the samples.

7. All control units of the three high voltage power supplies, are located inside a screened Faraday cage made of copper mesh, and is well grounded to minimize the influence of the electromagnetic interference. All metallic objects in the vicinity are grounded, and all measuring equipment are shielded to enhance the accuracy of the measurements.

4.6 Test Procedure

The flashover voltage is defined as the maximum voltage which the insulating gap withstands just prior to the collapse of the applied voltage to a very low level and the flow of a large current through the gap. The following test procedure is used.

1. The gap between the electrodes is levelled before the spacer is introduced between the electrodes.

2. The spacer is placed in the centre of the bottom electrode and then raised until it made contact with the top electrode. A good contact of the spacer with both electrodes is essential to avoid deleterious effects on the flashover voltage measurements.

3. The breakdown chamber is first evacuated to a background pressure < 10 Pa using a rotary vacuum pump for at least 2h., then flushed twice with a fresh sample of the gas being used in the test.

4. The chamber is pressurized with the test gas to the desired pressure and left for 1/2h. before starting the measurements.

5. During the breakdown measurements, the voltage is applied initially at about 60% of the estimated value of the breakdown voltage, then increased gradually until breakdown occurs.

6. The reported flashover voltage is the average of at least 15 tests. It is corrected to $T_0 = 20^\circ$ C as

commonly used, assuming a linear dependence of the gas pressure on temperature for small changes in the gas density.

$$V \text{ reported} = \frac{273 + T}{273 + T_o} \times V \text{ measured}$$

where T is the measured temperature in $^\circ$C at the time of pressurizing the chamber.

Chapter V

DC, AC (60 HZ) AND LIGHTNING IMPULSE FLASHOVER

VOLTAGE MEASUREMENTS

5.1   Introduction

The interest in using high voltage gas insulated systems
is steadily increasing in recent years.   The use of gas
insulated systems requires a spacer for the physical support
of the high voltage conductor. It is commonly accepted that
the flashover voltage along the spacer- gas interface limits
the voltage rating of GIS. An increase in the withstand
voltage capability of the spacer might result in a reduction
in the size, the weight and hence the cost of gas insulated
apparatus and equipment. For evaluation of the new designs
of spacers they should be tested using simulated operating
conditions under dc, ac, and lightning impulse voltages
which are likely to be encountered in practice.   In the
present chapter the dc, ac (60Hz) and lightning impulse
flashover voltages for different spacer profiles in air, N_2,
CO_2, H_2 and SF_6 are reported. The gas pressure is varied in
the range $(1-7) \times 10^5$ Pa depending on the type of gas.

5.2   Spacer_Profiles

Different spacers are machined from Plexiglas ($\varepsilon_2=3.2$) and having profiles "a", "b", "c" and "d" as shown in Fig.3.1. The spacer of profile "a" has $Ra=(q/\sin\theta)$, where θ is the contact angle with the electrode and q is the length of the concave section. The radius Rc of profile "c" can be determined from $Rc=(L/2\sin\theta)$, where L is the length of the spacer. For the sake of comparison, Rb of profile "b" is made equal to Ra of profile "a", and Bd of profile "d" is made equal to Rc of profile "c". The vertical portion near the electrodes in profiles "b" and "d" is fixed at 1 mm. In profiles "b" and "d", since it was difficult to machine the transition section between the vertical and the concave sections, for the small dimensions used in the experimental study, it was smoothed by polishing with sand paper. From two to four spacers are used for each test to check the reproducibility of the flashover voltage.

5.3 Flashover Voltage Measurements of Profiles 'a' and 'b' Spacers(Fig.3.1)

5.3.1 Conditioning effect

The dependence of the dc flashover voltage of 10 mm long spacer having profile 'a' with ($\theta = 45°$ and $Ra = 2.83$ mm) on the number of sparkings in 0.2 MPa and 0.4 MPa of N_2 is shown in Fig.5.1. Five minutes are allowed to elapse between successive sparks. It will be observed that the flashover level is independent of the number of sparkings after the third spark at 105 kV $\pm$ 1.4% in 0.4 MPa of N_2. At the lower gas pressure of 0.2 MPa in N_2 the flashover voltage is 56 kV $\pm$ 1.7 % (Fig.5.1). The variations in the value of the flashover voltage are shown at least once when comparisons are made, typically in Figs 5.9 to 5.10, 5.23 to 5.26 and in chapter 3 in the form of I for most experimental data taken in this work.

5.3.2 dc Flashover measurements of profile 'a' spacer in air, N_2, CO_2, H_2 and SF_6

The dc surface flashover of Plexiglas spacers is measured in SF_6, air, N_2, CO_2 and H_2 using profile 'a' (Fig.3.1a).

Fig.5.2 shows the flashover voltage of Plexiglas cylindrical spacer ($\theta = 0$) having a diameter $2R_0 = 10$ mm and length $L= 10$ mm in different gases. The gas pressure is varied in the range of 0.1 MPa to 0.4 MPa (1.0 to 4 bar). It will be observed that at a fixed gas pressure, the
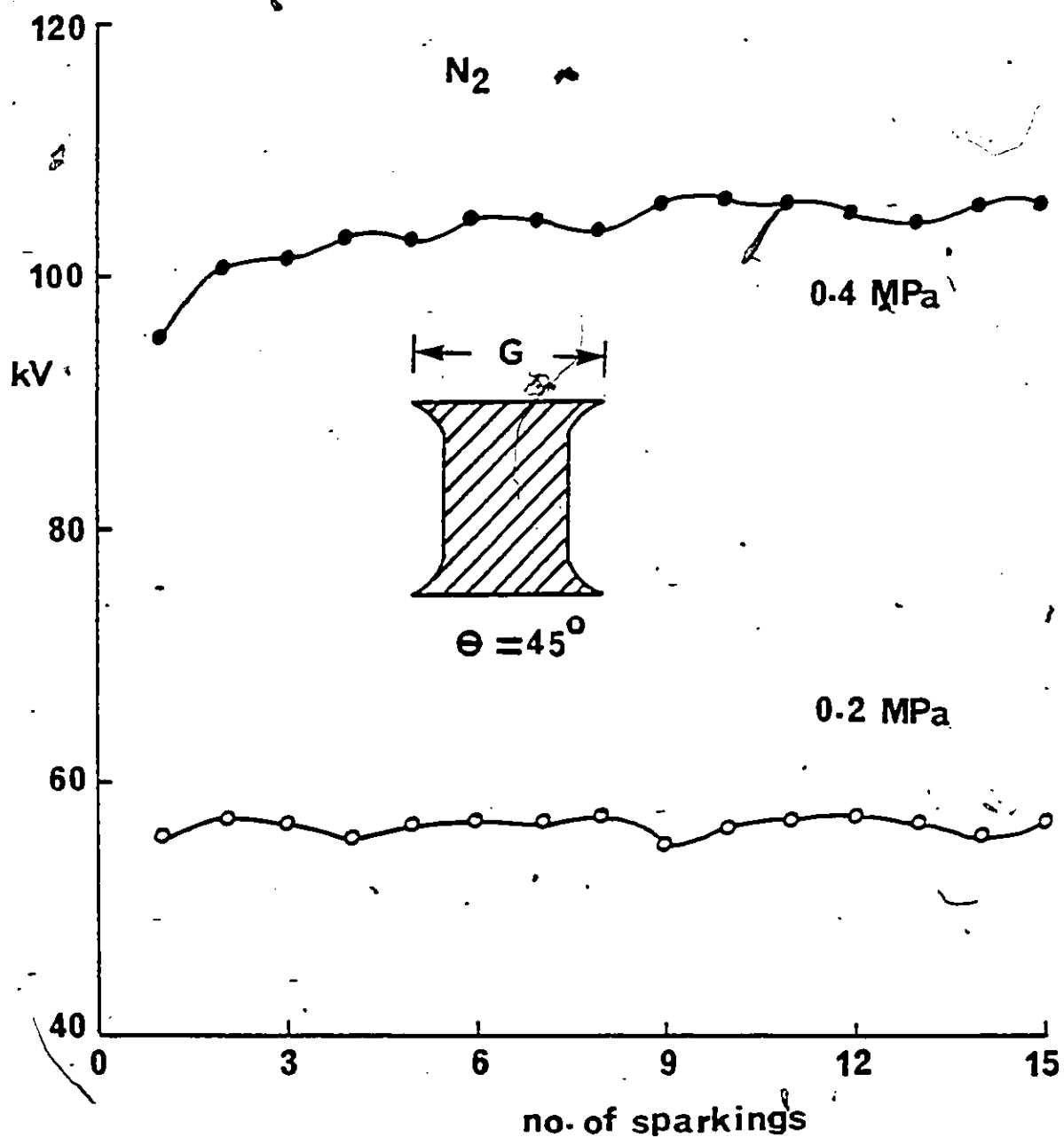
Figure 5.1: dc flashover voltage as a function of number of sparkings in N_2 using profile 'a'. Plexiglas $\varepsilon_2 = 3.2$, $2R_0 = 10$ mm., L = 10 mm, G = 11.65 mm and $\theta = 45°$. Measurements commenced at 0.2 MPa and after 15 shots was increased to 0.4 MPa.
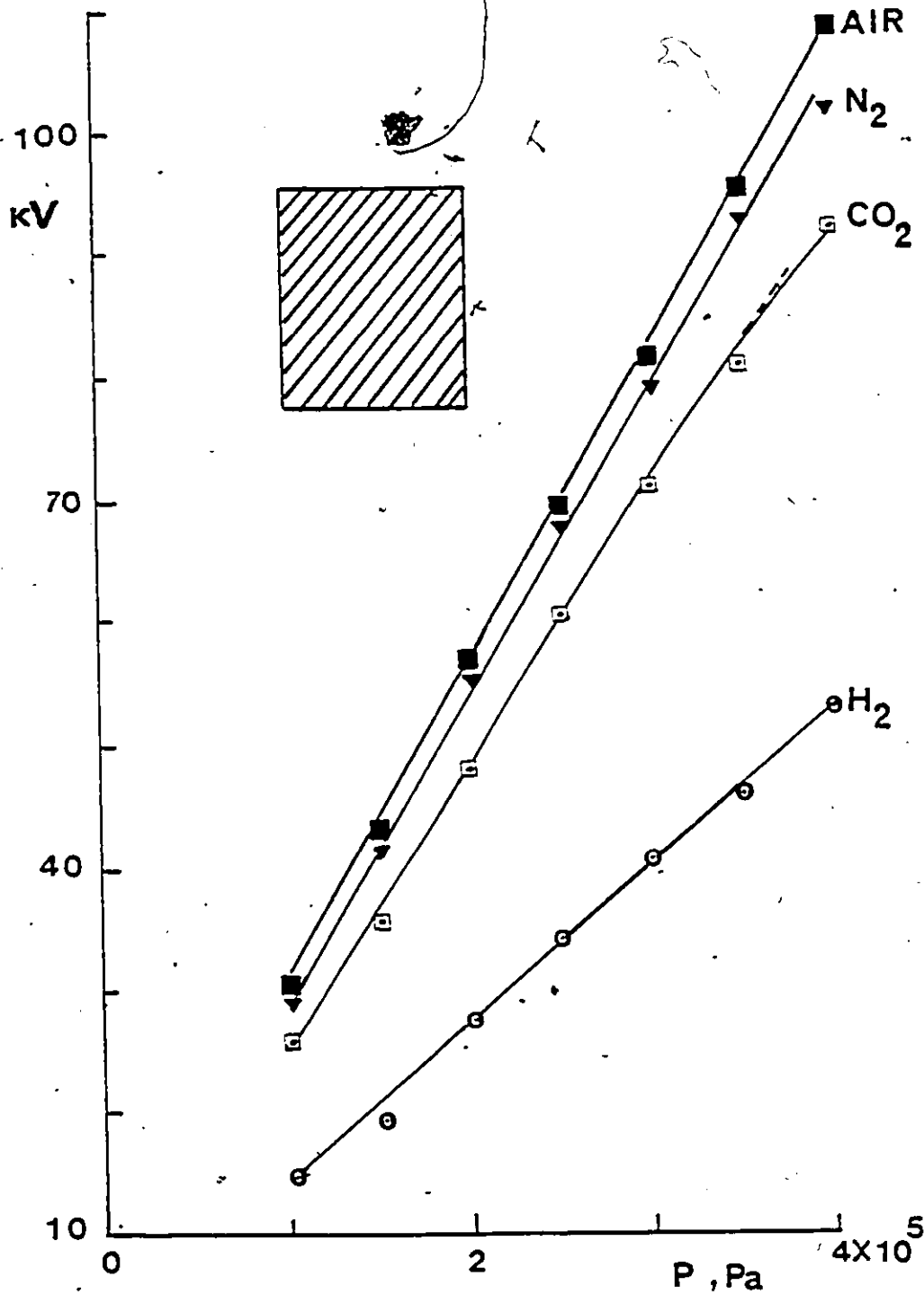
Figure 5.2: dc flashover voltage as a function of gas
pressure in air, N_2, CO_2 and H_2 for cylindrical
spacer $\theta = 0$, $\varepsilon_2 = 3.2$, $L = 10$ mm and $2R_0 = 10$ mm.

flashover voltage with air is higher than N_2, CO_2, and H_2. A linear dependence on pressure for air, N_2 and H_2 and a slight downcurving in CO_2 above 3 bar are observed.

The flashover voltage of Plexiglas spacers having a diameter $2R_0$ =10 mm and length L= 10 mm for θ =30°, 45°, and 80° are shown in Figs. 5.3 to 5.5, respectively in air, N_2, CO_2 and H_2. It has been found that the flashover voltage for θ = 45° is higher than at all other values of θ.

Fig.5.6 shows the flashover voltage in air, N_2, CO_2 and H_2 at the optimum angle of profile 'a' (θ = 45° and R_a = 2.83 mm) and compared with a cylindrical spacer. It can be seen from Fig.5.6 that there is an improvement in the withstand voltage for all gases used, and for the pressure range covered when using a profile 'a' having θ = 45° compared to the right angle cylindrical spacer.
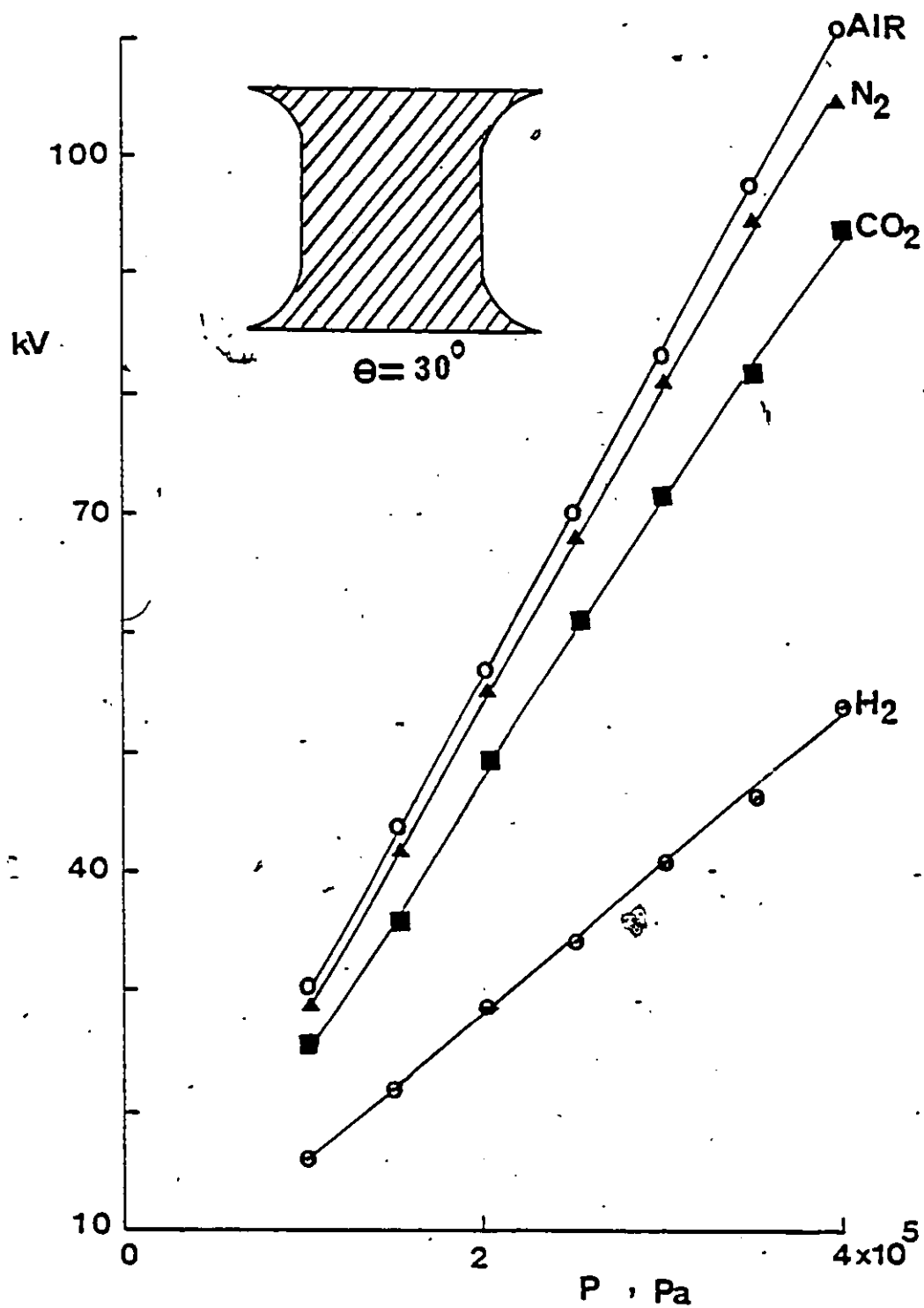
Figure 5.3: dc flashover voltage as a function of gas pressure for spacer 'a', θ= 30°and G=11.07 mm. Other conditions are as for Fig.5.2.
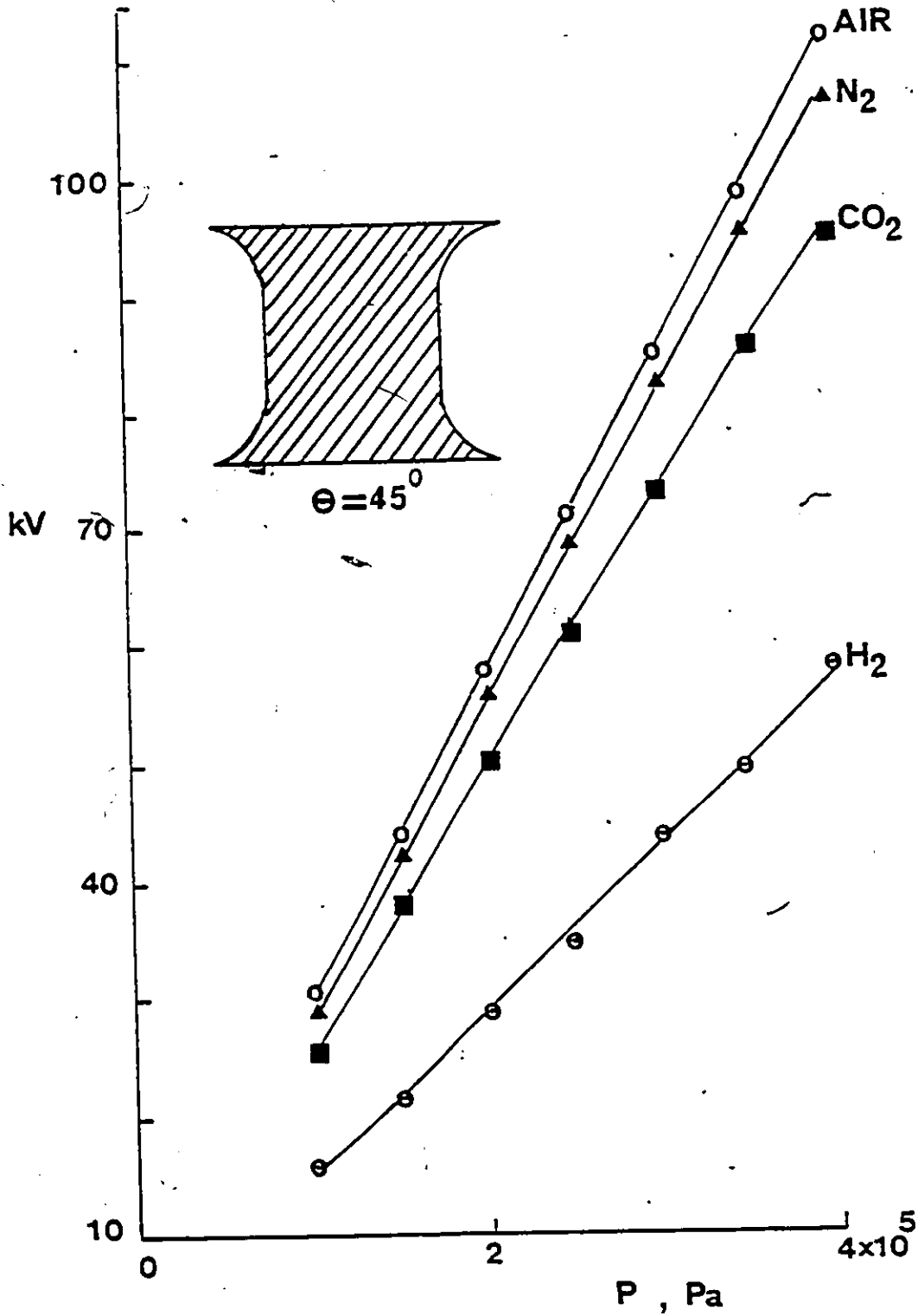
Figure 5.4: dc flashover voltage as a function of gas pressure for profile 'a', θ= 45° and G=11.65 mm. Other conditions are as for Fig.5.2.
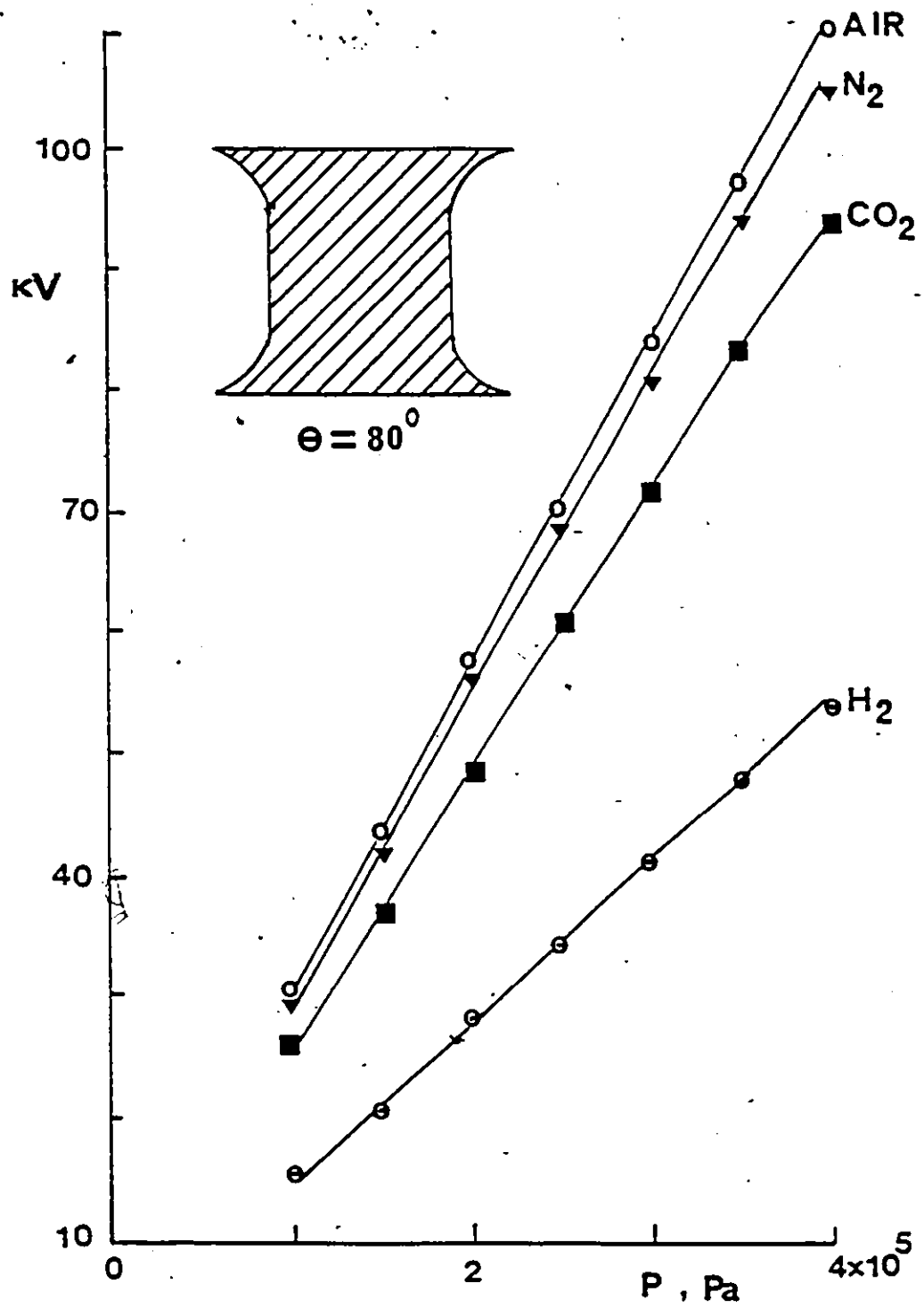
Figure 5.5:   dc flashover voltage as a   function. of gas
pressure for profile 'a', Ө= 8C° and G=13.35
mm. Other conditions are as for Fig.5.2.
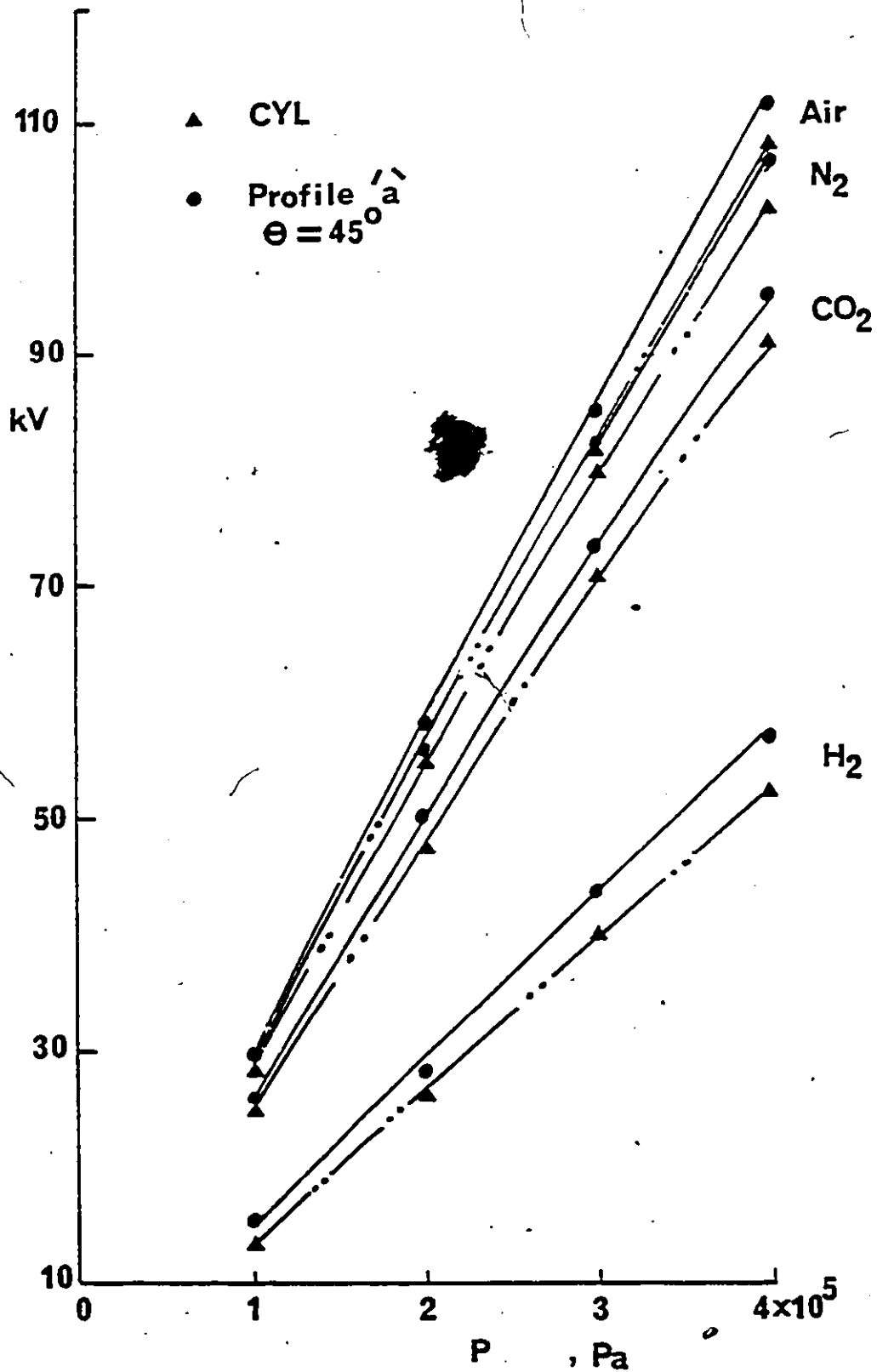
Figure 5.6: dc flashover voltage as a function of gas pressure for cylindrical spacer and spacer profile 'a', θ= 45° in different gases. ε_2= 3.2, $2R_o$= 10 mm and L= 10 mm.

The dc flashover voltage of Plexiglas spacers ($\varepsilon_2 = 3.2$), each having a diameter of $2R_0 = 20$ mm and length $L = 10$ mm and using different contact angles θ in the range 0 to $80°$ is measured in SF_6 and N_2 and shown in Figs. 5.7 and 5.8, respectively. The diameter G in contact with the electrodes is varied in the range 20.53 mm to 23.35 mm as θ varies from $15°$ to $80°$. It will be observed that at a fixed gas pressure, the surface flashover voltage for $\theta > 0$ is higher than that of the right angle cylindrical spacer ($\theta = 0$). Typically, for $\theta = 45°$ the flashover voltage at 0.3 MPa of SF_6 is 252 ± 5 kV while for $\theta = 0$ is 205 ± 6 kV (Fig. 5.7). In 0.7 MPa of N_2 the flashover voltage is 166 ± 3 kV for $\theta = 45°$ compared to 135 ± 5 kV for $\theta = 0$ (Fig.5.8).

The observed increase in the flashover voltage of the spacer of profile 'a' over the cylindrical spacer is due to the lower electric field at the cathode junction and beyond it as shown in chapter 3. As the electric field becomes lower, the production of the electrons by ionization will be lower and the field emission becomes lower also. This leads to a higher flashover voltage. In chapter 6 analysis will be presented to correlate the measured flashover voltage with the calculated fields.
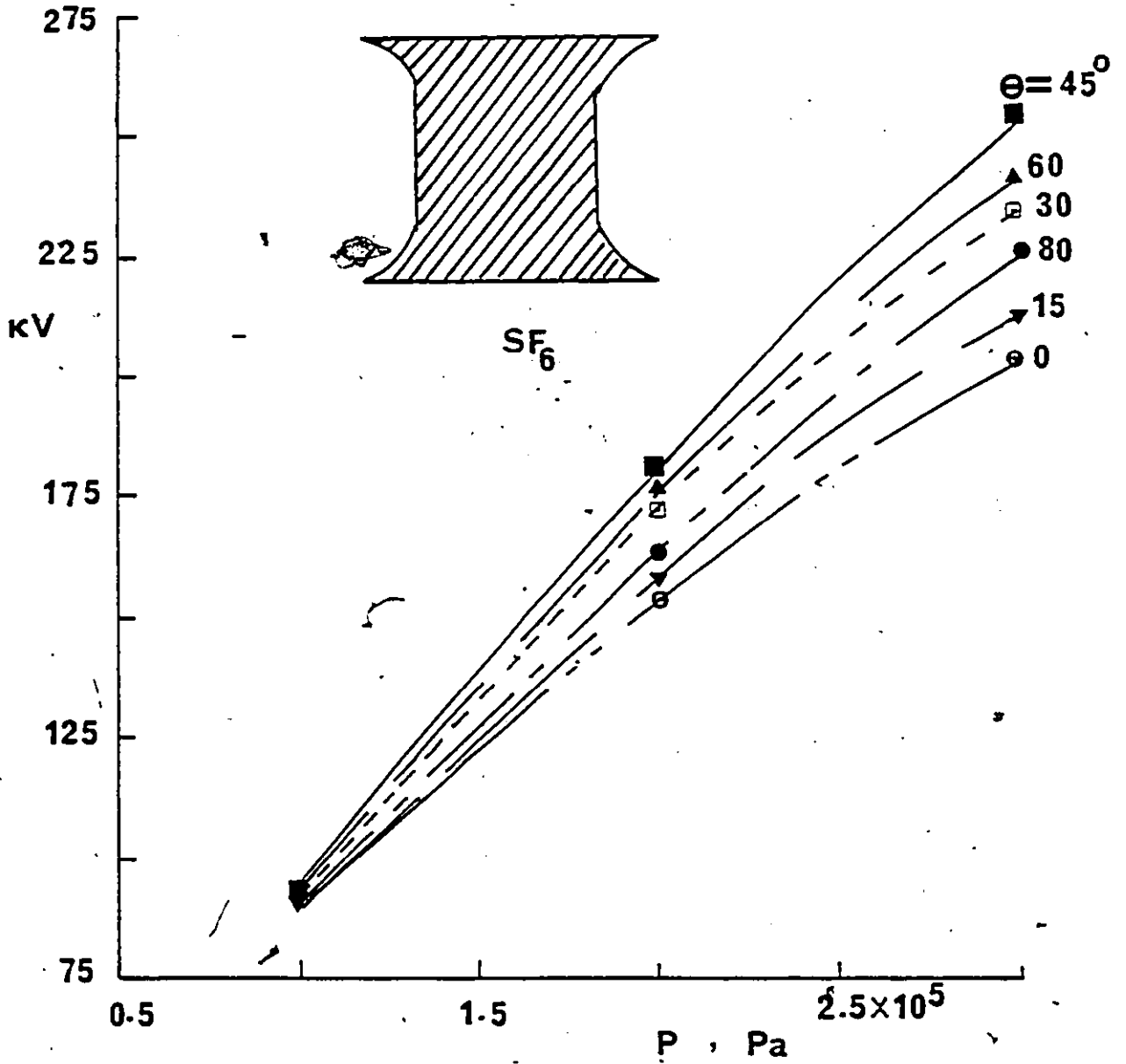
Figure 5.7: dc flashover voltage as a function of gas pressure in SF_6 for spacer 'a' and for different contact angle θ. $\varepsilon_2 = 3.2$, $2R_0 = 120$ mm, q= 2 mm, d= 6 mm, Ra= q/sin θ and L= 10 mm.
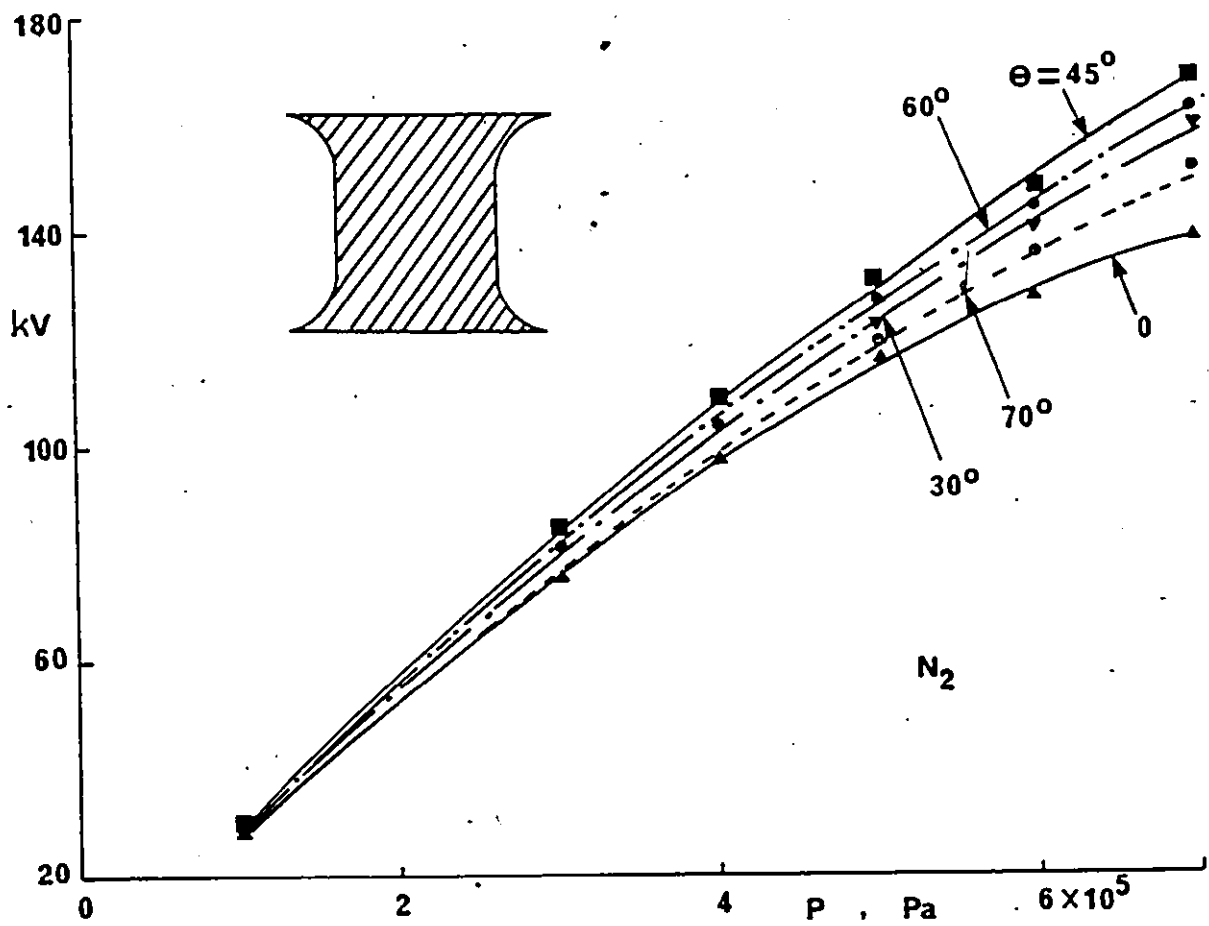
Figure 5.8: dc flashover voltage as a function of gas pressure in N_2 for spacer 'a'. Other conditions are as for Fig.5.7.

5.3.3 Flashover voltage measurements of profile 'b' spacer in SF_6 and N_2

Spacer 'b' is investigated here because it has stronger mechanical strength than spacer 'a' in the vicinity of the electrodes. It is important to ascertain the effect of the length h on the withstand voltage of profile 'b' before it can be seriously considered for practical applications.

The dc flashover voltage of a Plexiglas spacer having profile 'b'(Fig.3.1b) is measured in SF_6 and N_2. The radius of curvature Rb is varied and therefore the diameter G of the spacer in contact with the electrodes changes slightly with Rb but can be taken as constant. For example when L =10 mm, for Rb = 2.03, 2.83, 4.0, 7.73 mm, the diameter G = 20.5, 20.4 ,20.4, 20.1 mm, respectively. Hence the area effect on the flashover is negligible in this case [115].

Fig.5.9 shows the flashover voltage in N_2 for different radii of curvature Rb. The flashover voltage of a rectangular cylinder (θ = 0) is also shown as Vs at different gas pressures. It can be observed from Fig.5.9 the flashover voltage for all Rb values used is higher than that of the right angle cylindrical spacer. Typically, the flashover voltage at 0.7 MPa is 167±4 kV and 157±3 kV for Rb=2.83 mm and 7.73 mm, respectively. The corresponding flashover voltage of the rectangular cylinder is 135±5 kV. The percentage increases in the flashover voltage with respect to the right angle cylindrical spacer are 23% and 15%, respectively.
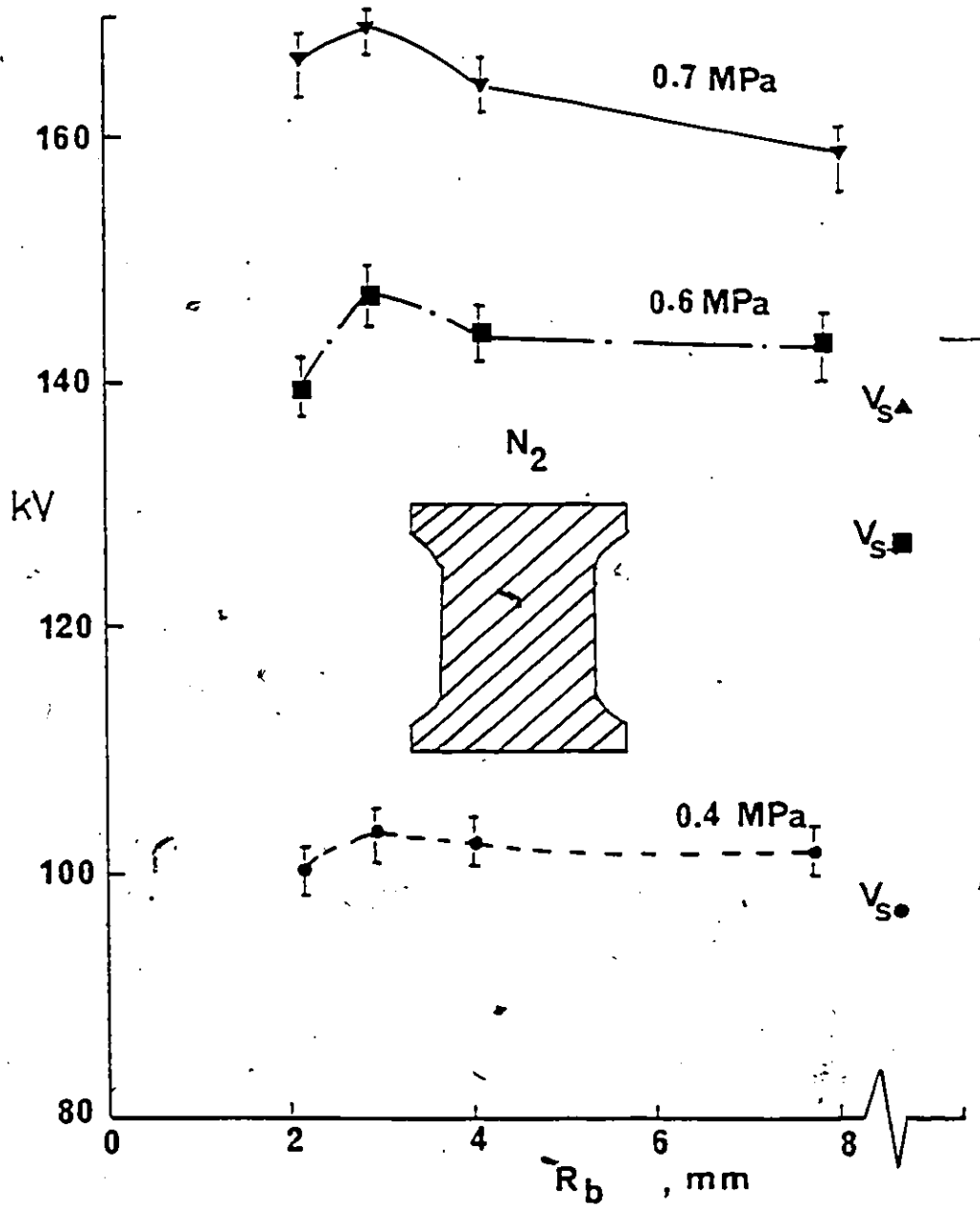
Figure 5.9: dc flashover voltage as a function of Rb for different gas pressures in N_2 for spacer "b" and h= 1 mm. Other conditions are as for Fig.5.7. Vs, flashover of a rectangular cylindrical spacer. $\varepsilon_2=3.2$, $2R_0=20$ mm, L=10 mm.
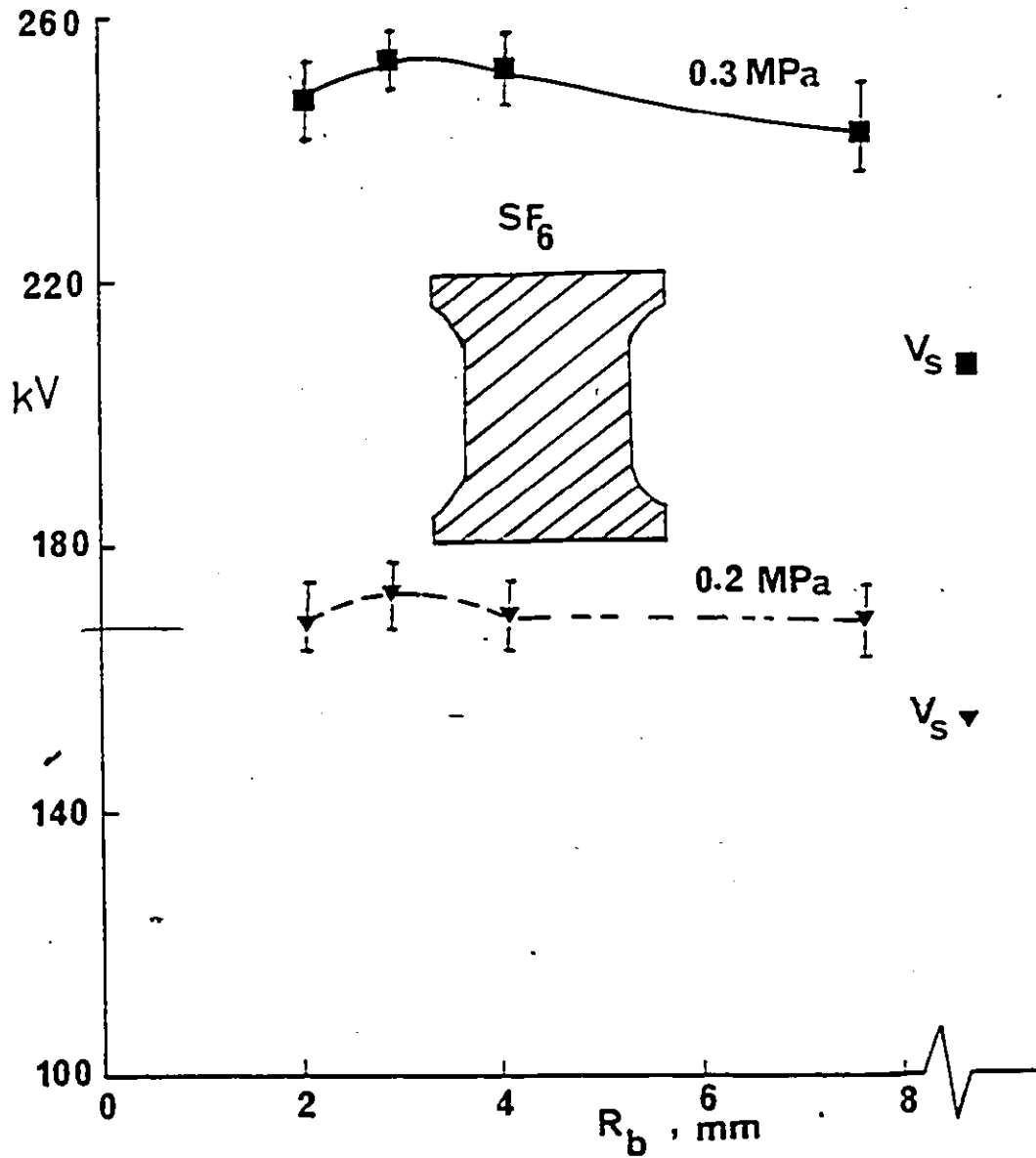
Figure 5.10: dc flashover voltage as a function of Rb in SF₆ for spacer profile "b". Other conditions are as for Fig.5.9.

The flashover voltage in SF$_6$ for profile "b" is shown in Fig.5.10. It will be observed that the flashover voltage is higher than for the right angle cylindrical post over this range of radii of curvature. Typical values of the flashover voltage at 0.3 MPa of SF$_6$ are 250±4 kV and 241±5 kV for Rb = 2.83 mm and 7.73 mm, respectively. The corresponding percentage increases in the flashover voltage with respect to the right angle cylindrical spacer are 22% and 17.2%, respectively.

From the measurements of the flashover voltage of profiles "a" and "b", it can be concluded that the withstand voltage of both profiles having Ra= Rb= 2.83 mm are almost the same in SF$_6$ and N$_2$. It can be inferred that the radius Ra and Rb are important parameters in the design as they reduce the electric field in the vicinity of the cathode junction and therefore the flashover voltage increases. For these pressures and dimensions, it is prefered to use spacer "b" because it has almost the same withstand voltage as that of spacer "a" in addition to its added mechanical strength in the vicinity of the electrodes.

Fig.5.11 shows the percentage increase in the flashover voltage with respect to the right angle cylindrical spacer using profile 'a' for different contact angles in SF_6 at a pressure of 0.3 MPa and in N_2 at a pressure of 0.7 MPa. It will be observed from Fig.5.11 that the withstand voltage of a concave edge profiled spacer with $\theta = 45°$ can be increased by as much as 20.8% in 0.7 MPa of N_2 and 23% in 0.3 MPa of SF_6, compared to a right angle cylindrical spacer. These are considered significant improvements as they are attainable while maintaining the same physical dimension of the gap and at the same gas pressure.
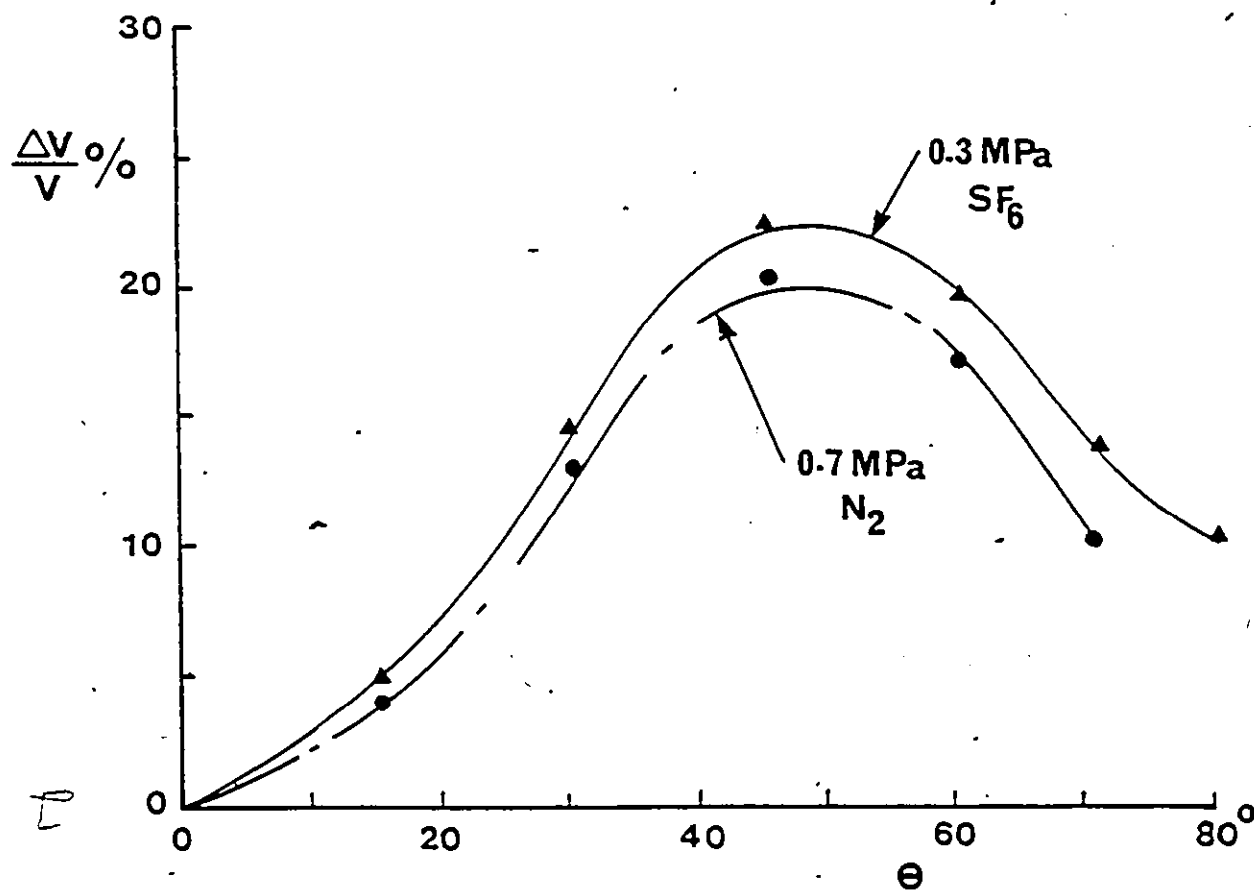
Figure 5.11: The percentage increase over a cylindrical rectangular spacer in the flashover voltage as a function of contact angle θ in SF_6 and N_2. Other conditions are as for Fig. 5.7.

5.3.4 Comparison of the flashover voltage of three types of spacers using dc, ac (60 Hz) and 1.2/50 us lightning impulse.

The flashover voltage using dc, ac (60 Hz) and 1.2/50 us lightning impulse of Plexiglas spacers having three different profiles: cylindrical, profile 'a' with θ = 45° and Ra = 2.83 mm and profile 'b' with Rb = 2.83 mm are measured in SF_6 and N_2. The radius of profile 'b' Rb=2.83 mm and the angle of profile 'a' spacers, θ= 45° are chosen to give the maximum withstand voltage.

5.3.4.1 dc Flashover voltage

The dc flashover voltage of the three profiles in SF_6 is shown in Fig.5.12. The gas pressure is varied in the range 0.1- 0.3 MPa. It will be observed that at a fixed gas pressure the flashover voltage for profiles 'a' and 'b' is higher than for the right angle cylindrical spacer. Typically, for a spacer of length L= 10 mm, the flashover voltage at P= 0.3 MPa is 250±4 kV for profile 'b', 252±5 kV for profile 'a' and 205±6 kV for the right angle cylindrical spacer. Profiles 'b' and 'a' give improvements of 22% and 23% in the withstand voltage capability, respectively, compared to a rectangular cylinder having the same length of L = 10 mm at 0.3 MPa.

Fig.5.13 shows the dc flashover voltage of the three profiles as a function of gas pressure in N_2. The gas pressure is varied in the range 0.1 - 0.7 MPa. Typical
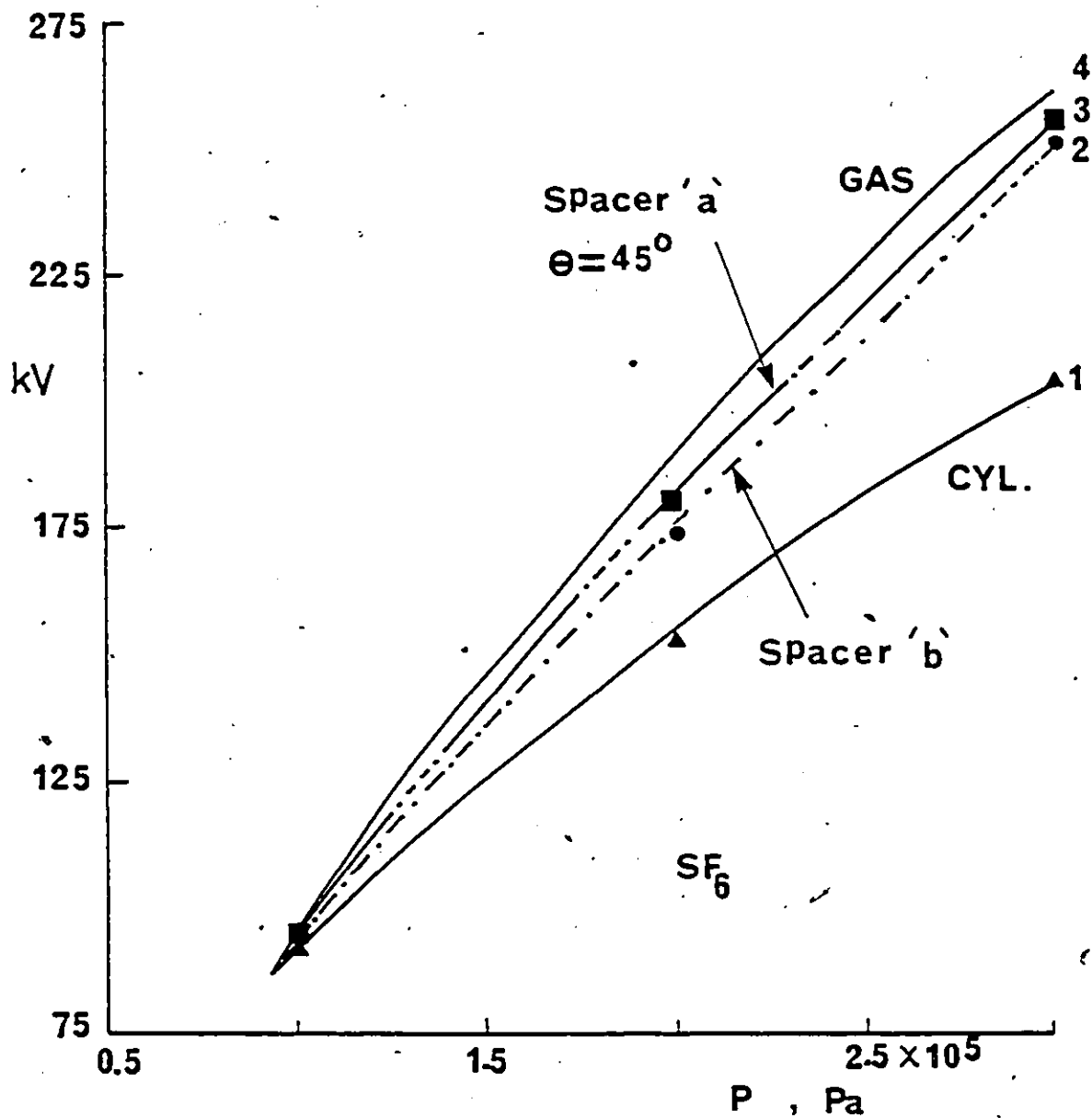
Figure 5.12: dc flashover voltage of a Plexiglas spacer as a function of gas pressure in SF₆ for different profiles. $\varepsilon_2 = 3.2$, L= 10 mm, $R_0 = 10$ mm, $R_a = R_b = 2.83$ mm, q= 2 mm, h=1 mm and $\theta = 45°$. Curve 1 corresponds to rectangular cylinder, curve 2 to spacer of profile 'b', curve 3 to spacer of profile 'a', curve 4 to SF₆ without spacer.
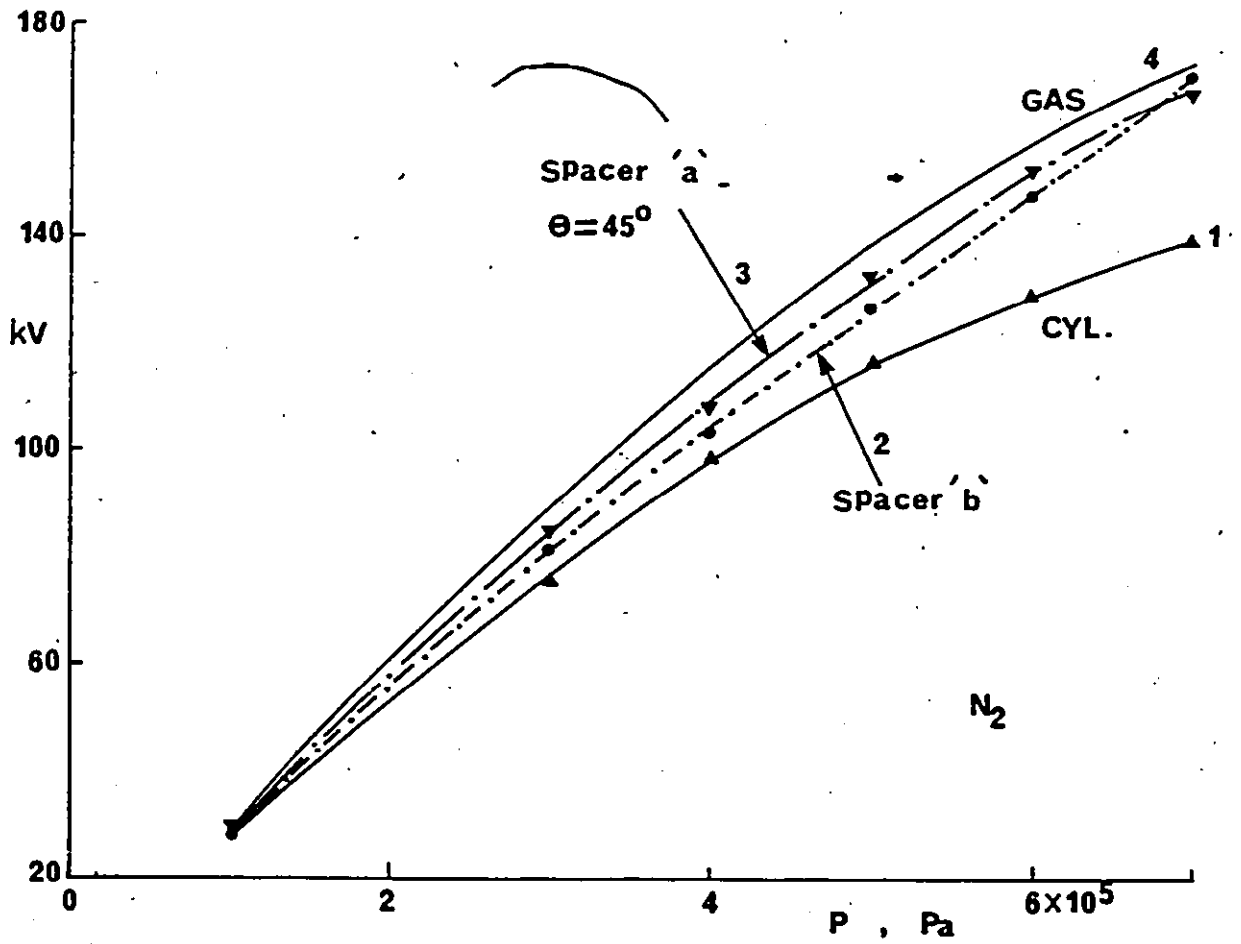
values of the flashover voltage at a pressure of 0.7 MPa of N_2 are 167±4 kV for profile "b", 166±3 kV for profile "a" and 135 kV for the right angle spacer. The latter value compares favourably with the dc measurement of 120 kV reported previously for a cylindrical Plexiglas spacer of the same length at 0.7 MPa of nitrogen [18]. Improvements of the withstand voltage of 23% and 22.6% for "b" and "a", respectively are obtained over the rectangular cylinder in 0.7 MPa of N_2. This is consistent with the improvements obtained using SF_6.

5.3.4.2 Lightning impulse flashover voltage

The 1.2/50 us impulse flashover voltage of the three profiles in SF_6 is shown in Fig.5.14. The gas pressure is varied in the range 0.1 - 0.4 MPa. It will be observed that the lightning impulse flashover voltage for profiles "a" and "b" is higher than that of the right angle cylindrical spacer at a fixed gas pressure. Typically, the lightning impulse flashover voltage at 0.4 MPa of SF_6 and L = 10 mm is 293±8 kV for profile "b", 307±6 kV for profile "a" and 261±9 kV for the right angle spacer. Profiles "b" and "a" give improvements of 12.5% and 18% in the lightning impulse withstand voltage capability, respectively, compared to a rectangular cylinder of length L= 10 mm at 0.4 MPa of SF_6.

Fig.5.15 shows the 1.2/50 us impulse flashover voltage of the three profiles in N_2. Typical values of flashover voltage at 0.7 MPa of N_2 are 165±4 kV for profile "b", 156±3
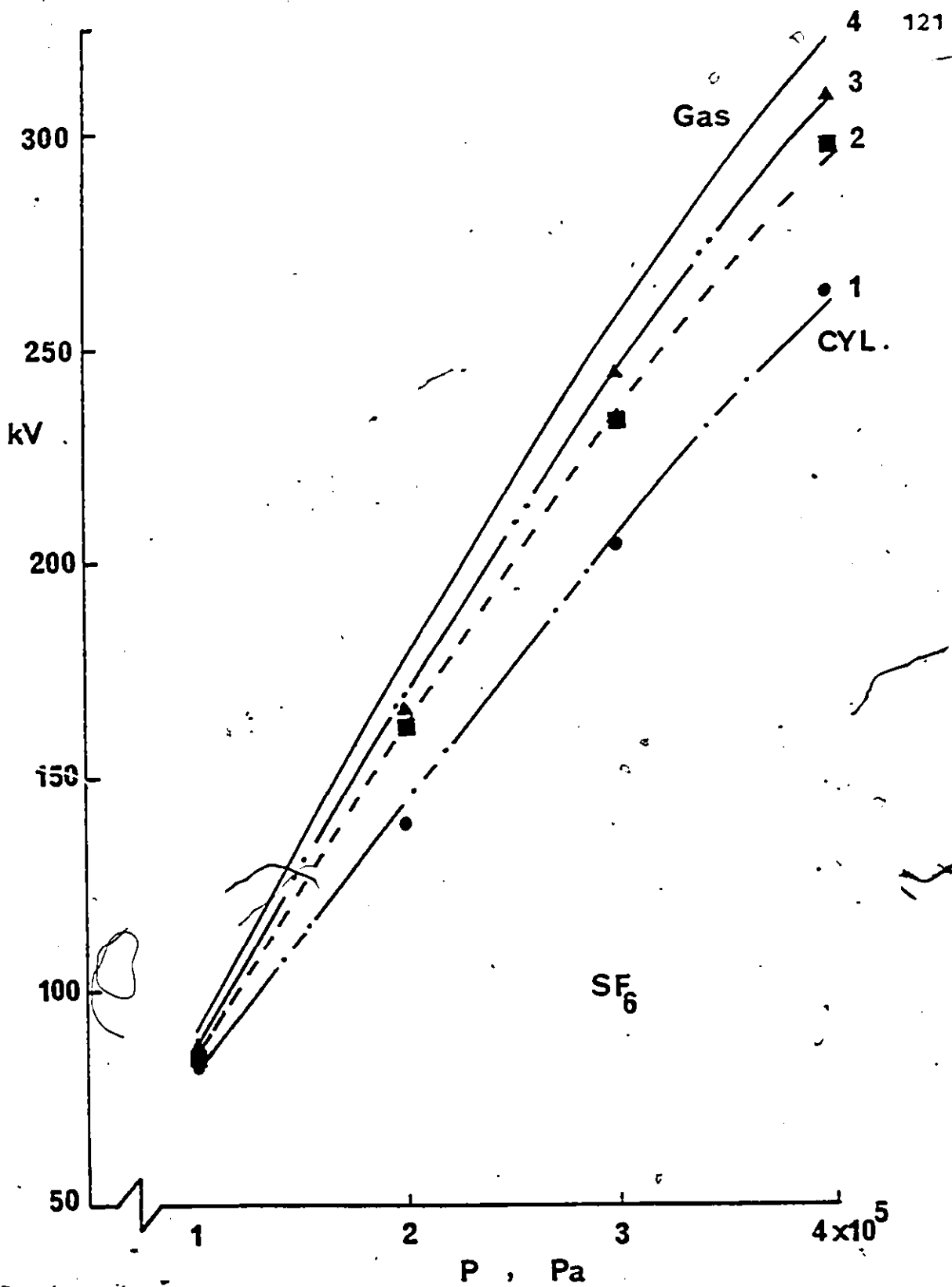
Figure 5.14: 1.2/50 us impulse flashover as a function of
gas pressure in SF₆ for different profiles.
Conditions are as for Fig.5.12.
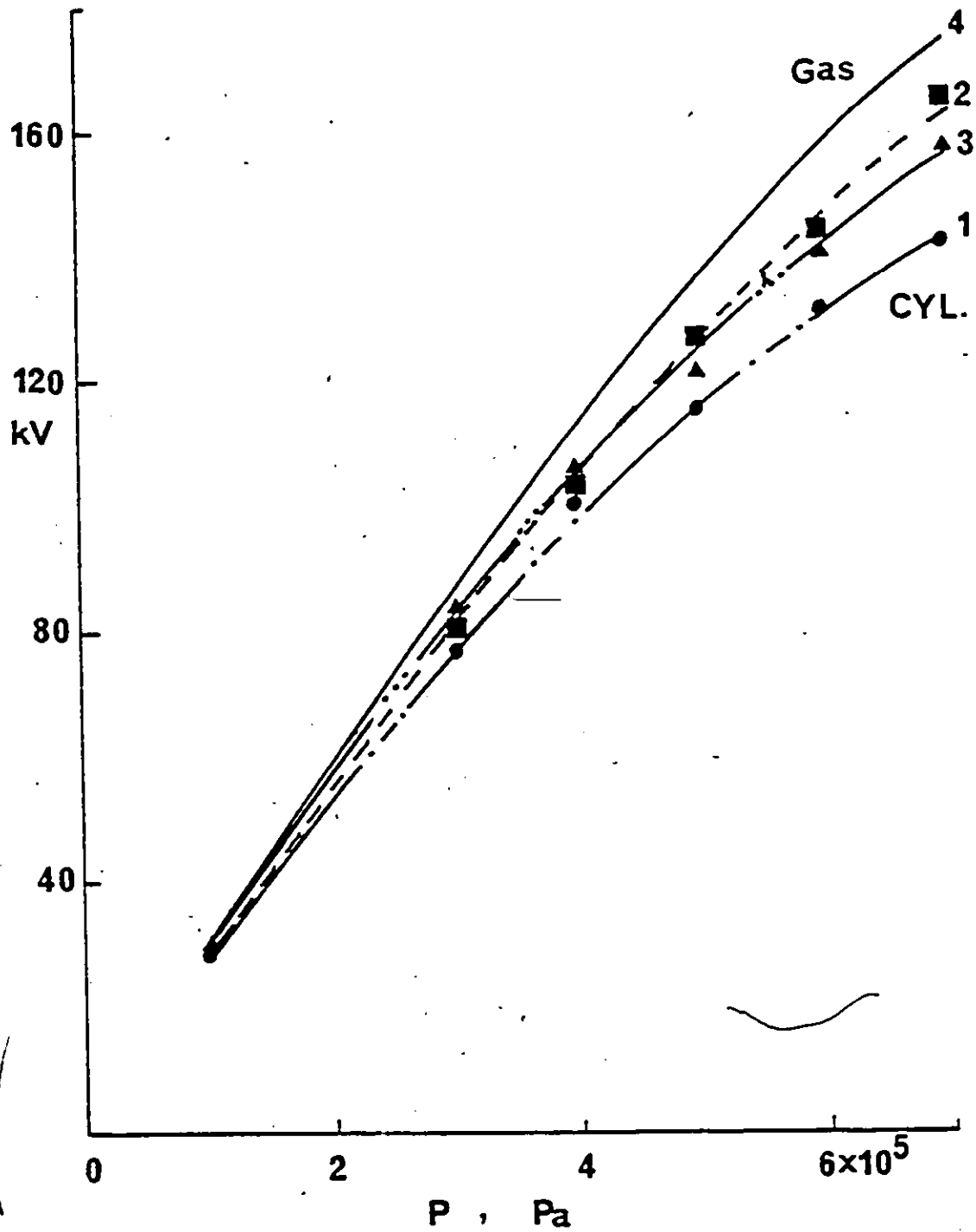
Figure 5.15: 1.2/50 us impulse flashover as a function of gas pressure in N₂ for different profiles. Conditions are as for Fig.5.12.

kV for profile 'a' and 141±4 kV for the right angle spacer. The improvements are 15.4% and 11.3%, respectively, using profiles 'b' and 'a' in 0.7 MPa of nitrogen over the cylindrical spacer at the same conditions.

It will be observed from Fig.5.15 that the flashover voltages of spacers 'a' and 'b' are almost the same in the pressure range up to 0.5 MPa. At higher pressure, the flashover voltage of spacer 'b' becomes higher than that of spacer 'a'. Similar behaviour is observed for the same conditions using ac voltage (Fig.5.17). Under dc the flashover voltage of spacer 'a' is higher than that of spacer 'b' in the range of pressure covered except at 0.7 MPa, where the flashover voltage of spacer 'b' becomes slightly higher (Fig. 5.13).

5.3.4.3   ac (60 Hz) Flashover voltage

The peak ac (60 Hz) flashover voltage of three fresh Plexiglas samples having three different profiles is shown in Fig.5.16. The gas pressure of SF_6 is restricted in this case to the range (0.1 - 0.2 MPa) due to the limitations of the ac supply to 150 kV (rms). It will be observed that the flashover voltages of profiles 'b' and 'a' are also higher than that of the right angle cylindrical spacer over the range of the gas pressure used.

Fig.5.17 shows the peak ac flashover voltage of the three profiles in N_2. The gas pressure is varied in the range 0.1 - 0.7 MPa. Typically, the peak ac flashover voltage at 0.7

MPa of nitrogen and L=10 mm is 153±5 kV for profile 'b',
144± kV for profile 'a' and 123±6 kV for the right angle
cylinder. The two shaped profiles lead to improvements of
the ac withstand voltage of 16% and 24% for 'a' and 'b',
respectively, over the rectangular cylinder in 0.7 MPa of
nitrogen when a length of 10 mm Plexiglas is used.

From the above measurements, it is clear that both
spacers 'a' and 'b' are suitable in the applications using
dc, ac and lightning impulse voltages.
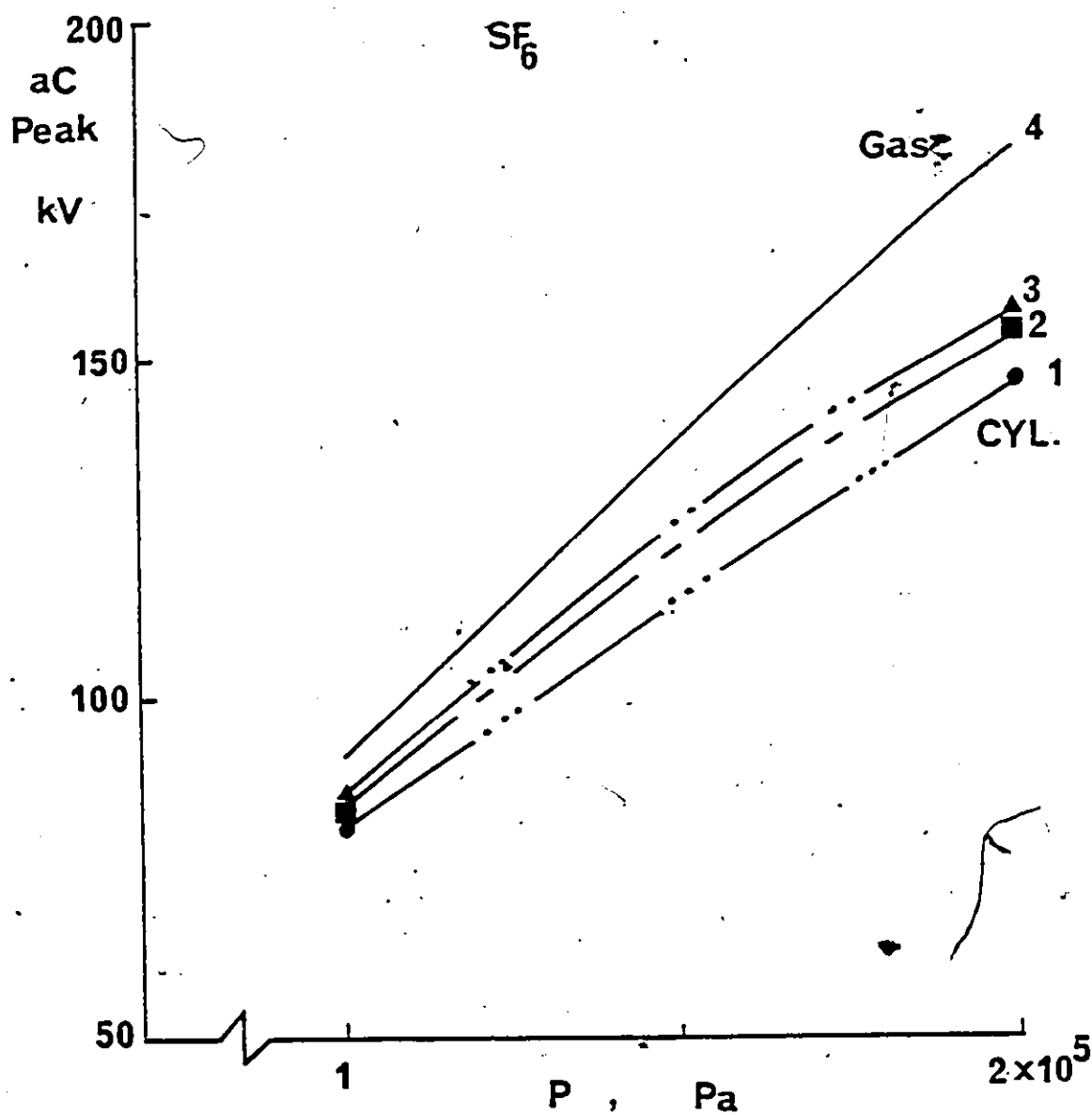
Figure 5.16: ac (60 Hz, peak) flashover voltage as a function of gas pressure in SF_6 for different profiles. Conditions are as for Fig.5.12.
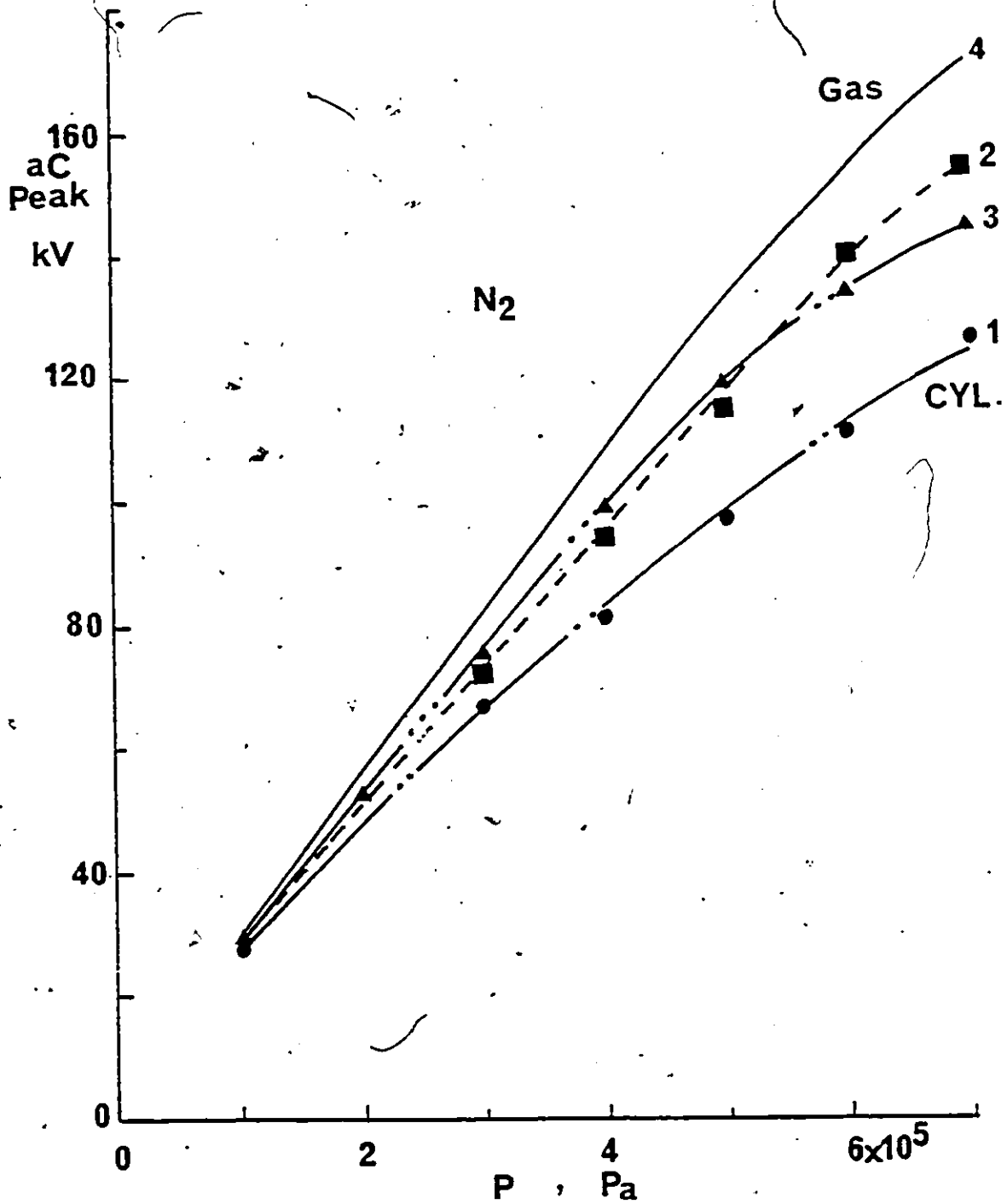
5.3.5   Comparison between dc, ac and lightning impulse
flashover voltages

The dc, ac (60 Hz) and 1.2/50 us lightning impulse
flashover voltages, for a 10 mm long spacer of profile 'b'
made of Plexiglas, in N_2 and in SF_6 are shown in Fig.5.18.
The data are reported in this section to compare the
dependence of the flashover voltage on the different applied
voltages for a given profile. It can be seen that the dc
and the lightning impulse voltages are close in values, but
the ac withstand voltage is lower typically by about 10% at
0.2 MPa of SF_6.   Fig.5.19 shows the flashover voltages of
profile 'a' using dc, ac (60 Hz peak) and 1.2/50 us
lightning impulse in SF_6 and N_2.   Fig.5.20 shows the
flashover voltages of a 10 mm long cylindrical spacer in N_2
and SF_6 using the three types of applied voltages. It will
be observed that the dc and the lightning impulse flashover
voltages are higher than the peak ac for both SF_6 and N_2.
Typically for N_2 at 0.4 MPa,   the peak ac flashover voltage
is lower than the dc and the lightning impulse by about 19%
(Fig.5.20).

The reason for the observed lower ac (crest) withstand
voltage is because half the ac wave acts as an opposing
pre-stress to the following half wave. Therefore, the
charges created on the surface of the spacer cause an
enhancement in the electric field at both electrode
junctions. This is in general agreement with the surface

flashover measurements in vacuum reported by Pillai and Hackam [98].

The flashover voltage ratio P, defined as the ratio of the flashover voltage of the spacer to the gas breakdown voltage without the spacer is also reported as it gives an indication of the insulation quality of the suggested designs of the spacers.

$$P = \frac{V \text{ spacer}}{V \text{ gas}}$$

Fig.5.21 shows the dependence of P on gas pressure for a Plexiglas spacer in SF_6 using dc. It will be observed that P can be increased from 0.78 at $\theta = 0$ to 0.96 at $\theta = 45°$ for spacer 'a' and to 0.95 at $Rb = 2.83$ mm for spacer 'b'. This is considered a remarkable improvement in the performance of the spacer.
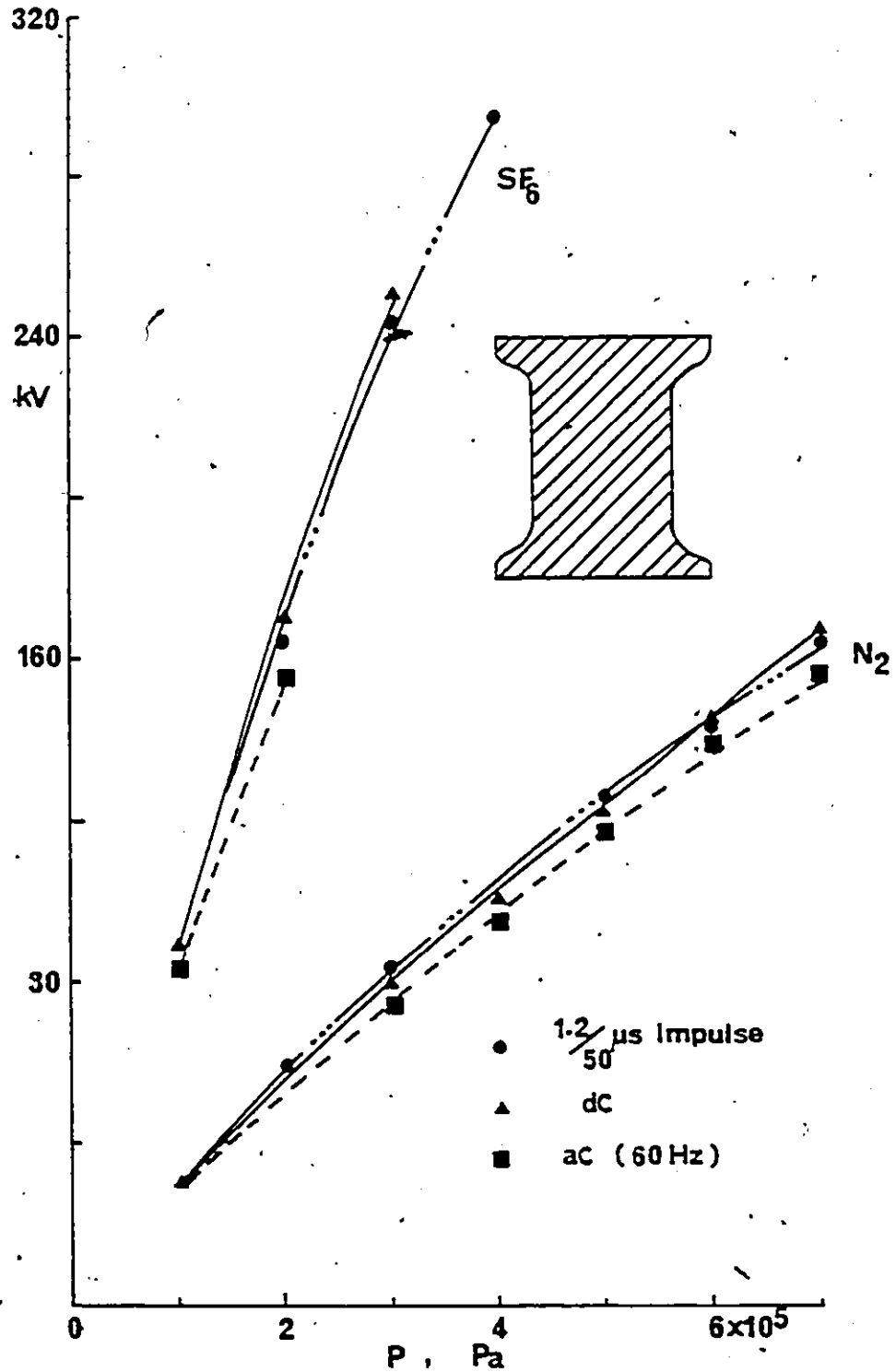
Figure 5.18: dc. ac (60 Hz. peak) and 1.2/50 us impulse flashover voltages as a function of gas pressure in SF_6 and N_2 for profile 'b'. Conditions are as for Fig. 5.12.
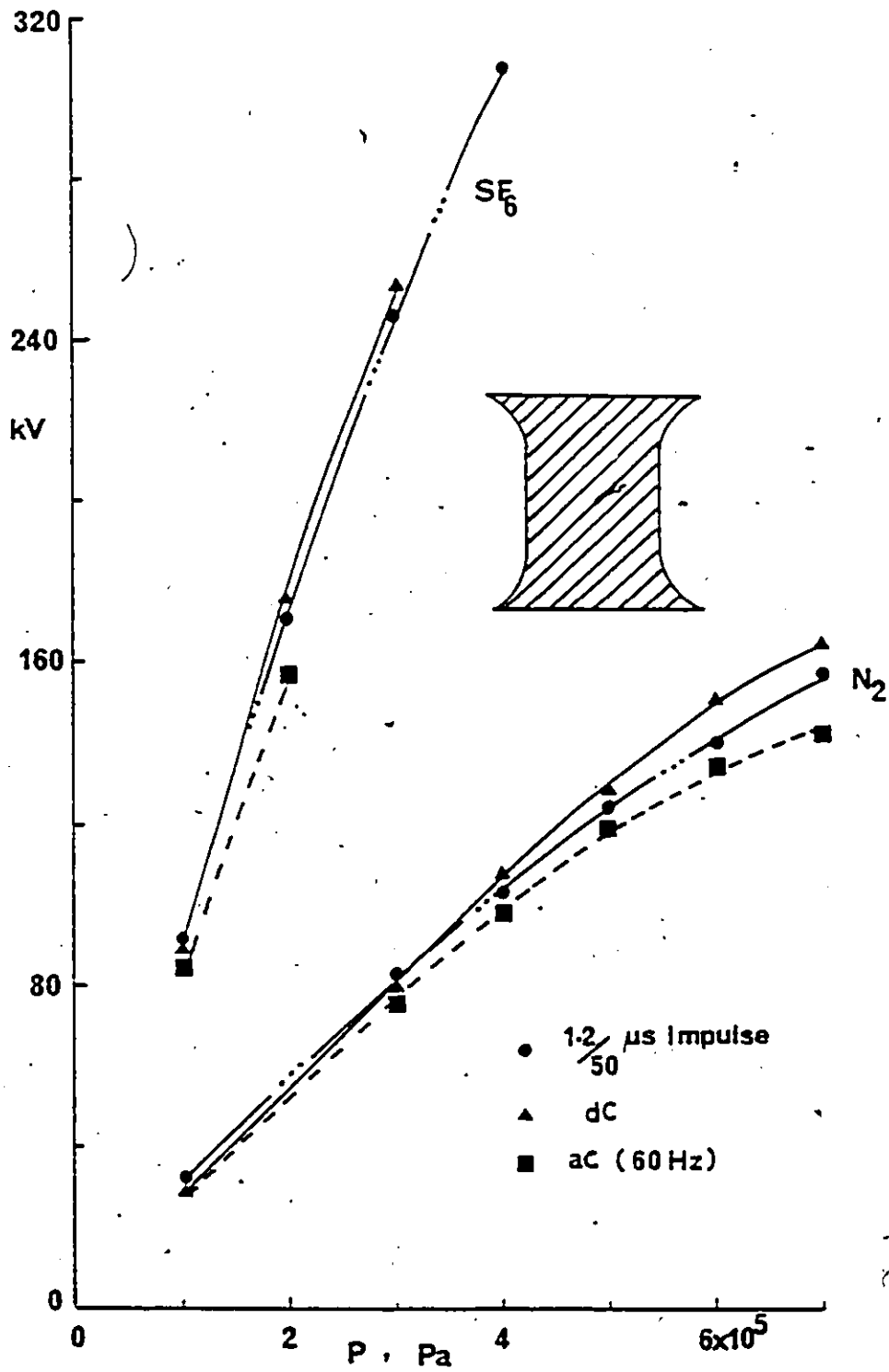
Figure 5.19: dc, ac (60 Hz, peak) and 1.2/50 us impulse flashover voltages as a function of gas pressure in SF6 and N2 for profile 'a'. Conditions are as for Fig.5.12.
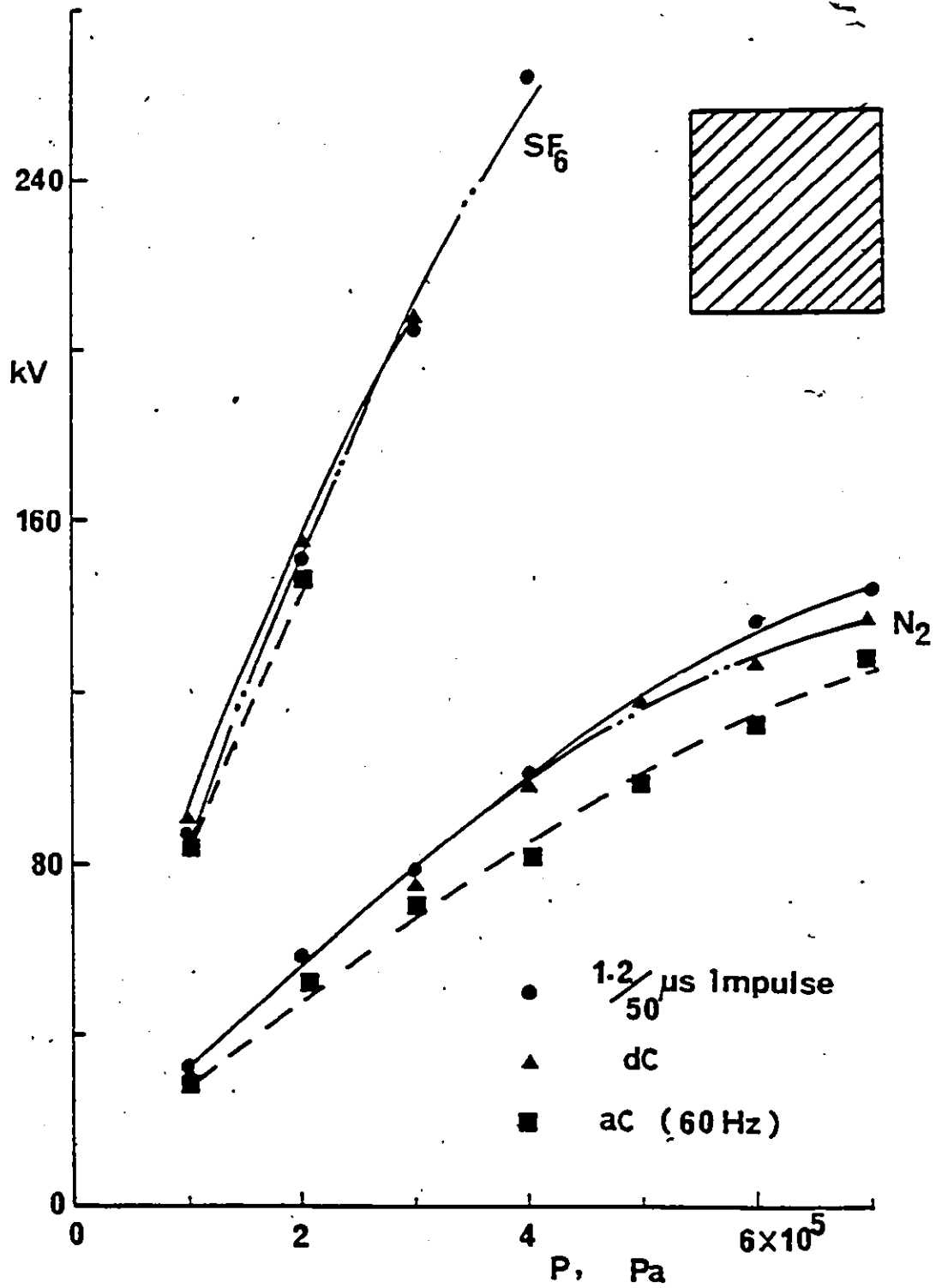
Figure 5.20: dc, ac (60 Hz, peak) and 1.2/50 us impulse flashover voltages as a function of gas pressure in SF₆ and N₂ for cylindrical spacer. Conditions are as for Fig.5.12.
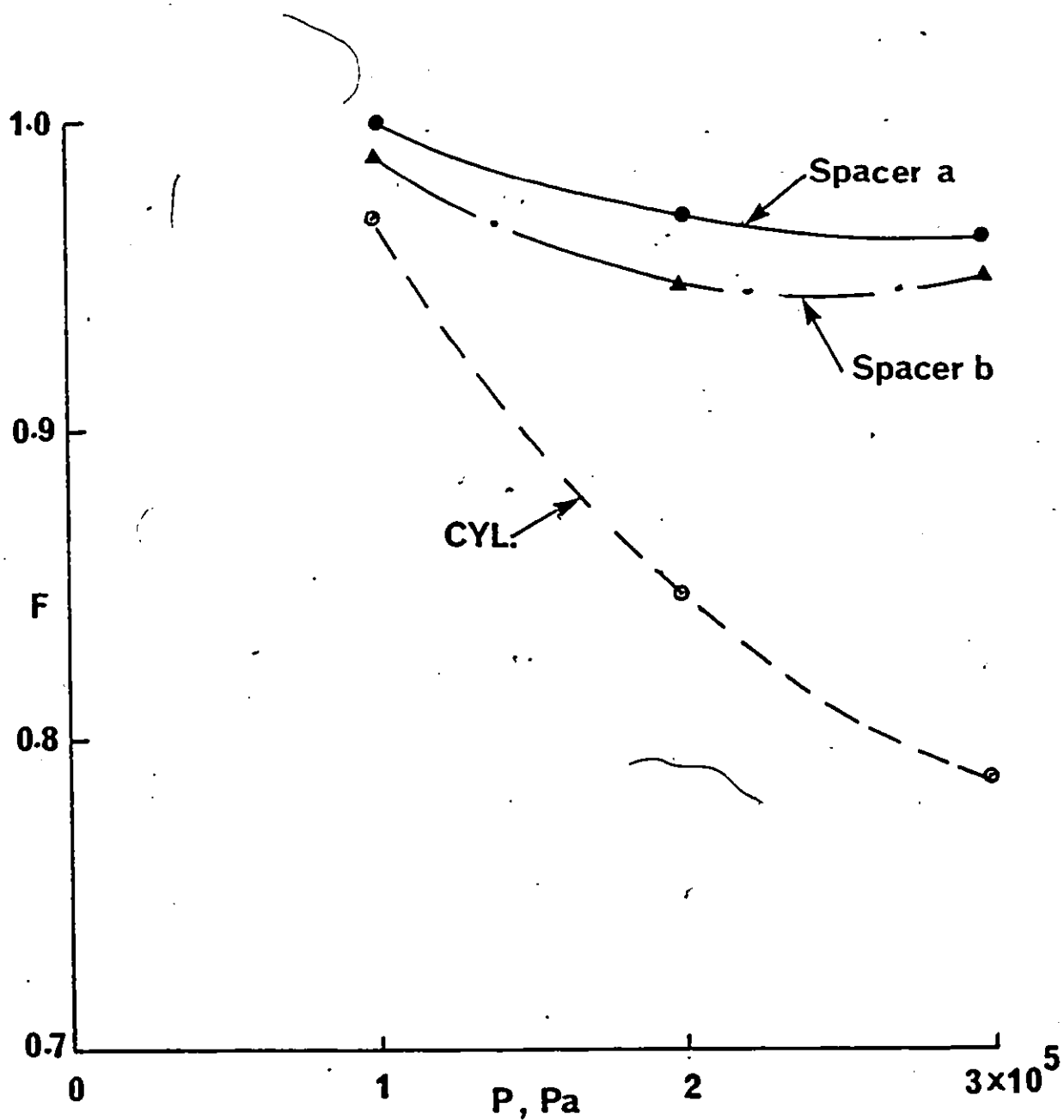
Figure 5.21: The dc flashover voltage ratio as a function of gas pressure in SF$_6$ for different spacer profiles. Spacer 'a', θ=45° and Ra=2.83 mm; Spacer 'b', Rb=2.83 mm. L=10 mm, ε$_2$=3.2 and 2R$_0$=20 mm.

5.4 Flashover Voltage Measurements of Profiles 'c' and 'd' Spacers

The flashover voltage of two Plexiglas spacers having profiles 'c' and 'd' is determined in the gases SF_6 and N_2. The gas pressure is varied in the range $(1-3) \times 10^5$ Pa in SF_6 and $(1-7) \times 10^5$ Pa in nitrogen. θ is varied in the range 0 to 70°. Rc and Rd are varied in the range 5.3 to 19.3 mm.

5.4.1 Conditioning Effect

Fig.5.22 shows the dependence of the dc, ac and lightning impulse flashover voltage of 10 mm long spacers having profiles 'c' ($\theta = 45°$ and Rc = 7.07 mm) and profile 'd' (Rd = 7.07 mm) on the number of sparkings in 0.1 MPa of SF_6. Five minutes are allowed between successive sparks up to the fiftieth breakdown of the spacer of profile 'c'. After that breakdown, the applied voltage is removed from the spacer for 12 hours to simulate a short shelf life time, then measurements of the breakdown voltage are resumed. It will be observed from Fig.5.22 that there is no evidence of conditioning either before or after removing the electric stress. The flashover level is essentially independent of the number of sparkings. Typically the flashover voltage of a Plexiglas profile 'c' spacer having L = 10 mm in 0.1 MPa of SF_6 is 86.5 ± 2.5 kV when 62 breakdowns are measured (Fig.5.22). The good reproducibility of the flashover voltage is attributed to the meticulously clean conditions, to the relatively small size specimen and to the relatively low field of 37 kV/cm.
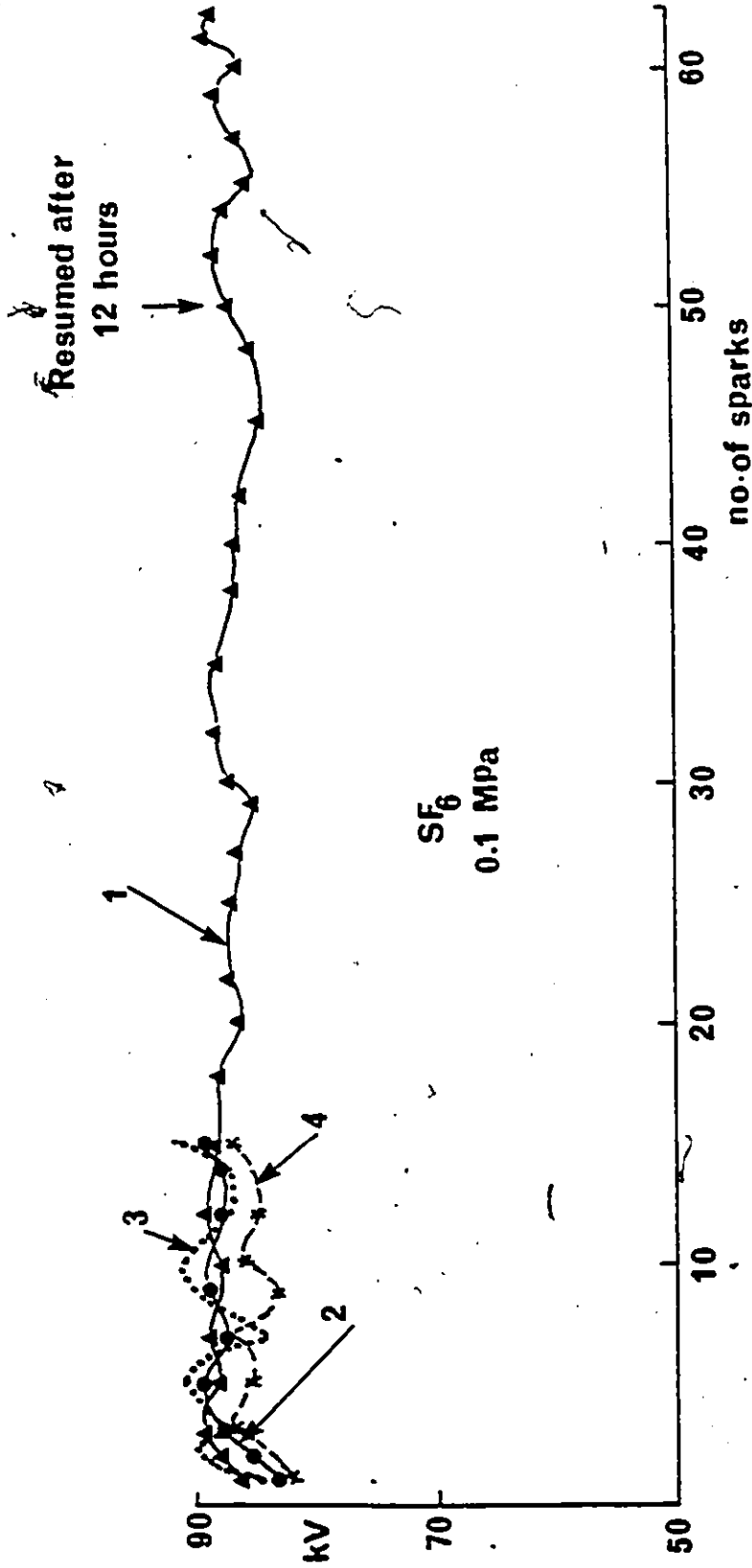
Figure 5.22: dc flashover voltage as a function of number of sparkings in SF$_6$ using concave spacers of profiles 'c' and 'd'. Material, Plexiglas, ϵ_2= 3.2, R_0= 10 mm, L= 10 mm, g= 1 mm, Rd= 7.07 mm, gas pressure = 0.1 MPa, curve 1, profile 'd', curve 2, profile 'c' with θ= 45° using dc voltage. Between breakdown 50 and 51 electric stress was removed for 12 h otherwise 5 min between breakdowns. Curve 3, profile 'd' using impulse voltage, curve 4, profile 'd' using ac voltage.

5.4.2   dc Flashover voltage measurements of profile 'c' spacer

The dependence of the dc flashover voltage of a spacer having profile 'c' on the contact angle θ and the radius Rc in SF$_6$ is shown in Fig.5.23.   The gas pressure is varied in the range 0.1- 0.3 MPa.. The diameter G is varied from 21.32 mm to 28.39 mm as θ varied from 15° to 80°. It will be observed that as θ increases the flashover voltage increases and reaches a maximum at θ =45° (Rc= 7.07 mm).   A further increase in θ results in a decrease in the flashover voltage.

Fig.5.24 shows the dependence of the flashover voltage of a spacer of profile 'c' on θ in N$_2$ at different gas pressures. It will be observed that the flashover voltage increases and reaches a maximum at θ =45°. It is evident from Figs.5.23 and 5.24 that the optimum contact angle to yield the highest improvement in the withstand voltage capability lies in the range 35 to 55° and the maximum is at θ = 45° in general agreement with the analysis of the electric field.

5.4.3   dc Flashover voltage measurements of profile 'd' spacer

The dependence of the dc flashover voltage of spacer 'd' on the radius Rd in SF$_6$ is shown in Fig-5.25 in the gas pressure range 0.1 to 0.3 MPa.   The flashover voltage of a rectangular cylinder termed Vs is also shown at different

gas pressures. It can be seen from Fig.5.25 that the flashover voltage is independent of Rd except at Rd = 5.3 mm where it is slightly lower particularly at 0.3 MPa.

Fig.5.26 shows the dependence of the dc flashover voltage of profile 'd' in N_2 on the radius Rd . It will be observed that the dependence of the flashover voltage in N_2 on Rd is similar to that in SF_6 which is depicted in Fig.5.25. The highest improvement in the withstand voltage is obtained in the range Rd= 7 to 8 mm .

In SF_6 and N_2 it is clear that the spacer of profile 'd' can be used with Rd > 6 mm to give a higher withstand voltage over a cylindrical spacer.
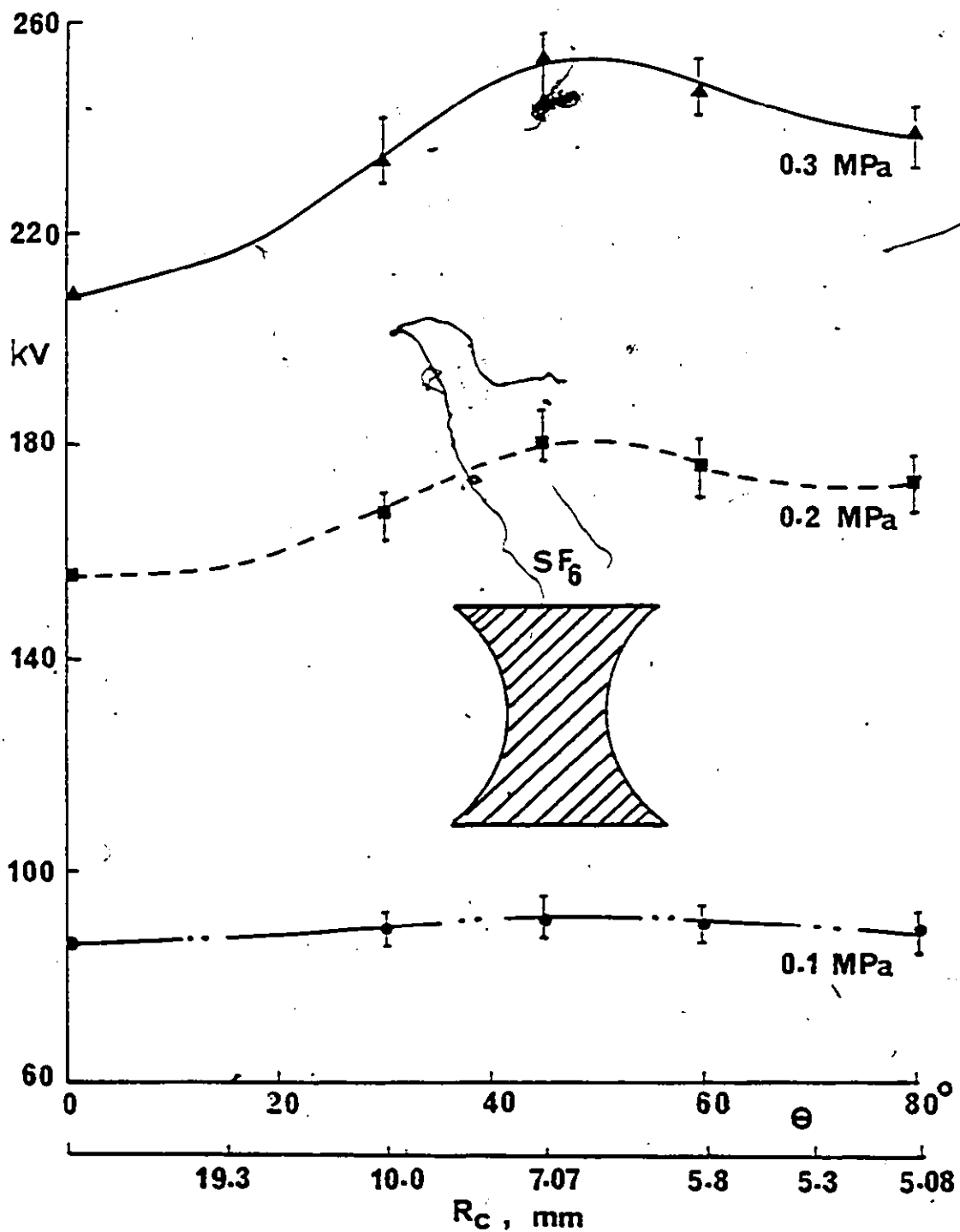
Figure 5.23: dc flashover voltage as a function of contact angle θ and Rc in SF₆ of a spacer having profile 'c'. $\varepsilon_2 = 3.2$, L= 10 mm, R_0= 10mm and Rc= L/2 sin θ.
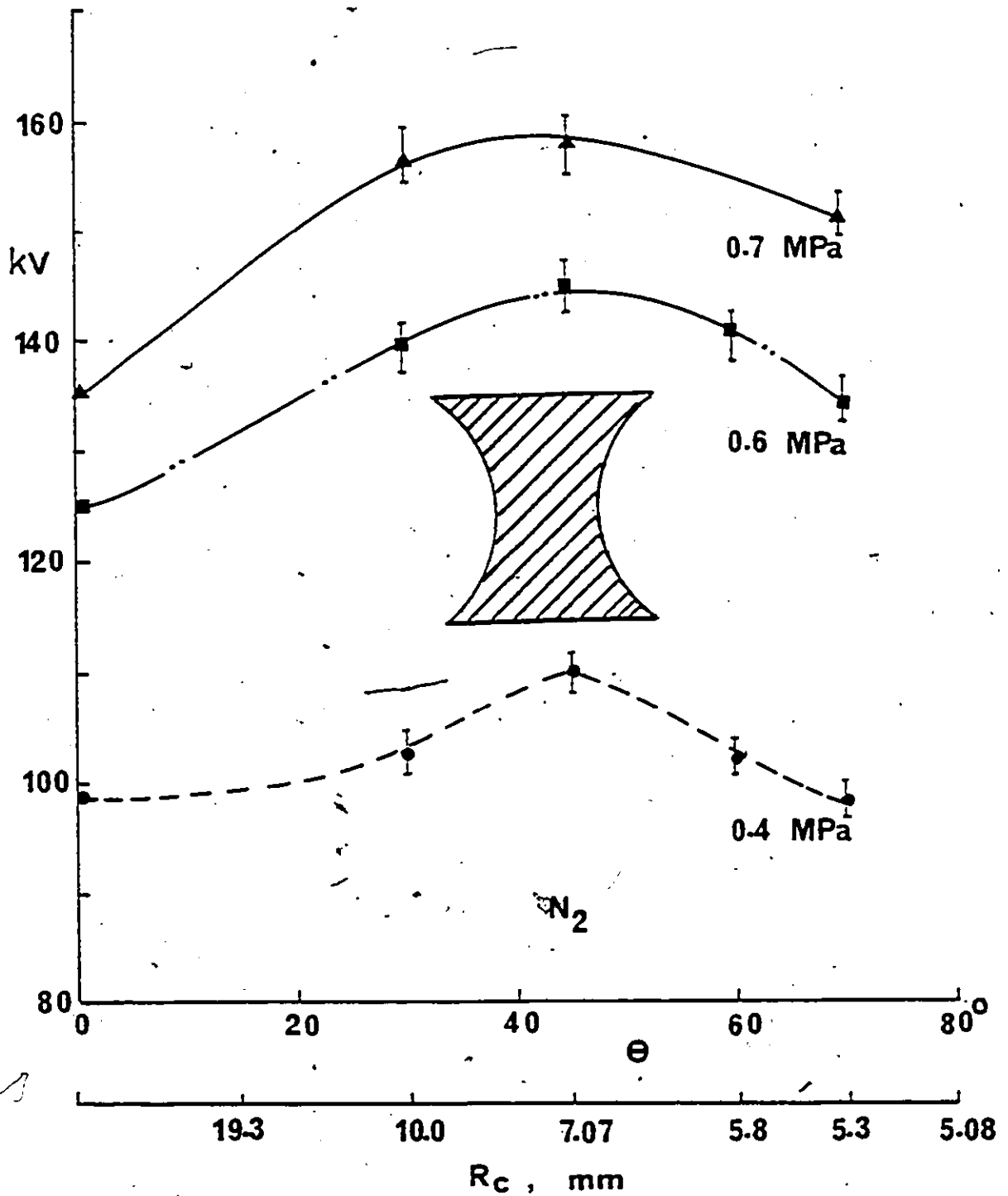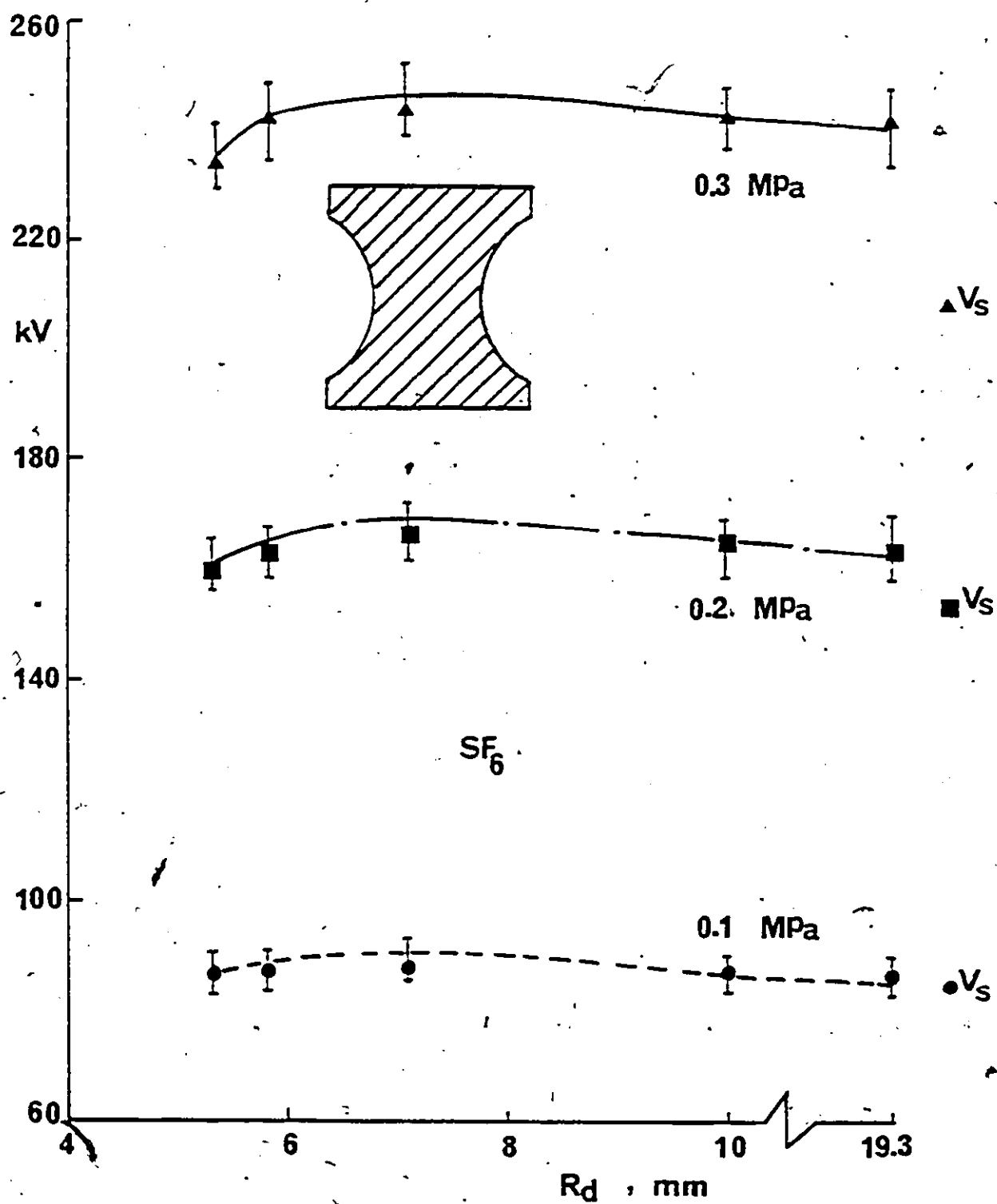
Figure 5 flashover voltage as a function of radius in SF6 using spacer of profile 'd'. $\varepsilon_2 = 2$, L= 10 mm, R$_o$= 10 mm and q= 1 mm.

5.4.4   Comparison of the flashover voltage of three types of spacers using dc, ac (60 Hz) and 1.2/50 us lightning impulse.

The flashover voltage measurements using dc, ac (60 Hz) and 1.2/50 us lightning impulse of a Plexiglas spacer having three different profiles, cylindrical, profile 'c' with $\theta = 45°$ and $Rc = 7.07$ mm and profile 'd' with $Rd = 7.07$ mm are measured in SF_6 and N_2. The radius of profile 'd' and the angle of profile 'c' spacers are chosen to be optimum to give the maximum withstand voltage.

5.4.4.1   dc Flashover voltage

The dc flashover voltage of the three profiles in SF_6 is given in Fig.5.27. The gas pressure is varied in the range 0.1- 0.3 MPa. It will be observed that at a fixed gas pressure the flashover voltages of profiles 'c' and 'd' are higher than that of the right angle spacer. Typically, the flashover voltage at p = 0.3 MPa and L = 10 mm is 242±6 kV for profile 'd', 251±5 kV for profile 'c' and 205±6 kV for the right angle spacers. Profiles 'd' and 'c' give improvements of 18% and 22.5% in the withstand voltage capability, respectively, compared to a rectangular cylinder having the same length of L = 10 mm at 0.3 MPa.

Fig.5.28 shows the dc flashover voltage of the three profiles as a function of gas pressure in N_2. The gas pressure is varied in the range 0.1 - 0.7 MPa. Typical values of the flashover voltages at a pressure of 0.7 MPa of

dc flashover as a function of radius Rd in N₂. Other conditions are as in Fig.5.25.
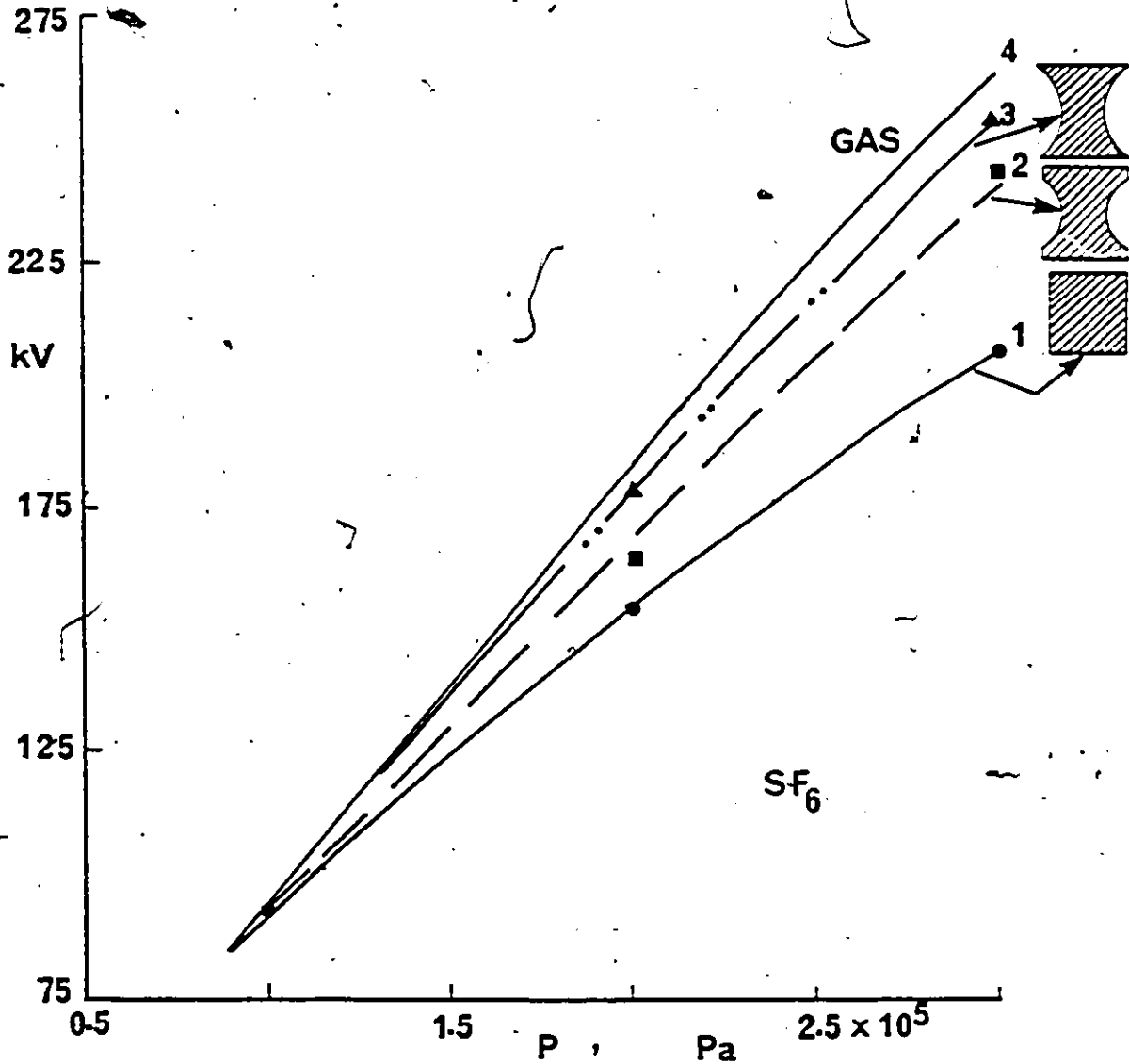
N_2 are 160±7 kV for profile "d", 156±5 kV for profile "c" and 135±5 kV for the right angle spacer. These values compare favourablly with the dc measurements of 120 kV reported previously for a cylindrical spacer of the same length at 0.7 MPa of nitrogen [18]. The two shaped profiles lead to improvements of the withstand voltage of 17.5% and 15% for "d" and "c", respectively over the rectangular cylinder in 0.7 MPa of N_2.

5.4.4.2 Lightning impulse flashover voltage

The 1.2/50 us impulse flashover characteristics of the three profiles in SF_6 is shown in Fiq.5.29. The gas pressure is varied in the range 0.1 - 0.4 MPa. It will be observed that the lightning impulse flashover voltage for profiles "c" and "d" is higher than that of the right angle spacer at a fixed gas pressure. Typically, the lightning impulse flashover voltage at 0.4 MPa of SF_6 and L = 10 mm is 293±8 kV for profile "d", 306±7 kV for profile "c" and 261±9 kV for the right angle spacer. Profiles "d" and "c" give improvements of 12.5% and 17.5% in the lightning impulse withstand voltage capability, respectively, compared to a rectangular cylinder.

Fiq.5.30 shows the 1.2/50 us impulse flashover characteristic of the three profiles in N_2. The gas pressure is varied in the range 0.1 - 0.7 MPa. Typical values of flashover voltage at 0.7 MPa of N_2 are 155±4 kV for profile "d", 159±5 kV for profile "c" and 141±6 kV for the right
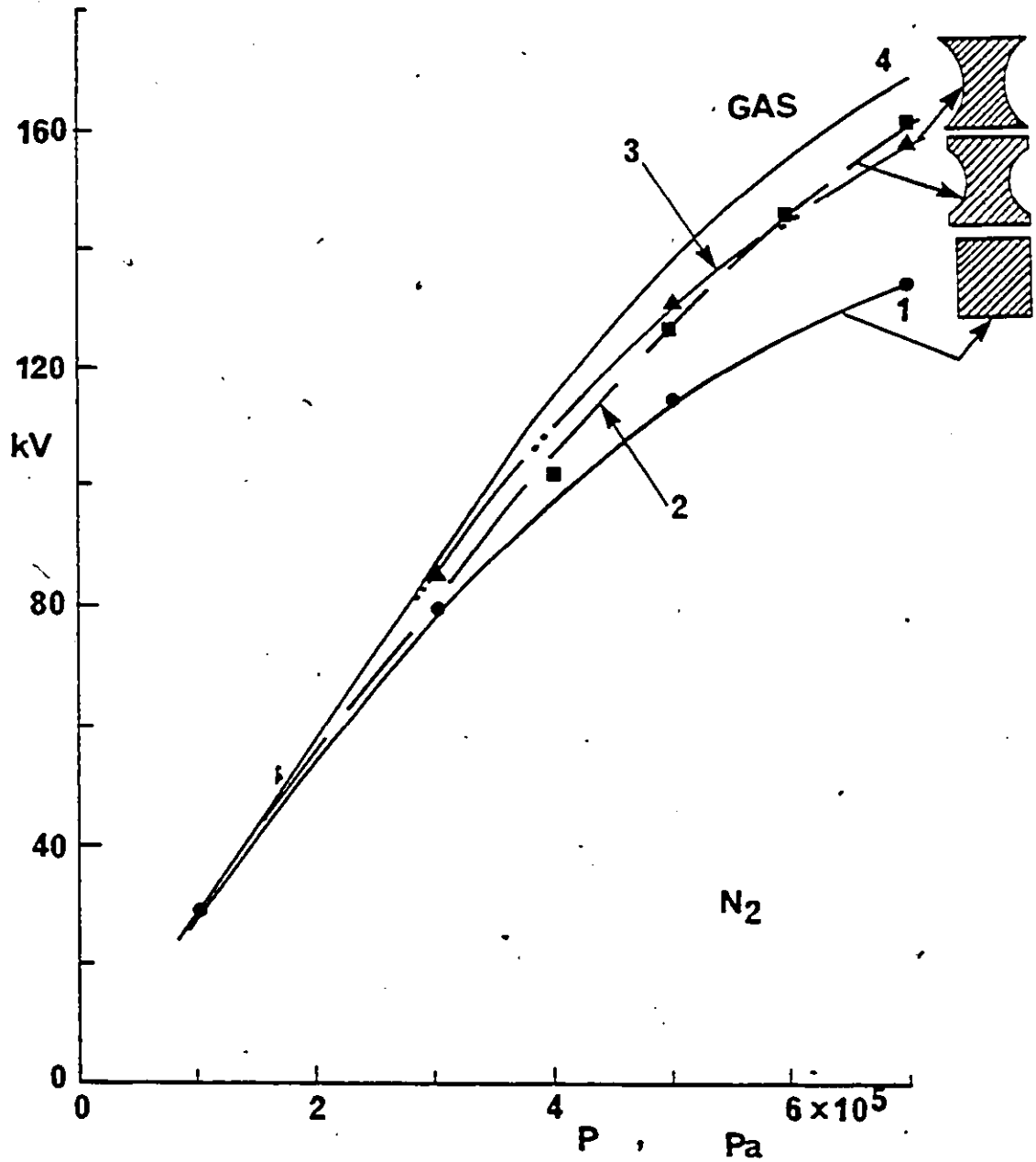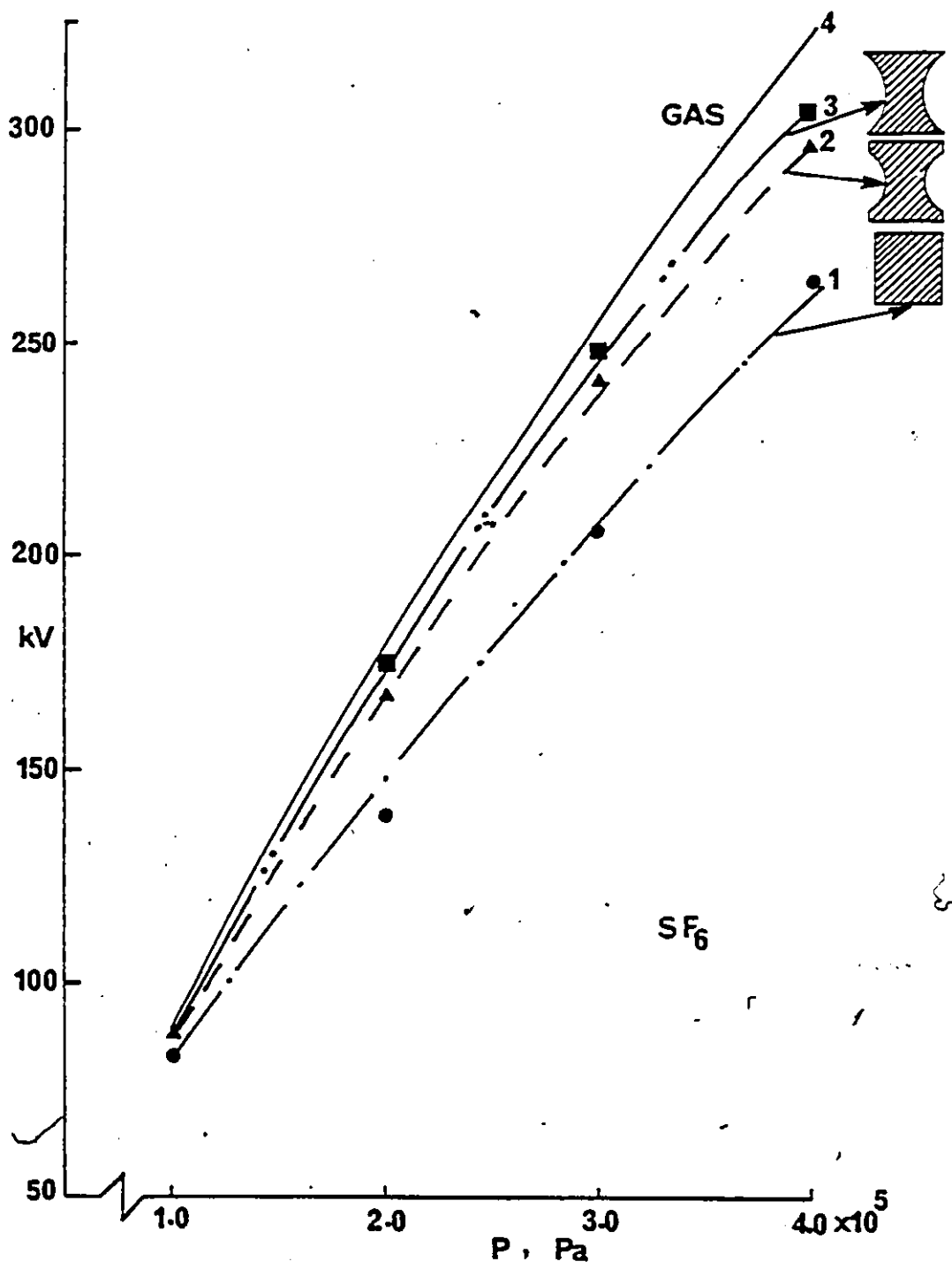
Figure 5.29: 1.2/50 us impulse flashover as a function of gas pressure in SF₆ for different profiles. Conditions are as for Fig.5.27.

angle spacer. The improvements are 11% and 13%, respectively, when profiles 'd' and 'c' are used in 0.7 MPa of nitrogen.

Profiles 'c' and 'd' give similar withstand voltages at the same gas pressure. Therefore profile 'd' might be preferable because it is mechanically stronger in the contact region with the electrodes.

5.4.4.3 ac (60 Hz) Flashover voltage

The crest value of ac (60 Hz) flashover voltage of three spacer profiles made of Plexiglas in SF_6 is shown in Fig.5.31. The gas pressure is restricted in this case to the range (0.1 – 0.2 MPa) due to the limitations of the ac supply to 150 kV (rms). It will be observed that the flashover voltages of profile 'd' and 'c' are also higher than that of the right angle spacer over the range of the gas pressure used.

Fig.5.32 shows the peak ac flashover voltage of the three profiles in N_2. The gas pressure is varied in the range 0.1 – 0.7 MPa. Typically, the peak ac flashover voltage at 0.7 MPa of nitrogen is 143±5 kV for profile 'd', 150±6 kV for profile 'c' and 123±6 kV for the right angle cylinder. The two shaped profiles lead to improvements of the ac withstand voltage of 15% and 21% for 'd' and 'c', respectively, over the rectangular cylinder in 0.7 MPa of nitrogen when a length of 10 mm Plexiglas is used.
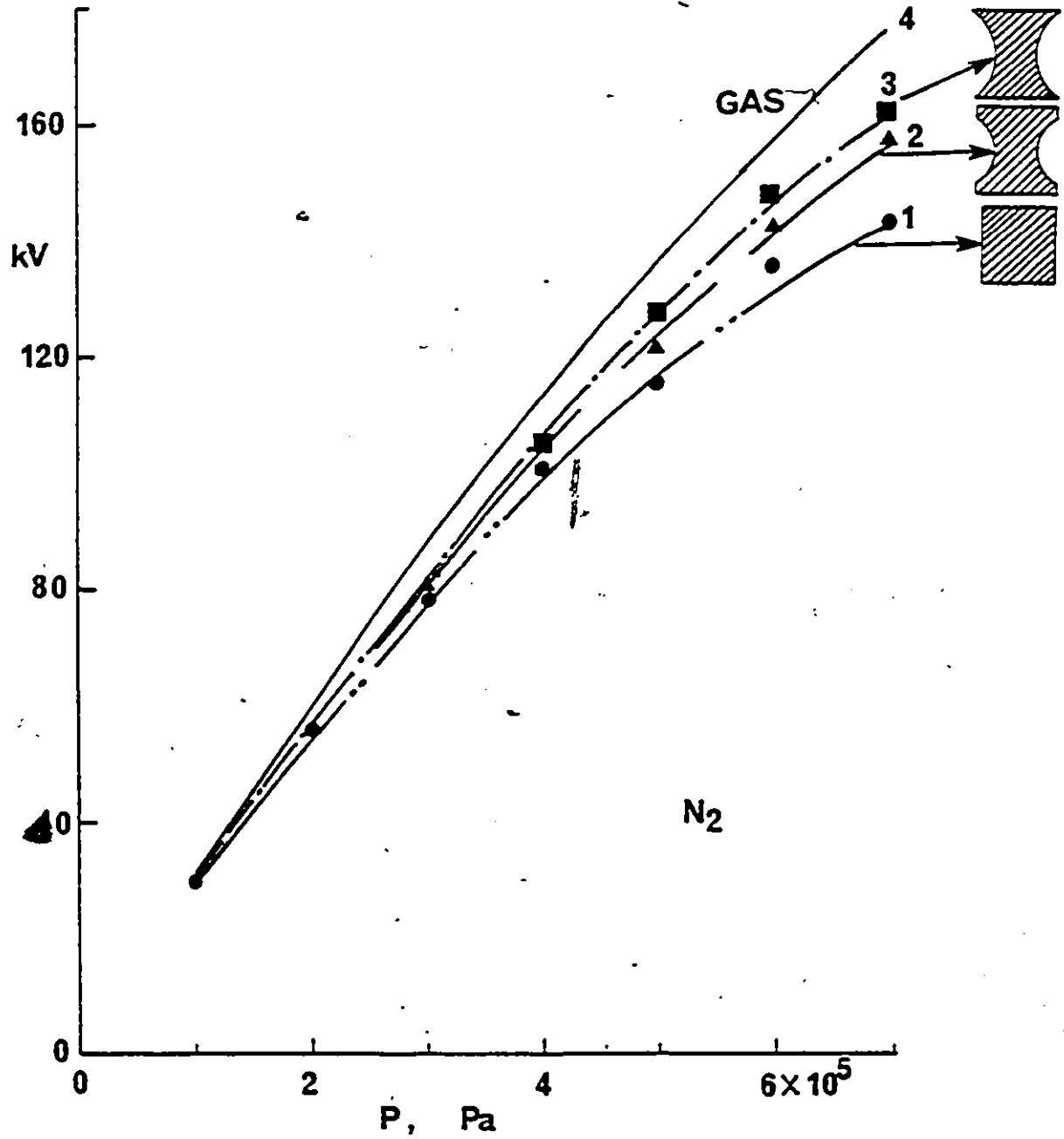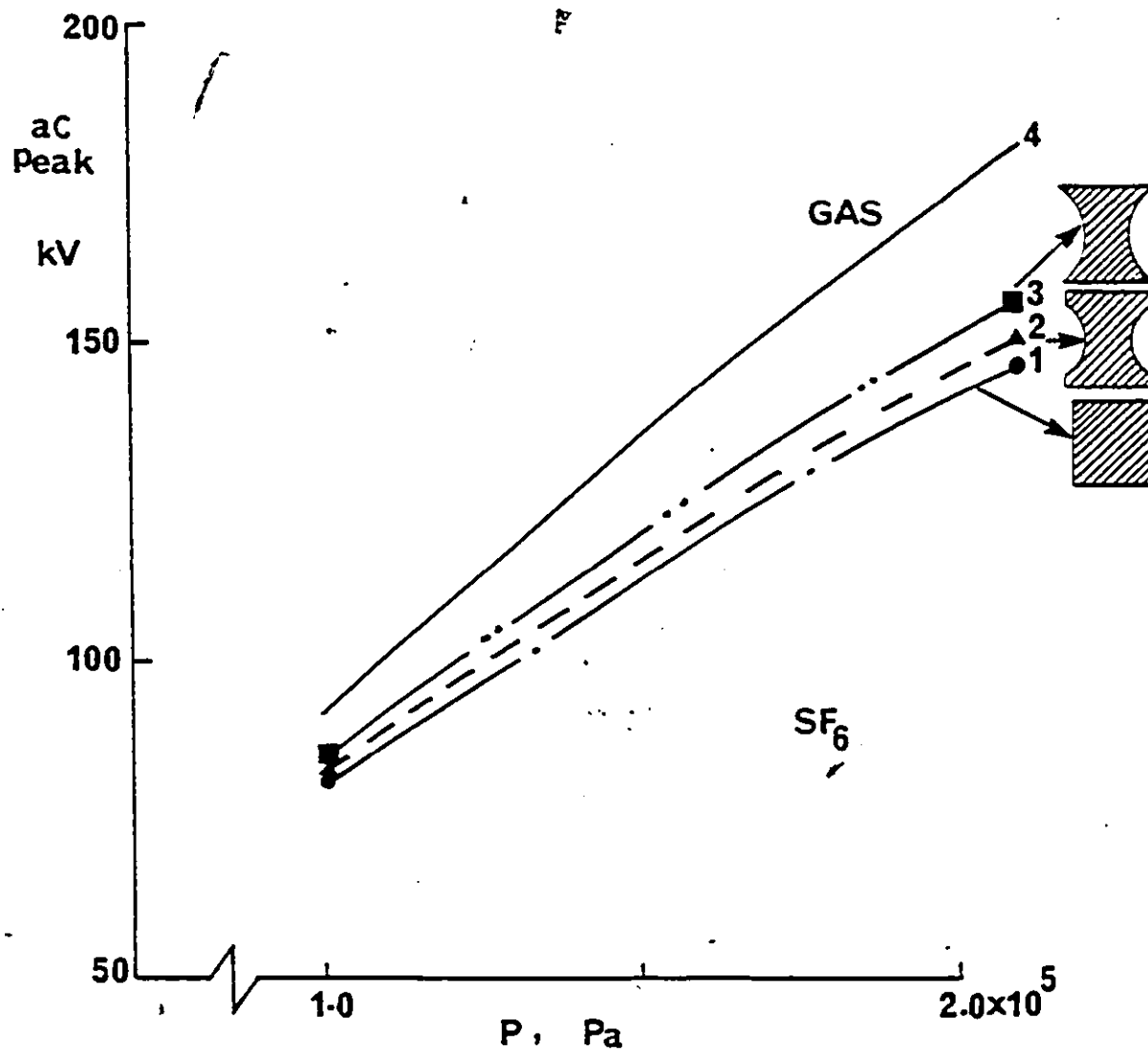
ac (60 Hz, peak) flashover voltage as a function of gas pressure in SF₆ for different profiles. Conditions are as for Fig. 5.27.
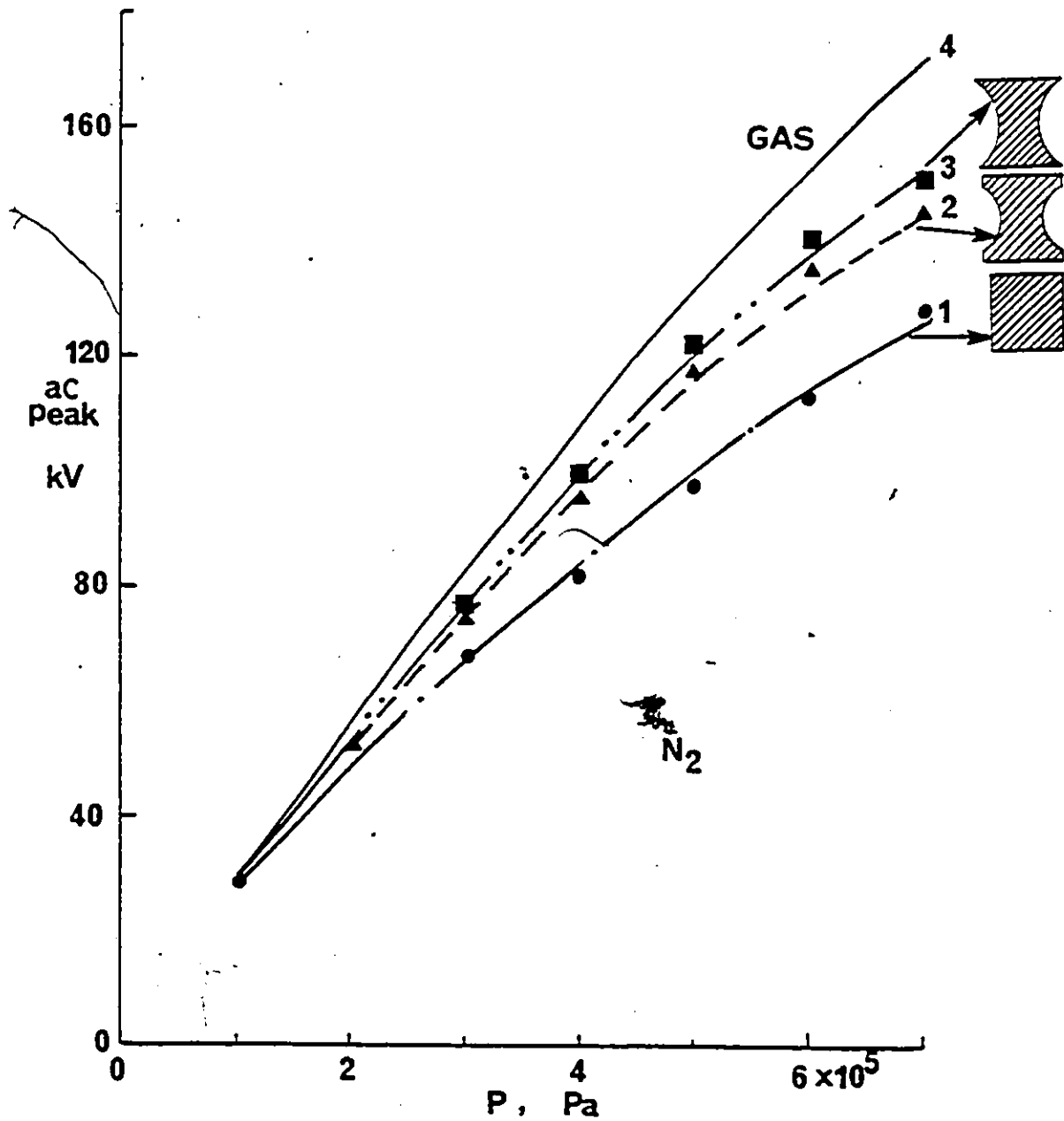
Figure 5.32: ac (60 Hz, peak) flashover voltage as a
function of gas pressure in N_2 for different
profiles. Conditions are as for Fig. 5.27.

5.4.5 Comparison between dc, ac and lightning impulse flashover voltages

A comparison of the flashover voltage using dc, ac and lightning impulse for different profiles are presented in this section to ascertain the capability of each profile in practice.

The dc, ac (60 Hz) and 1.2/50 us lightning impulse flashover voltages for a 10 mm long spacer of profile 'd' made of Plexiglas in N_2 and SF_6 are shown in Fig.5.33. It can be seen that the dc and the lightning impulse voltages are close in values, but the ac withstand voltage is lower by about 10% at 0.2 MPa of SF_6. Fig.5.34 shows the flashover voltages of profile 'c' using dc, ac (60 Hz peak) and 1.2/50 us lightning impulse in SF_6 and N_2. It will be observed that the dc and the lightning impulse flashover voltages are higher than the peak ac for both SF_6 and N_2. Typically for N_2 at 0.4 MPa, the peak ac flashover voltage is lower than the dc and the lightning impulse by about 10% (Fig.5.34).

The reason for the observed lower ac (crest) withstand voltage was discussed in section 5.3.5.
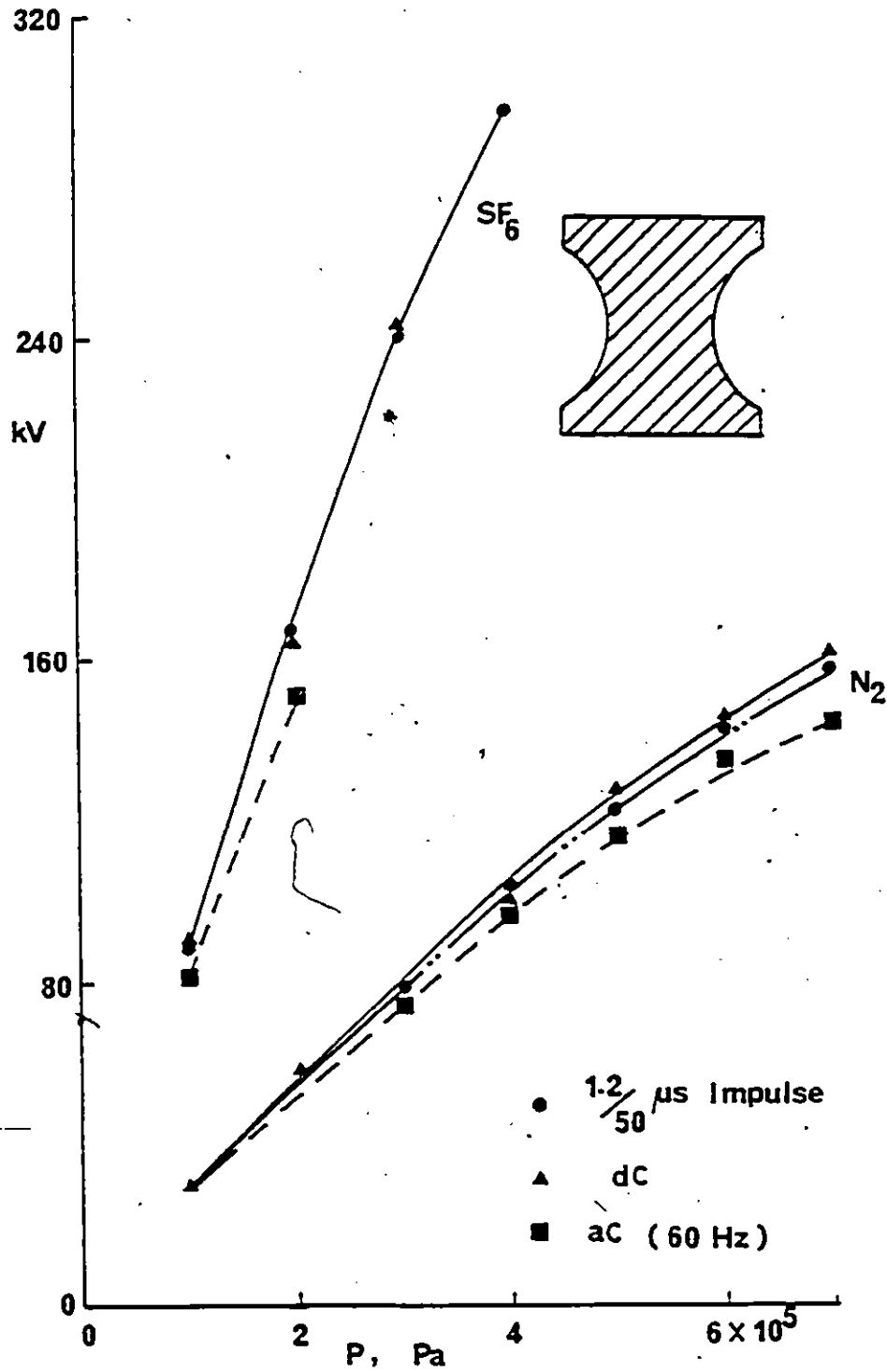
Figure 5.33: dc, ac (60 Hz, peak) and 1.2/50 us impulse flashover voltages as a function of gas pressure in SF$_6$ and N$_2$ for profile 'd'. Conditions are as for Fig.5.27.
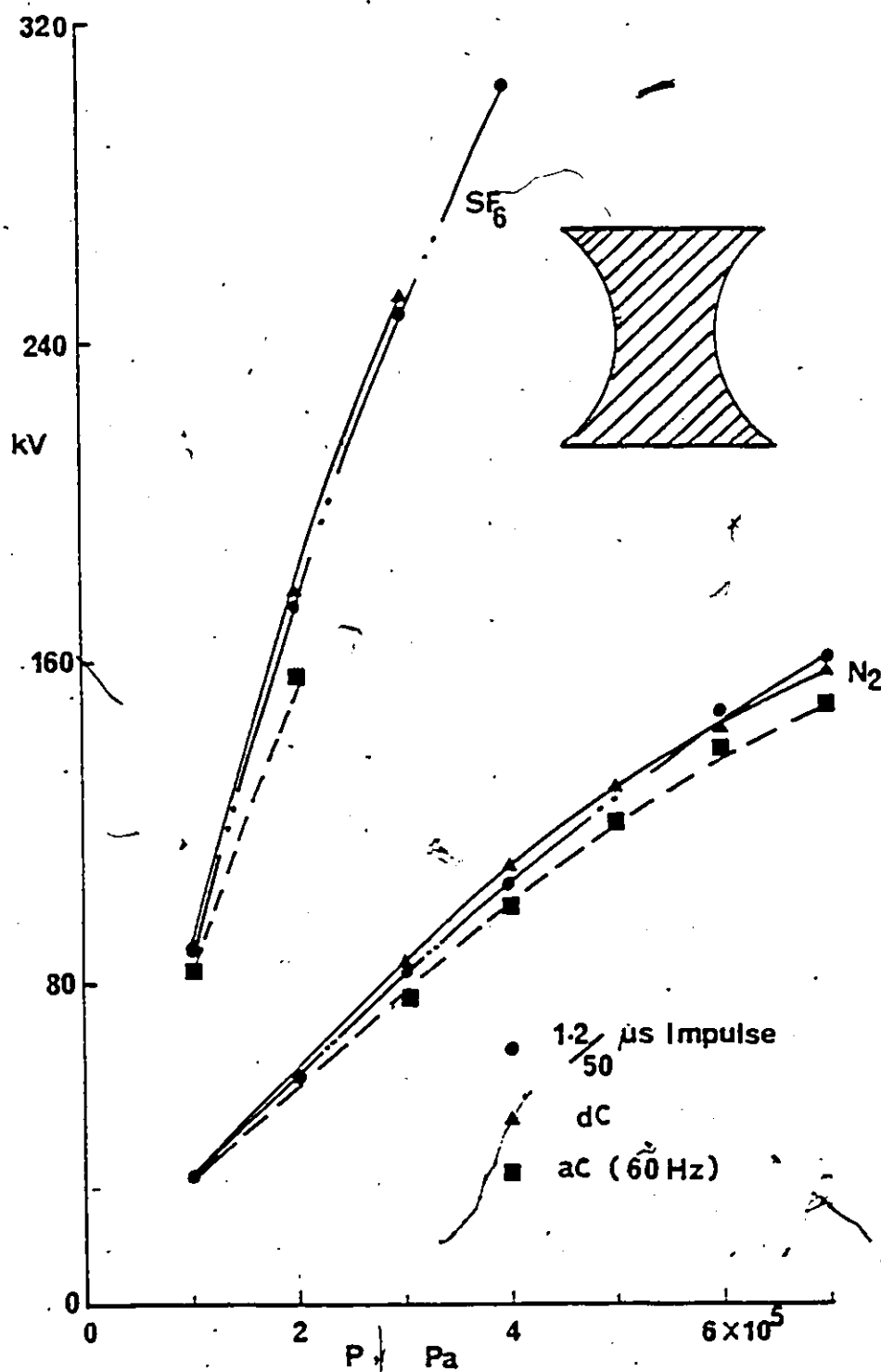
Figure 5.34: dc, ac (60 Hz, peak) and 1.2/50 us impulse
flashover voltages as a function of gas
pressure in SF₆ and N₂ for profile'c'.
Conditions are as for Fig.5.27.

## 5.5 Flashover Characteristics of Different Insulating Materials and Gases

The flashover voltage of three cylindrical spacers made of Plexiglas and having a length L=10 mm and $2R_0$=10 mm in 0.1 MPa of freon is shown in Fig.5.35. Five minutes are allowed between successive sparks for spacer 1, 10 minutes for spacer 2, and 30 minutes for spacer 3. It will be observed that the flashover voltage decreases rapidly after the third spark for the three specimens used. Visual examination of the spacers showed that there is carbon deposits on the spacer surface arising from the arc discharge and this appears to reduce the flashover voltage of the spacer.

The dc surface flashover of PTFE (Teflon) cylindrical spacer is measured in the gases air, N_2, CO_2 and H_2 and is shown in Fig.5.36. The length of the spacer is L=10 mm and the diameter is $2R_0$=10 mm. The gas pressure is varied in the range of 0.1 to 0.4 MPa. As can be seen from Fig.5.36 that the flashover voltage with air is higher than N_2, CO_2 and H_2 at a fixed gas pressure. In this range of pressure, a linear dependence is observed. However, Teflon has been found to be difficult to shape to the profiles of Fig.3.1.

The dependence of the flashover voltage, of a cylindrical spacer and a spacer having profile "a" (Fig.3.1a) with θ= 45°, made of Macor glass-ceramic on the number of sparkings in 0.4 MPa of N_2, is shown in Fig.5.37. The Macor
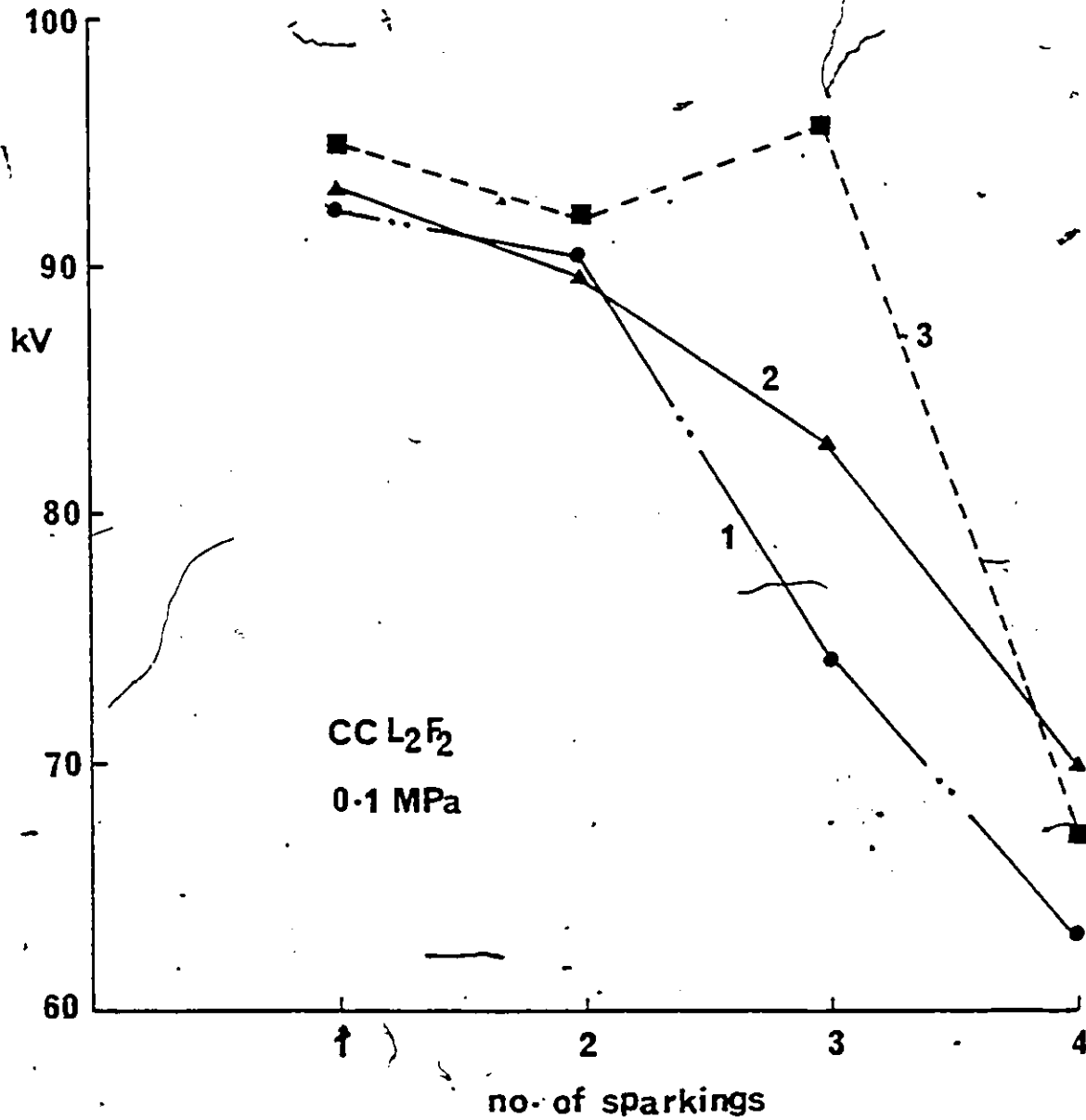
dc flashover voltage as a function of gas pressure in Freon for cylindrical spacer θ= 0, ε₂= 3.2, L= 10 mm and 2R₀= 20 mm. 1 to 3 are the sample numbers.
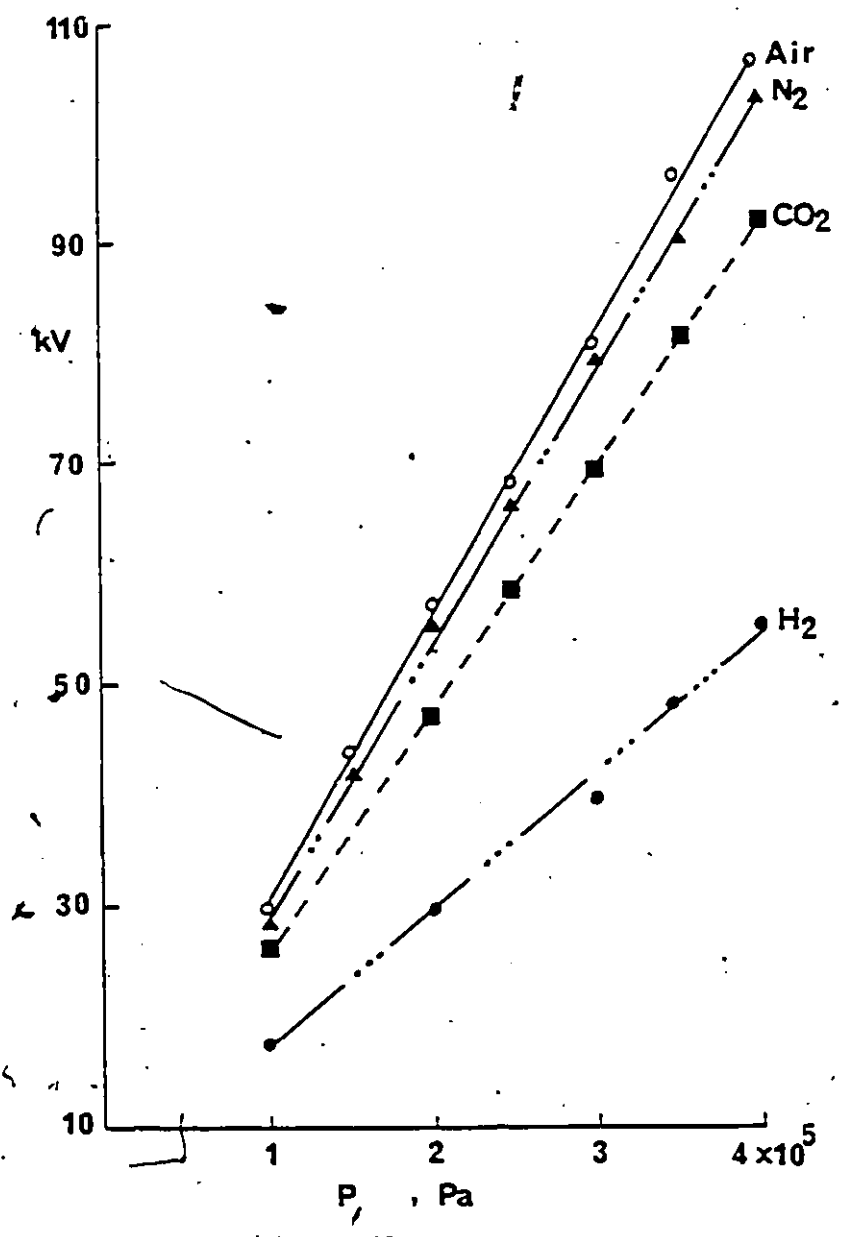
Figure 5.36: dc flashover voltage as a function of gas pressure in air, N_2, CO_2 and H_2 for cylindrical spacer $\theta = 0$. Teflon $(\varepsilon_2 = 2.1)$, $\delta = 10$ mm and $2R_0 = 20$ mm.

glass-ceramic has a partially crystalline structure which enables it to be machined with ordinary tools and does not require diamond tools like glass-ceramics. Five minutes are allowed between successive sparks. It will be observed from Fig.5.37 that the flashover voltage is not stable and after about 12 sparks starts to decrease rapidly. Visual examination of the spacer showed an arc mark on its surface implicating carbon deposits as being the reason for reducing the flashover voltage. Macor glass-ceramic has been considered a poor arc tracking material especially under high gas pressure.

Flashover voltage measurements have been carried out for PVC and PE in high gas pressure. Fig. 5.38 shows the ac (60 Hz) peak flashover voltage as a function of sparkings for PVC and PE in SF_6. The gas pressure is 0.1 MPa until spark number 10, then increased to 0.2 MPa of SF_6 until spark number 20. It can be seen that the flashover voltage in PVC is unaffected up to the tenth spark. Some conditioning is initially observed with increasing the pressure but deterioration rapidly occurs in both materials. It seems that both of these materials are not suitable in the application involving a high voltage strength.
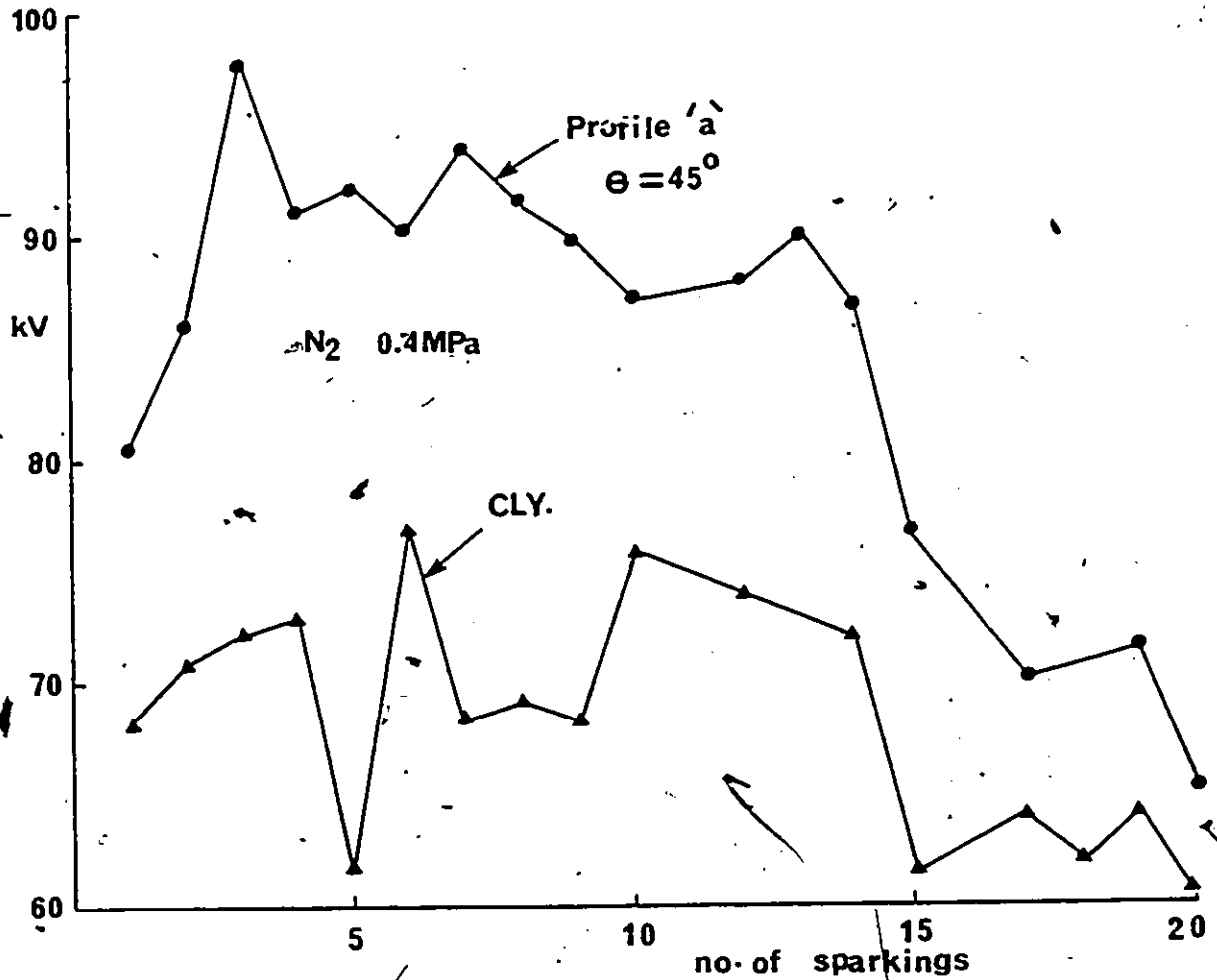
Figure 5.37: Dependence of the flashover voltage of glass-ceramic cylindrical and profile 'a' spacers on the number of sparkings in N_2. $L = 10$ mm, $2R_0$ and $\theta = 45°$.
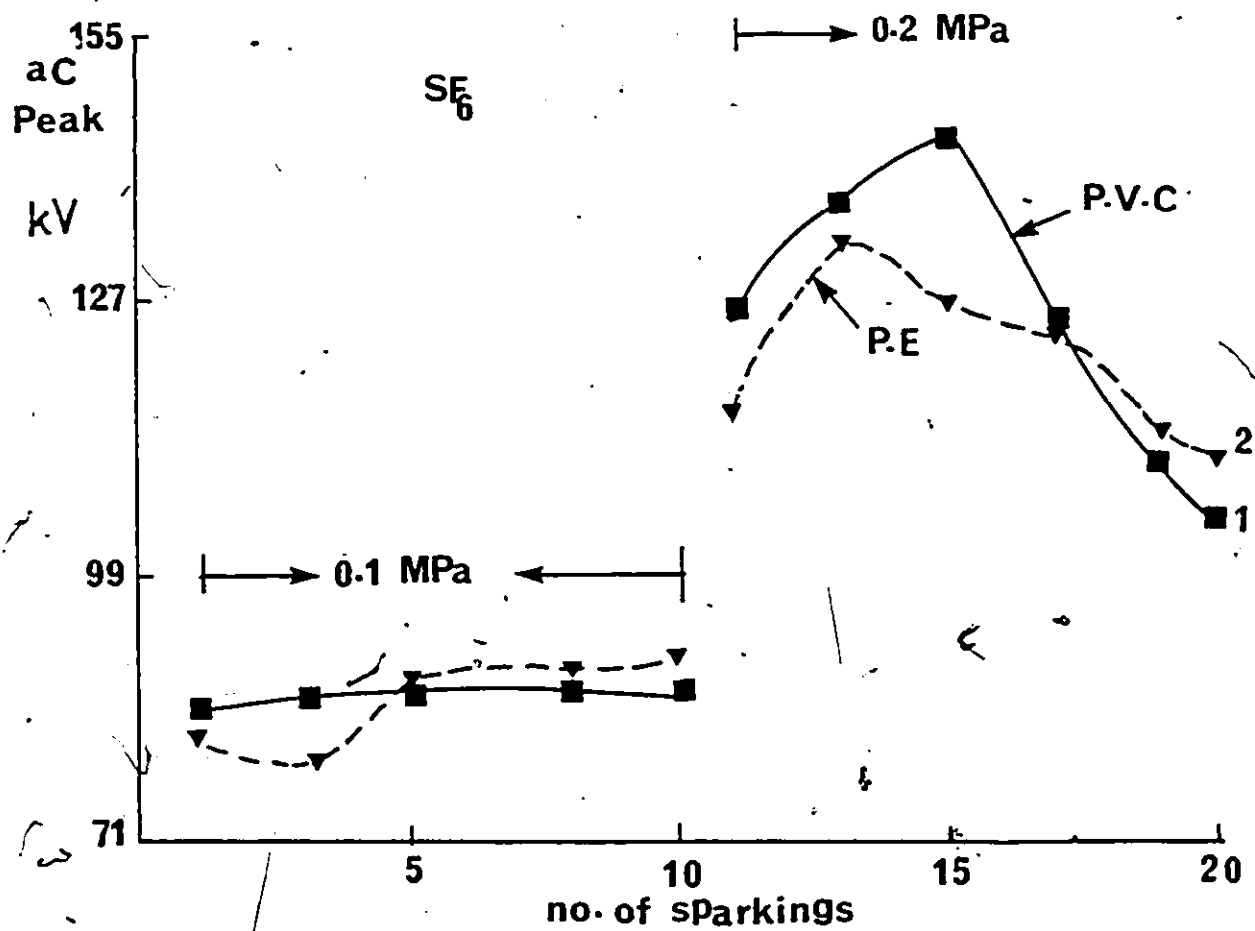
Figure 5.38: ac (60 Hz) peak flashover voltage as a function of sparkings for PVC and PE spacer profile 'c' in SF_6. L= 10 mm and $2B_0$= 20 mm and θ = 45°.

Chapter VI

ANALYTICAL DETERMINATION OF THE BREAKDOWN FIELD
STRENGTH FOR SHAPED SPACERS

The Townsend and Meek-Raether breakdown mechanisms in gases are briefly reviewed and then applied analytically to validate the field calculations.

6.1 Townsend Mechanism

From a single electron starting at the cathode, successive electron avalanches between the electrodes are developed until breakdown occurs. Under nonuniform field conditions, the number of electrons n at the anode is [99],

$$\frac{n}{n_0} = \frac{1 + \int_0^d \exp[\int_0^Z (\alpha - \eta) \, dz] \alpha \, dz}{1 - \nu \int_0^d \exp[\int_0^Z (\alpha - \eta) \, dz] \alpha \, dz} \qquad (6.1)$$

where α is Townsend's first ionization coefficient, η is the electron attachment coefficient, ν is the total secondary ionization coefficient, d the gap length and n_0 the initial electrons emitted from the cathode.

The Townsend's criterion for breakdown can be derived from equation (6.1),

$$\nu \int_0^d \exp[\int_0^Z (\alpha - \eta) \, dz] \alpha \, dz = 1 \qquad (6.2)$$

Under uniform field distribution, the criterion for breakdown becomes,

$$\frac{\nu \alpha}{\alpha - \eta} [\exp[(\alpha - \eta) d] - 1] = 1 \qquad (6.3)$$

The secondary ionization coefficient ν is very sensitive to the surface condition, the material of the electrodes and the type of gas. Since in high pressures of SF_6 the breakdown voltage was found to be independent of the electrode material it is not necessary to invoke the secondary electron production processes. However for nitrogen, particularly at the lower end of the pressure range (around 1 bar), the breakdown of the gas can only occur with the contribution to electron production from the secondary ionization processes.

6.2 Streamer Mechanism

In this mechanism, it is assumed that the breakdown of the gas occurs when the space charge field arising from the electrons produced by photoionization and other processes becomes of the same order as the local applied field. Loeb and Meek [100] developed the following criterion from the streamer formation in nonuniform fields.

$$(\alpha - \eta)_z \exp[\int_0^Z (\alpha - \eta) dz] = k E_z [z/N]^{0.5} \qquad (6.5)$$

Where N is the gas density, k is constant and z is the avalanche length and $(\alpha - \eta)_z$ is the net Townsend ionization coefficient at the avalanche head.

A similar criterion was proposed by Raether [101] who suggested that 10^8 is the critical number of electrons to form a streamer. The above equation of Loeb and Meek has been modified by Pedersen [99],

$$\int_0^Z (\alpha - \eta) \, dz = \ln N_c = k \qquad (6.6)$$

Where k is constant. From the available experimental uniform field breakdown, a suitable value for k is about 18 or $N_c = 10^8$ electrons.

In electronegative gases, the Meek-Raether streamer criterion suggests that the avalanche does not have to proceed all the way to the anode and therefore the avalanche length becomes a fraction of the distance between the electrodes. The limiting value of the breakdown strength in SF_6 is obtained when,

$$(\alpha - \eta) \, dz = 0 \qquad (6.7)$$

In this case $\alpha/p = \eta/p$

6.3 Calculation of Space Charge Field

Electrons and positive ions are produced in pairs. Because there is a large difference in the mobility between electrons and ions, the latter accumulate near the cathode and their number exceeds the electrons there while near the anode there are more electrons. The presence of the space charge distorts the originally uniform field according to Possion's equation,

$$\varepsilon_0 \frac{\partial E}{\partial z} = -\rho \qquad (6.8)$$

To calculate the electric field at the tip of an avalanche, starting from a single electron, it is assumed that the electrons are contained in a spherical volume at the tip of the avalanche. The number of electrons is exp $\int \bar{\alpha} dz$ where z is the distance from the cathode being the avalanche length. At the surface, of the sphere containing the electrons, the space charge field is [102],

$$E_r = \frac{e \; e^{\bar{\alpha} z}}{4 \pi \varepsilon_0 \; r^2} \qquad (6.9)$$

Where r is the diffusion radius of the sphere containing the electrons. The derivation can be found in [102] and in the final form,

$$E_r = \frac{e \; e^{\bar{\alpha} z}}{4 \pi \varepsilon_0 \cdot 2 \; v \; z} \; E \qquad (6.10)$$

In nonuniform field equation (6.10) becomes.

$$Er = \frac{e^{\int \bar{\alpha}\, dz}}{4\pi \varepsilon_0 \cdot 2\, v\, z} \quad E \qquad (6.11)$$

Where v is the electron energy and E is the average field from the cathode to the location z since ($vd = ke\, E$, where vd is the drift velocity and ke is the mobility of the electron). The criterion for breakdown is that it occurs when the space charge field Er becomes appreciable and close in value to the local field at that location.

There are no data available in the literature on the surface charge distribution along the surface of concave spacers. Therefore the computation, of the electric field distribution does not take into account the effect of the surface charge.

6.4 Correlation Between the Calculated Field and the Flashover Voltage Measurements in SF.

α, η, $\bar{\alpha}$ and $\int \bar{\alpha}\, dz$ are calculated as a function of z at a given gas pressure of SF. using the measured surface flashover voltage and the calculated electric field distribution for different spacers. Also the critical avalanche length $z = zc$ and the breakdown field strength (Er) are determined when $\int \bar{\alpha}\, dz$ equals to about 18 and the space charge field Er becomes close to Ez calculated from the charge simulation and the flashover voltage at location z.

6.4.1 Computation of α, $\int \alpha \, dz$, z_c and E_r in SF.

The values of α/p and η/p for SF. as functions of E/p have been reported in the literature with a high accuracy and can be approximated in the vicinity of the region where $\alpha/p = \eta/p$ by the following relationships [99] within the range 80 $V cm^1/Torr < E/p < 160 \ V cm^1/Torr$.

$$\alpha/p = 0.024 \ (E/p) - 1.76 \qquad (6.12)$$

$$\eta/p = -0.004 \ (E/p) + 1.52 \qquad (6.13)$$

E/p is in $V \ cm^1/Torr$, α/p, η/p are in $cm^1/Torr$ and P is the gas pressure in Torr at the ambient temperature of 20 °C.

From the flashover voltage measurements and the normalized electric field distribution for a certain pressure, the values of α/p, η/p and $\bar{\alpha}/p = (\alpha - \eta)/p$ and $\int_{0}^{z} \bar{\alpha} \, dz$ are calculated. The space charge field E_r can be calculated from equation (6.11). The values of the electron energy v were given in [103] as a function of E/N where.

$$N = 3.56 \times 10^{16} \times p_0 \qquad (6.14)$$

$$p_0 = P \times \frac{273}{T \ amb.} \qquad (6.15)$$

Where p_0 is the reduced pressure to 0°C in Torr, P the measured pressure in Torr and $Tamb$ the ambient temperature in K.

In order to determine whether the computed field is equal to the localized space charge field at the onset of the flashover an iteration technique is employed. Different values of z are first chosen commencing with low values and gradually increasing, then the corresponding values of v, $\int \bar{\alpha} dz$ and $E(z)$ are used in equation (6.11) until the space charge field E_r becomes equal to the local field $E(z)$ derived from the charge simulation and the flashover voltage at the same time as $\int \bar{\alpha} dz$ equals 18. This minimum value of z at this location becomes the critical avalanche length z_c. The path AC (Fig.3.1) is chosen because it is the most probable path of the flashover.

Tables 6.1 to 6.4 show the values of z_c, $\int_{0}^{z} \bar{\alpha} dz$, $E(z_c)$ and the space charge field E_r. Typical calculations of these values are shown in Appendices D and E. The negative values of $\bar{\alpha}$ are neglected as they do not contribute to the ionization of the gas.

For example it will be observed from Table 6.1 that for $\theta = 30°$, 45°, 60° and 70° of profile 'a' at 0.1 MPa of SF_6 the breakdown field E_r (calculated from equation 6.11) agrees with the field E_{zc} (calculated at location z_c from the flashover voltage and CSM) when $\int \bar{\alpha} dz$ approaches the range 17 to 18 at the critical avalanche length $z = z_c$. The present analysis also shows that similarly good agreement is obtained for profiles 'b', 'c' and 'd' over the pressure range of SF_6 where the Fowler- Nordheim field emission of electrons is negligible (< 2 bar).

It can be seen from Tables 6.1 to 6.4 that there are conditions (e.g. Table 6.1, $\theta = 15°$) where $\int \bar{\alpha}\, dz$ of about 18 can not be satisfied. The value of $\int \bar{\alpha}\, dz$ has been found tor the low flashover voltage (e.g. at $\theta = 15°$) to be either lower than that necessary to yield sufficiently large avalanche ($>10^7$ electrons) or entirely negative. This is because the field appears to be lower than that necessary to cause breakdown. It is suggested that if the effect of the surface charges, which could enhance the field by 5 to 15% in the vicinity of zc, had been included it would have been possible to satisfy equation (6.11). For the cases shown in Tables 6.1 to 6.4 where $\int \bar{\alpha}\, dz \simeq 18$ and $\text{Er} = \text{E(zc)}$ are satisfied the surface charge would have only marginal influence on the value of zc as the field there changes very strongly with small variation of z.

It will be observed from Tables 6.1 to 6.4 that the critical avalanche length zc is a fraction of the gap length and therefore the critical avalanche does not proceed all the way to the anode. This is in accordance with the streamer mechanism. The avalanche length depends on the electric field E(z). As the field increases zc becomes smaller. Also the values of $\int \bar{\alpha}\, dz$ for different profiles in 0.1 MPa and 0.2 MPa of SF$_6$ are of the order of 17 giving Nc = 2.4×10^7 electrons.

Table 6.1: zc, $\int \bar{\alpha}\, dz$, E(z) and Er as a function of θ in
SP$_6$ for a spacer having profile 'a'. L=10 mm,
R$_0$=10 mm, q=2 mm, d=6 mm and ε_2=3.2.

0.1 MPa of SP$_6$

θ°	zc, cm	$\int\limits_{0}^{Z}\bar{\alpha}\, dz$	Ezc, kV/cm	Er, kV/cm
15	1.0	8.16	72.2	—
30	0.4645	17.46	90.09	90.65
45	0.262	16.91	93.15	93.0
60	0.361	17.221	91.221	91.57
70	0.4855	17.51	90.86	90.38

0.2 MPa of SP$_6$

θ°	zc, cm	$\int\limits_{0}^{Z}\bar{\alpha}\, dz$	Ezc, kV/cm	Er, kV/cm
15	1.0	< 0	128.74	—
30	1.0	< 0	135.88	—
45	0.1912	16.16	186.3	185.2
60	0.3238	17.12	181.45	182.06
70	1.0	< 0	129.6	—

Table 6.2: z_c, $\int\bar{\alpha}dz$, $E(z)$ and E_r as a function of R_b in SF_6 for a spacer having profile 'b'. L=10 mm, R_o=10 mm, q=2 mm, d=6 mm, h=1 mm and ε_z=3.2.

0.1 MPa of SF_6

R_b, mm	z_c, cm	$\int_0^Z \bar{\alpha}\,dz$	E_{zc}, kV/cm	E_r, kV/cm
7.73	1.0	< 0	82.7	—
4.0	1.0	< 0	79.92	—
2.83	0.2953	17.06	92.5	92.64
2.3	0.510	17.50	89.39	89.79
2.13	0.3602	17.25	90.50	90.77

0.2 MPa of SF_6

R_b, mm	z_c, cm	$\int_0^Z \bar{\alpha}\,dz$	E_{zc}, kV/cm	E_r, kV/cm
7.73	1.0	< 0	163.5	—
4.0	1.0	< 0	157.08	—
2.83	0.2568	16.93	185.0	184.27
2.3	0.7394	17.956	182.05	182.82
2.13	0.8161	18.049	181.5	181.8

Table 6.3: zc, $\int_0^Z \bar{\alpha}\,dz$, $\mathcal{E}(z)$ and $\mathcal{E}r$ as a function of θ in SP_6 for a spacer having profile 'c'. $L=10$ mm, $R_0=10$ mm, and $\mathcal{E}_2=3.2$.

0.1 MPa of SP_6

θ°	zc, cm	$\int_0^Z \bar{\alpha}\,dz$	Ezc, kV/cm	Er, kV/cm
15	1.0	2.754	71.05	—
30	0.412	17.38	93.12	92.56
45	0.3118	17.12	94.6	94.24
60	0.3656	17.26	93.80	93.09
70	0.4206	17.388	92.93	92.0

0.2 MPa of SP_6

θ°	zc, cm	$\int_0^Z \bar{\alpha}\,dz$	Ezc, kV/cm	Er, kV/cm
15	1.0	< 0	129.97	—
30	0.5868	17.72	180.0	180.5
45	0.2394	16.86	186.5	185.9
60	0.3132	17.12	185.30	185.0
70	0.4314	17.42	183.0	182.46

Table 6.4: zc, $\int_0^Z \bar{\alpha}\, dz$, E(z) and Er as a function of Rd in
SF$_6$ for a spacer having profile "d". L=10 mm,
R$_0$=10 mm, q=1 mm and ε_2=3.2.

0.1 MPa of SF$_6$

Rd, mm	zc, cm	$\int_0^Z \bar{\alpha}\, dz$	Ezc, kV/cm	Er, kV/cm
19.3	1.0	9.0	75.20	—
10.0	0.4268	17.436	93.30	92.99
7.07	0.3113	17.165	95.5	95.36
5.77	0.3257	17.21	94.7	93.66
5.3	0.3099	17.173	94.94	93.79

0.2 MPa of SF$_6$

Rd, mm	zc, cm	$\int_0^Z \bar{\alpha}\, dz$	Ezc, kV/cm	Er, kV/cm
19.3	1.0	< 0	159.9	—
10.0	1.0	0.78	148.21	—
7.07	0.3882	17.37	184.15	184.6
5.77	1.0	16.84	132.03	—
5.3	1.0	13.52	127.76	—

The dependence of the critical avalanche length zc on the contact angle θ for profiles 'a' and 'c' in SF_6 is shown in Fig.6.1. It will be observed that the avalanche length zc shows a marked dependence on the contact angle θ. In the range from $\theta= 35^{\circ}$ to $\theta=60^{\circ}$, zc is higher at 0.1 MPa of SF_6 than that at 0.2 MPa of SF_6 for profile 'a' and 'c'. This is because the ratio of the flashover field to the pressure is slightly higher at 0.1 MPa than at 0.2 MPa of SF_6. Similarly E/p is higher at lower values of z for profile a than for profile c, at the same gas pressure, giving lower zc for profile a, as observed in Fig.6.1. At $\theta=45^{\circ}$ the flashover voltage and hence E/p is highest and therefore the avalanche length is expected to be the shortest as found here.

From these findings, it can be judged that the values of the calculated field for different profiles and the flashover voltage measurements satisfy the streamer criterion for breakdown in high pressure of SF_6.
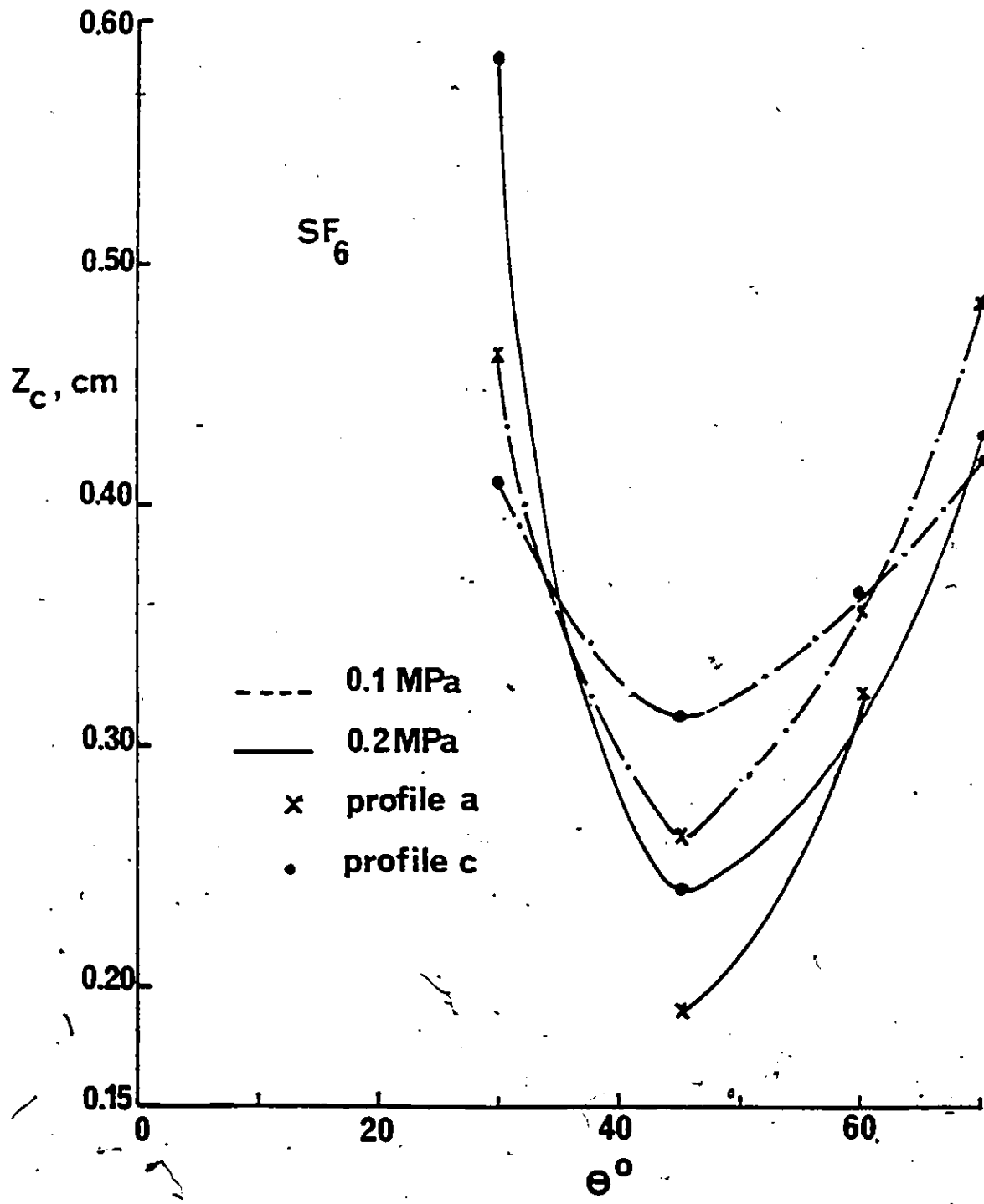
Figure 6-1: Dependence of zc on the contact angle θ in SF₆ for profile 'a' and 'c' spacers.. Other Conditions are as of Tables 6.1 and 6.3.

6.5 Correlation Between the Calculated Field and the

Flashover Voltage Measurements in N₂

Similar analysis to that described in section 6.4 is performed here for nitrogen. Since the attachment process to form negative ions is negligibly small $\int \bar{\alpha}\, dz = \int \alpha\, dz$.

From the measurement of the flashover voltage of the spacers and the calculated field distribution, the first ionization coefficient α can be determined as a function of z along the path AC (Fig.3.1) using the measured values of Heylen [104].

$$\alpha/p_o = A \exp(-Bp_o/E) \qquad (6.15)$$

Where $A=2.108$ cm⁻¹ torr⁻¹ and $B=224$ V cm⁻¹ torr⁻¹ at 0°C. The results of Heylen are widely used in the literature because they were reported over a wide range of E/p_o. They are slightly higher than the values reported by Cookson et al [105]. The values of v in equation 6.11 are taken from Ref. [103].

Typical calculation of α and $\int_o^Z \alpha\, dz$ are shown in Appendix F. The calculated zc, $\int \alpha\, dz$ and E(z) for a spacer having the highest withstand electric field which is profile 'a' with $\theta=45°$ and for different pressures in N₂ are shown in Table 6.5. It can be observed that in the range from 0.3 MPa to 0.6 MPa, the values of $\int \alpha\, dz$ satisfy the streamer criterion for breakdown and give space charge field values

of E_r in good agreement with the values of E_{zc} calculated from the flashover voltage and CSM at the same location z_c.

The calculation of the breakdown strength E_r is not possible at pressure < 0.2 MPa of nitrogen because it is dominant by the Townsend breakdown criterion which requires the secondary ionization coefficient γ. The latter is very sensitive to the electrodes surface and the gas conditions and is not available.

Table 6.5: z_c, $\int \alpha\,dz$, $E(z)$ and E_r as a function of P in N_2 for a spacer having profile 'a'. L=10 mm, R_0=10 mm, q=2 mm, d=6 mm and ε_2=3.2.

P, MPa	z_c, cm	$\int_0^Z \alpha\,dz$	E_{zc}, kV/cm	E_r, kV/cm
0.2	1.0	12.34	43.45	0.39
0.3	0.918	17.34	83.3	82.74
0.4	0.865	17.34	110.2	109.6
0.5	0.885	17.36	131.0	131.9
0.6	0.898	17.35	150.8	149.82
0.7	1.0	16.98	129.74	122.9

The dependence of z_c on the pressure shown in Table 6.5 is explained by the dependence of α and $\int \alpha\,dz$ on E/p in the pressure range covered. Typically at z= 0.9 cm α and

$\int \alpha dz$ increase from 0.2 to 0.4 MPa therefore zc decreases. Thereafter α and $\int \alpha dz$ decrease steadily and therefore zc should increase again as observed here. The values of α, $\int \alpha dz$ and zc are shown in a location z =0.9 cm near the critical avalanche length in Table 6.6. Similar dependence is found in the vicinity of z =0.8 cm.

Table 6.6: values of Ez/p, αz, $\int \alpha dz$ at locations close to the avalanche length and zc for profile a in N_2. Other conditions as in Table 6.5.

P, MPa	Ez/p, Vcm^{-1} $torr^{-1}$	$\alpha(0.9)$	$\int_0^z \alpha\, dz$	zc
0.2	37.27	11.92	11.55	1.0
0.3	37.11	17.48	17.06	0.918
0.4	35.62	18.475	18.02	0.865
0.5	34.16	18.05	17.64	0.885
0.6	33.02	17.36	17.39	0.898
0.7	31.80	16.18	15.96	1.0

Chapter VII

DESIGN OF SPACER-CONDUCTOR-GAS(TRIPLE JUNCTION)

7.1 Introduction

To improve the electrical insulation capability of gas insulated systems, the gap containing the spacer should be designed such that the flashover voltage with the spacer is close to the breakdown voltage of the gas with the absence of the spacer. An attempt to achieve this is made here by reducing the field at the conductor-spacer-gas triple junction and its vicinity in order to reduce the field emitted electrons. It has been reported that the electric field at the metal-dielectric junction of a cylindrical spacer can be reduced by incorporating a suitable end-cap design, by using a recessed electrode and by using a metal insert in the spacer [107-109]. Also an improved design of the cathode triple junction to avoid local field intensification has been investigated [106].

Experimental investigations in vacuum showed that the electrical field at the electrode junction is reduced by recessing the solid insulator into the cathode [110,111]. The best electrical performance of the solid insulator in vacuum was obtained when the angle between the solid insulator and the recessed electrode was 60°[110].

In compressed gas insulated systems, the use of metal inserts in the solid insulator produces a favorable field distribution and improves the flashover strength at high gas pressures [6]. It was reported that the surface flashover of cylindrical spacers in SF_6 increased when the electrodes extended into the insulator especially for higher gas pressures [9]. In this chapter, the effects of the recess angle γ, the depth of the recess, the length of the spacer and the permittivity of the spacer on the electric field distribution are investigated. Also the dependence on the radius and the metal insert is studied. The dependence of the flashover voltage on the recess angle γ was not studied previously and this is reported for the first time here at high gas pressures.

7.2 Spacer-Conductor Configuration

The cross-sections of several designs of spacer-electrode geometry is shown in Fig.7.1. System A shows a spacer which is placed in recessed electrodes at both ends to a depth d. γ is the angle between the spacer and the incline edge of the recessed electrodes. In Systems B, C and D only one conductor has a depression to hold the spacer which is useful for dc applications. The edge of the depression in the recessed electrode is rounded in systems B and C with a radius r (quarter of a circle) to avoid field intensification on the surface of the spacer and in the

vicinity of the cathode triple junction. System C shows a
cross-section of a spacer with a concave shape at one
conductor and placed in a recess in the other conductor. O
is the angle between the tangent to the surface of the
spacer and the normal at the contact with the conductor. W
and t are the diameter and the length of the metal inserts,
respectively. r_0 is the radius of the corner of the insert
and is chosen to be 1 mm. System D shows a depression to
hold the spacer and an inclined edge to reduce the electric
field at the spacer surface. r_1 is the radius of the contact
of the flat part of the electrode and the inclined section
and is chosen to be 1 mm throughout this study.
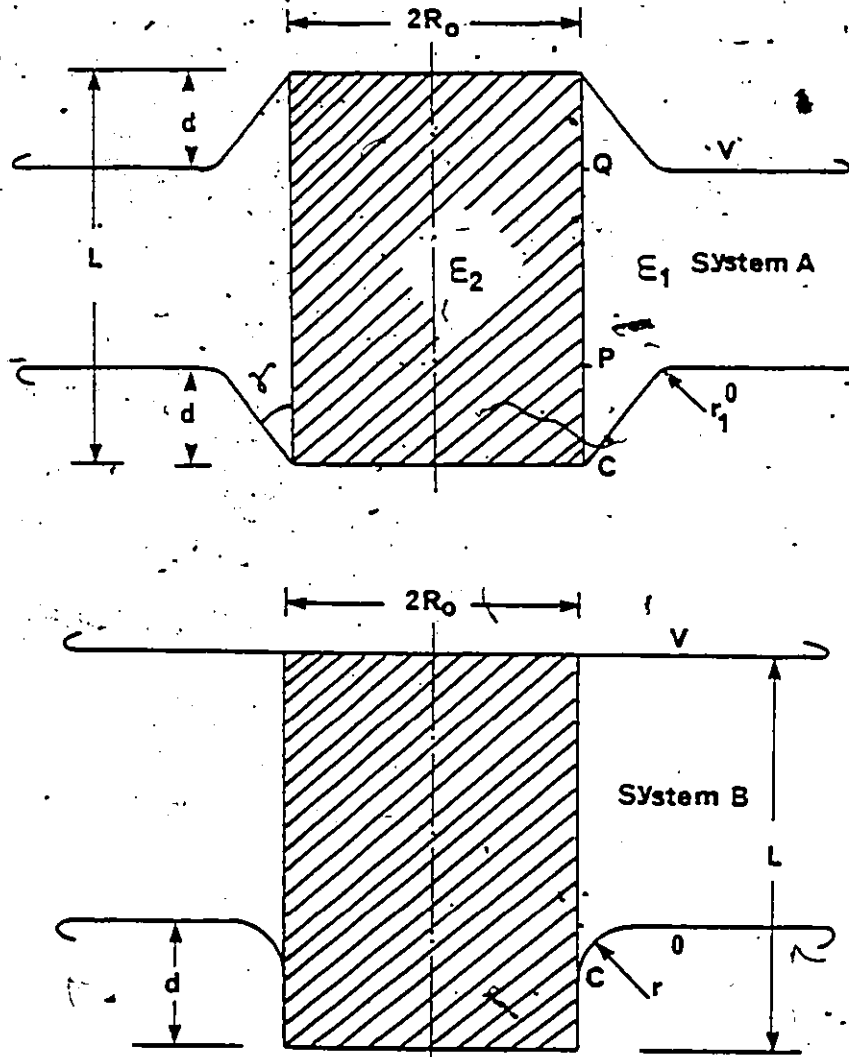
Figure 7.1: Spacer— electrode arrangements. $2R_0$ diameter of the spacer, L length, ε_2 permittivity of the spacer, ε_1 permittivity of gas. System A: cylindrical spacer placed in recessed electrode at both ends, γ angle between the spacer surface and the recessed electrode. System B: cylindrical spacer placed in a groove of one electrode only. d thickness of groove, r radius of groove edge. System C: concave-shaped spacer at one electrode and housed in a groove at the other electrode, θ angle between the tangent to the surface and the normal at the contact point. System D: cylindrical spacer placed in recessed electrode with a groove at one electrode only.

System C

System D
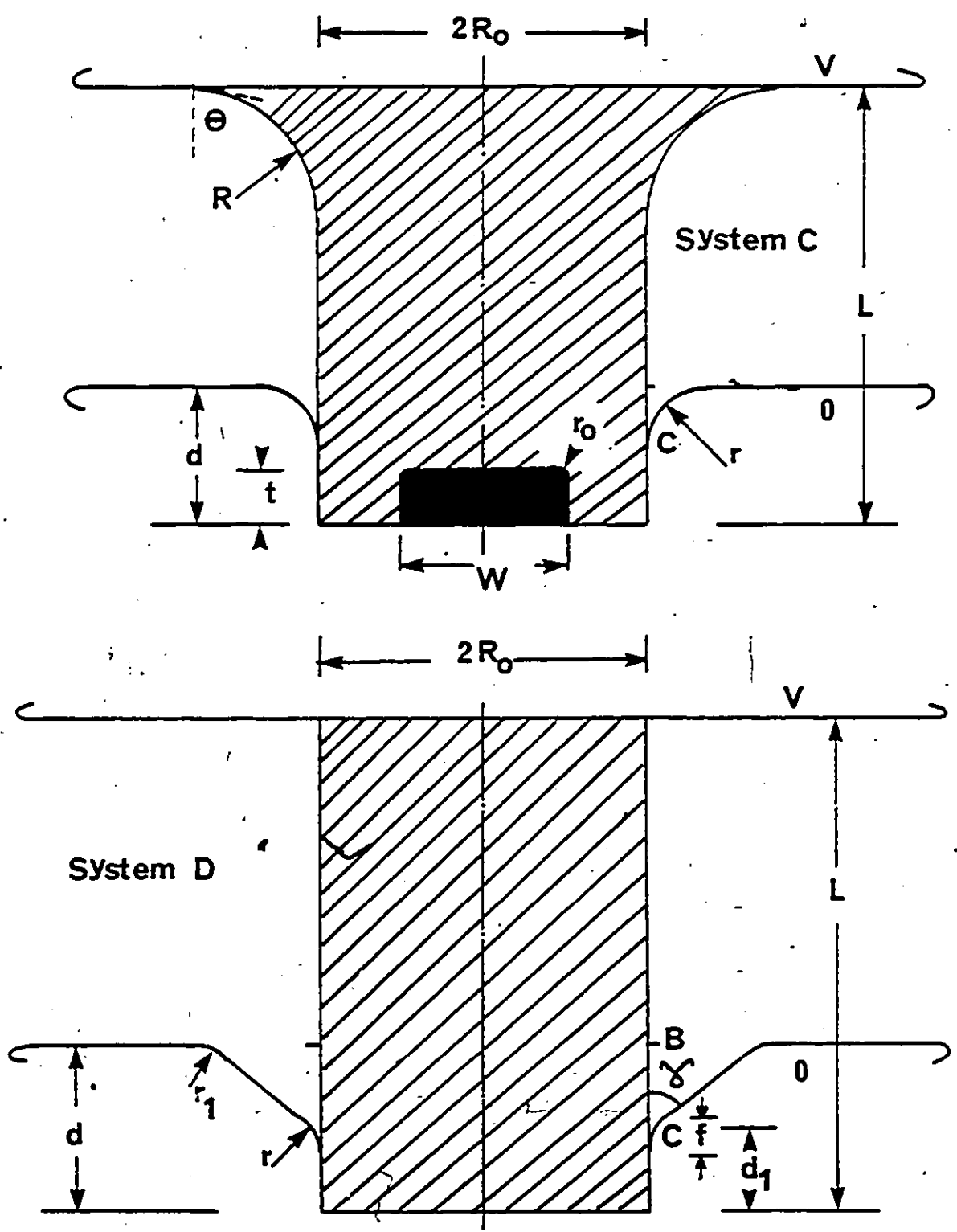
7.3 Analytical Results and Discussions

7.3.1 Effect of the recess angle

The electric field components at the cathode junction E^*t_1c, E^*n_2c and E^*T_1c and the maxima in both the tangential E^*t_1m and the total fields E^*T_1m of a Plexiglas spacer with a relative permittivity ($\varepsilon_2=3.2$) placed in recessed electrodes (System A) are shown in Table 7.1. E^*t_1m and E^*T_1m are in locations P and Q of (Fig.7.1, System A). The recess angle γ is varied from $5°$ to $90°$. It can be seen that E^*t_1c increases as γ increases while E^*t_1m decreases with increasing γ. E^*T_1c increases steadily as γ increases, but E^*T_1m shows a stronger dependence on γ. Typically E^*T_1m decreases from 3.3 at $\gamma=5°$ to 1.3 at $\gamma=30°$ and to 1.03 at $\gamma=80°$.

The dependence of the normal field E^*n_1c on the recess angle γ is also shown in Table 7.1. It will be observed that $|E^*n_1c|$ decreases as γ increases. Typically, it decreases from $E^*n_1c=0.65$ at $\gamma=5°$ to 0.09 at $\gamma=80°$.

The total electric field E^*T_1 distribution along the interface of a Plexiglas ($\varepsilon_2=3.2$) spacer placed in recessed electrodes (System A) is shown in Fig.7.2, for recess angles $\gamma=10$, 20, 45, 70, and $90°$ (cylindrical insulator between two planar electrodes). It will be observed from Fig.7.2 that E^*T_1 decreases with increasing γ in the region between P and Q and in the vicinity of these locations while it increases at the triple junctions. Hence there expected to be some γ values which yield a maximum withstand voltage of the gap.

Table 7.1: $E't_{1c}$, $E'n_{1c}$, $E'T_{1c}$, $E't_{1m}$ and $E'T_{1m}$ as a function of γ (System A). L=40 mm, $2B_0$=40 mm, d=5 mm, ε_2= 3.2. $E't_{1m}$ and $E'T_{1m}$ are in locations P and Q of Fig.7.1, and E_{av} = V/L.

γ	$E't_{1c}$	$\left|E'n_{1c}\right|$	$E't_{1m}$	$E'T_{1c}$	$E'T_{1m}$
5	0.135	0.65	1.31	0.66	3.3C
10	0.24	0.64	1.20	0.68	2.30
20	0.36	0.62	1.18	0.71	1.64
30	0.47	0.55	1.12	0.72	1:3
40	0.56	0.48	1.10	0.74	1.16
45	0.60	0.44	1.10	0.745	1.13
50	0.65	0.40	1.09	0.76	1.10
60	0.73	0.31	1.08	0.79	1.08
70	0.82	0.21	1.06	0.85	1.06
80	0.91	0.09	1.03	0.915	1.03
90	1.0	0	1.0	1.0	1.0

$E'T_1$ at and near the locations P and Q which are at Z'=0.1 and 0.9, respectively is enhanced particularly at low values of γ, below 45°.

Fig.7.3 shows $E'n_1$ along the spacer-gas interface of Plexiglas spacer(ε_2=3.2) for γ=10, 20, 45, 70 and 90° using System A. It will be observed from Fig.7.3 that the recess angle γ has also a strong influence on the normal field especially at and near locations P and Q. The effect is more
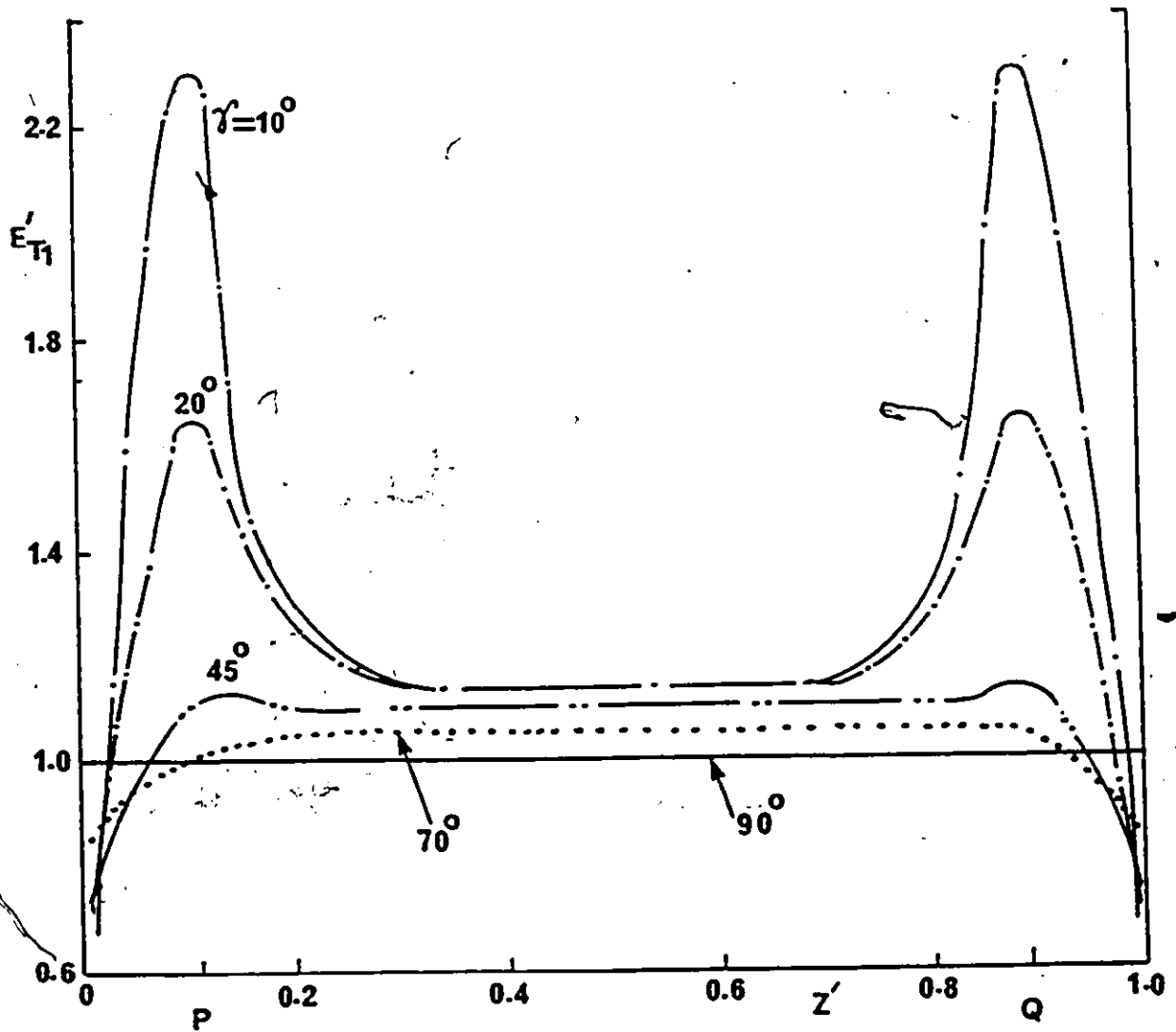
Figure 7.2: Total electric field $E'T_1$ along the spacer surface of system A (Fig.7.1) for different recess angles. ϵ_2= 3.2, L= 40 mm, $2R_0$= 40 mm, d= 5 mm and $Eav=V/L$.

significant for $\gamma < 45°$. Typically, E^*n_1m decreases from 2.1 at $\gamma = 10°$ to 0.54 at $\gamma = 45°$.

E^*T_1c and E^*T_1m as a function of the recess angle are shown in Fig.7.4 for system A. It can be observed that E^*T_1m decreases, initially rapidly, with increasing γ, while E^*T_1c increases with increasing γ. E^*T_1c and E^*T_1m are important parameters affecting the surface flashover voltage at high gas pressure. The first controls the electrons emission from the cathode while the latter affects the growth in the number of electrons. Therefore, for higher flashover voltage the recess angle γ should be chosen in such way to give lower E^*T_1c as well as E^*T_1m.

E^*t_1c, $|E^*n_1c|$ and E^*T_1c at the cathode triple junction for an epoxy spacer $\varepsilon_2 = 4.7$ placed in recessed electrodes (system A) with $d/L = 0.2$ are shown in Table 7.2 for different recess angles γ. Also shown in Table 7.2 E^*t_1m and E^*T_1m at locations P and Q of Fig.7.1. The ratio d/L has been chosen to be the same as that used in the experimental study. It will be observed that $|E^*n_1c|$, E^*t_1m and E^*T_1m decrease as γ increases. E^*T_1m decreases by 60% as γ increases from 10° to 45°. E^*t_1c and E^*T_1c increases as γ increases. E^*T_1c increases by 14% as γ increases from 10° to 45°.
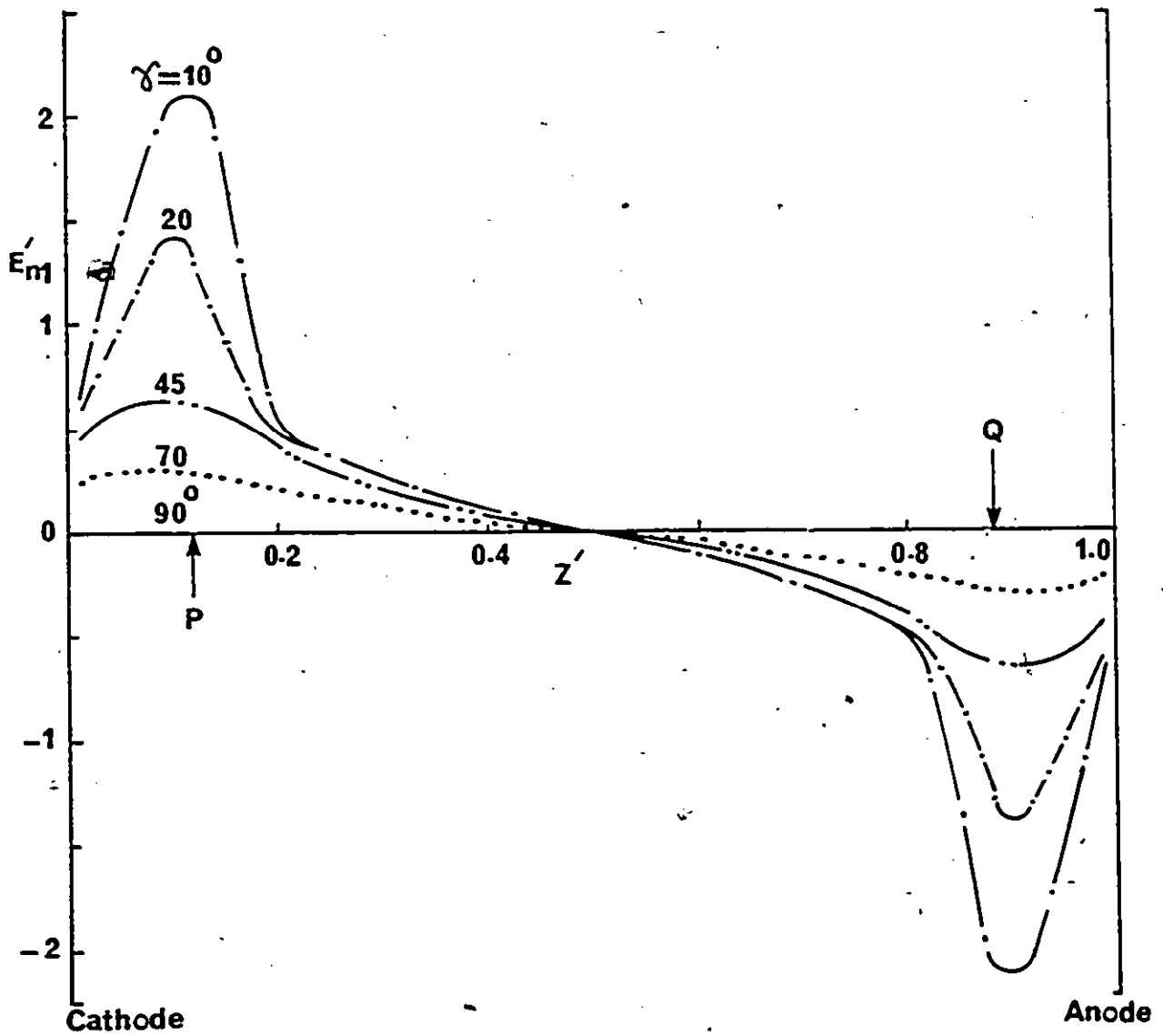
Figure 7.3: Dependence of the normal field E'n, on the gas
side of the interface of the spacer of system A
(Fig.7.1) on the recess angle. Other
conditions are as of Fig.7.2.
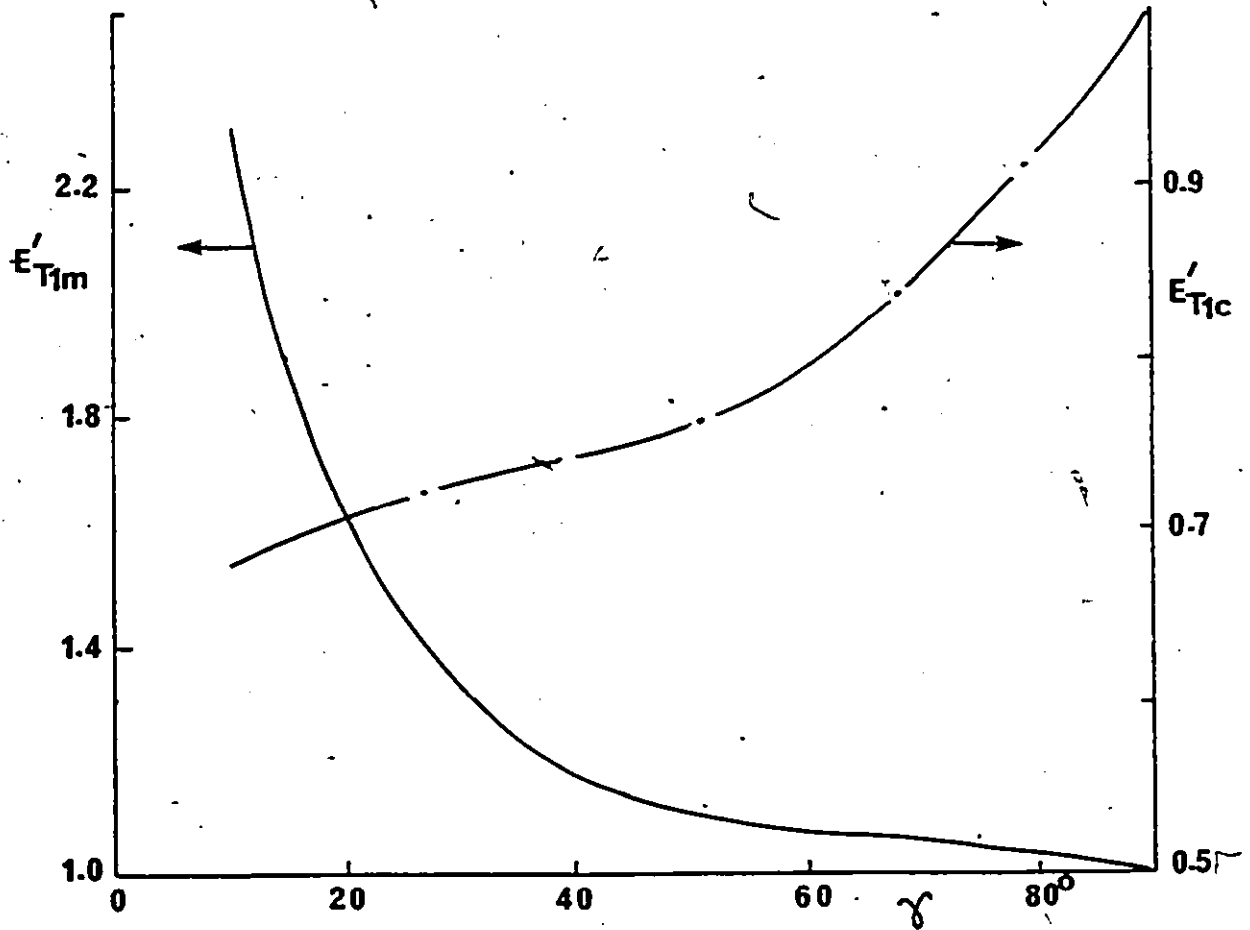
Figure 7.4: Total electric field at the cathode junction $E'T_1c$ and the maximum field $E'T_1m$ at locations P and Q of. Other conditions are as of Fig.7.2.

Table 7.2: $E't_lc$, $E'n_lc$, $E'T_lc$, $E't_lm$ and $E'T_lm$ as a function of γ (System A). $L = 40$ mm, $2R_0 = 40$ mm, $d/L = 0.2$ mm, $\epsilon_2 = 4.7$. $E't_lm$ and $E'T_lm$ are in locations P and Q of Fig.7.1, $E_{av} = V/L$.

γ	$\|E'_{nlc}\|$	E'_{tlc}	E'_{tlm}	E'_{Tlc}	E'_{Tim}
10	0.76	0.22	1.30	0.79	2.94
20	0.74	0.41	1.21	0.85	1.90
30	0.68	0.53	1.18	0.87	1.50
40	0.61	0.66	1.14	0.89	1.27
45	0.56	0.70	1.13	0.90	1.20
50	0.50	0.75	1.10	0.91	1.16
60	0.39	0.83	1.08	0.92	1.09
70	0.26	0.89	1.05	0.93	1.05
80	0.12	0.94	1.02	0.95	1.02
90	0	1.0	1.0	1.0	1.0

7.3.2 Effect of permittivity

Table 7.3 shows the dependence of the electric field components on the permittivity ϵ_2 of the insulating material placed in recessed electrodes of system A at a fixed recessed angle which is arbitrarily chosen to be 45°. It will be observed that with the exception of $E't_lm$ all the other fields increase as the permittivity of the insulator increases. $E'n_lc$ and $E'T_lc$ increase by 30% and 73%.

respectively when using a Porcelain spacer ($\varepsilon_2=9.0$) instead of Teflon ($\varepsilon_2=2.1$).

Table 7.3: $E't_1c$, $E'n_1c$, $E't_1m$, $E'T_1c$ and $E'T_1m$ as a function of ε_2 for "System A". L= 40 mm, $2R_0$= 40 mm, d= 5 mm, γ =45° and $Eav=V/L$.

ε_2	E'_{t1c}	$|E'_{n1c}|$	E'_{t1m}	E'_{T1c}	E'_{T1m}
2.1	0.34	0.50	1.12	0.60	1.12
3.2	0.52	0.50	1.10	0.72	1.14
4.7	0.69	0.52	1.08	0.86	1.15
5.8	0.74	0.57	1.07	0.93	1.18
9.0	0.81	0.65	1.06	1.04	1.24
30	0.95	0.78	1.04	1.23	1.36
50	0.98	0.81	1.04	1.27	1.38
80	0.99	0.83	1.04	1.29	1.40
100	1.0	0.84	1.04	1.30	1.40
1,000	1.02	0.85	1.03	1.33	1.42
12,000	1.03	0.86	1.03	1.34	1.43

7.3.3 Effect of the depth of recess d

The dependence of the electric field components on the recess depth d of Fig.7.1 (system A) for a Plexiglas ε_2= 3.2 and the recess angle γ = 45° is shown in Table 7.4. It will be observed that both $E't_1c$ and $E'T_1c$ decrease as d increases. Typically as d increases from 1 to 10 mm, $E'T_1c$

decreases by about 20%. The maxima in $E't_1m$ and $E'T_1m$ increase as d increases.

Table 7.4: $E't_1c$, $E'n_1c$, $E't_1m$, $E'T_1c$ and $E'T_1m$ as a function of depth d for "System A". $L= 40$ mm, $2R_0= 40$ mm, $\gamma =45°$, $\varepsilon_2=3.2$ and $r_1=1$ mm. Maximum occur at locations P and Q and $Eav=V/L$.

d,mm	E'_{t1c}	E'_{t1m}	$\lvert E'_{n1c} \rvert$	E'_{T1c}	E'_{T1m}
1	0.77	1.02	0.34	0.84	1.08
3	0.67	1.06	0.40	0.79	1.09
5	0.60	1.10	0.44	0.74	1.13
7	0.59	1.15	0.39	0.70	1.18
10	0.56	1.20	0.37	0.67	1.23

7.3.4 Effect of the length L

Table 7.5 shows the field components of a Plexiglas spacer ($\varepsilon_2 = 3.2$) placed between recessed electrodes for fixed d/L $=0.25$ and a recess angle $\gamma = 45°$. The spacer length is varied from 10 mm to 100 mm. It can be seen from Table 7.5 that $E't_1c$, $E'n_1c$ and $E'T_1c$ decrease as L increases. $E't_1c$ and $E'T_1c$ show a significant reductions

with increasing L. E^*t_1c and E^*T_1c decrease by about 49% and 42%, respectively as L increases from 10 mm to 100 mm. However, the maxima in both the E^*t_1m and E^*T_1m increase by 13% and 10%, respectively as L increases from 10 mm to 100 mm. In fact this finding is due to the combined effect of L and d.

Table 7.5: E^*t_1c, E^*n_1c, E^*t_1m, E^*T_1c and E^*T_1m as a function of length L for "System A". $2R_0$= 40 mm, d/L=0.25 mm, γ =45° and Eav=V/L.

L mm	E'_{t1c}	E'_{t1m}	E'_{n1c}	E'_{T1c}	E'_{T1m}
10	0.82	1.16	0.45	0.94	1.20
30	0.61	1.19	0.42	0.74	1.22
40	0.56	1.20	0.37	0.67	1.23
80	0.45	1.27	0.29	0.53	1.28
100	0.42	1.31	0.25	0.49	1.32

7.5   Effect of radius r (System B)

The field components at the cathode triple junctions of system B and the maxima in the normal, tangential and total fields as a function of the radius r for an epoxy spacer (ε_2=4.7) and a fixed depth d = 5 mm are shown in Table 7.6.

It can be seen from Table 7.6 that as r increases $E'n_1c$, and $E'T_1c$ decrease. A significant reduction in the field can be obtained by increasing the radius of the recess edge. Also $E'n_1m$, $E't_1m$ and $E'T_1m$, decrease as the radius r increases. $E'T_1c$ and $E'T_1m$ decrease by about 49% and 32%, respectively as r increases from 0.5 mm to 4 mm.

Table 7.6: $E'n_1c$, $E't_1c$ and $E'T_1c$ at point c as a function of r for "System B". $L=40$ mm, $2R_0=40$ mm, $\varepsilon_2=4.7$ and $d= 5$ mm. $Eav= V/(L-d)$.

r, mm	At point C			E'_{nlm}	E'_{tlm}	E'_{Tlm}
	E'_{nl}	E'_{tl}	E'_{Tl}			
0.5 —	4.76	0.87	4.84	4.75	2.34	4.83
1.0 _	4.30	0.33	4.31	4.56	1.84	4.73
1.5	4.00	0.24	4.01	4.49	1.49	4.65
2.0	3.70	0.23	3.72	4.38	1.25	4.47
2.5	3.55	0.27	3.56	4.35	1.05	4.41
4.0	2.45	0.34	2.48	3.25	0.91	3.29

7.3.6   Effect of the depth d (System B)

The dependence of the total field near the cathode junction (at point c) on the depth d in System B is shown in Fig. 7.5 as a function of the radius r. The total field $E \cdot T_{l}c$ is determined for d= 3, 5 and 10 mm using an epoxy spacer ($\varepsilon_2=4.7$). As can be seen from Fig. 7.5, $E \cdot T_{l}c$ decreases as r increases. Also it decreases as d decreases for a fixed value of r. A higher reduction in the field $E \cdot T_{l}c$ can be obtained the larger the value of r and the smaller the value of d. For practical applications d and r should be chosen to have reasonable values to satisfy the mechanical requirements of firmly holding the spacer as well as to minimize the local field at the cathode junction. The reduction in the field $E \cdot T_{l}c$ calculated for d =3 mm is 33% as r increases from 0.5 to 2.5 mm. However, the reduction is almost 44% at r= 2.5 mm when d decreases from 10 mm to 3 mm.
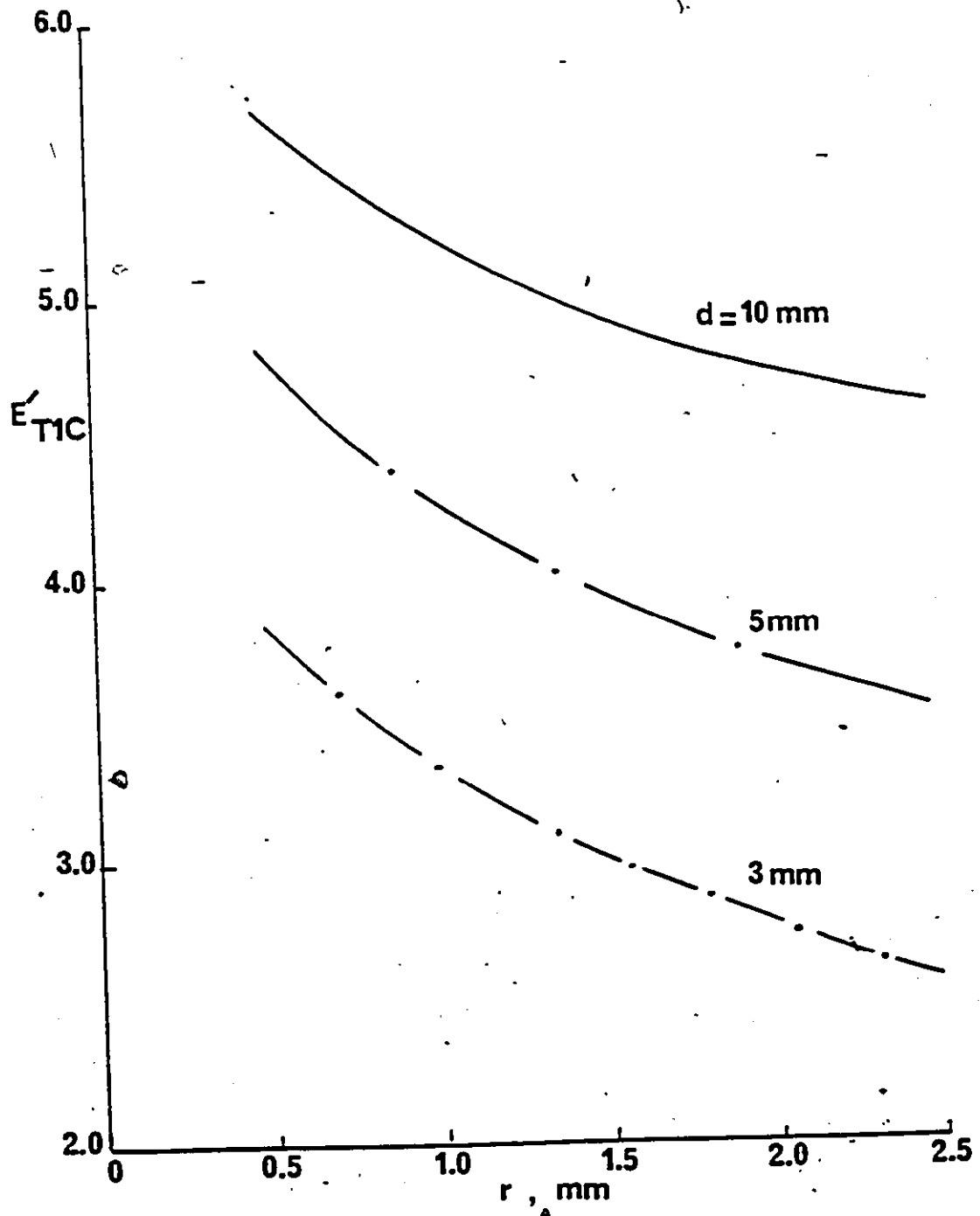
<u>Figure 7.5:</u> Total electric field at the cathode junction $E'T_1c$ of system B (Fig.7.1) as a function of r and for different value of d. ε_2= 4.7, L and R_0 are as of Fig.7.2 and E_{av}=V/(L-d).

7.3.7   Effect of metal insert

The effects on the field components of placing a metal insert in the bottom conductor of system B, at both the top and the bottom conductors of system B and of system C (Fig.7.1) are examined.   W and t are the diameter and the depth of all metal inserts, respectively.   Both W and t are varied to determine the effect of metal insert on the field distributions.

E^*t_1, E^*n_1 and E^*T_1 at both the cathode and the anode junctions for the different electrode geometries are calculated and shown in Table 7.7.   Also shown in Table 7.7 are the maxima in the field components E^*n_1m, E^*t_1m and E^*T_1m.   It can be seen from Table 7.7 that the presence of metal inserts at the cathode decreases the field components E^*t_1c, E^*n_1c and E^*T_1c, but there are slight increases in the field components E^*t_1a, E^*n_1a and E^*T_1a at the anode junction.   A significant reduction in the field at the cathode junction can be obtained by increasing the diameter and the thickness of the metal insert though the field at the anode junction slightly increases.   The effect of the presence of metal inserts at both anode and cathode are also shown in Table 7.7.   It will be observed that the metal inserts have strong influence on the field components at the anode and the cathode junctions (Table 7.7, configurations 8 and 9). In order to attain a reduction of the electric field at the cathode and the anode junctions the spacer- conductor

geometry of system C is used. A concave shape of the spacer surface at the anode junction with a metal insert at the cathode (Fig.7.1, system C) helps to reduce the electric field significantly at both electrode junctions.

The total field $E^.T$, along the insulator gas interface for the different spacer conductor configurations (1,5,9,10,14, described in Table 7.7) is presented in Fig.7.6. It will be observed that the lowest field value at the cathode can be attained by using configuration 5, while the lowest value at the anode junction can be obtained by using configuration 9. As can be seen configuration 14 has the advantage of reducing the field at both the cathode and the anode junctions.

Table 7.7. E'_{nl}, E'_{tl} and E'_{Tl} at both triple junctions for different electrode geometrics. L=40 mm; $2R_0$=40 mm; d/L=0.25; r/d=0.5 ; ε_2=47; θ=45; and R=14.14 mm. E_{av}=V/(L-d).

Configuration	Insulator-conductor geometry	Cathode			Anode			Maximum		
		E'_{nlc}	E'_{tlc}	E'_{Tlc}	E'_{nla}	E'_{tla}	E'_{Tla}	E'_{nlm}	E'_{tlm}	E'_{Tlm}
(1)	System B without insert	2.48	0.26	2.50	0.006	0.86	0.86	3.55	0.88	3.58
	System B with insert at the cathode only									
(2)	W=10 mm; t=5 mm	1.70	0.27	1.72	0.004	0.90	0.90	3.0.	0.90	3.03
(3)	W=10 mm; t=10 mm	1.23	0.19	1.24	0.002	0.95	0.95	2.19	0.95	2.21
(4)	W=15 mm; t=5 mm	1.30	0.20	1.33	0.005	0.91	0.91	2.4	0.91	2.44
(5)	W=15 mm; t=10 mm	0.50	0.07	0.50	0.004	0.98	0.98	0.93	0.98	0.98
	System B with insert at both electrodes									
(6)	W=10 mm; t=5 mm	1.83	0.29	1.85	0.02	0.73	0.73	3.22	0.95	3.26
(7)	W=10 mm; t=10 mm	1.45	0.22	1.47	0.02	0.63	0.63	2.59	1.03	2.62
(8)	W=15 mm; t=5 mm	1.48	0.23	1.50	0.10	0.33	0.34	2.72	1.01	2.76
(9)	W=15 mm; t=10 mm	0.66	0.09	0.67	0.04	0.26	0.26	1.25	1.26	1.34
(10)	System C θ=45°	2.40	0.82	2.54	0.55	0.27	0.61	2.95	0.98	3.06
	System C with insert at cathode									
(11)	W=10 mm; t=5 mm	2.07	0.70	2.20	0.56	0.28	0.62	2.56	1.00	2.66
(12)	W=10 mm; t=10 mm	1.52	0.52	1.60	0.58	0.29	0.64	1.88	1.05	1.96
(13)	W=15 mm; t=5 mm	1.66	0.58	1.76	0.56	0.28	0.62	2.07	1.01	2.16
(14)	W=15 mm; t=10 mm	0.64	0.22	0.68	0.59	0.30	0.66	0.82	1.09	1.11
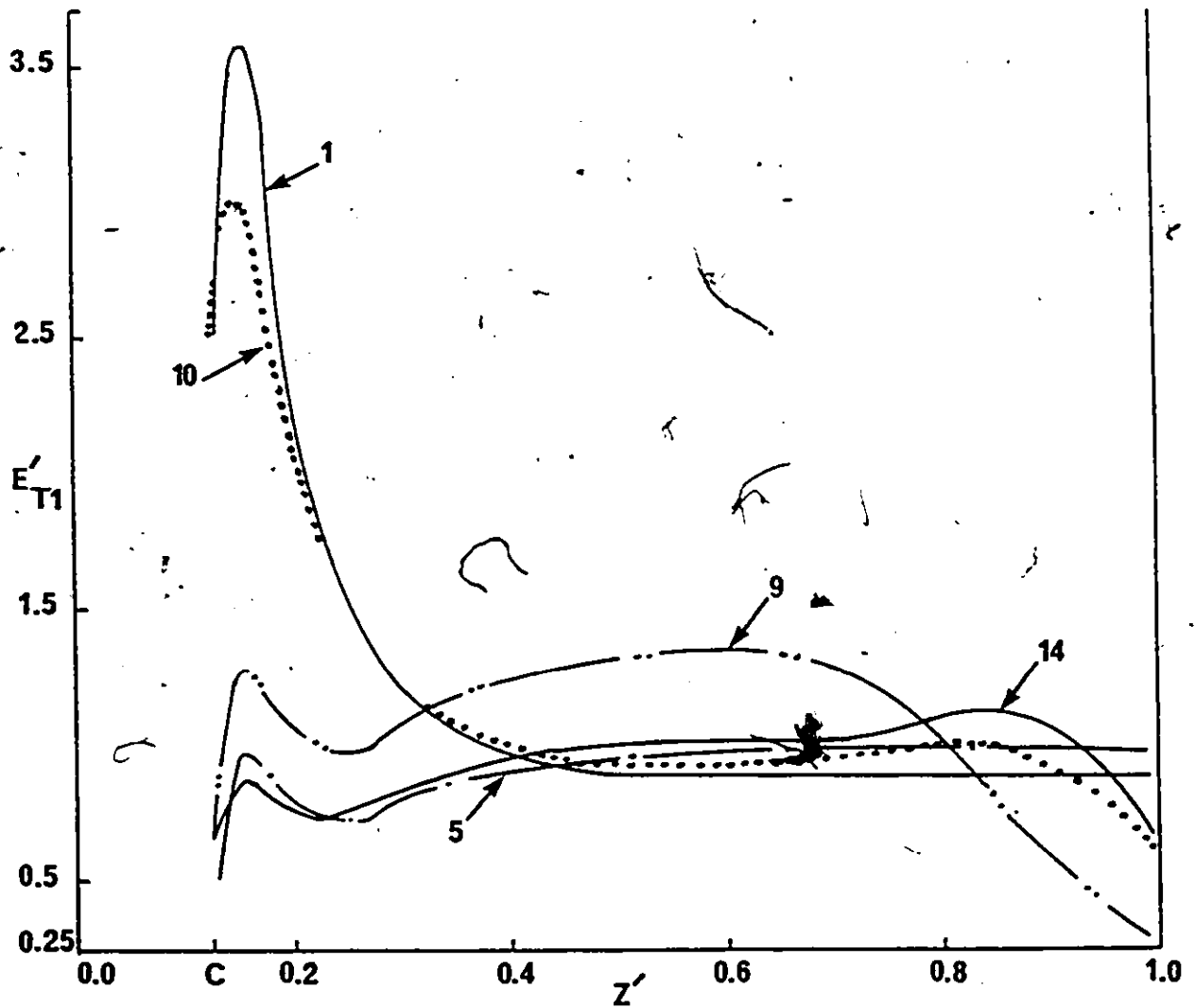
Figure 7.6: Total electric field $E'T_1$ distribution along the insulator surface and for different spacer-electrode configurations. $L = 40$ mm, $2B_0 = 40$ mm, $\varepsilon_2 = 4.7$. Curve 1, system B; curve 5, system B with insert ($W = 15$ mm , $t = 10$ mm) at the cathode only; curve 9, inserts at both electrodes ($W = 15$ mm, $t = 10$ mm); curve 10, system C ($\theta = 45°$, $R = 14.14$ mm); curve 14, system C with inserts at cathode only ($W = 15$ mm, $t = 10$ mm). Number of curves refer to geometries in Table 7.7.

7.3.8 Effect of the angle γ (System D)

In system D, the curvature of the cathode is a part of a circle which is tangential to the incline of the electrode and the spacer surface. The relation between the radius of curvature r and the angle γ is, $f = r \tan\left(\gamma/2\right)$.

E^*t_1c, E^*n_1c and E^*T_1c are calculated at the triple junction for a glass-ceramic spacer ($\epsilon_2 = 5.8$) of system D and shown in Table 7.8. It will be observed that as γ increases, both E^*n_1c and E^*T_1c decrease and they show a marked dependence on γ. The reduction in E^*n_1c and E^*T_1c is almost 53% and 35%, respectively when using $\gamma = 90°$ instead of 20°. But the tangential field E^*t_1c increases as γ increases. It increases by about 4 times at $\gamma = 90°$ than that at $\gamma = 10°$. For the case of $\gamma = 90°$, the small radius of curvature (r=1 mm) is responsible for the high field components at the triple junction.

The total electric field distribution along the spacer interface of a glass-ceramic spacer (system D) for various angles γ is shown in Fig.7.7. The spacer length is 40 mm and the diameter $2R_0 = 40$ mm. It can be seen from Fig.7.7 that E^*T_1m occurs at $\gamma = 10°$. For larger γ the highest field E^*T_1m occurs near the cathode junction. The total field E^*T_1 decreases as the axial distance increases away from the cathode junction.

Fig.7.8 shows the effect of the angle γ on E^*T_1c calculated at location c for system D (Fig.7.1). It can be

Table 7.3: $E'n_lc$, $E't_lc$ and $E'T_lc$ at point c as a function of for "System D". L= 40 mm, $2R_0$ = 40 mm, ϵ_2= 5.8 and d/L=0.25 mm, d_1/d=0.5 and f/d_1=0.2 , ϵav= V/(L-d).

γ	T'_{tlc}	E'_{nlc}	E'_{Tlc}
10	0.40	3.42	3.45
20	0.74	3.46	3.53
30	0.98	3.16	3.30
40	1.15	2.86	3.08
50	1.29	2.57	2.88
60	1.39	2.30	2.70
70	1.49	2.06	2.54
80	1.59	1.82	2.42
90	1.66	1.62	2.30

seen that $E'T_lc$ decreases as γ increases. Also for a fixed γ the total field decreases as f (or r) increases. Therefore to reduce the electric field γ should be chosen as close to 90° as possible and f should be large but within a suitable range values depending on the system dimension. For γ =90° the curvature is formed using a quarter of a circle and
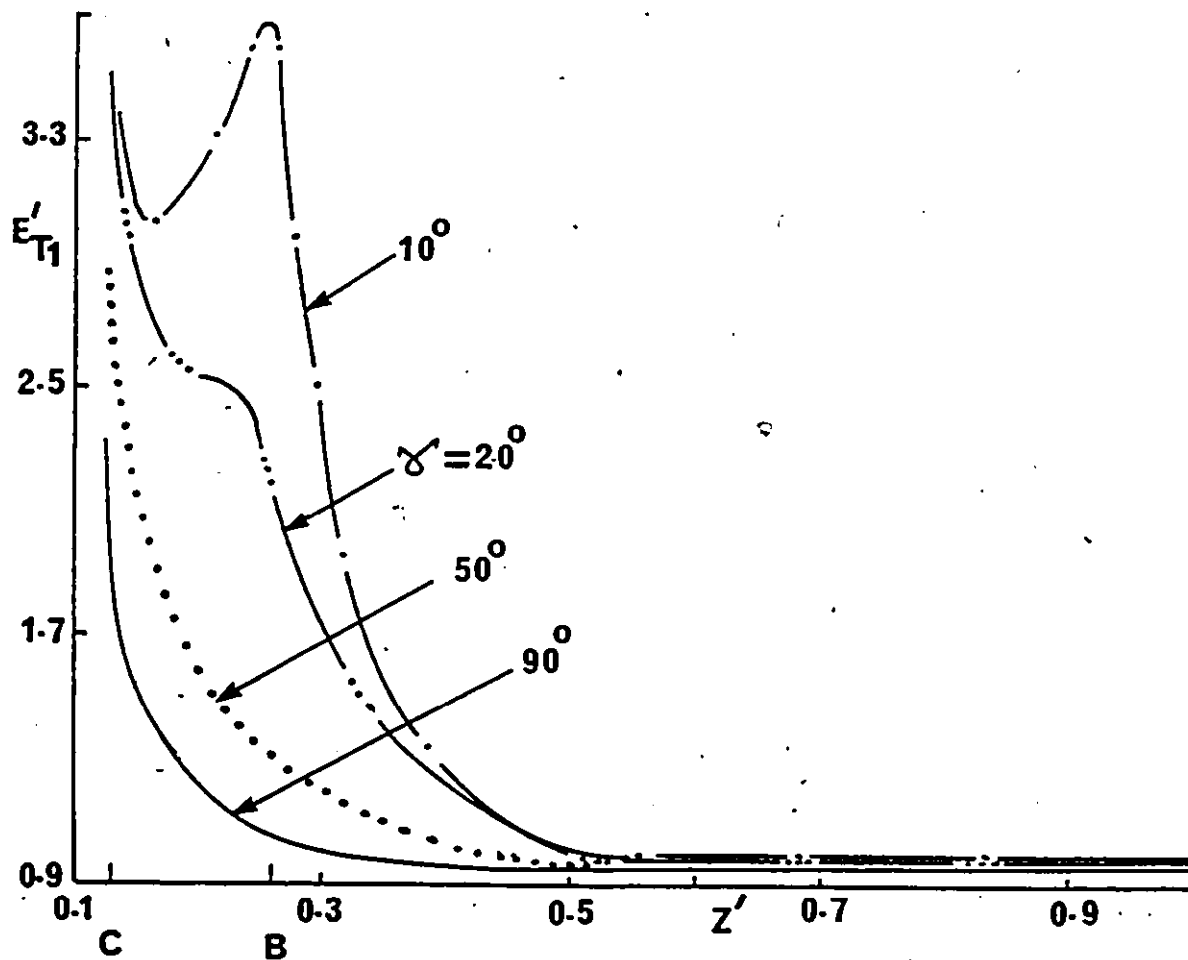
Figure 7.7: Total electric field $E'T_1$ distribution along the interface of a glass-ceramic spacer System "D" for different angle. $L = 40$ mm, $\varepsilon_2 = 5.9$, $2R_0 = 40$ mm, $d/L = 0.25$, $d_1/d=0.5$, $f/d_1=0.2$, $r_1=1$ mm and $E_{av} = V/(L-d)$.

therefore $r_1 = r$. However, it should be remembered that the field at the triple junction is higher than for some of the other profiles investigated in this work and therefore this is not an attractive profile. The purpose of these calculations is primarily to investigate the effect of the inevitable curvature which is introduced when the sharp surfaces on the electrode are rounded to give a smooth finish.
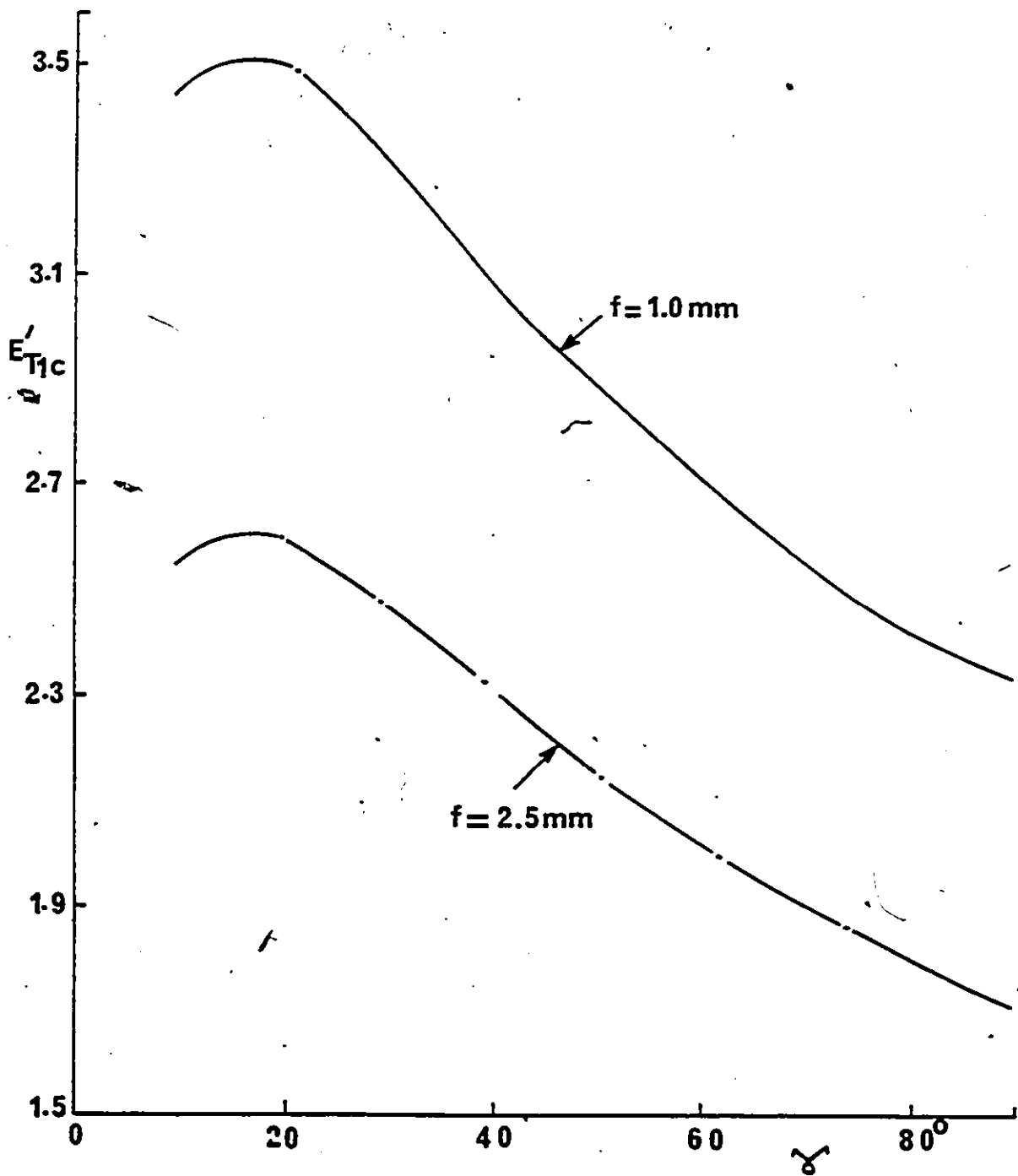
Figure 7.8: Total electric field $E^{\bullet}T_{1}c$ at the triple cathode junction as a function of γ for 'system D'. $L = 40$ mm, $\varepsilon_2 = 5.8$, $2R_0 = 40$ mm, $d/L = 0.25$ and $d_1/d = 0.5$, $r_1 = 1$ mm.

7.4 Effect of Recessed Angle on the Flashover Voltage

Measurements

The flashover voltage of an epoxy spacer placed between recessed electrodes has been measured. The recessed angle is varied in the range from 20° to 75°.
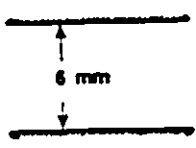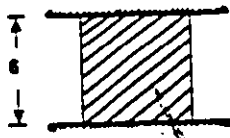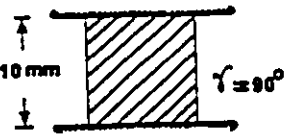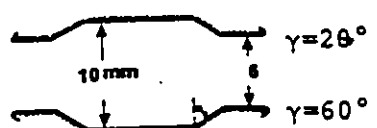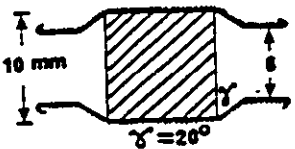
Table 7.9 shows the flashover voltage in SF_6 and in N_2 and at different pressures. It can be seen that the flashover voltage of a cylindrical spacer is lower than the breakdown of the gas by itself. It will be observed that the breakdown voltage of SF_6 and of N_2 when using recessed electrodes with a gap distance of L=10 mm and a recess depth of d= 2 mm (for γ =20 and 60°) is close (within ± 3%) to the breakdown voltage of SF_6 and of N_2 under uniform field condition with a gap distance of 6 mm between the electrodes. The flashover voltage of cylindrical spacers placed in recessed electrodes for γ =20, 45, 60 and 75° is measured and compared with γ =90° (right angle cylindrical spacer) with gap lengths of 6 mm and 10 mm. It has been found that the efficiency of the spacer can be increased to 98% at 0.2 MPa of SF_6 and to 100% at 0.6 MPa of N_2 using recessed electrodes with γ =60° (Table 7.9).

ET_1c is responsible for the emission of electrons from the cathode by the Fowler-Nordheim field tunnelling process since the electric field there is high. ET_1m which occurs at a location near the cathode causes an exponential growth in the number of electrons. Therefore in the range γ =5-20° a

lower flashover voltage than for the case without recesses is obtained because a higher number of electrons are produced in the gas due to the high ET_1m values (Table 7.2). As γ is increased to and above 45° ET_1m decreases giving a reduced ionization growth, despite the availability of more initiatory electrons with the slightly higher ET_1c. Therefore higher withstand voltage should be obtained with lower ET_1m at 60°. As γ is increased further ET_1c increases much more while ET_1m changes only slightly hence the flashover should decrease again as has been observed experimentally (Table 7.9).

Table 7.9: ac (60 Hz peak) flashover voltage for different conductor- spacer geometries in SF_6 and N_2 for an epoxy spacer. $2R_0=20mm$ and $d= 2$ mm.

Conductor-spacer geometry	F.O.V (kv) in SF_6		F.O.V. (kv) in N_2	
	P=0.1MPa	P=0.2MPa	P =0.3MPA	P=0.6MPa
6 mm	61.0	112.0	51.0	95.0
6	51.0	85	47.0	81.0
10 mm, $\gamma=90°$	75	135	65.0	110.0
10 mm, $\gamma=20°$	58.0	107.5	54.0	96.0
$\gamma=60°$	59.0	110.0	54.0	96.0
10 mm, $\gamma=20°$	47	71.0	49.5	78.0
$\gamma = 45°$	56.5	-99.0	51.0	87.5
$\gamma = 60°$	58	105	54	95
$\gamma = 75°$	55	100.9	52.5	86.5

7.5 Comparison of ac (60 Hz) Flashover Voltage of Four

· Spacer Geometries ·

The crest value of the ac (60 Hz) flashover voltage is measured in four spacer–conductor geometries: 1. cylindrical spacer between planar electrodes, 2. cylindrical spacer between recessed electrodes, 3. cylindrical spacer with metal inserts in both electrodes and 4. a concave spacer between planar electrodes, in SF_6 and in N_2. The breakdown of the gas by itself is also measured for comparison. The gas pressure is restricted to 0.2 MPa in SF_6 due to the limitations of the ac supply voltage and to 0.7 MPa in N_2.

Fig.7.9 shows the flashover voltage of Plexiglas spacers having a length of L= 10 mm in SF_6. It can be seen from Fig.7.9 that the flashover voltage of the cylindrical spacer (curve 4) is the lowest and this can be increased using any one of the profiles examined in this work. It will be observed that the spacer placed in recessed electrodes (curve 1) and the spacer with metal inserts (curve 2, t= 2.5 mm and W =10 mm) have a higher flashover voltage than that of profiles 3 and 4. Both profiles 1 and 2 have almost the same flashover strength. The efficiency can be increased from 81% using profile 4 to 91.5% for profile 1, 90% for profile 2 and 87% for profile 3 at 0.2 MPa of SF_6.

The ac flashover characteristics in N_2 are shown in Fig.7.10. It will be observed that the withstand voltage of a spacer between recessed electrodes and a concave spacer
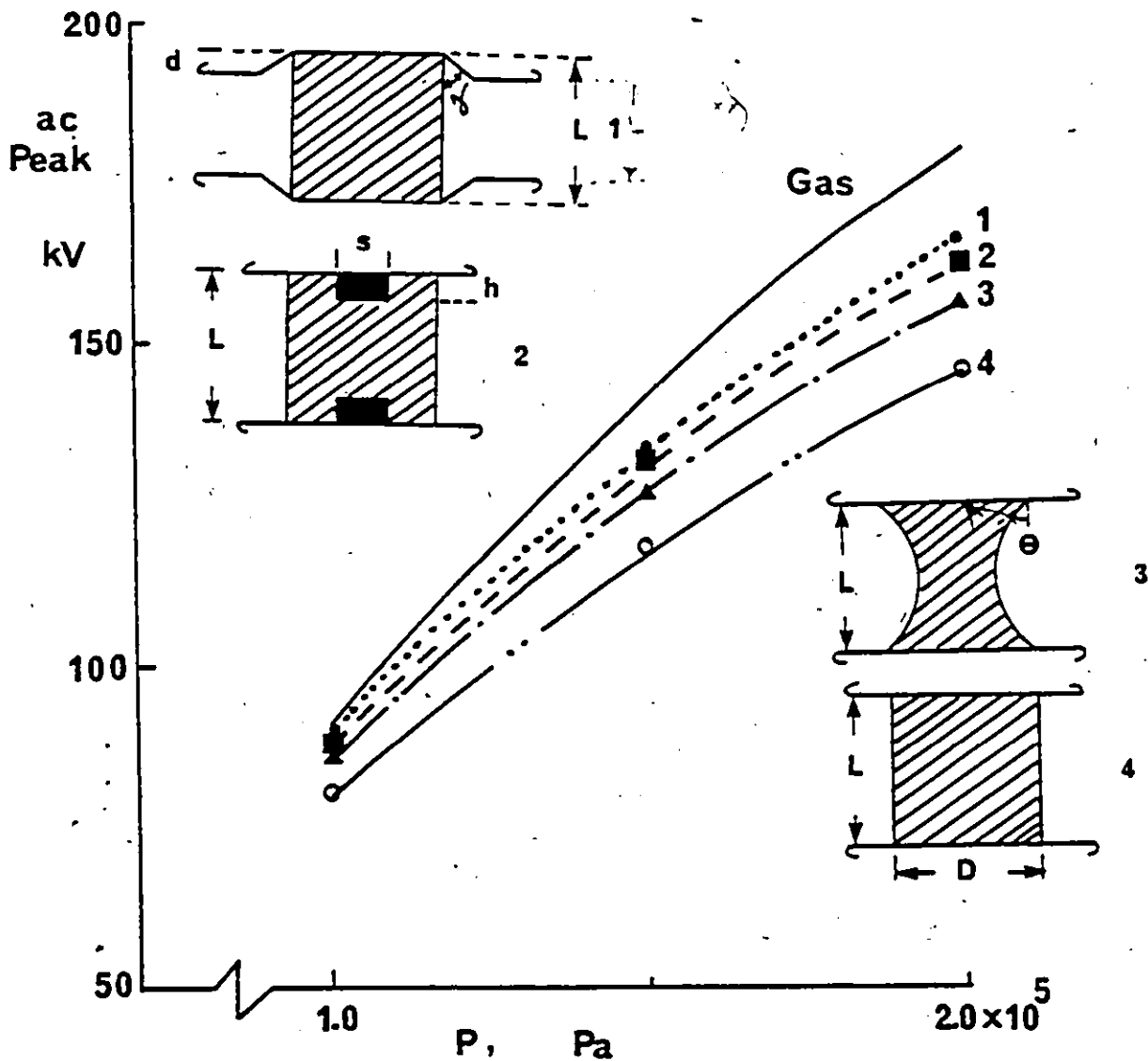
Figure 7.9: ac crest (60 Hz) flashover characteristic of four different insulator- conductor geometries in SF_6. Conditions: L= 10 mm, D=2R_0= 20 mm, d= 2 mm, γ = 60°, t=2.5 mm, W= 10 mm, θ=45°and ϵ_2= 3.2.
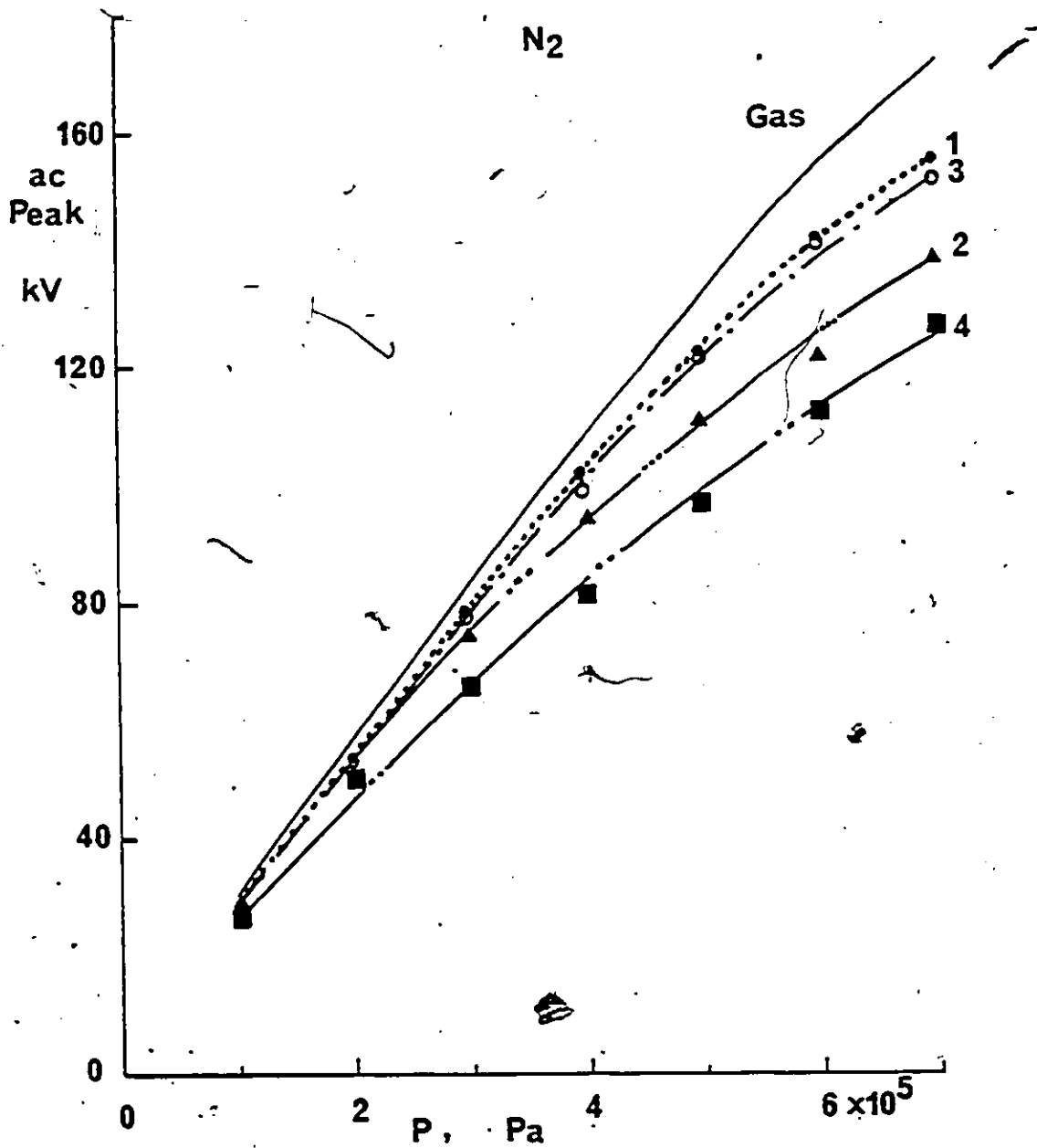
Figure 7.10: ac crest (60 Hz) flashover characteristic of four different spacer- conductor geometries in N_2. Conditions are as for Fig.7.10.

are higher than the others. The efficiency is improved from 74% when using a cylindrical spacer (profile 4) to 90% with recessed electrodes (profile 1) and 89% with a concave spacer (profile 2) at 0.7 MPa of N_2.

Chapter VIII

EFFECT OF THE CONTACT AREA AND THE NUMBER OF

PARALLEL SPACERS ON THE FLASHOVER VOLTAGE

8.1 Introduction

In practical applications, the design of an insulation
system often requires multiple spacers in parallel. It has
been reported that the electrical strength decreases with
increasing the number of parallel insulators [112] and the
diameter of a single spacer in vacuum [115], and with
increasing the area of electrodes in SF_6 [113,114].

The decrease of electrical strength has been attributed
to increasing the number of weak points in the larger
system, resulting in a higher probability of the occurrence
of an electrical breakdown [105]. Alternatively it was
attributed to the larger stored energy in the electrostatic
field with the larger capacitance [116,117].

There is a scarcity of data on the effect of varying the
number of parallel spacers and the spacer diameter and
therefore the contact area with the electrodes on the
surface flashover in high pressures of SF_6 and N_2. In the
present chapter, the dependence of the dc and ac flashover
voltages on the number of spacers placed in parallel and on
the diameter of a single spacer is reported in SF_6 and N_2
over a wide range of gas pressures.

8.2   Results And Discussion

8.2.1   Effect of number of parallel spacers

The dc surface flashover voltage of multiple Plexiglas spacers, each having a diameter of 10 mm and a length of 10 mm is determined in SF_6 and N_2 in a uniform field. The gas pressure is $(1-3) \times 10^5$ Pa in SF_6 and $(1-7) \times 10^5$ Pa in nitrogen. The number of parallel spacers n is varied in the range from 1 to 5.

Fig.8.1 shows the dependence of the surface flashover voltage on the number of spacers placed in parallel in SF_6 and for different gas pressures. It can be observed that as n increases, the surface flashover voltage decreases, and the dependence becomes more pronounced at higher gas pressures. Typically when the number of spacers is increased from 1 to 5, the dc surface flashover in SF_6 decreases by about 12% at 0.3 MPa.

The dependence of the surface flashover voltage in N_2 on n is shown in Fig.8.2, for different gas pressures. It can be observed that the surface flashover decreases as n increases. Typically the flashover voltage decreases with increasing n from 1 to 5 by about 12% at 0.5 MPa of N_2 .

The reduction in the breakdown voltage of the system can be explained in statistical terms. Increasing the contact area and the number of spacers placed in parallel will increase the probability of finding a "weak link" in the system and hence increase the probability of the breakdown at lower voltage [116,117].
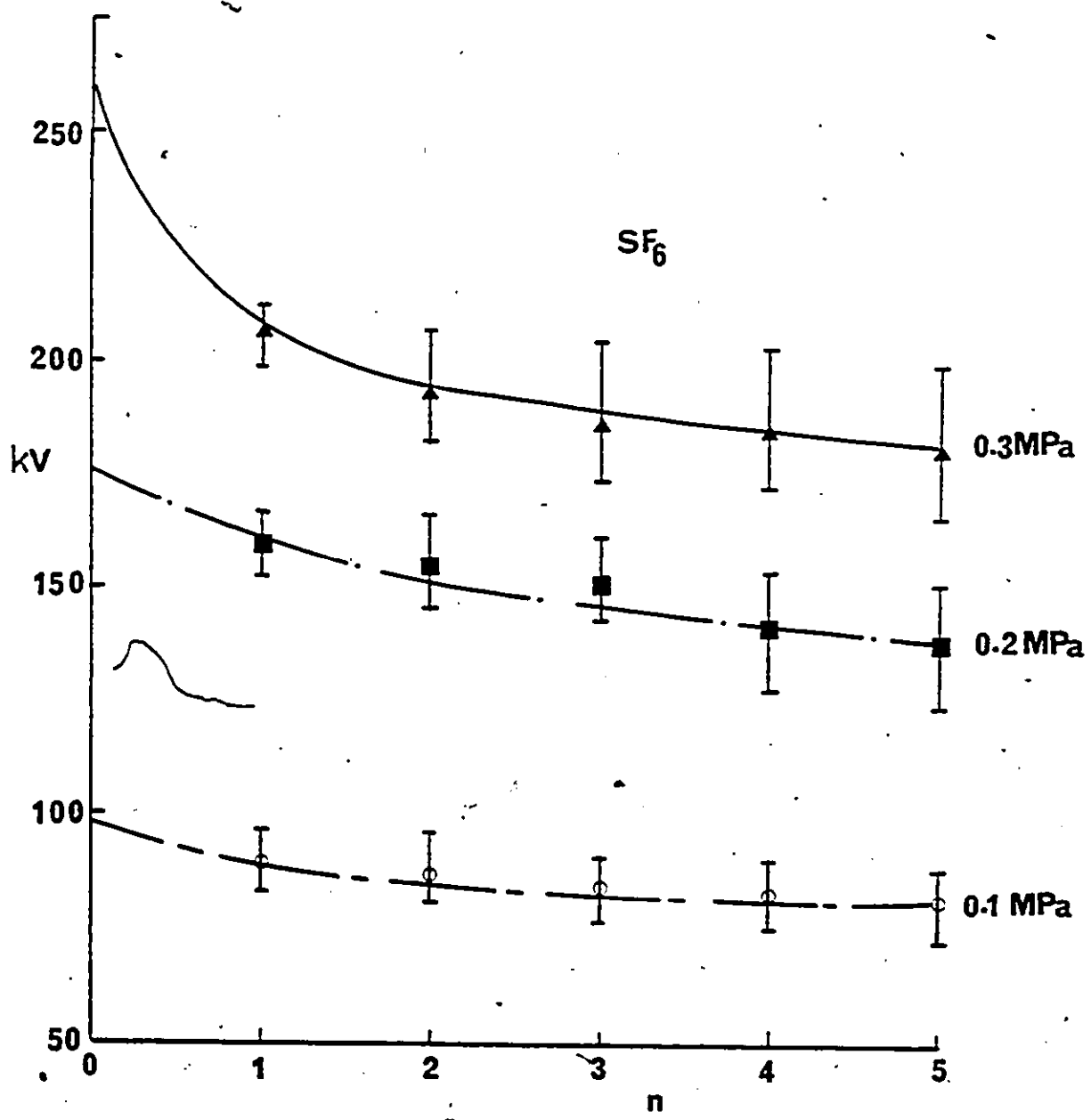
Figure 8.1: dc surface flashover voltage in SF₆ as a function of number of spacers placed in parallel. Material, Plexiglas, $\varepsilon_2 = 3.2$, diameter, 10 mm, length = 10 mm. n = 0 gas breakdown.
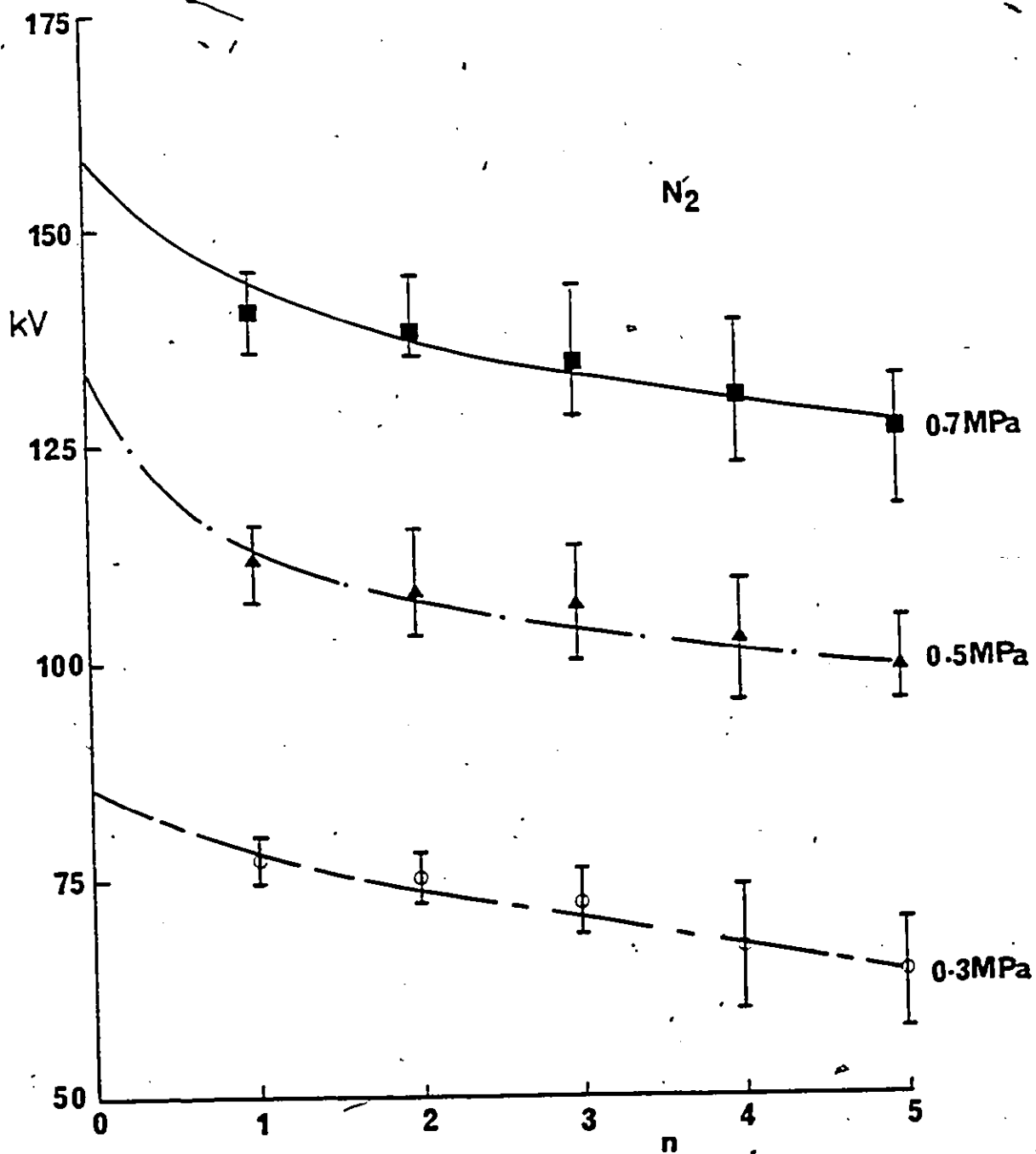
Figure 8.2: dc surface flashover voltage in N_2 as a function of number of spacers placed in parallel. Conditions are as for Fig.8.1.

The probability Pi(V) of the surface flashover of a single insulator is determined by the applied voltage V, where V is a certain applied voltage before flashover.

For n insulators placed in parallel in the system the probability of the flashover Pf(V) at the same voltage V is given by [112].

$$Pf(V)=1- \prod_{i=1}^{n} [1- Pi(V)] \qquad (8.1)$$

If we assume that Pi(V) is the same for all insulators then,

$$Pf(V)=1 - [1- Pi(V)]^{n} \qquad (8.2)$$

when Pi(V) << 1/n, the equation (8.2) becomes,

$$Pf(V) \simeq n \, Pi(V) \qquad (8.3)$$

Equation 8.3 shows that the probability of the surface flashover increases with increasing the number of spacers in parallel. The higher probability of the occurrence of flashover leads to lower insulating strength of the complete system as is observed here.

Table 8.1 shows the variation in the contact area, the total capacitance of the gap and the energy stored in the system $W=(1/2) CV^2$ for different number of parallel spacers. C is the total capacitance of the gap and V is the breakdown voltage. It can be seen from Table 8.1 that increasing the number of spacers increases slightly the total capacitance of the gap. The stored energy just prior to the breakdown of

the gap decreases as the number of spacers increases in SF_6 and N_2. This suggests that the reason for the lower breakdown voltage can be interpreted by the "weak link" in the system as the stored energy hypothesis requires a higher available energy in the gap to yield a lower breakdown voltage.

Fig.8.3 shows the effect of the number of parallel spacers on the efficiency of the system in SF_6 and N_2. It can be observed that the efficiency of the total system decreases as the number of spacers increases. It decreases from 0.88 for n = 1 in 0.7 Mpa of N_2 to 0.80 with 5 spacers. In 0.3 Mpa of SF_6 it decreases from 0.79 for n=1 to 0.69 for n= 5.

Table 8.1: Dependence of the surface flashover voltage on the contact area of the spacers, with one electrode, the total capacitance C and the energy stored (W) in the gap just prior to flashover. Diameter =10 mm, $\varepsilon_z \approx 3.2$.

No. of spacer in parallel n	Contact area with one electrode (mm^2)	Total Capacitance (P.F)	$P = 0.3$ MPa of SF_6 V(kV)	W(J)	$P = 0.7$ MPa of N_2 V(kV)	W(J)
1	78.5	9.33	209.0	0.2038	141.0	0.091
2	157.0	9.48	193.5	0.1774	137.5	0.0896
3	235.5	9.63	187.5	0.1692	134.5	0.0871
4	314.0	9.78	182.5	0.1628	130.0	0.0826
5	392.5	9.94	180.0	0.1610	127.5	0.0796
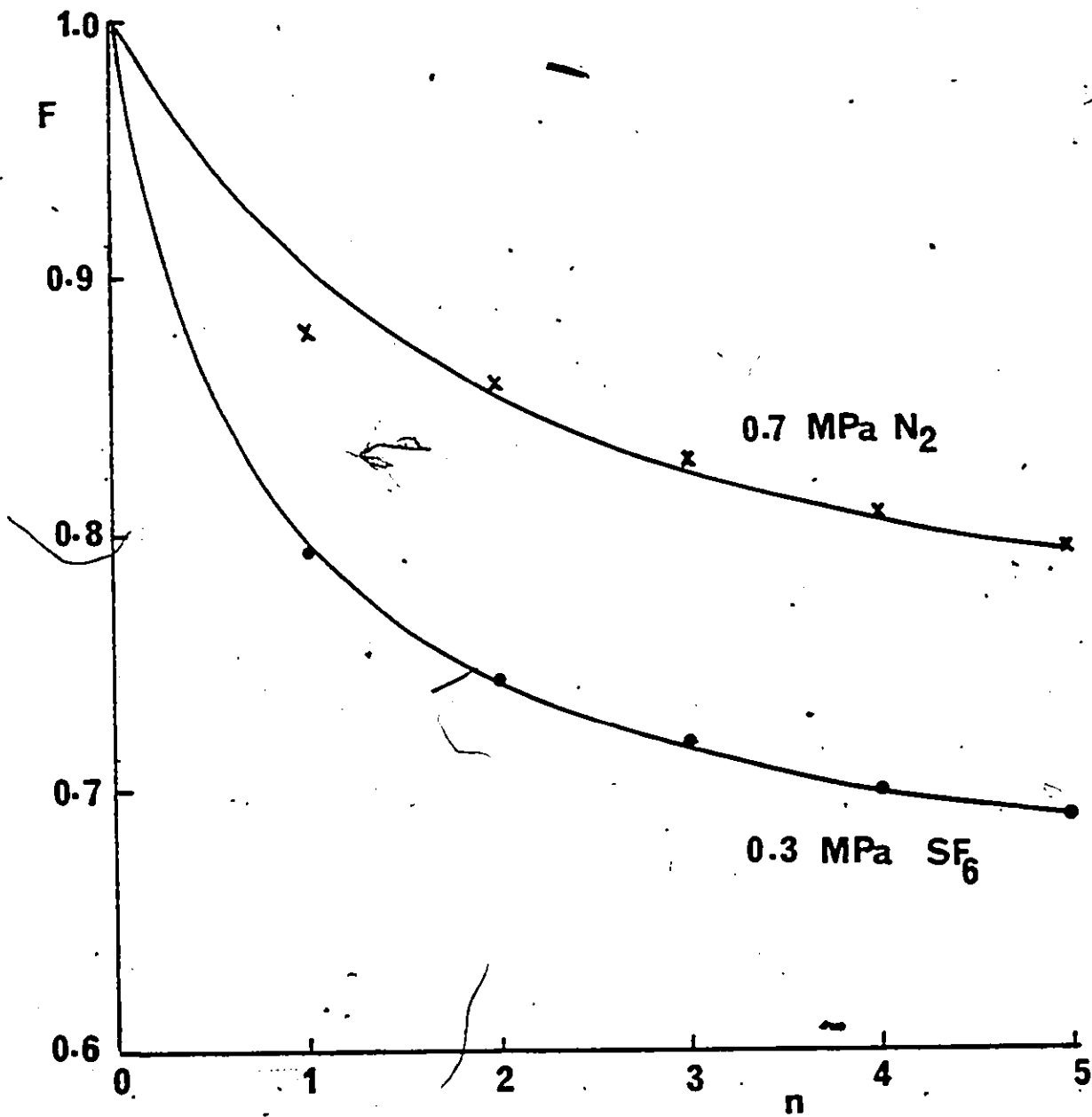
Figure 8.3: Flashover voltage ratio F as a function of number of parallel spacers. Other conditions are as of Fig.8.1.

8.2.2   Effect of varying diameter of spacer

The dc surface flashover voltage of a single Plexiglas spacer having a length of 10 mm and different diameters is measured in SF₆ and N₂. The diameter of the spacer is varied in the range from 5 mm to 50 mm.

Figs.8.4 and 8.5 show the surface flashover voltage in SF₆ and N₂, respectively, as a function of spacer diameter at different gas pressures. It can be observed that the surface flashover voltage decreases slightly up to 30 mm and the reduction becomes smaller at d > 30 mm (Table 8.2) for all gas pressures.

The dependence of the surface flashover voltage in SF₆ and N₂ on the contact area of the spacer (with one electrode), the total capacitance of the gap and the stored energy $W=(1/2)$ CV^2 is given in Table 8.2. It will be observed that the flashover voltage decreases as the contact area with the electrodes and the total capacitance of the system increase. The stored energy in the gap initially decreases with increasing diameter from 5 to 20 mm and then increases slightly thereafter. The observed decrease of the flashover voltage with increasing diameter of the spacer is such that it also follows the "weak link" hypothesis.

The effect of varying the spacer diameter on the spacer efficiency is presented in Fig.8.6. It will be observed that the efficiency of the spacer decreases as the diameter increases. In 0.3 Mpa of SF₆ it decreases from 85% for a
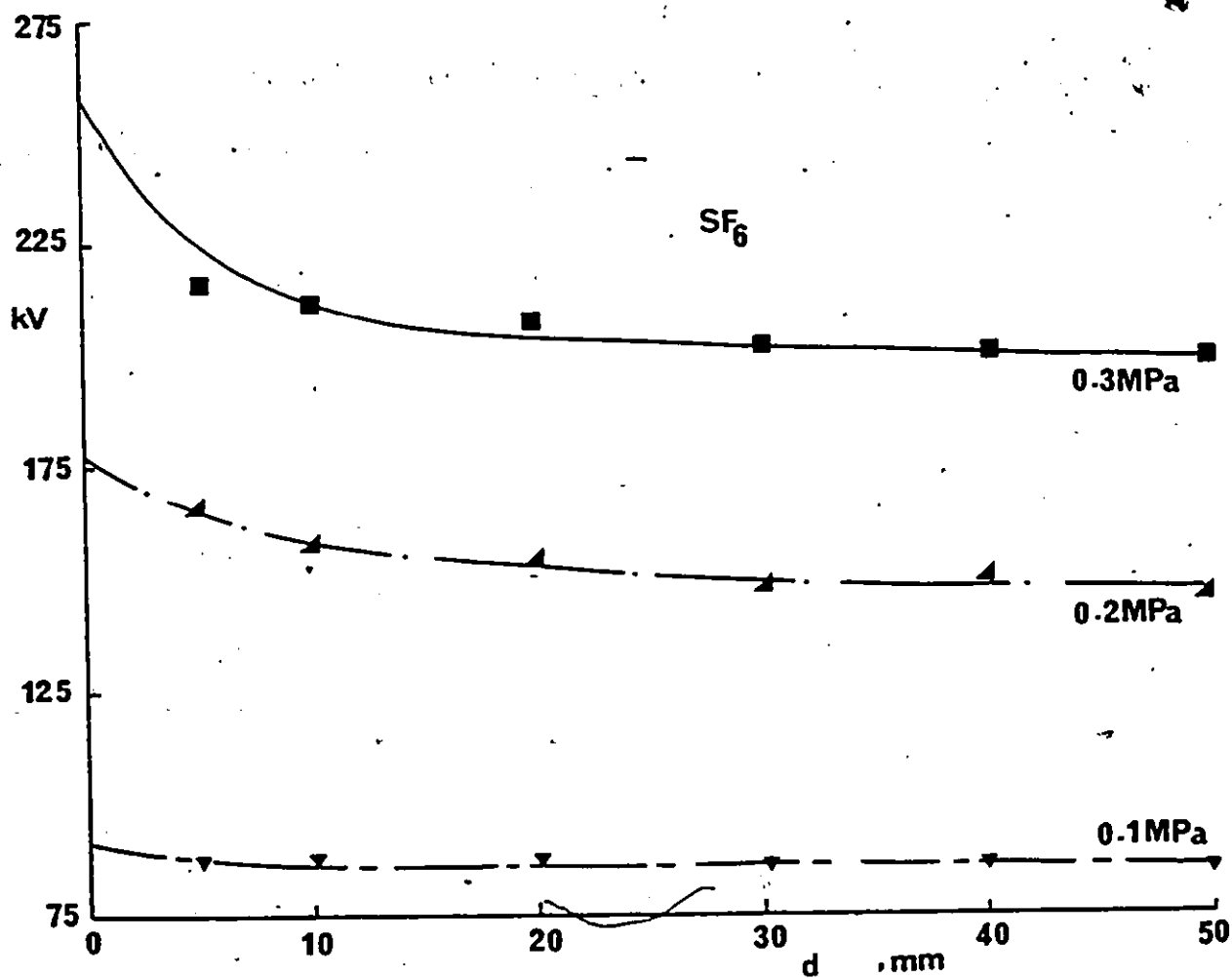
Figure 8.4: dc surface flashover voltage in SF$_6$ as a function of spacer diameter. Conditions are as for Fig.8.1.
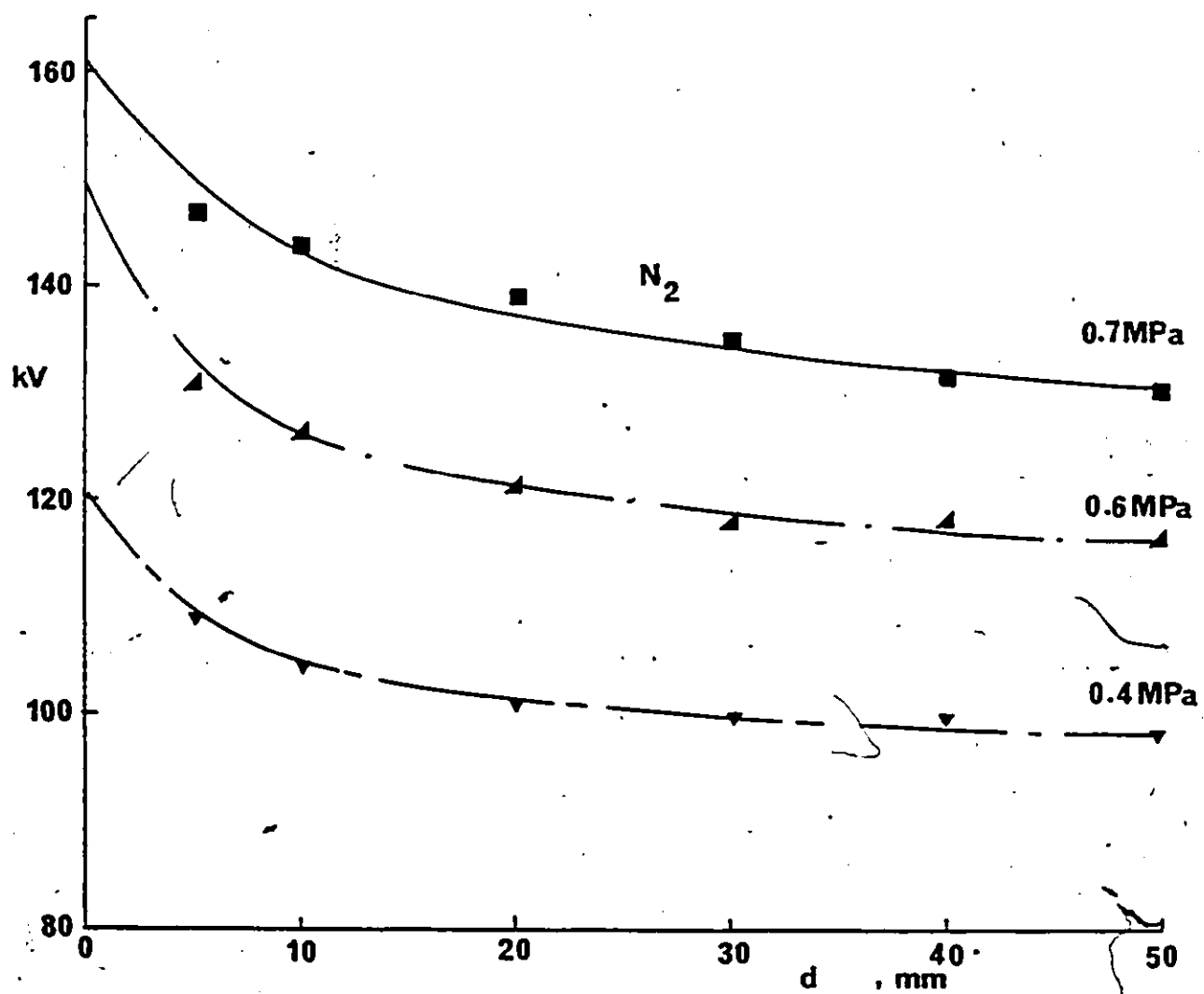
Figure 8.5: dc surface flashover voltage in N_2 as a function of spacer diameter. Conditions are as for Fig.8.1.

Table 8.2: Dependence of the surface flashover voltage on the contact area of spacer, the total capacitance of the gap C and the stored energy W in SF₆ and N₂. length of the spacer 10 mm.

Diameter of spacer (mm)	Contact area (mm^2)	Total Capacitance (P.F)	P = 0.3 MPa of SF$_6$		P = 0.7 MPa of N$_2$	
			V(kV)	W(J)	V(kV)	W(J)
5	19.6	9.2	216.0	0.2146	146.0	0.0980
10	78.5	9.3	210.0	0.2050	144.0	0.0964
20	314.2	9.8	208.0	0.2120	139.5	0.0954
30	706.9	10.5	203.0	0.2163	135.0	0.0956
40	1256.6	11.6	200.5	0.2331	131.0	0.0995
50	1963.5	13.0	198.0	0.2548	130.0	0.1098

spacer of 5 mm in diameter to 76% for a spacer of a 50 mm in diameter.

The ac flashover characteristics in SF_6 and N_2 using parallel spacers and spacers with different diameters are shown in Fig.8.7. It can be seen that the flashover voltage decreases as the number of parallel spacers or the diameter of the spacer increase. The reduction in the flashover voltage is higher when using parallel spacers than varying the diameter of the spacer for the same ratio of change. It decreases from 148 kV to 118 kV in 0.2 MPa of SF_6 and from 134 kV to 104 kV in 0.7 MPa of N_2 by using 5 spacers instead of 1. The coressponding values when using a single spacer with a diameter 10 mm and 50 mm are 148 kV and 133 kV in 0.2 MPa of SF_6 and 134 kV and 113 kV in 0.7MPa of N_2. It can be seen that the same behaviour is obtained in both dc and ac voltages and the explanation given for dc is also valid for ac.
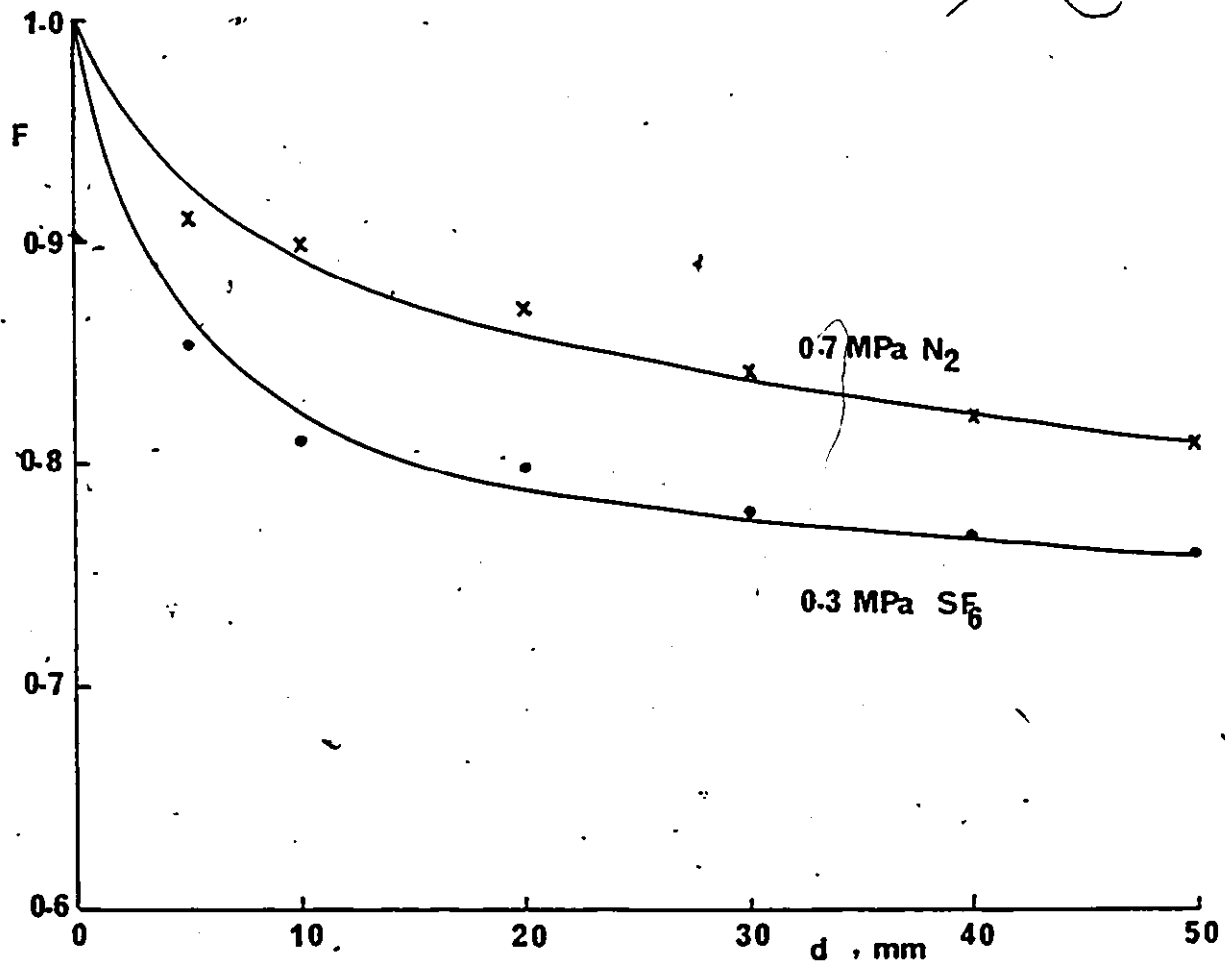
Figure 8.6: Flashover voltage ratio F as a function of insulator diameter in SF6 and N2. Conditions are as for Fig.8.1.

8.3   Effect of the Area of Spacer

The effect of the area of the flat end of the spacer on
the flashover voltage in SF_6 and N_2 when using multiple
spacers in parallel or when varying the diameter of spacer
is shown in Fig.8.8. It will be observed that the flashover
voltage decreases as the area increases. It will be seen
that a larger reduction in the flashover voltage is found
for increasing the area when using parallel spacers than
with increasing the diameter. It is clear from Fig.8.8 that
the effect of the flat end area on the flashover voltage of
the system is important but it is difficult to rely on it to
explain the phenomena.
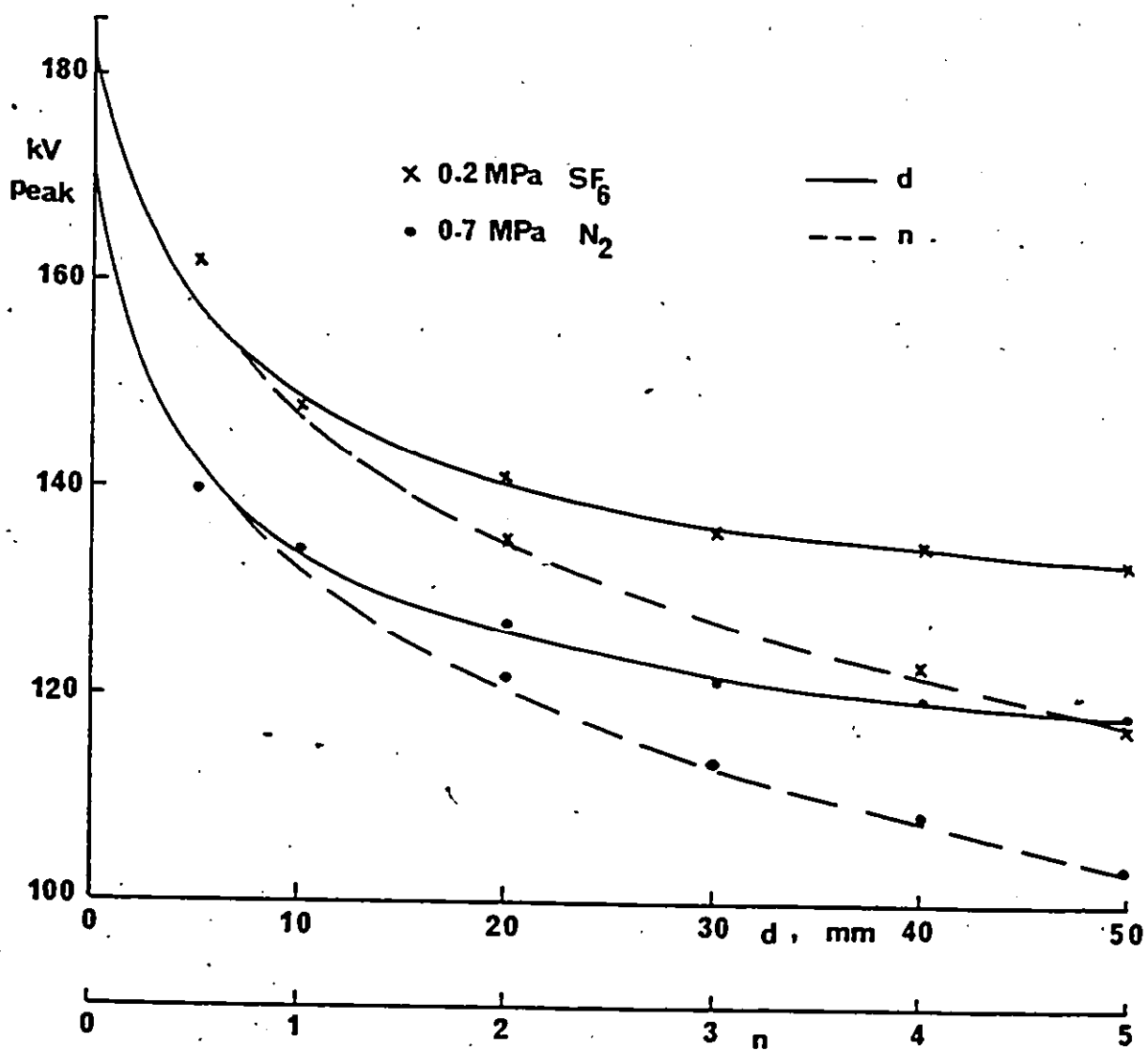
Figure 8.7: ac crest (60 Hz) flashover voltage as a function of number of parallel spacers n and spacer diameter in SF6 and N2. Conditions are as for Fig.8.1.
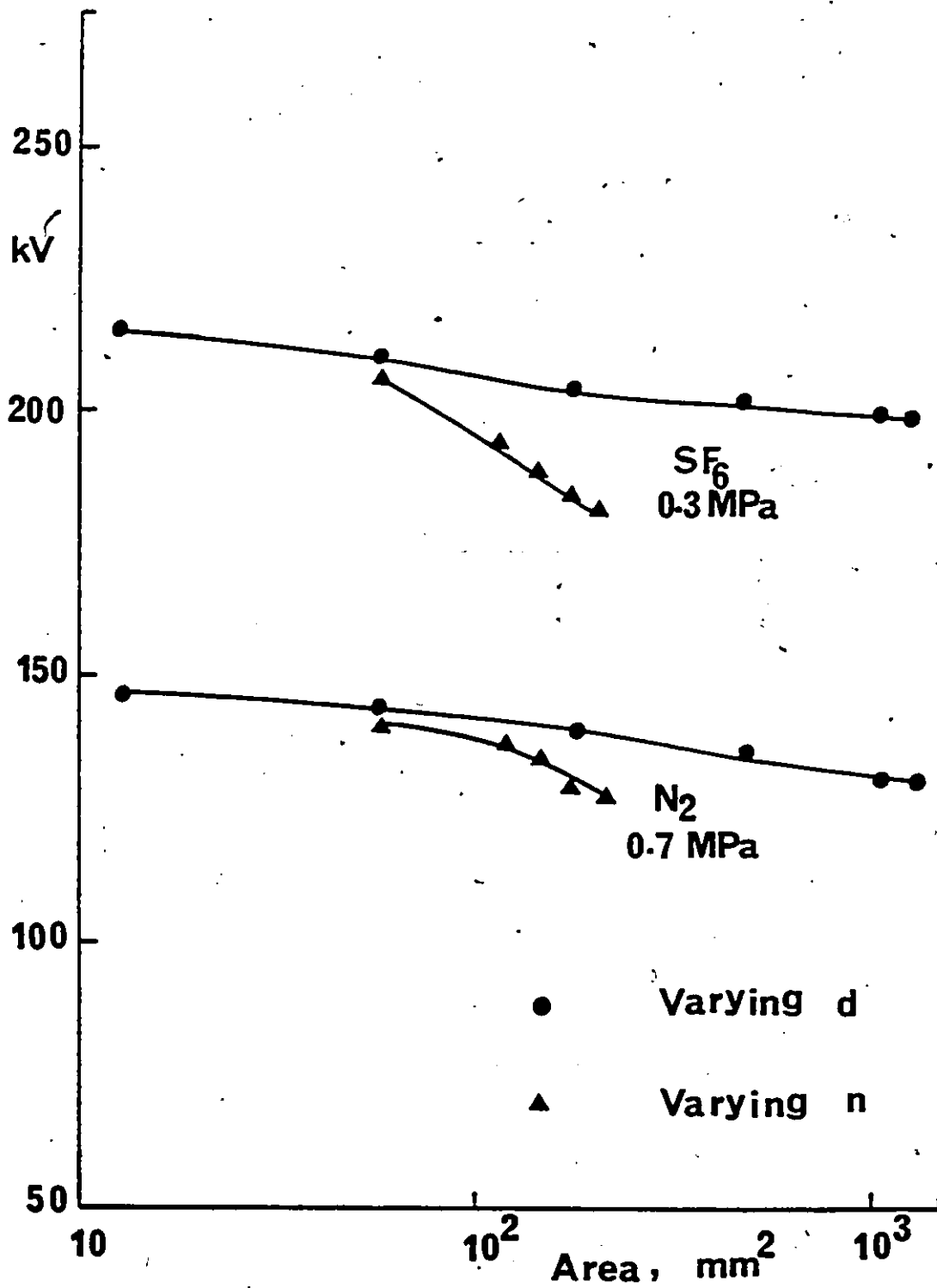
Figure 8.8: dc flashover voltage as a function of the area of the flat end of the spacer. Conditions are as for Fig. 8.1.

Chapter IX

CONCLUSIONS AND RECOMMENDATIONS FOR FUTURE WORK

9.1   Conclusions

The electric field and the potential distributions have been calculated along the surface of the proposed profiles as well as in the gas region. Spacers fabricated in accordance with the proposed profiles have been tested using dc, ac and lightning impulse. The following conclusions can be drawn:

1.   The flashover field calculated from the flashover voltage and the charge simulation method agrees with the space charge field calculated at locations where $\int \alpha \, dz$ equals about 17 in SF_6 and N_2. This confirms that the streamer criterion is also applicable for gaseous gaps bridged by spacers. It is believed that this is the first time that such analysis are successfully demonstrated in a gap bridged by a spacer.

2.   The most critical parameter in the spacer design is the total electric field at the cathode triple junction and its vicinity. As the field decreases in the vicinity of the electrodes the withstand voltage of the spacer increases.

3. The tangential and the total electric fields for a concave spacer are lower in the vicinity of the triple junction than the average applied field in the gap. The reduction in both fields depends on the contact angle θ between the spacer and the normal to the electrode and on the radius of curvature of the spacer.

4. The optimum contact angle to yield a maximum reduction in the electric field at the triple junctions is found to be 45° for profiles a and c.

5. The vertical portion near the electrodes in spacer 'b' and 'd' should be kept as small as possible to maintain a low electric field near the electrodes.

6. The electric field distribution for the proposed profiles (a,b, c and d) is symmetrical inside the solid dielectric despite the asymmetrical applied voltage to the electrodes. However, at a location away from the insulator surface the electric field is found to be higher near the high voltage electrode than at the other electrode.

7. The radius of the spacer has a small influence on the electric field distribution.

8. The radius of the transition region in spacers b and d has a small influence on the electric field components, except on the maximum normal field which decreases when the radius increases.

9.   The withstand voltage capability of a 10 mm Plexiglas spacer can be increased by as   much as 23% in   high   pressure of SF$_6$ and N$_2$ compared to the   right angle cylindrical spacer.   This significant improvement in the flashover voltage of the spacer can be attained while maintaining the same physical dimension of the gap and at the same gas pressure.

10. The flashover voltage of a 10 mm Plexiglas spacer under dc and lightning impulse are close in values. The ac flashover voltage is lower by about 10% in both SF$_6$ and N$_2$.

11. The dc flashover voltage of a Plexiglas spacer having profile a can be increased in 0.3 MPa of SF$_6$ to 96% of the breakdown voltage of the gas.

12. The recess angle γ of the electrodes   and the dimensions of the metal insert into the spacer have a strong influence on the electric field components at and in the vicinity of the cathode triple junction and on the flashover voltage. The optimum recess angle to yield the lowest field at the junction lies in the range 40° to 60°.

13. The total electric field at the cathode junction of system B decreases with increasing the radius of the groove or with decreasing the depth of the groove.

14. The ac flashover voltage of an epoxy spacer placed in recessed electrodes with γ =60° in 0.2 MPa of SF$_6$ is typically 98% of the breakdown voltage of the gas.

15. Multiple spacers in parallel decrease the dc and ac surface flashover voltages. Typically, by 12% as the number of spacers increases from 1 to 5 in SF_6 and N_2. Increasing the contact area of a single spacer with the electrodes also decreases the flashover voltage but to a lesser extent. Typically by 6% when the contact area is increased by 5 times.

9.2 Recommendations For Future Work

1. The flashover characteristics of a spacer are strongly affected by contamination. Also the flashover voltage strength depends on the type, shape and the size of the free particles. Therefore, the proposed profiles must be tested under contaminated environment.

2. There is a scarcity of data in the literature on the surface charge accumulated on the spacer and its effect on the electric field and the flashover voltage of the gap. Therefore, the surface charge distribution on the surface of these spacers need to be measured in high gas pressure of SF_6 and N_2 under different conditions of applied voltages. The analysis performed in chapter 6 can be refined with the inclusion of the field produced by the surface charge distribution. This may then enable the calculation of the flashover voltage of a rectangular cylinder which has not been possible hitherto as the apparent applied field is lower than that required for a flashover.

3. Recently, there has been a great deal of research and discussion on using SF$_6$ and nitrogen mixtures in gas insulated systems. Therefore, it is suggested that these profiles are to be tested in gas mixtures.

4. The search for better performance of spacers can be advanced by studying the dependence of the field distribution and the flashover voltage on the surface and volume resistivity of the proposed spacers as well as other shapes including tapered cones.

5. The performance of the proposed spacers in a coaxial geometry should also be investigated.

APPENDIX A

Expressions for the potential and field coefficient elements for ring charges [79].
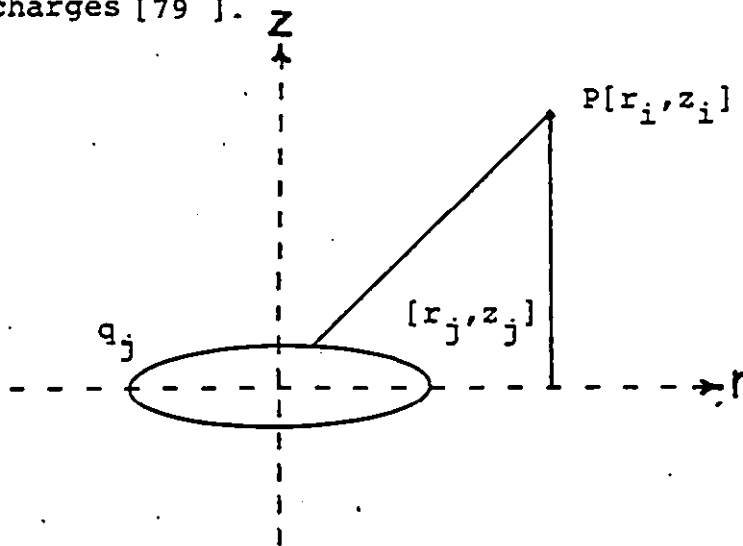
$$P_{ij} = \frac{1}{4\pi\varepsilon_0} \cdot \frac{2}{\pi} [\frac{K(K_1)}{a_1} - \frac{K(K_2)}{a_2}]$$

$$F_{ij} = - \frac{1}{4\pi\varepsilon_0} \cdot \frac{1}{\pi r_i} \frac{(r_{qj}^2 - r_{pi}^2 + (z_{pi} - z_{qj})^2)\, E(K_1) - b_1^2\, K(K_1)}{a_1 b_1^2}$$

$$- \frac{(r_{qj}^2 - r_{pi}^2 + (z_{pi} - z_{qj})^2)\, E(K_2) - b_2^2\, K(K_2)}{a_2 b_2^2}$$

where,

$$a_1 = ((r_{pi} + r_{qj})^2 + (z_{pi} - z_{qj})^2)^{\frac{1}{2}}$$

$$a_2 = ((r_{pi} + r_{qj})^2 + (z_{pi} + z_{qj})^2)^{\frac{1}{2}}$$

$$b_1 = ((r_{pi} - r_{qj})^2 + (z_{pi} + z_{qj})^2)^{\frac{1}{2}}$$

$$b_2 = ((r_{pi} - r_{qj})^2 + (z_{pi} + z_{qj})^2)^{\frac{1}{2}}$$

$$K_1 = \frac{2(r_{pi} r_{qj})^{\frac{1}{2}}}{a_1}$$

$$K_2 = \frac{2(r_{pi} r_{qj})^{\frac{1}{2}}}{a_2}$$

$$K(K_1) = \int_o^{\pi/2} \frac{1}{(1 - K_1^2 \sin^2 \theta)^{\frac{1}{2}}} \, d\theta$$

Complete elliptic integral of the first kind.

$$E(K_1) = \int_o^{\pi/2} (1 - K_1^2 \sin^2 \theta)^{\frac{1}{2}} \, d\theta$$

Complete elliptic integral of the second kind.

r_{qj} the radius of the ring charge Q_j

z_{qj} the z-coordinate of the ring charge Q_j

r_{pi} the radius of the contour point P_i

z_{pi} the z-coordinate of the contour point P_i .

Appendix B

CALCULATION OF RX
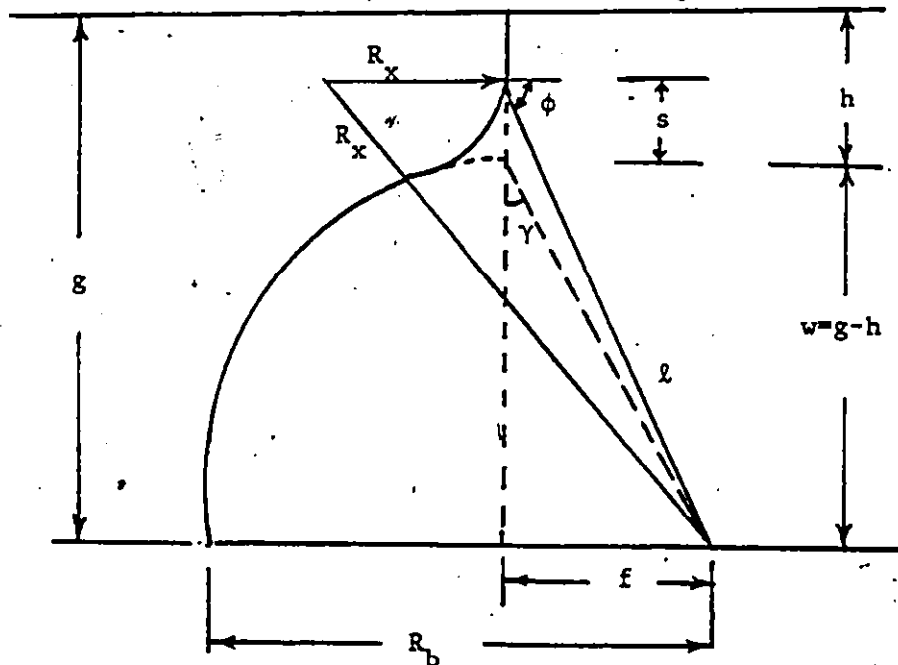
$$(Rx + Rb)^2 = Rx^2 + l^2 + 2Rx\ l\ \cos\phi$$

$$l^2 - Rb^2 = 2Rx\ (Rb - l\ \cos\phi) \qquad\qquad (B.1)$$

$$f^2 = Rb^2 - w^2$$

$$f = \sqrt{Rb^2 - w^2}$$

$$\tan\phi = \frac{w + s}{\sqrt{Rb^2 - w^2}}$$

$$\phi = \tan^{-1}\left(\frac{w + s}{\sqrt{Rb^2 - w^2}}\right) \qquad\qquad (B.2)$$

$$l^2 = Rb^2 + s^2 + 2Rb\, s\, \cos\gamma$$

$$\cos\gamma = \frac{w}{Rb}$$

$$l^2 = Rb^2 + s^2 + 2\, s\, w \tag{B.3}$$

From equations (B.1), (B.2) and (B.3),

$$Rx = \frac{l^2 - Rb^2}{2(Rb - l\cos\emptyset)}$$

$$Rx = \frac{s^2 + 2\, w\, s}{2\left(Rb - \sqrt{Rb^2 + s^2 + 2\, s\, w} \cdot \cos\left(\tan^{-1}\dfrac{w + s}{\sqrt{Rb^2 - w^2}}\right)\right)} \tag{B.4}$$

Appendix C

CALCULATION OF RY
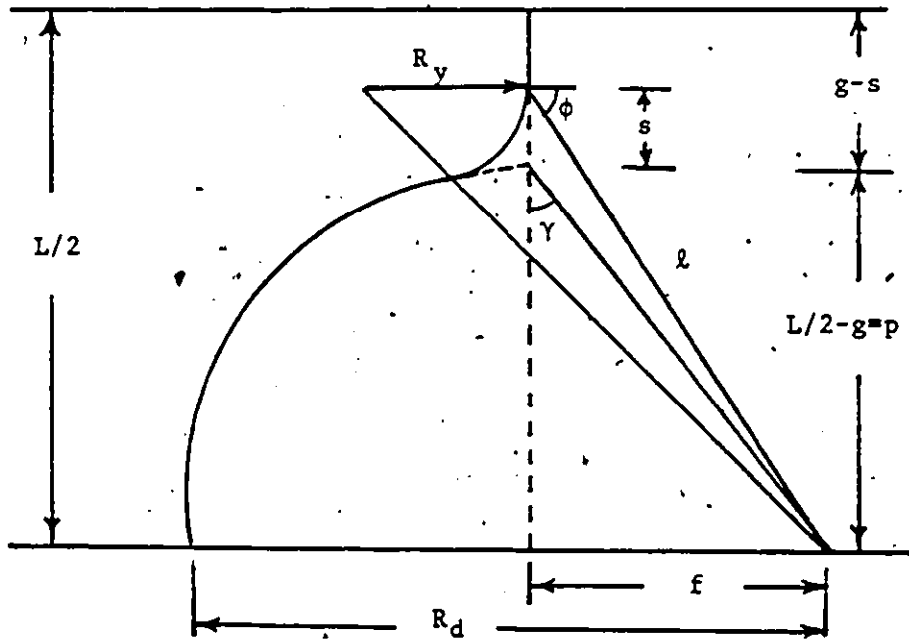
$$(Ry + Rd)^2 = Ry^2 + l^2 + 2Ry\ l \cos \phi$$

$$l^2 - Rd^2 = 2Ry\ (Rd - l \cos \phi) \qquad (C.1)$$

$$f^2 = Rd^2 - p^2$$

$$f = \sqrt{Rd^2 - p^2}$$

$$\tan \phi = \frac{p + s}{\sqrt{Rd^2 - p^2}}$$

$$\phi = \tan^{-1}\left(\frac{p + s}{\sqrt{Rd^2 - p^2}}\right) \qquad (C.2)$$

- 236 -

$$l^2 = Rd^2 + s^2 + 2Rd\ s\ \cos\gamma$$

$$\cos\gamma = \frac{p}{Rd}$$

$$l^2 = Rd^2 + s^2 + 2\ s\ p \tag{C.3}$$

From equations (C.1), (C.2) and (C.3),

$$Ry = \frac{l^2 - Rd^2}{2(Rd - l\cos\varnothing)}$$

$$Ry = \frac{s^2 + 2\ p\ s}{2(Rd - \sqrt{Rd^2 + s^2 + 2\ s\ p}\ \cdot\ \cos(\tan^{-1}\frac{p + s}{\sqrt{Rd^2 - p^2}}))} \tag{C.4}$$

Appendix D

Table D.1: TYPICAL CALCULATION OF $\bar{\alpha}$, AND $\int \bar{\alpha}\, dz$ FOR

PROFILE 'a', $\theta=60^\circ$ IN 0.2 MPA OF SF_6

$V_b=$ 176 kV, L= 10 mm.

z, cm	Ez, kV/cm	E, kV/cm	$\bar{\alpha}=\alpha-\eta$	$\int_0^Z \bar{\alpha}\, dz$
0	139.06	139.06		
0.02	151.36	145.0		
0.04	161.56	150.75		
0.06	167.2	155.17	< 0	< 0
0.08	172.3	158.75		
0.10	175.29	161.7		
0.12	177.4	164.08	-18.4	
0.14	179.0	166.07	26.4	0.15
0.16	180.22	167.5	60.56	1.02
0.18	181.05	168.94	83.8	2.46
0.20	181.56	170.15	98.08	4.28
0.22	181.56	171.36	104.8	6.30
0.24	181.96	172.21	109.28	8.44
0.26	181.96	172.92	109.28	10.62
0.28	181.8	173.54	104.8	12.76
0.30	181.63	174.06	100.04	14.80
0.32	181.45	174.53	95.0	16.75
0.34	181.40	174.91	93.60	18.65
0.36	181.10	175.25	85.20	20.45

D.1: Calculation of the space charge field E_r

From equation (6.11) and for the condition given in

Appendix D, Table D.1.

$$E_r = \frac{e \quad e^{\int_o^Z \bar{\alpha}dz}}{4\pi\varepsilon_o.2 \quad v \quad z} E$$

$$E_r = 7.1934 \times 10^8 \quad \frac{e^{\int_o^Z \bar{\alpha}dz}}{v \quad z} E$$

at z=0.32 cm

$$E_r = 7.1934 \times 10^8 \quad \frac{\exp(16.75)}{5.8 \quad x \quad 0.32} \quad 174.53 = 127.25 \text{ kV/cm}$$

at z=0.325 cm

$$E_r = 7.1934 \times 10^8 \quad \frac{\exp(17.225)}{5.8 \times 0.325} \quad 174.53 = 201.47 \text{ kV/cm}$$

at z=0.324 cm

$$E_r = 7.1934 \times 10^8 \quad \frac{\exp(17.13)}{5.8 \times 0.324} \quad 174.53 = 183.78 \text{ kV/cm}$$

at z=0.3238 cm

$$E_r = 7.1934 \times 10^8 \quad \frac{\exp(17.12)}{5.8 \times 0.3238} \quad 174.53 = 182.06 \text{ kV/cm}$$

Where E is an average value of the field between the

cathode and Z.

The applied field E_z calculated from the charge simulated method and the flashover voltage in the range $z= 0.32$ to 0.34 cm is 181.45 kV $\pm$ 0.03% (Appendix D, Table D.1).

The space charge field E_r equals to the applied field E_z to within $\pm$ 0.17% at the location $z=0.3238$ cm and at the same time satisfying the Pederson criterion of $\int \bar{\alpha} \, dz = 17.12$ hence $zc= 0.3238$ cm.

It will be observed that the space charge field E_r is very strongly dependent on z in the vicinity of zc. Hence if a change in the applied field by about 10% is included due to incorporation of the accumulated surface charges this would have only a negligible influence on the value of zc.

Appendix E

Table E.1: TYPICAL CALCULATION $\bar{\alpha}$, and $\int \bar{\alpha}\ dz$ FOR

PROFILE "c", $\theta=45°$ IN 0.1 MPA OF SF_6

Vb= 88 kV and L= 10 mm.

z, cm	Ez, kV/cm	E, kV/cm	$\bar{\alpha} = \alpha - \eta$	$\int_0^z \bar{\alpha}\,dz$
0	64.25	64.25		
0.02	70.70	67.5		
0.04	76.79	70.55		
0.06	80.9	73.33	< 0	< 0
0.08	83.91	75.62		
0.10	86.14	77.5		
0.12	87.87	79.08	-32.44	
0.14	89.23	80.43	5.64	0.008
0.16	90.37	81.56	37.56	0.44
0.18	91.29	82.56	63.32	1.45
0.20	92.0	83.45	83.2	2.91
0.22	92.72	84.23	103.36	4.77
0.24	93.30	84.96	119.6	7.04
0.26	93.78	85.62	133.04	9.52
0.28	94.19	86.21	144.52	12.29
0.30	94.51	86.73	153.48	15.27
0.32	94.86	87.22	163.28	18.43
0.34	95.12	87.65	170.56	21.77

E.1 Calculation of the space charge field Er

From equation (6.11) and Appendix E, Table E.1.

$$Er = \frac{e \cdot e^{\int \bar{\alpha} dZ}}{4\pi\varepsilon_0 \cdot 2 \quad v \quad z} \; E$$

$$Er = 7.1934 \times 10^{8} \; \frac{e^{\int \bar{\alpha} dZ}}{v \quad z} \; E$$

at z=0.3 cm

$$Er = 7.1934 \times 10^{8} \; \frac{\exp(15.27)}{5.8 \times 0.3} \; 56.73 = 15.35 \text{ kV/cm}$$

at z=0.31 cm

$$Er = 7.1934 \times 10^{8} \; \frac{\exp(16.85)}{5.3 \times 0.31} \; 86.98 = 72.3 \text{ kV/cm}$$

at z=0.313 cm

$$Er = 7.1934 \times 10^{8} \; \frac{\exp(17.376)}{5.8 \times 0.313} \; 87.0 = 121.35 \text{ kV/cm}$$

at z=0.312 cm

$$Er = 7.1934 \times 10^{8} \; \frac{\exp(17.166)}{5.8 \times 0.312} \; 87.0 = 98.62 \text{ kV/cm}$$

at z=0.311 cm

$$Er = 7.1934 \times 10^{8} \; \frac{\exp(17.008)}{5.8 \times 0.311} \; 87.0 = 84.47 \text{ kV/cm}$$

at z=0.3115 cm

$$Er = 7.1934 \times 10^{8} \; \frac{\exp(17.1)}{5.8 \times 0.3115} \; 87.0 = 92.47 \text{ kV/cm}$$

at z=0.3118 cm

$$Er = 7.1934 \times 10^{8} \; \frac{\exp(17.12)}{5.8 \times 0.3118} \; 87.0 = 94.24 \text{ kV/cm}$$

The values of Ez in the range z= 0.3 to 0.32 cm is 94.51 kV ± 0.37% (Appendix E, Table E.1).

At z= 0.3118 cm, Er= Ez within ± 0.25% and at the same time satisfying $\int \bar{\alpha} dz = 17.12$, therefore zc= 0.3118 cm.

Appendix F

Table F.1: TYPICAL CALCULATION OF α , AND $\int \alpha\, dz$ FOR

PROFILE 'a', $\theta=45°$ IN 0.3 MPA OF N_2

Vb= 84 kV and L= 10 mm.

z, cm	Ez, kV/cm	E, kV/cm	α	$\int_0^z \alpha\, dZ$
0	64.89	64.89	3.25	0
0.02	72.48	68.5	6.92	0.1
0.04	78.04	71.75	10.96	0.279
0.06	81.08	74.33	13.73	0.526
0.08	83.18	76.25	15.88	0.822
0.10	84.62	77.8	17.48	1.155
0.12	85.63	79.0	18.65	1.516
0.14	86.3	80.0	19.46	1.897
0.16	86.8	80.81	20.08	2.29
0.18	87.14	81.5	20.51	2.698
0.20	87.36	82.05	20.78	3.11
0.22	87.4	82.54	20.83	3.53
0.24	87.38	82.96	20.81	3.95
0.26	87.23	83.3	20.62	4.36
0.28	87.14	83.57	20.51	4.77
0.30	86.97	83.8	20.29	5.18
0.32	86.8	84.0	20.08	5.59
0.34	86.72	84.15	19.98	5.98
0.36	86.55	84.28	19.77	6.377
0.38	86.47	84.39	19.67	6.77
0.40	86.39	84.47	19.57	7.16
0.42	86.38	84.57	19.56	7.55
0.44	86.30	84.64	19.46	7.94
0.46	86.29	84.69	19.45	8.33
0.48	86.27	85.125	19.43	8.72
0.5	86.22	85.16	19.36	9.108

Since the electric field distribution along the spacer surface is symmetrical, $\int_0^{1\,Cm} \alpha\, dz = 18.216$

F.1 Calculation of the space charge field Er

From equation (6.11) and Appendix F, Table F.1.

$$Er = \frac{e \cdot e^{\int \alpha dz}}{4\pi \varepsilon_0 .2 \quad v \quad z} \varepsilon$$

$$Er = 7.1934 \times 10^8 \frac{e^{\int \alpha dz}}{v \quad z} \varepsilon$$

at z=1.0 cm

$$Er = 7.1934 \times 10^8 \frac{\exp(18.216)}{2.38 \times 1.0} \quad 85.16 = 209.74 \text{ kV/cm}$$

at z=0.96 cm

$$Er = 7.1934 \times 10^8 \frac{\exp(17.937)}{2.8 \times 0.96} \quad 35.71 = 141.41 \text{ kV/cm}$$

at z=0.92 cm

$$Er = 7.1934 \times 10^8 \frac{\exp(17.394)}{2.82 \times 0.92} \quad 85.93 = 85.33 \text{ kV/cm}$$

at z=0.918 cm

$$Er = 7.1934 \times 10^8 \frac{\exp(17.3607)}{2.82 \times 0.918} \quad 85.95 = 82.74 \text{ kV/cm}$$

The values of the applied field Ez at the above locations are

$$Ez(1.0) = 64.89 \text{ kV/cm}$$

$$Ez(0.96) = 78.04$$

$$Ez(0.92) = 83.18$$

$$Ez(0.918) = 83.324$$

At z= 0.918 cm. Er= Ez within ± 0.35% and $\int \alpha dz = 17.36$

hence zc=0.918 cm.

BIBLIOGRAPHY

1. A.H. Cookson, "Gas Insulated Cables", IEEE Trans. Vol. EI-20, PP.859-890, 1985.

2. K.Itaka and G.Ikeda, "Dielectric Characteristic of Compressed Gas Insulated Cables", IEEE. Trans. Vol, PAS-89, PP. 1986-1994, 1970.

3. H.Ryan, D.Lightle and D.Milne, Factors Influencing Dielectric Performance of SF_6 Insulated GIS", IEEE. Trans. Vol, PAS- 104, PP. 1527-1535, 1985.

4. A.H.Cookson, "Review of High Voltage Gas Breakdown and Insulators in Compressed Gas", Proc. IEE. Vol, 128, PP.303-312, 1981.

5. D.J.Skipper, "Impulse Strength Measurements on Compressed Gas Insulation for Extra High Voltage Power Cables", Proc.IEE, Vol, 112, PP. 103-105, 1965.

6. S.Fukuda, "EHV Cables with Compressed SF_6 Gas Insulation", IEEE. Trans. Vol, PAS-86, PP. 60-64, 1967.

7. C.Cooke and J.Trump, "Post Type Support Spacers for Compressed Gas Insulated Cables", IEEE. Trans. Vol, PAS- 92, PP. 1441-1447, 1973.

8. J.Cronin and E. Perry, "Optimization of Insulators for Gas Insulated Systems", IEEE. Trans. Vol, PAS-92, PP.558-564, 1973.

9. T.Nitta, Y.Shibuya, Y.Fujiwara, Y.Arahata, H.Takahashi and H.Kuwahara, "Factors Controlling Surface Flashover in SF_6 Gas Insulated Systems", IEEE. Trans. Vol, PAS- 97, PP. 959-965, 1987.

10. C.Cooke, "Surface Flashover of Gas/ Solid Interface", Proc. of 3 rd Int. Symp. on Gaseous Dielectric, 1982, paper 3.

11. T.J.Gallagher and A.J.Peamain, "Surface Flashover in N_2 and SF_6 at High Gas Pressures", IEEE. Proc.

of Int. Symp. on Electrical Insulation, 1980, PP.52-55.

12. N.Trinh, F.M.Rizk and C.Vincent, "Electrostatic Field Optimization of the Profile of Epoxy Spacers for Compressed SF₆ Insulated Cables", IEEE. Trans. Vol, PAS- 99, PP.2164-2174, 1980.

13. A.H.Cookson, "Electrical Breakdown for Uniform Fields in Compressed Gases", Proc. IEE. Vol, 117, PP. 269-280, 1970.

14. T.Takuma and T.watanabe, "Optimal Profiles of Disc Type Spacers for Gas Insulation", Proc. IEE. Vol, 122, PP. 183-188, 1975.

15. C.N.Reddy, R.Lakshmipathi and K.V. Abraham, "Surface Flashover Characteristics of Epoxy Spacers in Compressed Gases", Proc. of 4 th Int. Symp. on Gaseous Dielectric, 1984, PP.396-404.

16. J.H.Mason, "Discharges", IEEE. Trans. Vol, EI-13, PP. 211-238, 1978.

17. P.Paul and C.Reddy, "Breakdown Characteristics of Solid Dielectrics Immersed in High Pressure Gaseous Media and Subjected to Direct Voltages with Ripple", IEEE. Trans. Vol, EI- 15, PP. 43-52, 1980.

18. J.Trump and J.Andrias, "High Voltage DC Flashover of Solid Insulators in Compressed Nitrogen", AIEE Trans. Vol, 60, PP. 986-990, 1941.

19. N.Trinh, "Consideration of Insulator Surface Flashover and its Influence on Gas Insulated Substation Design", Paper Presented at the CEA, Spring Meeting, Montreal, Quebec, 1985.

20. B.Blankenburg, "Surface Flashover Behaviour of Cylindrical Insulators in SF₆, N₂ and SF₆ - N₂ Mixtures", Proc. of 3 rd Int. Symp. on High Voltage Engineering, 1979, Paper 32.03.

21. R.Lee, H.Rhinehart, J.E.Thompson and T.S.Sudarshan, "Predischarge Current Measurements and Optical Surface Field Measurements Associated with Insulator Surface Flashover", Proc. of 3 rd Int. Symp. on Gaseous Dielectric, 1982, PP. 349-355.

22. M.Giesselmann and W.Pfeiffer, "Influence of Solid Dielectrics upon Breakdown Voltage and

Predischarge Development in Compressed Gases",
Proc. of 4th Int. Symp. on Gaseous Dielectric,
1984, PP.431-435.

23. T.Takuma, T.Watanabe and T.Kuono, "Effect of a
Narrow Gas Gap on the Surface Flashover of
Spacers in SF₆", Proc. of Int. Symp. on High
Voltage Engineering, 1975, PP.443-450.

24. K.Itaka and T.Hara, "Influence of Local Field
Concentration on Surface Flashover
Characteristics of Spacers in SF₆ Gas", Proc. of
Int. Symp. on Electrical Insulation, 1980,
PP.56-60.

25. I.B.Jorden and R.S.Araraud, "Triple - Junction :
Metal - Gas - Solid Dielectric", 1980 Annual
Report, Conf. on Elec. Insulation and Dielectric
Phenomena, PP. 443-450.

26. A.S.Pillai and R.Hackam, "Improved Performance of
Cylindrical Solid Insulators with Concave Curved
Edges in Vacuum", IEEE. Trans. Vol, PAS- 103,
PP. 2418-2427, 1984.

27. M.S.Rizk and R.Hackam, "Up Grading of Gas
Insulated Systems with Concave Shaped
Insulators", IEEE. Proc. of Int. Symp. on
Electrical Insulation, 1986, PP. 289-292.

28. P.R.Howard, "Insulation Properties of Compressed
Electronegative Gases", AIEE. Trans. Vol, 104,
PP. 123-138, 1957.

29. B.F.Hampton, "Impulse Flashover of Particle
Contaminated Spacers in Compressed
Sulpherhexafluoride", Proc. IEE. Vol, 120,
PP.514-518, 1973.

30. P.M.Clark, "Insulating Materials for Design and
Engineering Practice", John Wiley & Sons, Inc.,
New York, 1962.

31. A.Bargigia, R.Brambilla, A.Pigini and G.Rizzi,
"Influence of Solid Insulation on the Dielectric
Performance of SF₆ Configurations", Proc. of 4th
Int. Symp. on Gaseous Dielectric, 1984,
PP.437-442.

32. T.Mizukami, H.Sato and N.Ando, "Gas Insulated
Transmission Cables with Prefabricated Unit",
IEEE. Trans. Vol, PAS- 98, PP.1709-1716, 1979.

33. P.Greenwood, "Surface Flashover in Compressed SF6", IEE. 2nd Int. Conf. on Gas Discharge, PP.233-235, 1972.

34. R.J.Meats and B.G.Williams, "The Flashover of Dielectric Spacers in Cold Compressed Helium", IEE. 3rd Int. Conf. on Gas Discharge, PP. 643-647, 1974

35. J.R.Laghari, "Spacer Flashover in Compressed Gases", IEEE. Trans. vol, EI- 20, PP.83-92, 1985.

36. G.W.Supple, R.J.Kyle and R.V.Snow, "Installation of a 230 kV Compressed Gas Insulated Bus", IEEE. Trans. Vol, PAS - 93, PP. 349-353, 1974.

37. M.S.Mashikian, B.P.Whitney and J.J.Freeman, "Optimal Design and Laboratory Testing of Post Type Spacers for Three Phase SF6 Insulated Cables", IEEE. Trans. Vol, PAS- 97, PP. 919-925, 1978.

38. T.Takagi, H.Hayashi, T.Higashino, K.Itaka, T.Araki, E.Kusakabe, M.Morita and H.Hata, "Development of 550 kV Gas Spacer Cable: Part II: The Voltage Characteristic and Construction", IEEE. Trans. Vol, PAS- 97, PP. 1740- 1748 , 1978.

39. T.Kobayashi, S.Mori, M.Koshishi, K.Ninomiya, M.Mastsuki, H.Yokoyama and T.Hara, "Development of Compact 500 kV 8000 A Gas Insulated Transmission Line ", IEEE. Trans. Vol, PAS - 103, PP. 3154-3164, 1984.

40. M.S.Mashikian, B.F.Whitney and J.J.Freeman, "Optimal Design and Laboratory Testing of Post Type Spacers for Three Phase SF6 Insulated Cables", IEEE. Trans. Vol, PAS- 97, PP. 914-918, 1978.

41. S.L.Johnson and H.C.Doepken,Jr. "Discussion", IEEE. Trans. Vol, PAS- 92, PP.558-564, 1973.

42. H.Hayashi, T.Higashino, S.Nishihara and K.Itaka, "Dielectric Strength of SF6 Gas and 3 Core Type CGI Cables under Inter - Phase Switching Impulse Voltages", IEEE. Trans. Vol, PAS - 93, PP. 354- 359, 1974.

43. B.O.Pederson, H.C.Doepken,Jr. and P.C.Bolin, "Development of Compressed Gas Transmission Line", IEEE. Trans. Vol, PAS- 90, PP.2631-2638, 1971. ;

44. N.G.Trinh, G.R.Mitchel and C.Vincent, "Influence of an Insulating Spacer on the V-t Characteristics of Coaxial Conductors with Compressed SF₆ Insulation", Proc. of 4th Int. Symp. on Gaseous Dielectric. 1984, PP.335-343.

45. E.M.Spencer, R.W.Samm, J.Artbuer and F.Schatz, Research and Development of a Flexible 362 kV Compressed Gas Insulated Cable", CIGRE. Paris, 1980, Paper 21.02.

46. D.B.Miller, E.M.Spencer, P.J.Kroon and P.C.Netzel, "Flexible Gas Insulated Cable for 230 kV, 345 kV, and 500 kV", IEEE. Trans. Vol, PAS - 103, PP.2480 - 2485,1984.

47. S.Menju and K.Takahashi, "DC Dielectric Strength of a SF₆ Gas Insulated System", IEEE.Trans. Vol, PAS -97, PP.217-224, 1978.

48. G.R.Bar, A.Diessner and G.F.Luxa, "420 kV SF₆ Insulated Tubular Bus for the Wehr Pumped Storage Plant - Electrictests", IEEE. Trans. Vol, PAS - 95, PP.469-477, 1976.

49. S.Meju, Y.Tsuchikawa and N.Kobayshi, "Electric Potential and Field of Conical Insulators for SF₆ Metalclad Switchgear", IEEE. Trans. Vol, PAS - 91, PP.390-398, 1972.

50. B.F.Hampton, D.N.Browning and R.M.Mayes, "Outline of a Flexible SF₆ Insulated EHV Cable", Proc. IEE. Vol, 123, PP.159-164, 1976.

51. N.Trinh, and C.Vincent, "Bundled Conductors for EHV Transmission Systems with Compressed SF₆ Insulation ", IEEE. Trans. Vol, PAS - 97, PP.2198-2206, 1978.

52. A.Knecht, "Development of Surface Charges on Epoxy Resin Spacer Stressed with Direct Applied Voltages ", Proc. of 3rd Int. Conf. on Gaseous Dielectric, 1982, PP.356-364.

53. T.Stoop, J.Tom, H.F.A.Verhoart and A.J.L.Verhage, "The Role of Electrostatic Charge in Insulator Flashover in SF₆", Proc. of Int. Conf. on Gas Discharge and Their Application, 1985.

54. N.Nakanishi, A.Yoshioka, Y.Shibuya and T.Nitta, "Charge Accumulation on Spacer Surface at DC Stress in Compressed SF₆ Gas ", Proc. of 3rd Int. Conf. on Gaseous Dielectric, 1982, PP.365-368.

55. A.Pillai and R.Hackam, "Modification of Electric Field at the Solid Insulator - Vacuum Interface Arising from Surface Charges on the Solid Insulator", J.Appl.Phys. 54, 1983, PP.1302-1313.

56. C.W.Mangelsdorf and C.M.Cooke, "Bulk Charging of Epoxy Insulating under DC Stress", IEEE. Proc. of Int. Conf. on Electrical Insulation, 1980, PP.146-149.

57. K.Nakanishi, A.Yoshioka, Y.Arahata and Y.Shibuya, "Surface Charging of Epoxy Spacer at DC Stress in Compressed SF_6 Gas", IEEE. Trans. Vol. PAS- 102, PP.3919-3927, 1983.

58. M.Eteiba, F.A.M.Rizk, N.G.Trinh and C.Vincent, "Influence of a Conducting Particle Attached to an Epoxy resin Spacer on the Breakdown Voltage of Compressed Gas Insulation", Proc. of 2nd Int. Symp. on Gaseous Dielectric, 1980, PP.250-255.

59. "Compressed Gas Cables in Use Internationally", CIGRE Working Group 12.12, Electra No.94, PP.55- ,1984.

60. J.R. Laghari and A.M. Qureshi, "Surface Flashover of Spacers in Compressed Gas Insulated Systems", I.EEE. Trans. vol. EI- 16, PP. 373-387, 1981.55- ,1984.

61. A.H.Cookson, D.R.James, R.Eaton, R.Hackam, K.Nakanishi, J.J.Pachot, A.Pigini and F.Pinnekamp, "Group Discussion on Requirements of Gas Mixtures for Power Transmission and Distribution Lines", Proc. of 4th Int. Symp. on Gaseous Dielectric,1984, PP.561-573.

62. A.H.Cookson, S.A.Boggs, B.F.Hampton, D.Miller, A.Rein, R.W.Samm, T.Takuma and J.Vigreux, "Forum I: Gas Insulated Equipment", Proc. of 3rd Int. Symp. on Gaseous Dielectric, 1982, PP.545-551.

63. "Panel Discussion on Charging and Flashover of Insulator in Compressed Gases", Proc. of 3rd Int. Symp. on Gaseous Dielectric, 1982, PP.556-567.

64. T.Takuma and T.Kawamoto, "Field Intensification Near Various Points of Contact with a Zero Contact Angle Between a Solid Dielectric and an Electrode", IEEE. Trans. Vol. PAS- 103, PP.2486- 2494, 1934.

65. M.D.R.Beasley, J.H.Pickles, L.Beretta, M.Famelli, G.Giuseppetti, A.di.Monaco, G.Gallet, J.P.Gregoire and M.Morin, "Comparative Study of Three Methods for Computing Electric Fields", Proc. IEE. Vol. 126, PP.126-134, 1979.

66. P.K.Mukherjee and C.K.Roy, "Computation of Fields in and Around Insulators by Fictitious Point Charges", IEEE. Trans. Vol, EI-13, PP.24-31, 1978.

67. M.S.Rizk, R.Hackam and M.M.A.Salama, "Calculation of the Inception Voltage in Voids Within Dielectric Materials", IEEE. Proc. of Int. Conf. on Electrical Insulation,1986, PP.129-134.

68. C.M.Dorney, "Finite Difference Method for Determining Capacitance Relationship Among Arbitrary Shape Conductors", IEEE. Trans. Vol, PAS- 90, PP.876-881, 1971.

69. K.J.Binns and P.J.Lawrenson, "Analysis and Computation of Electric Field Problems", 2 nd ed. Pergamon Press, 1973.

70. M.M.A.Salama, M.S.Rizk and R.Hackam, "Electrical Stress and Inception Voltage of Discharges in Gaseous Cavities in an Anisotropic Dielectric Material", J.Appl. Phys. Vol, 60, 1986, PP.2600-2608.

71. S.G.Kellison, "Fundamentals of Numerical Analysis", Irwin. Homewood, Ill, 1975.

72. H.Thornton, "The Finite Element Method for Engineering", 2 nd ed. Jhon Wiley & Sons, 1982.

73. W.Janischewskyj and G.Gela, "Finite Element Solution for Electric Fields of Coronating DC Transmission Lines", IEEE. Trans. Vol, PAS- 98, PP.1000-1012, 1979.

74. O.W.Andersen, "Finite Element Solution of Complex Potential Electric Fields", IEEE. Trans. Vol, PAS-96, PP.1156-1160,1977.

75. K.Kuffel and W.S.Zaengle, "High Voltage Engineering", Pergamon Press, 1984.

76. J.H.Pickles, "Monte Carlo Field Calculations", Proc. IEE. Vol, 124, PP.1271-1276, 1977.

77. J.Daffe and R.G.Olsen, "An Integral Equation Technique for Solving Rotationally Symmetric Electrostatic Problems in Conducting and Dielectric Materials". IEEE. Trans. Vol. PAS-98, PP.1609-1616, 1979.

78. R.F.Harrington, K.Potappin, P.Abrahamsem and N.C.Albertsen, "Computation of Laplacian Potentials by an Equivalent Source Method". Proc. IEE. Vol. 116, PP.1715-1720, 1969.

79. H.Singer, H.Steinbigler and P.Weiss, "A Charge Simulation Method for The Calculation of High Voltage Fields". IEEE. Trans. Vol. PAS-93, PP.1660-1668, 1974.

80. T.Takuma, T.Kawamoto and H.Fujinami, "Charge Simulation Method With Complex Fictitious Charges for Calculating Capacitive- Resistive Fields". IEEE. Trans. Vol. PAS-100, PP.4665-4672, 1981

81. A.S.Pillai, R.Hackam and P.H.Alexander, "Influence of Radius of Curvature, Contact Angle and Material of Solid Insulator on Electric Field in Vacuum(and gaseous) Gaps". IEEE.Trans. Vol. EI-18, PP.11-22, 1983.

82. M.Akazaki and K.Mishijima, "Calculation of Three Dimensional Axisymmetric Fields by Charge Simulation Method". Electrical Engineering in Japan, Vol. 98, PP.1-7, 1973.

83. T.Takuma, T.Kouno and H.Metsuda, "Field Behavior Near Singular Points in Composite Dielectric Arrangements". IEEE. Trans. Vol. EI-13, PP.426-435, 1978.

84. A.Yializis, E.Kuffel and P.H.Alexander, "An Optimized Charge Simulation Method for the Calculation of High Voltage Fields". IEEE.Trans. Vol. PAS-97, PP.2434-2438, 1978.

85. M.M.A.Salama and R.Hackam, "Voltage and Electric Field Distributions and Discharge Inception Voltage in Insulated Conductors". IEEE. Trans. Vol. PAS-103, PP.3425-3433, 1984.

86. M.M.A.Salama, R.Hackam and A.Nosseir, "Voltage Rating Of a Three Core Cable From Considerations of Discharge in Voids". IEEE. Trans. Vol. PAS-103, PP.3442-3447, 1984.

87. M.Abou-Seada and E.Nasser, "Digital Computer Calculation of the Potential and its Gradient of a Twin Cylindrical Conductor", IEEE. Trans. Vol. PAS-88, PP.1802-1814, 1969.

88. M.Abou-Seada and E.Nasser, "Calculation of The Potential Gradient of Twin Cylinderical Bipolar Conductors", IEEE. Trans. Vol. PAS-90, PP.1822-1829,1971.

89. M.S.Rizk and R.Hackam, "Performance Improvement of Insulators in a Gas Insulated System", IEEE. Trans. Vol. EI-22, PP. 439-446, 1987.

90. M.S.Rizk and R.Hackam, "Insulator Shaping to Render Enhanced Withstand Voltage", IEEE. Trans. EI, 1988 TO Be Published.

91. J.J. Thwaites, "The Electric Field at any Point of a Sphere gap", Proc. IEE. PP.600-605,1969.

92. G.W. Carter and S.C. Loh, "The Calculation of the Electric Field in a Sphere gap by means of Bipolar Co-ordinates", Proc. IEE. PP. 108-111, 1959.

93. S.K. Nkusi, P.H. Alexander and R. Hackam, "Potential and Electrical Field Distributions at High Voltage Insulator Shed", Accepted for publication, IEEE. Trans. EI, 1988.

94. H.L.Saums and W.W.Pendleton, "Materials for Electrical Insulating and Dielectric Functions", Hayden Book Company, Inc., 1973.

95. L.L.Alston, "High Voltage Technology", Oxford University Press, 1968.

96. P.M.Bruce, "Calibration of Uniform Field Spark Gaps for High Voltage Measurements at Power Frequencies", Proc. IEE. Vol.-94 , 1947, PP.138-154.

97. J.A.Harrison, "A Computer Study of Uniform Field Electrodes", Brit. J. App. Phys., 1967, Vol. 18, PP.1617-1627.

98. A.S.Pillai and R.Hackam, "Effect of dc Pre-Stress on ac and dc Surface Flashover of Solid Insulator in Vacuum", I.E.E.E. Trans. on Elec. Insulation, Vol. 18, 1983. pp. 292-300.

93. A.Pedersen, "Criteria for Spark Breakdown in Sulfur Hexafluoride", IEEE. Trans. Vol- PAS-89, 1970, PP.2043-2048.

100. J.M. Meek and J.D. Craggs, "Electrical Breakdown of Gases", John Wiley & Sons, 1978.

101. Raether, "Electron Avalanches and Breakdown in Gases", London Butter Worths, 1964.

102. Essam Nasser, "Fundamental of Gaseous Ionization and Plasma Electronics", Wiely- Inter science, 1970.

103. G.R.G. Raju and R. Hackam, "Breakdown Field Strength of SF_6, N_2O, SF_6+N_2, and SF_6+N_2O", J. Appl. Phys. 52, 1981, PP. 3912-3920.

104. A.E. Heylen, "Townsend's First Ionization Coefficient in Pure Nitrogen", Nature, No.4674, 1959, PP. 1545-1546.

105. A.H. Cookson, B.W. Ward and T.J. Lewis, "Townsend's First Ionization Coefficient for Methane and Nitrogen", Brit. J. App. Phys., 1966, Vol, 17, PP.891-903.

106. K.Itaka, T.Hara, T.,Misaki and H. Tsuboi, "Improved Structure Avoiding Local Field Intensification on Spacers in SF_6 Gas", I.E.E.E. Trans. Vol. PAS-102, PP. 250-255, 1983.

107. A.S. Pillai and R. Hackam, "Electric Field Distribution at Solid Insulator- Vacuum Interface of Different Electrode Insulator Geometries", I.E.E.E. Trans. Vol. EI-19, PP.502-511, 1984.

108. A.S.Pillai and R. Hackam, "OPtimal Electrode Solid Insulator, Geometry with Accumulated Surface Charges", I.E.E.E. Trans. Vol. EI-19, PP.321-331, 1984.

109. M.S.Rizk and R.Hackam, "Application of Charge Simulation Technique to the Design of GIS Spacer", Int. Conf. on High Voltage Engg. Braunschweig, Germany, 1987.

110. M.J.Kofoid, "Effect of Metal- Dielectric Junction Phenomena on High Voltage Breakdown Over Insulators in Vacuum", Trans. AIEE. Vol.79, PP.993-1004, 1960.

111. T.S.Sudarshan and J.D.Cross, "DC Electric Field Modifications Produced by Solid Insulators Bridging a Uniform Field Vacuum Gap", I.E.E.E. Trans. Vol. EI-8, PP.122-128, 1973.

112. J.Junchnicwicz, B.Mazurek and A.Tyman, "The Effect of The Number of Spacer Insulators on The Breakdown Voltage of Vacuum Insulation", I.E.E.E. Tran. on Elec. Insulation, Vol.EI-14, PP.107-110,1979.

113. T.Nitta, N.Yamada and Y.Fujiwara, "Area Effect of Electrical Breakdown in Compressed SF₆", I.E.E.E. Trans. Vol. PAS-93, PP.623-629, 1974.

114. T.Nitta, Y.Fujiwara, F.Fndo and J.Ozawa, "Effects of Electrode and Solid Insulator on the Flashover in Compressed SF₆", CIGRE, 1976, Paper 15-04.

115. A.S.Pillai and R. Hackam, "Surface Flashover of Solid Insulators in Atmospheric Air and Vacuum", J. Appl. Phys. Vol. 85, PP.146-152, 1985.

116. B.Mazurek and J.D.Cross, "An Energy Explanation of the Area Effect in Electrical Breakdown in Vacuum", IEEE. Trans. Vol. EI-22, PP.341-346, 1987.

117. J.D.Cross and B.Mazurek, "Area Effect on Surface Flashover Voltage in Vacuum", Proc. XII th. Int. Symp. on Discharge and Electrical Insulation in Vacuum, 1986, PP.84-85.

VITA AUCTORIS

1978	Graduated from Ain Shams University, Cairo, Egypt with B.Sc. degree in Electrical Engineering in Electrical Engineering.
1978 - 1982	Lecturer in the Electrical Engineering Department.
1983	Graduated with a M. A. Sc. degree in Electrical Engineering.
1984	Joined the Electrical Engineering Department, University of Windsor, Ontario, Canada, for Ph.D. program.
1988	Candidate for the degree of Doctor of Philosophy.